Boron chalcogenides under extreme conditions

Kirill Cherednichenko

To cite this version:

Kirill Cherednichenko. Boron chalcogenides under extreme conditions. Chemical Physics [physics.chem-ph]. Université Pierre et Marie Curie - Paris VI, 2015. English. NNT : 2015PA066602 . tel-01660119

HAL Id: tel-01660119

https://theses.hal.science/tel-01660119

Submitted on 10 Dec 2017

École Doctorale №397 :
Ecole Doctorale Physique et
Chimie des Matériaux

Thèse présentée par

Kirill Cherednichenko

Pour obtenir le titre de

Docteur de l'Université Pierre et Marie Curie

Boron Chalcogenides under Extreme Conditions

Date de Soutenance : 8 Décembre 2015

Composition du jury :

Dr. Jean-Louis Hodeau	Rapporteur
Prof. Fernando Rodriguez	Rapporteur
Prof. Chrystèle Sanloup	Examinateur
Prof. Domingo Martinez-Garcia	Examinateur
Dr. Stefan Klotz	Directeur de thèse
Dr. Jean-Paul Itié	Co-Directeur de thèse
Dr. Yann Le Godec	Encadrant
Prof. Vladimir Solozhenko	Encadrant

Thèse préparée au sein du laboratoire

Synchrotron SOLEIL

L'Orme des Merisiers Saint-Aubin - BP 48, 91192, Gif-sur-Yvette, CEDEX, France.

Dedicated to my parents

Remerciements

Le travail présenté dans cette thèse a été réalisé dans le cadre du projet ANR programme Blanc «BCNOP» (Synthesis of Novel High-Pressure Phases in the B–C–N–O–P System) au sein des laboratoires synchrotron SOLEIL, IMPMC (UPMC) et LSPM-CNRS (Université Paris 13). Je tiens à remercier l'Agence Nationale de la Recherche pour le financement de ce projet.

J'exprime toute ma reconnaissance au Prof. Fernando Rodriguez et au Dr. Jean-Louis Hodeau qui m'ont fait l'honneur de rapporter et examiner ce travail. Je tiens aussi à remercier la Prof. Chrystèle Sanloup et le Prof. Domingo Martinez-Garcia pour avoir accepté de participer à mon jury de thèse.

Toute ma reconnaissance et ma sympathie vont également au directeur « administratif » de ma thèse Dr. Stefan Klotz, ainsi qu'au co-directeur de la thèse Dr. Jean-Paul Itié et à mes encadrants, le Prof. Vladimir L. Solozhenko et Dr. Yann Le Godec, pour m'avoir accueilli, orienté, encadré et soutenu, pour leurs conseils et leur interminable patience tout le long de ma thèse.

Je remercie aussi les membres de la ligne PSICHE du synchrotron SOLEIL, en particulier Nicolas Guignot, Andrew King pour leur aide, patience, soutien et gentillesse, et Pierrick Zerbino pour le support technique. Je dois mes remerciements à Aleksandr Kalinko pour les calculs *ab initio* qui était une grande contribution à la thèse. Mes remerciements vont aussi à Stéphanie Blanchandin, Francois Baudelet, Lucie Nataf, Leonardo Properzi, Manh-Hung Chu, Arlensiú Celis et Maya Narayanan Nair.

Je remercie également l'équipe de l'IMPMC à l'Université Pierre et Marie Curie. Je dois ma reconnaissance à Hicham Moutaabbid pour son aide dans les mesures SEM dont les résultats ont été utilisés dans cette thèse, à Pascal Munsch et à Gilles Le Marchand pour leur disponibilité et aide dans la préparation des CEDs, à Keevin Beneut pour son aide et assistance dans les mesures Raman sous haute pression et à Benoit Baptiste pour son aide dans les mesures XRD. Je voudrais remercier Alain Polian pour son soutien, sa gentillesse, l'échange d'information et une grande contribution à la thèse. Mes remerciements vont aussi à Oleksandr Kurakevych, Frederic Datchi, Sandra Ninet et Simon Ayrinhac.

Je dois mes remerciements à l'équipe ID27 du synchrotron ESRF en particulier à Mohamed Mezouar, Gaston Garbarino et Volodymyr Svitlyk pour leur disponibilité et leur amabilité ainsi que pour une partie des mesures XRD sous pression qui ont été également utilisées dans ce manuscrit. Je remercie aussi les membres d'équipe de LSPM-CNRS à l'Université Paris 13, en particulier à Petr Sokolov et Vladimir Mukhanov pour leur aide et assistance dans l'apprentissage de travail sur les presses de grand volume et pour une grande contribution à la thèse. Je dois remercier aussi Alexandre Tallaire pour son aide et assistance dans les mesures du Raman sous les conditions ambiantes et extrêmes.

Un grand merci à tous mes collaborateurs et collègues, j'associe ma famille et mon amie à ces remerciements pour leur soutien constant au cours de ces trois années.

List of abbreviations

ADX	Angle Dispersive X-Ray
AP	Ambient Pressure
BM	Bending Magnet
BRC	Boron-rich compounds
CN	Coordination Number
MDAC	Membrane Diamond Anvil Cell
DFT	Density Functional Theory
ECP	Effective Core Potential
EDX	Energy Dispersive X-Ray
EL	Edge Length
EoS	Equation of State
ESRF	European Synchrotron Radiation Facility
EXAFS	Extended X-ray Absorption Fine Structure
FWHM	Full Width at Half Maximum
HP	High Pressure
HT	High Temperature
HF	Hartree-Fock
ID	Insertion Device
LCAO	Linear Combination of Atomic Orbitals
LINAC	Linear Accelerator
LVP	Large Volume Press
PBE	Perdew-Burke-Ernzerhof
PEP	Paris-Edinburgh Press
PSICHE	Pressure, Structure and Imaging by Contrast at High Energy
RT	Room Temperature
SOLEIL	Source Optimisée de Lumière d'Énergie Intermédiaire du LURE
SD	Sintered Diamonds
TEL	Truncation Edge Length
TTP	Toroid Type Press
XAFS	X-ray Absorption Fine Structure
XANES	X-ray Absorption Near Edge Structure
XRD	X-ray Diffraction
XRS	X-ray Raman Scattering

Contents

Introduction

The "hunt" for the synthetic diamond in the 50s of the last century and corresponding development of the modern high pressure equipment permitting to reach extreme conditions, opened new horizons in inorganic chemistry and material science. Among a great number of completely new compounds synthesized at high pressure (HP) and high temperature (HT), the boron(-based) compounds possessing the outstanding properties should be emphasized. These compounds were found to be applicable in many fields of industry. For instance, one of the common features of the boron compounds is the high neutron capture cross-section of boron ^{10}B isotope. The isotope enriched boron compounds (e.g. boron carbide, boron nitride, metal borides) are widely used as the materials for the control rods (in nuclear reactors) or the biological protection from the neutron irradiation. Due to this property boron compounds can be also used in boron neutron capture therapy, which is a binary type of tumor therapy utilizing the special properties of the ^{10}B nucleus to capture thermal neutrons and undergo a nuclear disintegration.

The metal borides were found to be rather hard and wear resistant, which allows to use these compounds, for example, as abrasive materials. It should be noticed that the boron compounds with non-metal light elements (like e.g. c-BN, B_6O_{1-x}, B_4C, c-BC_2N, β-B_2O_3, etc.) obtained at extreme conditions revealed the same or even higher hardness values. So, many compounds with the hardness values next after the diamond one contain boron and light elements. Ones of the most popular and widespread in the industry boron compounds are boron nitride (BN), boron carbide (B_4C) and boron suboxide (B_6O_{1-x}). Hexagonal boron nitride is a soft, electrically nonconducting material of high chemical resistance, and a very good heat conductor. However its cubic phase is one of the hardest materials in the world and is used for specialized applications because of its excellent oxidation stability. Boron carbide (B_4C) is also very hard and, at the same time, lightweight material. Its excellent mechanical properties even at high temperatures have resulted in it being used, as a grinding material, material in the bullet-proof vests, in the tools and mechanical parts exposed to high strain (turbine and rotor blades, sports equipment). The composite materials of aluminum and boron carbide have been investigated as high value construction materials (e.g. in airplane construction and the aerospace industry). Boron suboxide being the hardest known oxide is only slightly less hard than B_4C. As well as boron carbide, B_6O_{1-x} is a low dense material with high chemical inertness and resistance to wear. Thus, it can be applied for the same with B_4C industrial applications. It should be noted, that despite hardness the boron compounds with non-metal elements revealed other interesting physical (electronic, optical, mechanical, etc.) and chemical (oxidation resistance, thermal stability, etc.) properties as well. Actually, apart from superhard boron suboxide there is one more compound in the B-O system possessing the hardness comparable with one of WC-Co hard alloy (~16 GPa): high-pressure phase of boron (III) oxide (β-B_2O_3). Thus, one can deduce that investigation of B-O binary system or more generally, of the boron chalcogenides at extreme conditions is rather promising and interesting field/direction of the modern inorganic chemistry. However, the majority of the scientific studies on the boron chalcogenides under extreme conditions are devoted to B-O system (generally to B_6O_{1-x}). Until today only a few studies on B-S and B-Se systems under extreme conditions have been performed.

Many researches have noticed that the prominent physical and chemical properties of the boron compounds can be explained by their particular electronic structure with different types of interatomic bonds which are defined by the complex hybridizations. So, for instance, the high hardness values of boron compounds with light elements (like C, O, N, etc.) can be explained by the fact that light elements do not possess the *d*- and *f*-electrons and form basically short covalent interatomic bonds. Thus, the three-dimensional nets of the short and strong covalent bonds lead to very high melting temperatures and extreme hardness values. It should be also underlined that boron plays a major role in the formations of the interatomic bonds. Thus, the accurate investigation of the physical properties of already known boron compounds at ambient and under extreme conditions is no less important (and, many times, it is more important) than the discovery of new boron compounds.

On other side, despite the high level of modern analytical equipment, one should always bear in mind that some of the physical properties of boron compounds have not in all cases been described beyond doubt until now. For example, even a small contaminations in boron compounds can have an influence on the electronic structure and cause considerable changes in such properties as electrical conductivity and hardness. The providing of the reproducible HP-HT synthesis even of already known compounds requires the high phase purity of the reagents, use of the appropriate high-pressure apparatus and other stuff, precise control of the synthesis conditions, etc. Due to low *Z*-number of B, the investigation of the boron compounds by means of conventional analytical techniques (powder X-ray diffraction (PXRD), X-ray absorption spectroscopy (EXAFS, XANES), etc.) is rather challenging and requires many specialized approaches, for instance *in situ* measurements using high brilliance synchrotron radiation. So, the investigation of the physical properties of the boron compounds (especially with light elements) is still rather challenging, complicated and time consuming.

Thus, the present work has been devoted to the investigation of the boron chalcogenides under extreme conditions. We believe that detailed study of the known boron chalcogenides at ambient and high pressures using precise analytical equipment and synchrotron radiation will expand and refine already existing information about physical properties of these compounds.

Taking into account the time limits of this PhD work and the complexity of the investigation of the boron chalcogenides in each binary system (B-O, B-S and B-Se), the properties of only two known compounds in B-O and B-S systems have been accurately studied at ambient and under high pressures: high-pressure phase of B_2O_3 (β-B_2O_3) and rhombohedral BS (*r*-BS). We presume that these investigations will give an important and valuable information for the further studies and practical applications of β-B_2O_3 and *r*-BS. In this framework, the preliminary investigation of the poorly studied B-Se system under extreme conditions in order to explore the new binary compounds has been also performed.

Thus, the basic aims of this thesis are:

1) The clarification of the differences among literature results on the equation of state (EoS) of β-B_2O_3. In spite of the fact that there are a few reports proposing the different bulk modulus values, the latest and the most reliable study of β-B_2O_3 EoS misses the important low-pressure range. Thus, the β-B_2O_3 equation of state will be measured using synchrotron X-ray diffraction. The experimentally determined EoS parameters will be compared with those theoretically predicted from our *ab initio* calculations;
2) The complete and detailed investigation of the phonon properties of β-B_2O_3 at ambient and high pressures (at room temperature). The results of *ab initio* calculations performed for the phonon properties of β-B_2O_3 will be compared with experimental ones. Based on these data the phonon modes assignment and the complete description of the modes under compression will be performed;
3) The accurate measurements of *r*-BS equation of state and study of its phase stability in a wide pressure range using synchrotron radiation. X-ray diffraction will help to discriminate the probable phase transition and to obtain the information about the new high-pressure phase structure. The *ab initio* theoretical calculations of *r*-BS EoS and phase stability in a wide pressure range will be also provided. The obtained experimental and theoretical results will be compared with the structural analogs of *r*-BS;
4) The complete and detailed study of the phonon properties of *r*-BS at ambient and high pressures (at room temperature). The results of *ab initio* calculations performed on the phonon properties of *r*-BS will be compared with experimental ones. Based on these data the phonon modes assignment and the complete description of the modes behavior under compression will be given;
5) The preliminary HP-HT study of B-Se system. The bright synchrotron radiation will be used in order to follow the possible synthesis of new phases (eventually metastable). The Raman measurements of the recovered samples will be used to complete the XRD data of the recovered samples.

The body of the manuscript is subdivided in five chapters:

Chapter I. This chapter provides a brief review of the different boron phases, boron-rich compounds and boron chalcogenides obtained at extreme (HP-HT) conditions. The descriptions of structural particularities, physical and chemical properties and of HP-HT synthesis are given.

Chapter II. This chapter provides a brief description of the all high-pressure devices used in frames of this work for HP-HT synthesis and *in situ* measurements. The chapter also gives a short introduction to the synchrotron radiation, the PSICHE beamline of SOLEIL and the principles of the techniques (XRD (ADX and EDX), Raman and IR spectroscopy) used for the experimental work. The main principles of *ab initio* theoretical calculations are also described.

Chapter III. This chapter contains the results of our studies on β-B_2O_3. In this chapter we present the results of equation of state obtained from *in situ* XRD measurements and compare them with literature data and our theoretical estimations. The XRD studies are followed by β-B_2O_3 phonon measurements (Raman and IR) at ambient and under extreme conditions. Thanks to our *ab initio* calculations of the phonon frequencies at ambient and high pressures, the assignment of experimentally observed bands to the phonon modes has been done. The phonon modes behavior at high pressure is explained using the results of the theoretical calculations and information of β-B_2O_3 structure changes during compression.

Chapter IV. This chapter contains the results of our studies in B-S system on *r*-BS. The results of *r*-BS EoS measurements are presented and compared with those of other compounds structurally relative to *r*-BS. The formation of the new metastable high-pressure phase of BS is considered and discussed. Then the description and discussion of the results of *r*-BS phonon measurements (Raman and IR) at ambient and under extreme conditions is given. Again, thanks to *ab initio* calculations all observed phonon modes are assigned. The explanation of *r*-BS phonon modes behavior under compression based on the results of *ab initio* calculations and *in situ* XRD measurements is presented.

Chapter V. This chapter presents the description of our preliminary studies of B-Se system. The first results obtained during our HP-HT synthesis coupled with synchrotron radiations are presented. The first suppositions on the chemical composition and structure of the synthesized new B-Se compounds based on the results of *in situ* XRD studies and Raman measurements of recovered sample at ambient conditions are made.

Chapter VI. Finally, this chapter will present our conclusions and perspectives.

Chapter I

1 Chemistry of boron and boron-rich solids

1.1 Boron: state of art

Boron is the 5th chemical element of the Mendeleev periodic Table with the standard atomic weight 10.806÷10.821. It has $1s^22s^22p^1$ electron configuration and refers to the metalloid element category. Boron has the formal oxidation state III due to its electron configuration in the majority of familiar compounds. Boron can form stable covalently bonded molecular networks, as well as its nearest neighbor carbon. Nevertheless, chemical properties of boron are more similar to those of silicon ones. Boron has two naturally occurring and stable isotopes, ^{11}B (80.1%) and ^{10}B (19.9%). In spite of the fact that boron seems to be rather thoroughly studied, nowadays it still remains one of the most poorly understood chemical elements. Even the history of discovery and recovery of the pure element is rather intricate. Besides the fact that some glazes based on boron compounds (e.g. $Na_2[B_4O_5(OH)_4]\cdot 8H_2O$) had been known since ancient times in China and in Arabic world, the element was explored almost simultaneously by two independent scientific groups only in XIX century: Humphry Davy [1] and Louis Joseph Gay-Lussac and Louis-Jacques Thénard [2]. It is a widespread assumption that the pure element (~90%) was obtained by W. Weintraub between 1909 and 1911 [3]. There were the works (for example [4]) declaring the investigation of a pure boron and even the boron structural modifications [5] before Weintraub's work but in all of them the boron was contaminated by by-products, thus the boron content was less than 90%. For instance, in 1943 the so-called I-tetragonal phase (T-50 or t-I) was obtained [6] and its structure was refined in 1951 [7,8]. The structure established as pure boron (e.g. [9]) turned out to be a compound of composition $B_{50}C_2$ or $B_{50}N_2$ [10,11]. In fact, the first pure boron polymorph is documented only after 1957 [12,13].

The example cited above clearly shows the complexity of boron allotropes investigation. The main reason of these difficulties is that boron reveals extreme sensitivity to even small amount of impurities. Hence, different samples of the same polymorph might show significant structural and thermodynamic differences which in its turn leads to contradictions of the relative stability of the boron phase at ambient conditions [14]. Even modern chemical industry cannot always avoid undesired by-elements to the base element during boron's preparation and conversion.

Nowadays at least 16 crystalline allotropes have been described [15,16]. Some of them have not ever been reproduced as for example: β'- and β''-B_4 [17], t-B_{50} [8], "HP form" of Wentorf [18], "HPHT form" of t-B_{192} [19], etc. Most of the reported phases are likely to be boron-rich borides rather than pure element [11,14,16]. So far only five allotropes are generally accepted: rhombohedral α-B_{12} (α-phase) [20], β-B_{106} (β-phase) [21], orthorhombic γ-B_{28} (γ-phase) [22], tetragonal t-B_{192} [23] and t-B_{52} [10,24,25]. It has been recently proved, that t-B_{52} exists, although its crystal structure has not been unambiguously established so far. Two more phases have been predicted by using *ab initio* structural evolution algorithm [26], i.e. orthorhombic *o*-B_{52} [2726], closely related to t-B_{52}, and metallic boron with α-Ga crystal structure [22]. Quite recently pseudo-cubic t'-B_{52} of the t-B_{52} structural family has been discovered [28]. It was recovered after experiments at 20 GPa and 2500 K. The density of pseudo-cubic allotrope has been found to be quite close to the γ-B_{28} one, higher than the common low-density of t-B_{52} phase. t'-B_{52} seems to be a good candidate for a HP-HT allotrope, instead of reported strongly distorted "t-B_{192} structure".

Taking into account all the facts noticed above, in further literature review of the boron allotropes, only the three main boron allotropes: α-B_{12}, β-B_{106} and γ-B_{28} will be considered. The regions of thermodynamic stability of these polymorphs were confidently established in Ref. 29. We will avoid the t-B_{192}, t-B_{52} and t'-B_{52} allotropes in our review due to uncertainty of their thermodynamic stability regions [29]. However, in spite of the progress of the past few years in understanding and refinement of the phase diagram of boron, there are large uncertainties on the phase boundaries.

1.1.1 α-rhombohedral boron (α-B_{12})

α-rhombohedral boron is red or brown in color and non- or semiconducting at room temperature. It was obtained for the first time by the pyrolytic decomposition of BI_3 on a surface (tantalum, tungsten or boron nitride) heated at 800-1000°C [30,31]. α-B can also be obtained by crystallizing amorphous boron in a platinum melt [32]. Amorphous boron itself can be obtained by the methods described in Ref. [1,2]: from chemical reaction between B_2O_3 (or $B(OH)_3$) with potassium, or by electrolysis. It was investigated [20,30,31] that α form of boron is stable up to 1200°C and above 1500°C it transforms into "rhombohedral form" obtained from boron melt [12]. The structure of this rhombohedral form was later worked out and defined as β-B_{106} [13]. The question of the thermodynamical stability of two boron allotrope modifications will be discussed in the next part devoted to β-B_{106}. Herein it should be only noted that according to the latest investigations β-B_{106} is believed to be more thermodynamically stable at ambient pressure than α-B_{12}, while the latter is more stable at pressures above 2 GPa [22].

The Vickers hardness of α-B was found to be 42 GPa, which is lower than in case of β-B [33]. The theoretical estimations of bulk modulus are 208-218 GPa [34,35], whereas experimentally measured values are 213-224 GPa [36]. The density of α-B was estimated to be 2.46 g/cm^3.The indirect and direct band gap values of α-rhombohedral boron are 1.5 eV and 1.9 eV respectively [35], the Debye temperature (θ_D) is 1430 K [36].

It is well known, that structures of boron allotropes and majority of boron-rich compounds contain the octahedral and icosahedral subunits [37]. The α-boron allotrope has rhombohedral crystal system and $R\bar{3}m$ (№166) space group. There are 12 boron atoms in unit cell. The icosahedral units B_{12} are the building blocks located in the corners of a primitive rhombohedral unit cell. The unit cell of α-rhombohedral boron can be presented in a hexagonal (a) and rhombohedral (b) settings (Figure I.1).

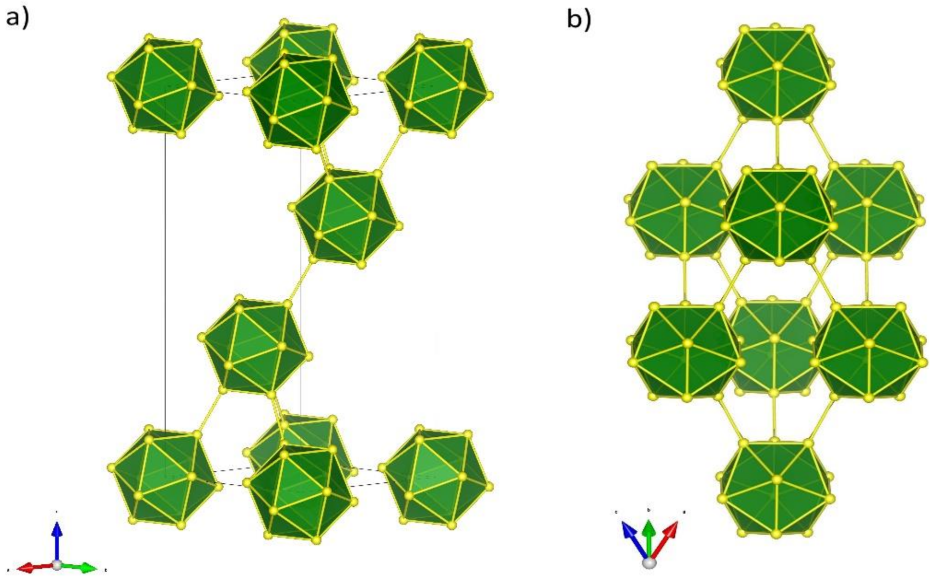

Figure I.1. Unit cells of α rhombohedral boron: a) in hexagonal setting; b) in rhombohedral setting.

The icosahedral arrangement in α-B_{12} can be compared to the image of a cubic close packing of spheres with the layer sequence ABC. Thus each icosahedron is surrounded by 12 neighbor icosahedra. According to various reports, the packing density is given as 34% [22] or 41% [35].

The minimum bond length in α-boron occurs in the intericosahedral bonds, but not in the intraicosahedral bonds [20]. A B_{12} molecule has 36 valance electrons. 26 electrons are distributed among 13 intraicosahedral bonding orbitals. The 10 remaining electrons are distributed among 12 intericosahedral orbitals [34]. Two electrons are deficient for fulfilling the bonding requirement of the B_{12}. To supply the two deficient electrons, boron atoms tend to gather each other by forming triangles or polyhedra. This is an economical way for a small number of electrons to be shared by many atoms. In the cubic close packed motive, each icosahedron forms six two electron–two-center bonds with the icosahedra of neighboring layers, and six closed two electron-three-center bonds with the neighboring icosahedra in its own layer [37]. Two electron–two-center bonds should be shorter than polycentric intraicosahedral bonds. Although B_{12} is a favorable unit for satisfying the bonding requirement of boron atoms, B_{12} itself is not stable. Consequently the presence of two electron-three-center bonds explain the thermodynamic stability of α-B_{12}. This is a general rule for all the boron allotropes containing B_{12} icosahedra. It was noticed [34], that the bonding requirement can also be satisfied by doping impurities, as for example, in compounds: $B_{12}P_2$, $B_{12}As_2$, and maybe $B_{12}C_3$. More recent results of IR spectroscopy studies have implicated the structural formula $B_{12}B_2$ for α-rhombohedral boron and proposed the substitutive mechanism of formation of derivative compounds [38].

1.1.2 β-rhombohedral boron (β-B_{106})

β-rhombohedral boron is a grayish black semiconductor. It is a commercially available product and its purity can reach 99.99%. The first discovered pure boron phase was β-boron, obtained from boron melt at He atmosphere [12]. Later the method of β-B purifying was suggested [39]. As it has been described above, the β form could be obtained from α-B_{12} by heating above 1500°C at ambient pressure. This is not necessarily a direct transformation and it can go through metastable intermediate phases. Moreover, the boundary temperature (α-$B_{12} \rightleftarrows$ β-B_{106}) depends on the way of α phase preparation: 1300 K in the hot filament [40], from 1300 to 1500 K in the reduction of boron chalcogenides [41], and 1500 K in the crystallization of amorphous boron [42]. Nevertheless, many papers in the literature show that the phase transformation from α- to β-form is still not well established [37].

β-boron has a rhombohedral Bravais lattice with the space group $R\bar{3}m$ in its perfect form. As well as in α-B_{12} the icosahedral units B_{12} are the building blocks of β-B_{106}. The complex crystal structure of β-B_{106} is illustrated in Figure I.2 in rhombohedral and hexagonal settings.

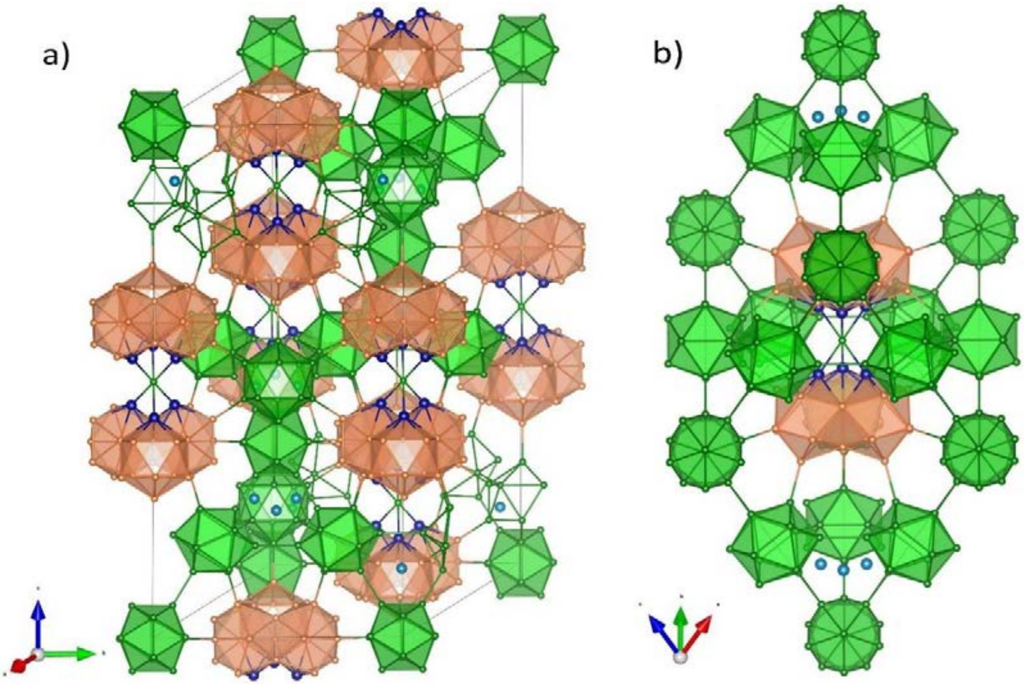

Figure I.2. Unit cells of β rhombohedral boron: a) in hexagonal setting, b) in rhombohedral setting, showing B_{12} icosahedra (green), two B_{28} clusters (triply-fused icosahedra, ochre), partially occupied interstitial sites (B13, dark blue) with an occupancy of 73.4% and partially occupied interstitial sites (B16, blue) with an occupancy of 24.8% [43].

The first β-B structure description appeared in 1963 [21]. Since that time β-boron structure still remains discussible due to uncertainty of crystallographically independent positions (15 or 16) per rhombohedral unit cell, presence of partially occupied boron atom positions and additional interstitial positions [37,43]. The latest report on structure refinement of β-B reports 2 partially occupied boron atom positions B13 and B16 with occupancy of 74.5% and 27.2% respectively; and 4 additional interstitial positions with partial occupations (≤ 8.5%), yielding about 106.5 atoms per rhombohedral unit cell [44,45]. Thus, β-boron might be called β-B_{106}.

The B_{12} icosahedra are placed in the corners and in the middle of the edges of rhombohedral unit cell. There are two B_{28} units on the body diagonal, each consisting of three condensed icosahedra and linked via an insulated B atom in the center of the rhombohedral unit cell. The single boron atom in the center of the unit cell is coordinated trigonal-antiprismatically by 6 boron atoms of the B_{28} units. The ~2/3 of the occupancy of B13 positions (dark blue in Figure I.2) leads to B_{27} units and results in a distorted tetrahedral coordination of the central boron atom. All icosahedra and B_{28} units were found [46] to be bonded by two electron-two center bonds, while the B16 interstitial atoms (blue in Figure I.2) are bonded to the surrounding icosahedra by two electron-three center bonds. It is now well understood, that all intrinsic structure defects in β-B_{106} (imbalance of electron requirements between B_{12} and B_{28} units [47-51], intrinsic instability of B_{28} [47,51] and conversion of two electron-two center bonds to two electron-three center bonds due to partial occupation of crystallographic sites and presence of self-interstitials) lead to a nearly perfect closed shell-electronic structure [47,52]. It turned out, that the defects are necessary for stabilization of β-B_{106}, hence these defects have a negative formation energy [33,35,47,53,54]. This is a unique feature among known elements: macroscopic numbers of interstitial sites and vacancies are needed to form almost closed shell-electronic structure of β-boron.

The partially occupied sites and additional interstitial positions in β-boron, significantly influence on electronic properties and physical properties. For example, the transport properties of β-B_{106} are similar to those of nearly closed shell-electronic structure of solid. The partially occupied sites generate localized electronic states in the band gap. They are split-off from valance band, which is left completely occupied. Consequently, β-B_{106} is a semiconductor of *p*-type [55-57]. At temperatures lower than 700 K partially occupied sites more or less determine such properties, as for example, thermal expansion [58], electronic conductivity [44,56,57], Seebeck coefficient [56], optical absorption [59] and electron paramagnetic resonance [60,61]. An experimentally determined band gap is 1.6 eV [37], whereas the theoretically estimated one is 1.4 eV [35]. According to [36] the Debye temperature (θ_D) is 1300 K. The bulk modulus were determined to be 185 GPa [36] and 210 GPa [62], whereas density is 2.33 g/cm^3 [37]. β-boron has a Vickers hardness value of 45 GPa [33]. Hence, β-B_{106} is harder than corundum, but less dense and harder than α-B_{12}.The melting point at ambient pressure is stated to be between 2350 K and 2370 K [28,63,64].

The question of the thermodynamical stability of β-B_{106} and α-B_{12} is still highly discussed in the scientific world and requires a special consideration. Herein we will just briefly note some of the latest findings. At ambient pressure, liquid boron solidifies into the β-rhombohedral phase, indicating that this phase is the thermodynamically stable one at high temperature [39,65]. Early works [17,21,66,67] reported that β-B is thermodynamically stable phase for all temperatures below melting to ~1400 K at ambient pressure. On the other hand, recent experimental investigation [29] of the $\alpha \rightleftarrows \beta$ phase transformations in 2-6 GPa pressure range and at temperatures up to 2500 K has shown that α-B_{12} is more stable than β form at low temperatures and high pressures. The linear extrapolation of the P-T boundary indicated that α-boron would be more stable than β-boron at ambient conditions. The theoretical calculations [31] also supported these experimental observations, showing that α-B is the stable form at low temperature (0 K) and should transform to β-B only at 970 K. β phase cannot be considered thermodynamically stable at all temperatures and ambient pressure due to it does not have a closed-shell electronic structure and a perfect crystal structure, if the partially occupied sites and additional interstitial positions are not accounted [52].

At the same time according to another very recent study [46], β allotrope was found to be more stable than α-B_{12} for all temperatures up to 2000 K at ambient pressure. The latter becomes stable only at high pressures. It is also underlined that the ground-state energies of α and β-boron are nearly identical [46]. On the other hand, it has been shown [35,47] that including zero-point energies in the calculation of boron modifications stability by first-principles method and taking into consideration experimentally observed partial occupancies in β-B_{106} structure, makes the latter more stable than α-B by 3 eV. Without these zero-point energies and the partial occupancy, α-B appears to be a more stable modification by 1 eV. At ambient conditions, α-B_{12} and β-B_{106} should have similar static energies [33,35]. Now, it is well proved that β-B_{106} is the most favorable allotrope of boron at ambient pressure and at all temperatures below melting, when a macroscopic amount of defects is present [35,47,54,68].

A few structural transitions in β-B_{106} have been observed at low temperatures. The optical absorption of β-B exhibited a dramatic change at 150-200 K [69]. However, the X-ray measurements at these temperatures did not reveal some structure changes. The authors of [52] note that it could be a disorder-to-order phase transition. Another phase transition near 550 K based on calorimetric measurements has been recently observed [44]. According to these observations, only a limited number of boron atoms changed their sites by hopping. However, the nature of this transition is yet to be determined.

1.1.3 γ-orthorhombic “ionic” boron (γ-B_{28})

The orthorhombic γ-boron phase has been recently discovered [22]. It can be synthesized from *β*-boron by applying high pressures (above 8.5 GPa) and at high temperatures (from 1800 to 2000 K) [22,70]. The theoretical calculations USPEX [22] discovered for the first time the boron phase dynamically stable and thermodynamically more favorable than any other known or hypothetical form of boron between 19 GPa and 89 GPa at 0 K. This boron allotrope was possibly obtained already in 1965 [71]: the transformation of β-B_{106} and amorphous boron to another, “unknown phase” at pressures above 10 GPa and temperatures of 1800–2300 K was observed. However, the chemical composition was not analyzed and the data probably have not been used to propose a structural model. According to the boron phase diagrams [29],[72] (see Figure I.3), at pressures higher than 10 GPa and temperatures higher than 2500 K the phase transition from γ-B_{28} to t’-B_{52} polymorph occurs.

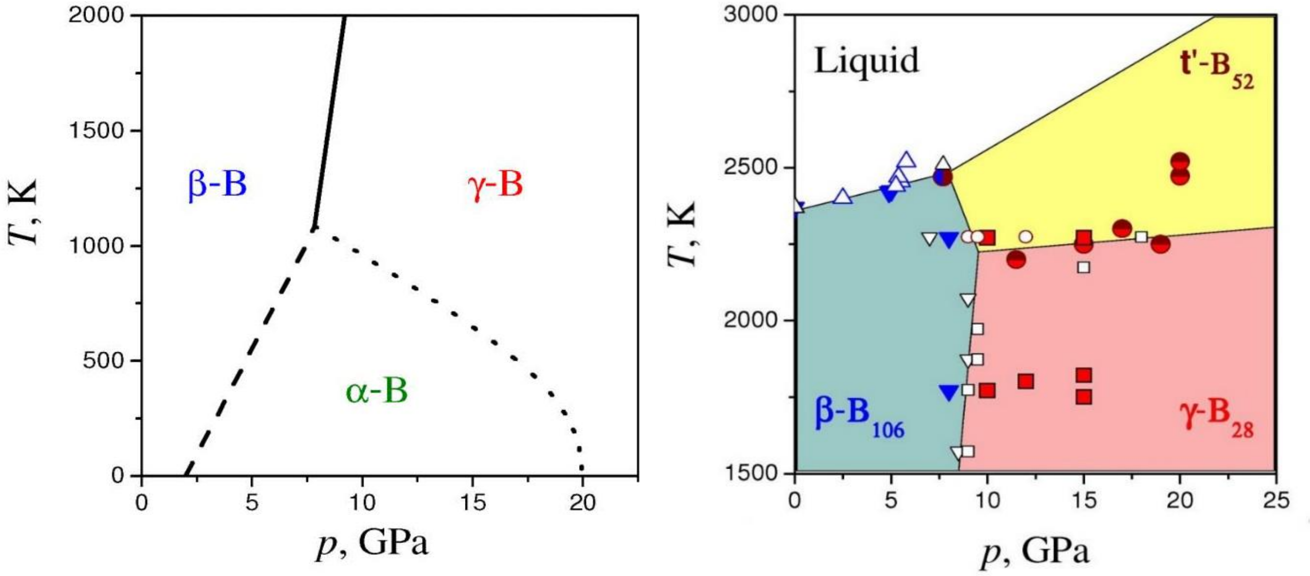

Figure I.3. The boron phase diagram [29]. The symbols show the experimental data: open and solid triangles refer to β-B_{106}, squares refer to γ-B_{28} and circles refer to t’-B_{52}. The solid lines represent the equilibria between different allotropes.

The γ-B structure was confirmed by the *ab initio* crystal structures prediction, the XRD studies [22] and the single-crystal XRD studies [70]. The Figure I.4 presents the structure of γ-B_{28}. The provided measurements showed that γ-B_{28} is the hardest known boron allotrope with Vickers hardness of 50(11) GPa, which agrees with the calculated hardness value of 48.8 GPa [33]. The best experimental estimates of γ-B_{28} hardness are 45 GPa, 42 GPa [73] and 58 GPa [69]. The density of 2.54 g/cm^3 was determined based on XRD data [33]. The band gap is 1.5 eV at ambient conditions [37].

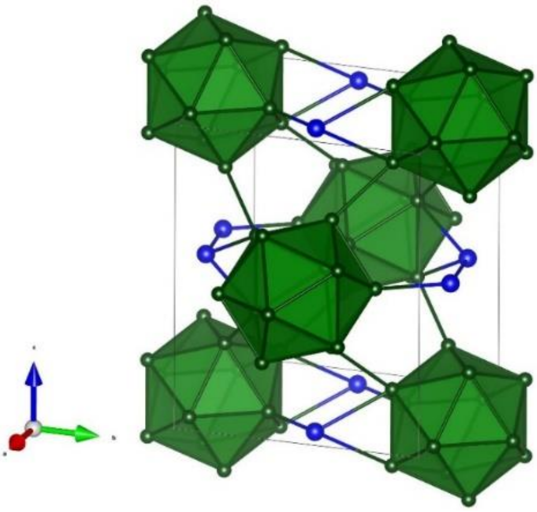

Figure I.4. Unit cell of γ-orthorhombic boron, showing "negatively charged" B_{12} icosahedra (green) and "positively charged" boron pairs (B1, blue).

As well as β-B_{106} and α-B_{12}, γ-orthorhombic boron also contains the B_{12} icosahedra. The unit cell contains 28 atoms and belongs to the *Pnnm* space group. As one can note, this phase contains icosahedral B_{12} and B_2 clusters. The centers of the icosahedra in γ-B_{28} form a slightly distorted cubic close packing as in α-B_{12}. Nevertheless, unlike α-B_{12} structure, all octahedral voids in γ boron are occupied by B_2 pairs (blue in Figure I.4), and the new phase is thus denser than α boron. Hence, B_{12} and B_2 clusters are placed in a NaCl-type arrangement. Detailed investigations showed that these two clusters have very different electronic properties and there is a charge transfer ($\delta \approx 0.48$) between them, leading to boron boride: $(B_2)^{\delta+}(B_{12})^{\delta-}$. Thus, B_2 clusters play the role of "cations", meanwhile B_{12} icosahedra are "anions". The exact magnitude of charge transfer depends on the definition of the atomic charge used. These observations also correlate well with the strong IR absorption and high dynamical charges on atoms [22]. The ionicity of γ-B_{28} was found to be 1.16 [37]. The use of such terms as "ionic", "cations", "anions" can be explained by the wish to emphasize the polar nature of the high-pressure boron phase, but it should be noticed that the chemical bonding in γ-B_{28} is predominantly covalent [74].

The properties of all boron allotrope modifications are summed up in the Table 1.

Physical properties	α-B_{12}	Ref.	β-B_{106}	Ref.	γ-B_{28}	Ref.
Vickers hardness, GPa	42	[33]	45	[33]	58	[33,70]
Bulk modulus, GPa	213-224	[36]	185, 210	[36,62]	237	[73]
Density, g/cm^3	2.46	[37]	2.33	[37]	2.54	[33]
Band gap, eV	1.9	[35]	1.6	[37]	1.5	[37]
Debye temperature, K	1430	[36]	1300	[36]		

Table 1. Physical properties of the three main allotrope modifications of boron: α-B_{12}, β-B_{106}, γ-B_{28}.

1.2 General review of boron-rich solids

Boron-rich compounds (BRC) attract constantly increasing interest in the last decades. Physical properties such as hardness, thermoconductivity/thermoisolation, chemical inertness, superconductivity and others make these compounds rather promising for many application in the various fields of industry and interesting as model materials for fundamental researches. Boron carbide (B_4C) is one of the good examples of wide using of BRC in different fields of industry as: an abrasive material, a component of abrasive blasting, a material for cutting tools, a scratch and a wear resistant coating, a material of brake linings of vehicles, an armor plating, a neutron absorbent and a material for neutron detectors [76-80].

As it has been mentioned in the review of boron and its polymorphs, the BRC have been synthesized as long ago as in the beginning of XIX century. For instance, the boron carbide B_4C has been already known since 1864 [37]. But at that time, the great majority of BRC were taken by mistake for polymorphs of pure boron. All the reports about the extraction of pure boron until 1957 seemed to be false. Indeed, the discovered "boron polymorphs" were found to be contaminated by other chemical elements (e.g. C, N, O, Mg, etc.), which have a stabilizing effect on the polymorph's structure. Such delusions of the chemists can be explained by the lack of good analytical instrumentation at that time. Improvement of analytical and theoretical bases and discovery of the real pure boron allotropes in the middle of last century gave rise to intense start of investigations of born-rich compounds.

In the very beginning of this BRC description, we must underline the fact that these compounds have not been described without a doubt [37]. BRC possess rather sophisticated structures with large unit cells and partial occupations. There are usually various types of chemical bonds in BRC: covalent, ionic and metallic. It is very well known that even a small amount of contamination in inorganic solids may cause considerable changes in electrical conductivity and hardness. Due to all of this, there are many controversial experimental and theoretical data about the physical properties and structural arrangement of BRC.

The majority of the observed BRC unit cells can be referred to those of the elemental boron: α-B_{12} or β-B_{106}. Carbon, silicon, nitrogen, phosphorous, arsenic, oxygen, sulfur and selenium react with boron at high temperatures (and high pressures) forming boron subcarbide (although usually it is called carbide), subsilicide, subnitride, subphosphide, subarsenide, suboxide, subsulfide and subselenide with the structures derived from α-B. These compounds crystallize in the space group $R\bar{3}m$ (№ 166). The BRC schematic unit cell is presented in Figure I.5.

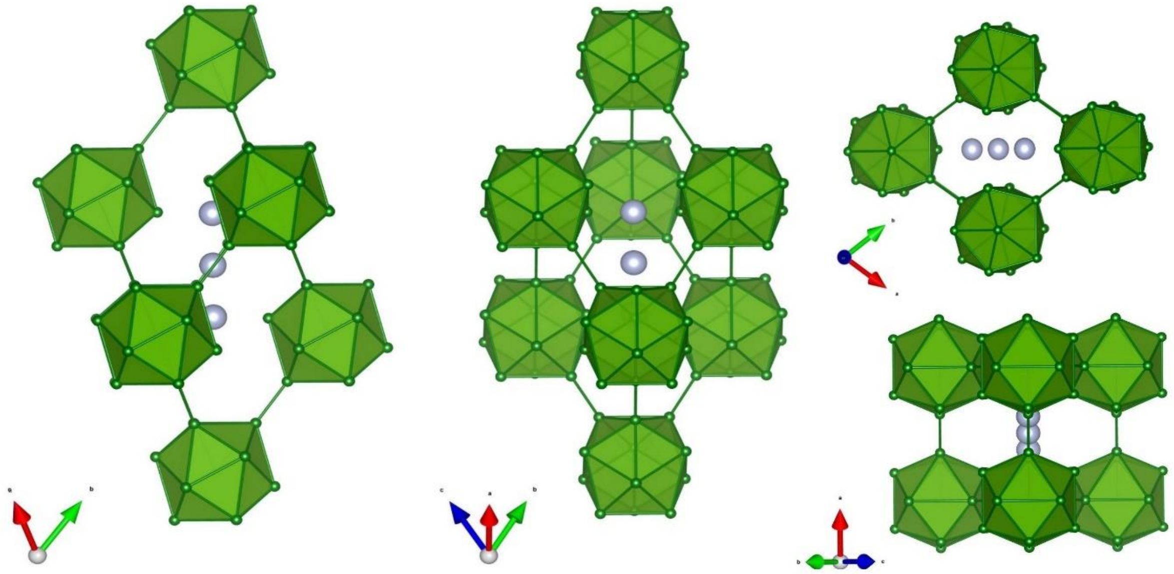

Figure I.5. Generally presented unit cell of boron-rich compounds in rhombohedral setting, showing B_{12} icosahedra (green) on the corners of unit cell and non-boron atoms (grey) on the spatial {111} diagonal.

As one can see in Figure I.5, the B_{12} icosahedra are situated on the corners of the rhombohedral unit cell as in α-B_{12}. As we know from review of α-B_{12}, there are three voids (two tetrahedral and one octahedral) formed by the shells of B_{12} icosahedra. These voids are situated along {111} axis in the unit cell. The tetrahedral voids have a coordination number 4, diameter of 1.14 Å and occupy the 6c sites. Meanwhile, the octahedral void has a coordination number 6, diameter of 2.09 Å and occupies 3b site [81]. It is assumed that non-boron atoms occupy these voids. When the interstitial atoms fit into the α-B structure, they change the volume of the unit cell, which triggers changes in crystal density and mechanical properties. Based on the great amount of experimental data, it could be concluded, that the central 3b site can be occupied only by Be, B and C atoms. One of the possible reasons is the small values of covalent radii of these atoms compared to 2.09 Å. Thus, the entrance of these atoms will not dramatically increase the unit cell volume. The 6c sites may host C, N, O, Si, P, S, As, Se and other non-boron atoms; and the occupation of these sites will determine the properties of the compound. But it could be called an ideal case. In fact, the boron and interstitial atoms can replace each other in the unit cell. For instance, one may think that bruto-formula "B_4C" means $B_{12}C_3$ and it means that there are three carbon atoms on the spatial diagonal. In fact, it was shown [82,83], that boron atom can replace carbon and occupies 3b site. The non-boron atoms in BRC can also replace some of the boron atoms in icosahedra [84]. Even a small change of boron/non-boron atoms ratio can lead to the big variety of different structural units. For example, the B-C-B, B-B-C, B-□-B, B_{12} and $B_{11}C$ structural units have been observed in boron carbide at various compositions [85]. The electronic structure of BRC differs dramatically: the two electron-two-center bonds to non-boron atoms in BRC replace the two electron-three-center ones in α-B, which lead to a significant reduction of the c/a ratio but not to a reduction of unit cell volume [37].

1.3 Boron suboxide B_6O – the hardest oxide. Motivation of the present study

A boron-rich oxide or boron suboxide B_6O is one of the most well studied BRC as well as boron carbide. Such great interest to this compound can be explained by its physical properties, and first of all, by its high harnesses, low density, chemical inertness and high resistance to wear [86-88]. The reported B_6O hardness of ~35 GPa [87,88] is a little less than that of B_4C – 38 GPa [89] and 40-45 GPa [90]. There have even been the reports stating that boron suboxide scratched the softer {100} face of diamond [91]. However, it seems unlikely due to the absence of another reports about this phenomenon. Up to now, B_6O is considered to be the hardest known oxide and one of the hardest materials. Such prominent hardness is believed to be due to the structural particularities of boron suboxide and electronic structure of oxygen and boron. Indeed, even a small doping of oxygen atoms into β-boron increases its hardness on 34% [92]. Apart from B_6O, there are other compounds in B-O binary system, as for example B_2O_3, which possesses remarkable hardness and wear resistance [93].

We believe that overall investigation of binary systems of boron chalcogenides (O, S, Se and Te) in wide ranges of pressures and temperatures may result in discovery of new phases possessing outstanding properties and in expending and refinement of information about already known compounds. In the next sections a detailed review of binary systems B-O, B-S and B-Se will be presented. We will not take into consideration B-Te system, as the Te chemistry dramatically differs from those of O, S and Se due to its higher number of valance electrons.

2 Boron chalcogenides systems

2.1 General review of VIa group of Mendeleev Periodic Table of Elements

The VIa group of Mendeleev Periodic Table includes oxygen (O), sulfur (S), selenium (Se) and tellurium (Te). These elements have s^2p^4 external electron shell structure. Increasing of Z-number tends to decrease ionization energy, dissociation energy, electronegativity, while metallic properties, covalent and ionic radii increase. Nevertheless, these are no metals in this group. Selenium and tellurium exhibit pronounced semiconductor properties.

2.2 B-O system

B-O system is the best studied one among boron-chalcogenides systems, first of all due to B_6O. A great number of studies have been devoted to the research of crystal structure of boron suboxide [94-102]. The synthesis and investigation of various boron suboxides B_xO with another stoichiometry (where x = 2, 4, 7, 8, 10, 12, 14, 16, 18, 20, 22, 26) have been also reported [103-105]. A large number of studies have been done on B_2O suboxide [103,106-111]. It was reported [103] that B_2O with a graphite-like structure can be obtained as a result of the boron interaction with B_2O_3 at pressures to 7.5 GPa and temperatures to 2100 K. B_2O diamond phase was observed during oxidation of BP with CrO_3 at 4 GPa and 1500 K [106,107]. However, we agree with the suggested arguments [111], concluding that the synthesis of B_2O was impossible. Besides the class of boron suboxides there are also three forms of boron (III) oxide: vitreous (g-B_2O_3) and two crystalline (α-B_2O_3 [112] and β-B_2O_3 [113]).

In this section we will provide a review of all already known and proved solids in B-O system. We will avoid a description of gaseous compounds, as, for example, B_2O_2. We also will intentionally avoid a detailed description of the thermodynamical aspects, as it does not completely refer to the topic of this present work. The review of B-O system will be started with simple boron oxides (α-B_2O_3 and β-B_2O_3) and will be concluded by the description of boron suboxide (B_6O).

2.2.1 Low-pressure phase of boron trioxide α-B_2O_3

Solid diboron trioxide B_2O_3 had been known only in the vitreous state until 1938, when α-B_2O_3 (or I-B_2O_3) was synthesized as a fine powder during dehydration of metaboric acid HBO_2 under carefully controlled conditions [112]. In spite of the fact that the first structural study has been provided in 1954 [114], the first reliable XRD data are dated by 1964 [115] and its X-ray structure has been completely determined in 1970 [116]. Actually, the α-B_2O_3 can be obtained from vitreous form of boron trioxide at a wide range of temperatures (up to 1000°C) and pressures (up to 4 GPa) [112,115-117]. In its turn, the vitreous form can be obtained by decomposing of either HBO_2 or H_3BO_3 at high temperatures (~1000°C) and ambient pressure. Meanwhile, the direct chemical reaction between elemental boron and oxygen at 7 GPa and above 1300 K have been recently reported [118]. Using this method, the α-B_2O_3 has been synthesized at 1500 K and 6 GPa in a diamond anvil cell [111]. α-B_2O_3 has also been observed during the studies of B_6O melting curve [119]: it can be obtained by rapid quench of B_6O melt (~2710 K, ~6 GPa) by switching off the heating.

At atmospheric pressure α-B_2O_3 was found to melt between 455°C and 475°C [115]. Low-pressure phase of B_2O_3 has been found to be an insulator with a band gap of 6.2 eV and static dielectric constant of 2.3 [120]. The estimated density is 2.46 g/cm^3 [115], 2.56 g/cm^3 [116,121].

The phase diagram of B_2O_3 established in Ref. 115,121,122 later revised in Ref. 123 is presented in the Figure I.6.

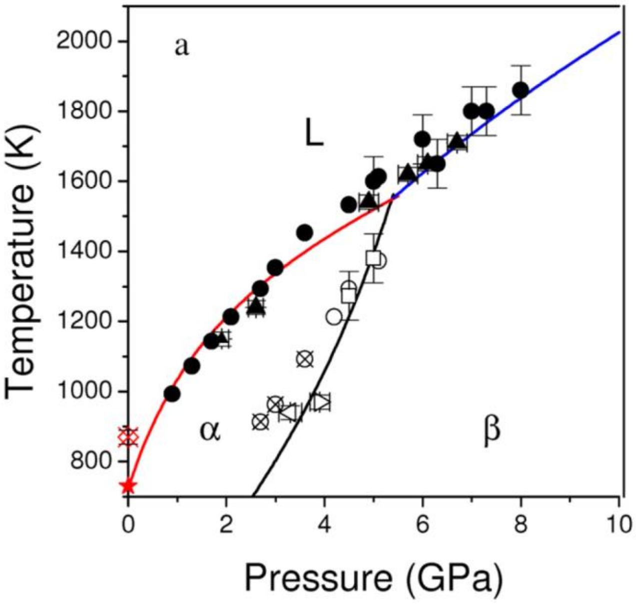

Figure I.6. Equilibrium phase diagram of B_2O_3 presented in Ref. 123. The solid lines represent the calculated equilibrium curves, the solid and open symbols represent the experimental data.

The structure of the α-modification has a hexagonal unit cell and *P*31 (№ 144) space group. Boron and oxygen atoms form the triangles, which are the building blocks of α-B_2O_3 (Figure I.7). It is evident that boron atoms coordination number is 3. According to the first-principle calculations using a local-density approximation, it was determined that *sp*^{2} planar bonding in α-B_2O_3 is stronger than the *sp*^{3} tetrahedral bonding in β-B_2O_3 [120].

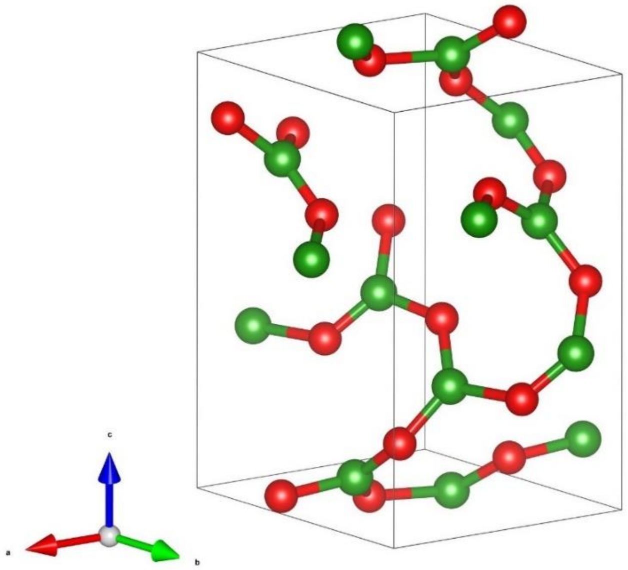

Figure I.7. Unit cells of α-B_2O_3 in hexagonal setting, consisting of BO_3 structural units (B atoms are green, O atoms are red).

It has been also noted that the structure of α-form is the closest to the local structure of vitreous B_2O_3 [93]. Due to this fact, low-pressure phase of boron oxide might evoke the interest and can be applied in the glass industry. On other hand, α-B_2O_3 does not possess any strengths in mechanical properties compared to high-pressure phase (β-B_2O_3). Due to this fact, the α-B_2O_3 polymorph will not be studied in the present work.

2.2.2 High-pressure phase of boron trioxide **β-B_2O_3**

High-pressure phase of B_2O_3 is a light yellow compound and is formed at higher pressures than α-B_2O_3. First reports about β-B_2O_3 synthesis occurred in 1959 [113,117]. The high-pressure form was only slowly attacked by water and diluted by the hydrofluoric acid [117]. Its structure has been refined a few years later from XRD data of single crystals [124]. At pressures above 2 GPa and temperatures above 700°C α-B_2O_3 undergoes a phase transition into β-B_2O_3 [115]. This is the easiest way for β-B_2O_3 synthesis and it is still being used nowadays [93]. As one can see from the phase diagram proposed in Ref. 123 (see Figure 6), B_2O_3 transformation under high pressure and high temperature undergoes the following sequence: $g \rightarrow \alpha \rightarrow \beta$. However, a direct synthesis from the elemental boron and oxygen under high pressures and temperatures in diamond anvil cell is possible also [111,118,125]. Despite the considered β-B_2O_3 thermodynamic metastability at ambient conditions, the high-pressure phase was established [115] as a stable one and no β→α transformation has been observed up to *α*-B_2O_3 melting temperature at ambient pressure. At rather rapid heating rates high-pressure phase of B_2O_3 can be heated to 520°C before fusion occurs. Moreover the fusion sequence was suggested to be β→α→liquid [115].

The main interest to β-B_2O_3 is drawn due to its hardness and mechanical properties. It has been recently found out [93], that the hardness of the sintered β-B_2O_3 is of the same value (16±5 GPa) with that of tungsten carbide alloy WC-10%Co [126]. The bulk modulus value proposed in Ref. [121] is equal to 90±15 GPa. On other work, the bulk modulus measured in *in situ* experiments in diamond anvil cell after a direct reaction between elemental boron and oxygen was determined to be 169.9 GPa [111]. However, since β-B_2O_3 was formed from elemental boron and oxygen at ~40 GPa, V(P) dependence measured between 12 and 42 GPa and fitted by Vinet equation of state (EoS) misses the low pressure region, which makes entire bulk modulus value doubtful. The density of a high-pressure polymorph varies from 2.95 to 3.11 g/cm^3 [113,115-117,121]. The studies of the electronic structure and optical properties of both polymorphs of B_2O_3 showed that β-B_2O_3 is more ionic than α-B_2O_3 [120]. According to the same studies β-B_2O_3 has been found to be an insulator with a band gap of 8.9 eV and a static dielectric constant of 2.4.

The β-B_2O_3 unit cell is shown in Figure I.8. The unit cell has an orthorhombic syngony, *Cmc*2_1 space group.

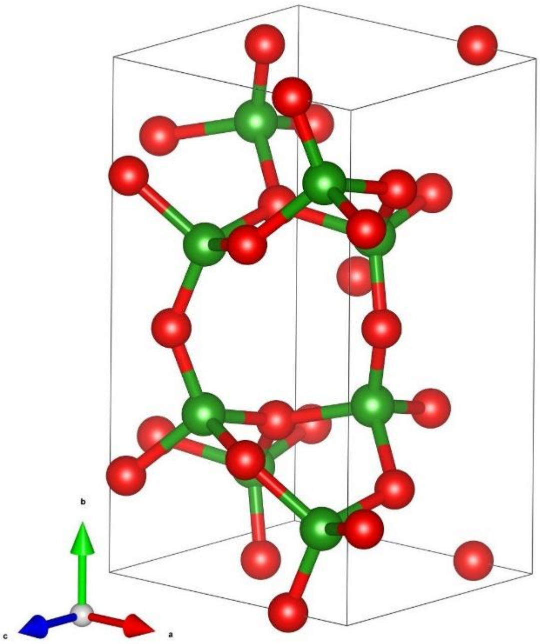

Figure I.8. Unit cells of β-B_2O_3 in orthorhombic setting, consisting of BO_4 distorted tetrahedrons (B atoms are green, O atoms are red).

As one can see in Figure I.8 the crystal structure of β-B_2O_3 is based on distorted BO_4 tetrahedrons [124]. As it was underlined in Ref. 93, the structure of high-pressure boron trioxide is not of maximal density and there could be an isotropic dense phase of B_2O_3 (γ-B_2O_3) with the structure of corundum and the highest hardness (30 GPa). In spite of rather big interest to the β-B_2O_3 due to its mechanical properties, high-pressure phase is not still completely studied: no information about the hardness of the monocrystalline β-B_2O_3, very poor data on phonons and etc. In present work we provided *in situ* investigation of β-B_2O_3 phonon modes at ambient pressure and under compression. We also have measured the EoS of β-B_2O_3 from 0 up to 22 GPa in order to complete V(P) curve in low pressures range.

2.2.3 Boron suboxide B_6O

Boron suboxide is a red-orange semiconductor and may even be obtained in grains up to 40μm from high temperature-high pressure (HT-HP) synthesis [99] (see Figure I.9.).

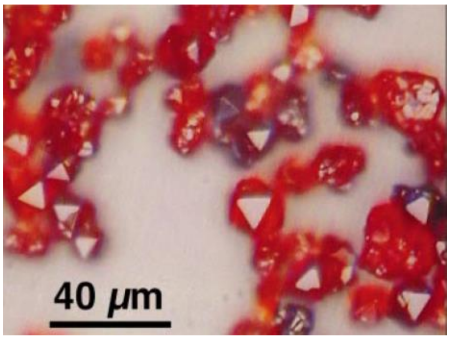

Figure I.9. Reflected-light optical image of B_6O icosahedral particles/grains [99].

As it is seen in Figure I.9, these grains have an icosahedral shape. Such grains shape contradicts the classical theory of crystallography denying five-fold symmetry for the crystals and X-ray diffraction pattern, which is fully consistent with rhombohedral symmetry [99]. Such a strange and "impossible" morphology of B_6O grains has been explained by "Mackay packing" [99,100], in which successive shells of icosahedral B_{12} units formed around a central icosahedral nucleus [127].

The first report about boron suboxide compound with presumable composition B_7O occurred in 1909 [128]. The first proposed crystal structure was considered to be orthorhombic [129]. Then, in 1961 it has been simplified to a rhombohedral one [130], which turned out to be correct. Actually few ways of B_6O synthesis are known at ambient conditions and at high temperatures (from 1365 K to 2100 K) and pressures (up to 20 GPa [111]). These ways can be divided by the reaction type on three main groups: reduction of B_2O_3 [130,131], oxidation of a boron [98,105,132] and reactions of comproportionation of boron [89,90,95-97,99-102,111,119,133,135-137] as for example: B + B_2O_3 or B + H_3BO_3. The latter is the most popular and wide spread. It has been found that pressure of 4-5.5 GPa and temperature of 2000-2100 K are ideal conditions for the synthesis of a practically stoichiometric B_6O of an icosahedral habit. The synthesis of the almost stoichiometric phase is possible even at pressures above 1 GPa if crystalline β-B_{106} is used instead of amorphous boron [133,134]. The authors of Ref. 110 notice that the molten B_2O_3 and the lower pressures (< 6 GPa) lead to the higher reaction ratio (the recovered sample is almost pure B_6O instead of mixture of β-B_2O_3 and B_6O). As one can note, the synthesis temperature of 2000 K does not exceed the melting point of β-boron. Consequently, during the synthesis of boron suboxide, oxygen atoms have to diffuse through solid boron in order to produce B_6O. Recently, it has been suggested [81] that the key to obtain the stoichiometric boron suboxide is not the high pressures or high temperatures. After the examination of dozens of works on B_6O and their own calculations it was assumed [81] that the synthesis duration (even at ambient conditions) plays a dramatic role in obtaining of stoichiometric compound. The high pressures cannot accelerate the oxygen diffusion through the solid boron and are probably necessary only to prevent B_2O_3 evaporation during the synthesis.

B_6O was found [89] to be very stable at atmospheric pressure and it starts to decompose into boron and oxygen at temperatures around 2000 K, therefore, the congruent melting of this phase can evidently be observed at high pressures only. B_6O melts congruently at high pressures and forms two eutectic equilibria with α-B_2O_3 and β-B_{106}, respectively [135,138]. The melting temperature at 4.3 GPa has been found to be 2620 K and ~2710±40 K at 5.8 GPa. Thus, boron suboxide melts at higher temperatures than β-rhombohedral boron. According to the recent theoretical work [139], B_6O undergoes phase transition into β-B_6O with monoclinic *Cc* structure above 245 GPa. The theoretical polymorph exhibits metallic behavior and greater elastic and hardness anisotropy (Vickers hardness ~ 20.7 GPa). Experimentally no new polymorphs of B_6O have been observed till now.

The boron suboxide has a rhombohedral Bravais lattice and crystalizes in $R\bar{3}m$ space group. It is a typical BRC with eight icosahedra in the corners of rhombohedral unit cell and two oxygen atoms (in 6c sites) aligned along {111} diagonal. B_6O unit cell can be presented in rhombohedral and hexagonal settings (Figure I.10). As it was marked in Ref. 80 the oxygen atoms are located 1.53 Å away from rhombohedral cell unit center and are not exactly in the tetrahedral voids, formed by near located icosahedra. A long distance between oxygen atoms indicates no bonding. Thus, oxygen atoms are coordinated/bonded only with three icosahedra. Due to rather large covalent radius, the oxygen atoms move these three icosahedra aside, which leads to the increased unit cell volume compared to α-B_{12} one. However, B_6O has the smallest unit cell volume among all the BRC derived from α-B.

It should be also underlined that the structure presented in Figure I.10 is an ideal case, which is almost unreachable in real experiments. In fact, oxygen atoms occupy the 6c sites only partially. Many scientific groups, who have worked on this compound, have observed different occupation of 6c sites by interstitial oxygen atoms. The assumption, made in Ref. 133 suggests that all the oxygen atoms, which are absent in 6c sites are replaced by boron atoms. So, it is more correct to replace $B_{12}O_2$ formula by $B_{12}O_{2-x}B_x$ where x can change from 0 to 1. As boron atoms have a larger diameter than oxygen atoms, one can expect an expansion of unit cell volume with increasing of x value. The analysis of many studies of B_6O supports the idea that the smallest unit cell volume is the stoichiometric one [81].

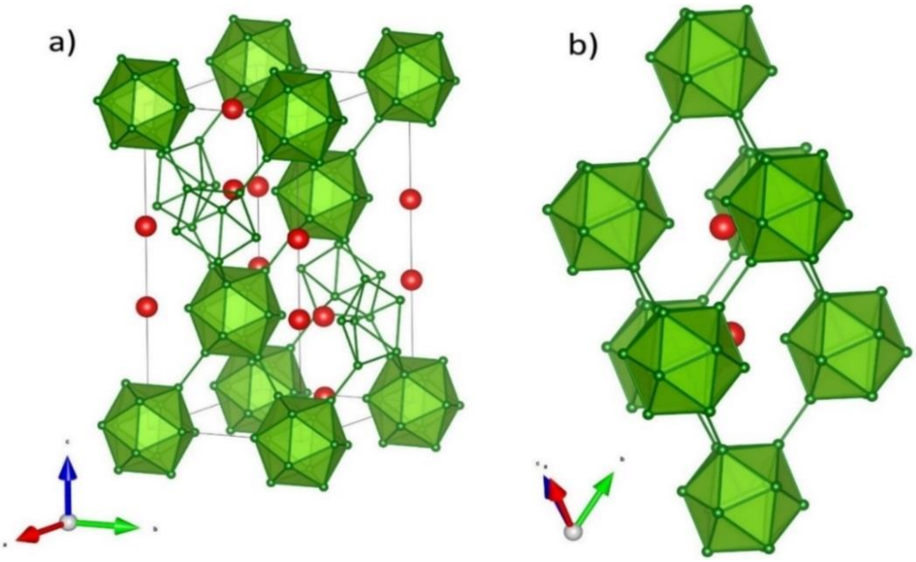

Figure I.10. Unit cells of B_6O: 1) in hexagonal setting, 2) in rhombohedral setting, showing B_{12} icosahedra (green), a pair of oxygen atoms (red) in interstitial sites 6c.

As it has been mentioned above there are two electron-two center bonds to non-boron atoms in BRC. This fact determines the chemical stability of stoichiometric BRC and of B_6O in particular. The rhombohedral unit cell consists of 12 Boron atoms and 2 oxygen atoms. Each oxygen atom gives its three electrons for bonding with three boron atoms. Moreover, it donates one electron to adjacent B_{12} icosahedra. The B_{12} "sphere", missing two valence electrons in α-B_{12}, becomes saturated as there are two O atoms donating one electron each in boron suboxide. All of the 12 B atoms in each "sphere", in their turn, give their three electrons to the bonding. During all of these processes, the electron shell structures of oxygen and boron atoms change: $1s^2 2s^2 2p^4 \rightarrow 1s^2 2s^2$ and $1s^2 2s^2 2p^1 \rightarrow 1s^2$ respectively. The latter electron structures are found to be essentially inert due to a high ionization energy of *s* electrons. Thus, the chemical stability of boron suboxide relates to *s*-shell electrons stability [81]. It should be also pointed out that, due to a high affinity of boron for oxygen, B_6O is one of the most frequently overlooked contaminations in boron and BRC [37].

Thus, it might be expected, that almost all the physical properties of boron suboxide will be influenced by oxygen content in $B_{12}O_{2-x}B_x$. For instance, as far as B-O bonds are stronger than B-B ones, the bulk modulus increases as B/O ratio increases ($x \rightarrow 1$). However, there is only one report on B_0 value which is equal to 181 GPa [111]. The density also changes in a wide range: from 2.44 g/cm^3 up to 2.67 g/cm^3 [81,89,95-102,105,111,119,131-133,135-137]. Vickers hardness (H_V) of boron suboxide is predicted to be 66.8 GPa [81]. The ratio of microhardness and bulk modulus (H_V/B_0) of $B_{12}O_{2-x}B_x$ should be constantly independent of x [140]. The band gap value of $B_{12}O_2$ is believed to be 2.0 eV [37]. All these properties make boron suboxide $B_{12}O_2$ one of the most outstanding BRC and oxides.

2.3 B-S system

Despite the fact that B-S system is less studied than B-O, there is a large number of publications on boron sulfides and other different compositions [141-147]. Nevertheless, among this great variety of boron sulfide forms only B_4S, B_2S_3, B_2S_5, $(BS_2)_n$, B_8S_{16} [148-150] have been characterized by means of single crystal X-ray structure determination. All the mentioned compounds can be prepared at ambient pressures and high temperatures. For example, $(BS_2)_n$ can be prepared from the elements at temperatures of 1100 to 1300 K, meanwhile colorless B_8S_{16} is a product of the B_2S_3 and S_8 fusion. As far as the literature review of the present work is mainly dedicated to the boron chalcogenides obtained under extreme conditions, we will not provide the description of the simple compounds in B-S system, forming at ambient pressure. One can find a complete and detailed description of the boron-sulfur system at ambient pressure in Ref. 151,152.

Apart from the boron sulfides which can be obtained at ambient pressure there are the reports on HP-HT syntheses of boron monosulfide [153,154] and boron trisulfide [155]. In Ref. [153]

boron monosulfide was synthesized at 6 GPa in two modifications: an orthorhombic phase (*o*-BS) obtained at 1400°C and a cubic phase (*c*-BS) obtained above 1500°C. The crystal structure of *o*-BS has been revised and it was revealed to be rhombohedral [154]. *r*-BS is a $A^{III}B^{VI}$ semiconductor. This compound is rather interesting, as far as it has a layered structure, and therefore physical properties of *r*-BS should be affected by its anisotropic structure. The synthesis of *c*-BS has not been repeated since 1967 as well as crystal structures of this phase has not been determined yet. That makes these compounds rather doubtful. In present work we provided a series *in situ* experiments with *r*-BS and obtained the new high-pressure phase of BS at high pressures (>30 GPa) and at room temperature. This phase is presumably of cubic syngony.

B-S system also possesses its BRC. The work on $B_{12}S$ has been done as long ago as in 1962 [156]. Later, the synthesis of series of BRC in B-S system with general formula $B_{12}S_{2-x}$ (where $2 > x \geq 0.7$) have been reported [97]. In spite of boron subsulfide can be regarded to the group of compounds synthesized at ambient pressure, its detailed description will be done further.

Thus, in this section we will start a review of B-S system from B_2S_3, then it will be followed by boron monosulfide and ended by $B_{12}S_{2-x}$.

2.3.1 Rhombohedral boron monosulfide r-BS

Boron monosulfide does not have “ambient pressure” polymorphs and is formed only at high pressures. For the first time, it was synthesized in 1967 and called *o*-BS, which means orthorhombic phase [153]. It has been revised in 2001 and its real crystal structure has been determined as rhombohedral [154].

The conditions of HP-HT synthesis of *r*-BS are 3-6 GPa, 800-1200°C [154]. The P-T phase diagram has been also suggested in Ref. 154. According to this diagram, boron and sulfur do not react with each other at temperatures lower than 400°C. Above 800°C at 5 GPa a mixture of *r*-BS and B_2S_3 was observed. Only at temperatures >1100°C, *r*-BS was obtained as a bulk single phase.

r-BS was revealed to be a semiconductor with an estimated band gap value of 3.4 eV [154]. The measured density of *r*-BS was measured to be 2.57 g/cm^3 [154]. Its color varies from white to pale violet, which is assumed to be due to the presence of impurities and/or deficiencies.

Unlike the results in Ref. 153, where boron monosulfide was determined as orthorhombic, it was shown that BS can be assigned to a hexagonal, moreover, rhombohedral lattice [154]. Nevertheless, it should be underlined here that the proper Rietveld refinement was not performed, because of low-Z number of boron and low quality of XRD data.

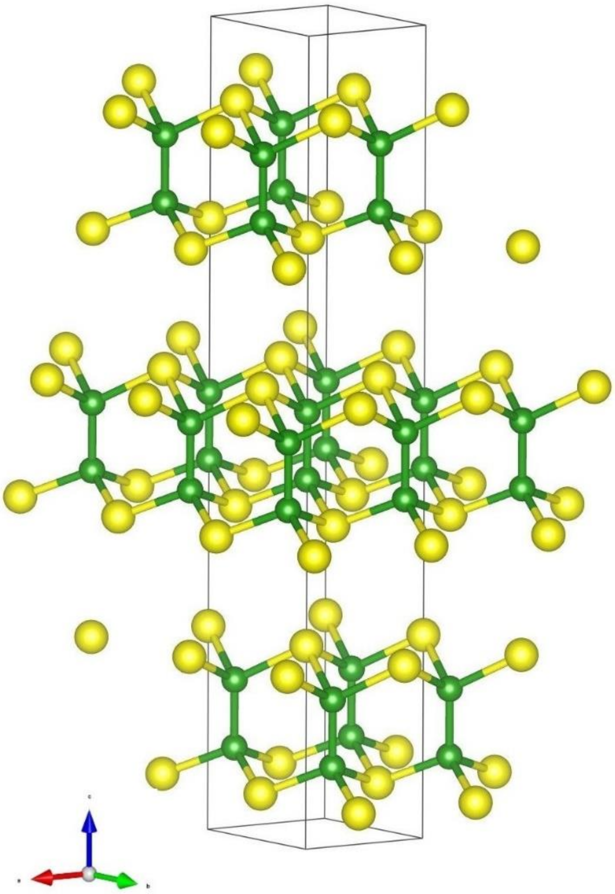

Figure I.11. Unit cells of *r*-BS in hexagonal setting, showing its layered structure (A-B-C motive). Each layer is composed from trigonal B_2S_6 antiprisms (boron atoms are green, oxygen atoms are yellow).

Rhombohedral boron monosulfide has the structural model of γ-GaS [157], C_{3v} point group, $R\overline{3}m$ space group (№166). The unit cell of *r*-BS in hexagonal setting is presented in Figure I.11. As one can see, *r*-BS has a layered structure with ABC alternation motive. One layer is built by B-B pairs aligned along the c-axis, placed between hexagonal layers of S atoms, rotated by π/3 relative to each other. If B-B bond is regarded as an M atom like in MX_2-type transition metal chalcogenides, it corresponds to the octahedral coordination of M atoms, and not to the trigonal prism coordination. Consequently, the coordination number of boron atoms in *r*-BS is four. The bonding scheme is the same as that of the $A^{III}B^{VI}$ layered compounds (GaS, GaSe, InSe, etc.), *i.e.* strong covalent intralayer bonds and weak van der Waals interlayer bonds. Hence, the physical properties of *r*-BS should be strongly affected by its anisotropic structure. Up to now *r*-BS remains a rather ill studied compound, as well as P-T phase diagram with nominal composition B:S = 1:1. In this work, we have provided HP-HT synthesis of *r*-BS in toroid type press, *in situ* measurements of equation of state and *in situ* measurements of phonon modes under compression at room temperature. The *ab initio* calculations also have been executed to estimate the phonon frequencies and such physical properties as bulk modulus (B_0) and its first derivation (B_0').

2.3.2 Boron trisulfide B_2S_3

B_2S_3 has at least three crystalline polymorphs [148,155] and is also known in vitreous state [158]. B_2S_3-I is a normal boron sulfide (synthesized at ambient pressure) according to the valencies, and has a layered structure. The sheets consist of two structural units: interconnected B_3S_3 and B_2S_2 rings extend throughout the crystal. Each of the B_3S_3 rings is connected by sulfur bridges to two B_3S_3 rings and one B_2S_2 ring. In the structure exocyclic B-S bond lengths are longer than endocyclic ones [148].

The two high-pressure forms of B_2S_3 have been reported [155]: B_2S_3-II and B_2S_3-III. However, only crystal structure of B_2S_3-III has been determined by single crystal XRD. Both polymorphs were obtained in HP-HT syntheses (3-6 GPa, 400-1600°C) in belt-type high-pressure equipment. From the experimental data the first P-T diagram for nominal composition B:S = 2:3 was proposed [155]. According to this diagram B_2S_3-II starts to form at 3 GPa above 600°C, whereas B_2S_3-III above 1000°C at the same pressure. The pressure of 5 GPa and temperature range 1300-1400°C were found to be a transition region between two high-pressure forms of B_2S_3.

B_2S_3-II has a white color, meanwhile B_2S_3-III forms the pale-yellow crystals. The densities of both high-pressure phases are higher than those of any other binary B-S compounds synthesized at ambient pressure. The measured density of B_2S_3-III is 2.48 g/cm^3 while that of B_2S_3-I is 1.95 g/cm^3 [148]. The density of B_2S_3-II is almost the same as of B_2S_3-III, which corresponds to the author's suggestion about the structural similarity between two polymorphs

According to a XRD analysis B_2S_3-II is anticipated to be amorphous and to have rather a disordered structure. Unlike B_2S_3-II, B_2S_3-III has tetragonal crystal system and $I4_1/a$ space group. (a = 16.086(2) Å, c = 30.488(4) Å and V = 7888(1) Å^3). It consists of nearly regular BS_4-tetrahedra and there are no B-B or S-S bonds in B_2S_3-III. In its turn, the BS_4-tetrahedra build two kinds of macrotetrahedra: 20 BS_4 and 34 BS_4. These units are linked to each other by sharing BS_4 tetrahedra at the corners. 20 BS_4 units are tetrahedrally coordinated by four 34 BS_4 units. Consequently, these units make an infinite three-dimensional network. The formation of such sophisticated structure would be impossible at ambient pressure but it seems to be easily organized under high pressure.

On other hand, B_2S_3 is a highly complicated and challenging compound for investigation by Raman, IR spectroscopies or by various X-ray techniques (XRD, XRS, etc.), as according to structural refinement [155] there are 33 (!) independent atom positions in the unit cell. The single crystal XRD spectrum of B_2S_3 contains 4630 unique reflections. The Raman and IR spectra of B_2S_3-III are not still reported, but taking into account the structure complexity they are expected to be rather sophisticated. Thus, in the frames of this thesis B_2S_3-II,III have not been studied.

2.3.3 Boron subsulfide $B_{12}S_{2-x}$

Among the great variety of boron sulfides there is a BRC in B-S system: boron subsulfide $B_{12}S_{2-x}$. It can be obtained as black powder in high-temperature and ambient pressure synthesis. Synthesis temperatures vary from 1200°C to 1700°C [97,156,159]. Elemental amorphous boron and crystalline sulfur can be used as starting materials. The stoichiometric quantities of reagents (with a little excess of sulfur) should be compacted into the pellets and placed into zirconia, BN or tantalum crucible and then in the high-frequency furnace. The reaction process undergoes under a flow of Ar. As it was mentioned in Ref. 156 the rate of heating is important, as the slow heating results in sublimation of S or B_2S_3, leaving boron as residue.

Boron subsulfide structure does not differ from another BRC: it has rhombohedral unit cell with B_{12} icosahedra in the corners, $R\overline{3}m$ space group (№166). S atoms are in 6c sites, hence a S-S pair is placed on the {111} diagonal tending to the expansion of the *a* and *b* axes and shrinkage of the *c* axis of the lattice. The reported distance between two sulfur atoms varies from 2.191 Å [97] to 2.386 Å [159]. In any case these distances are larger than the typical S-S tetrahedral bond length of 2.08 Å [160], which indicates a weak bonding interaction between sulfur atoms (unlike, for example, B_6O). The 6c sites occupancy also varies from one sample to another. For instance, there is a report on synthesis of stoichiometric $B_{12}S$ [156]. It is assumed, that the little deviations from this content can be caused by the presence of unreacted boron. Meanwhile the compounds of general formula $B_{12}S_{2-x}$ (where $2 > x \geq 0.7$) [97] and B_6S_{1-x} (where $0.4 \geq x > 0.37$) [159] have been obtained. It is very likely that some boron atoms replace sulfur atoms in 6c sites. The variation of sulfur atoms content could be explained by a notice made in Ref. 97: the longer heating time for sample in the furnace leads to "sulfur-poor" composition of boron subsulfide. In general, the 6c site occupancy in $B_{12}S_{2-x}$ is smaller than that reported for other BRC (e.g. [161,162]). The formation of a new phase with an unknown structure in samples with high sulfur content (~70% B_6S_{1-x}, x=0.372 and ~30% of unknown phase) was also reported [159].

The difference between boron suboxide and boron subsulfide (and boron subselenide as well) should be underlined here. In atomic arrangement of BRC, each chalcogen atom at non-bonding distance from each other makes a contribution of six electrons. Three of these six electrons are required for bonding to equatorial boron atoms (in three different B_{12}), two electrons constitute a lone electron pair and one electron from each chalcogen atom provides a stabilization of the icosahedra. In the case of the boron subselenide and the boron subsulfide, the size of the chalcogen atoms makes such arrangement impossible, as the distance between the chalcogen atoms and the equatorial boron atoms in the neighboring icosahedra would be too short. Thus, the stoichiometry for BRC of selenium and sulfur cannot have $x \approx 2$.

According to Ref. 159, the density of $B_{12}S_{2-x}$ samples depends on x value: $x = 0.38$ $\rho = 0.73$ g/cm^3, $x = 0.391$ $\rho = 1.12$ g/cm^3, $x = 0.401$ $\rho = 0.96$ g/cm^3. Meanwhile, the density measured in Ref. 155 turned out to be about 2.40 g/cm^3, which is higher than one predicted from XRD (2.33g/cm^3). According to [159], B_6S_{1-x} samples possess *p*-type conductivity and the electrical resistivity decreasing with temperature, which is typical for semiconductor materials. As well as in another BRC, the electrical resistivity of boron subsulfide depends on the density of material. For instance, low-density samples possess high electrical resistivity. It has been also found, that the thermopower of B_6S_{1-x} is similar to B_4C [159], with large Seebeck coefficients, which are increasing at higher temperatures. Thus, $B_{12}S_{2-x}$ can become a concurrent to boron carbide as a promising candidate for high-temperature thermoelectric conversation.

2.4 B-Se system

The chemistry of B-Se system is similar to that of B-S system. There are the same difficulties in its study, as: tendency towards vitrification, sensitivity to hydrolysis, high-temperature synthesis conditions, leading to contamination by capsule or crucible material, etc. Due to the fact that the chemistries of B-S and B-Se are the same, there are the same binary compounds: boron selenides BSe_2 [163] and B_2Se_3 [164], boron subselenides B_2Se [152], and $B_{12}Se_{2-x}B_x$ [165]. All of these compounds have been synthesized at high temperatures and ambient pressures. The reviews [149,151,152] present the detailed and complete description of properties and synthesis particularities of binary compounds in B-Se system.

Herein only $B_{12}Se_{2-x}B_x$ will be reviewed. This boron subselenide is formed at high temperatures and 1 atmosphere, but as well as boron subsulfide $B_{12}S_{2-x}$, being a structural analog of B_6O it reveals a big interest in its mechanical properties and structural details investigation.

2.4.1 Boron subselenide $\mathbf{B_{12}Se_{2-x}B_x}$

Boron subselenide $B_{12}Se_{2-x}B_x$ regards to BRC compounds type. Up to now there is only one publication devoted to the synthesis and characterization of boron subselenide [165]. It was obtained in the same manner as boron subsulfide $B_{12}S_{2-x}$: a mixture of elemental selenium and amorphous boron was heated in the furnace to 1600°C in inert gas atmosphere. This experimental procedure gave a dark brown sample.

Rietveld structure refinement showed that $B_{12}Se_{2-x}B_x$ has rhombohedral unit cell with $R\bar{3}m$ space group (№166). As well as in the other BRC interstitial atoms situate in 6c sites. To refine a structure of $B_{12}Se_{2-x}B_x$ the used Longuet-Higgins and Roberts electron counting (LHREC) was used [165]. According this method/counting a structure arrangement with two selenium atoms on the {111} diagonal, resulting in electron excess, is impossible, since BRC tend to be electron deficient rather than containing an excess of electrons. A few different structural arrangements of boron subselenide were tried to conform with LHREC. It turned out, that if 67% of the positions are occupied by chalcogen atoms and the rest by boron, the required number of electrons is obtained and LHREC is satisfied. A distance between Se and B atoms in 6c sites is believed to be 2.38 Å. The authors underlined that x value is always around 1. It cannot be dramatically less than 1, which means the occupancy of the 6c sites by Se atoms ≥50%.

As well as in case of boron subsulfide there is almost no information in the literature about $B_{12}Se_{2-x}B_x$ mechanical properties (Vickers hardness, bulk modulus, etc.) and electrical properties. However, the investigations in this filed may shed light on the question: how does the substitution of the chalcogenide in BRC influence on the physical properties?

Chapter II

3 High pressure techniques

A majority of experimental work performed in the thesis has been done using various high pressure (HP) devices. In combination with modern analytical equipment these devices allow to provide various *in situ* experiments at temperatures up to 2500 K and pressures up to 100 GPa. Such incredible variation of the physical variables gives rise to the new approaches in the conventional chemistry, which in its turn leads to synthesis of new type compounds possessing the outstanding properties.

3.1 Pressure generation techniques

Historically, the development of HP techniques owes its existence to attempts to obtain artificial diamond. This work was successfully done in 1953 in Sweden [166] and in 1954 in USA [167], but even after achieving the main goal the HP devices have been continued to be developed as they opened the way for synthesis of many materials with outstanding properties, as for example *c*-BN [168].

The large number of modern high pressure devices can be traced to the principles laid out by P.W. Bridgeman, the pioneer of HP techniques, who awarded the 1946 Nobel prize for his work on the physics at high pressures. One of the main principles used starting from the Bridgeman's works and onward is massive support principle, a laboratory analogue of the tapered foundation design, employed by civil engineers, since antiquity, to support the great loads of huge structures by the comparatively softer earth. That the taper reduces the large working stresses quickly to tolerable levels has been realized for a long time, thus even by applying a comparatively little loading forces on the base of truncated press anvil, very high pressures can be obtained on the opposite pressing side. The expression for the maximum pressure (P_{max}) which can be generated at the center of the truncated anvil is:

$$P_{max} = \frac{1}{2}B^2 \frac{e^{Ba}}{e^{Ba} - Ba - 1}(a + Z_b \, cot\alpha)^2 S_A, \text{where } B = \frac{2\mu}{h} \qquad (II.1),$$

where S_A is compressive strength of the anvil, a is radius of anvils, h is thickness of gasket, μ is the coefficient of friction between the anvil and gasket, Z_b is depth at which the tapered portion of anvil ends and α is the taper angle. As one can see from this formula, the higher maximum pressure (P_{max}) depends on many factors: materials of anvil and gasket, shape and mechanical properties of the anvils. Various materials like steel, tungsten carbide, boron carbide, sapphire, cubic zirconia, sintered diamond, and single crystal diamond have been used for anvils production. Their use for a specific technique and pressure ranges is related to their strength, available sizes and shapes, optical clarity, X-ray transmission, and other mechanical, thermoelectric and magnetic properties.

Another important principle of HP apparatus work is a hydrostaticity of the compression. It is evident that only with nearly same pressure in all sample volume the confident experimental data can be retrieved. Pressure transmitting medium (PTM) and gaskets are crucial/necessary components of the hydrostatic or quasi-hydrostatic compression. The gaskets, prepared usually from the materials with low coefficient of internal friction, fill the space between two or more anvils. Under compression the gaskets deform in all directions, including the directions toward the assembly center, thereby transferring anvils pressure on the sample area. It should be noted that the gasket materials and shapes depend on the HP apparatus type and even on the concrete experimental conditions. PTM uniformly transmits external compression directly on the sample and thus it should have low internal friction coefficient value too. As far as it contacts with the sample it should be chemically inert. As well as in case of gaskets, for different types of HP apparatus and different HP measurements various PTM are applied.

Nowadays there are a plenty of HP device types: the diamond anvil cell (DAC), the Paris-Edinburg press (PEP), the supported anvil Drickamer cell, the toroid type press (TTP), Bridgman anvils, multi-anvil press (MAP), etc. But all of these HP devices could be divided onto two main groups: the HP apparatus with two opposed anvils (DAC, PEP, TTP) and with a few (4÷8) anvils (Bridgman anvils, MAP). The choice of a specific pressure device strictly depends on the measurements to carry out. In the next parts all types of HP devices used in present work will be reviewed.

3.2 Diamond anvil cell (DAC)

The diamond anvil cell (DAC) is currently the device that reaches the highest static pressure (~400 GPa [169]). One of the greatest advantages of DAC is transparency of its anvils. So a sample can be observed during compression and *in situ* studied by various techniques: X-ray diffraction, X-ray spectroscopy, Raman, IR, UV, etc. In case of the optical experiments it is very important to know the type of diamond, as a different stones has different impurities which might give rise to strong fluorescence. A special lettering system from D to Z is using to classify the diamonds by color and therefore by their experimental application. For example, the diamonds with D class are rare, totally colorless. Thus stones with color grades D or E, with low fluorescence, are suitable for Raman scattering experiments. A good "Raman" diamond should have a flat background. The essentially impurity-free synthetic diamonds are also available (little or no observable fluorescence), but they are still difficult to obtain and are expensive. In case of X-ray diffraction (XRD) experiments, diamond anvils do not cause the problems, except for the study of liquids where the Compton signal of diamonds becomes a problem. Diamond has a simple crystal structure, its diffraction pattern is simple and easily identified. Moreover, as the diamond anvils are single crystals, their diffraction leads to few well-defined spots within the Laue zone that are easily identified in angle-dispersive (ADX) experiments.

The DAC gasket is a thin sheet of metal that has a small hole about 1/2 diameter of the diamond anvil (cutlet face). Gaskets are typically prepared by indenting the diamonds into a thin metal sheet and then drilling a tiny hole through the indented portion of the gasket. The holes can be done either by electroerosion or by high-energy micro-focused laser. The indentation thickness also influences on the maximum reachable pressures. Rhenium is commonly used for the gasket, but tungsten, stainless steel 301, Kapton, *c*-BN, Cu, Be are also mentioned in the literature.

The PTM for DACs are weak solids and liquids or fluids. The role of PTM is to transmit pressure to the sample while minimizing the shear stress transmitted to the sample. Common PTM are N_2, Ar, He, Ne, ethanol, methanol and NaCl. "Gasses" such as He, Ne or Ar are a highly desirable PTM, due to their chemical inertness. They are loaded into the cell only in a fluid state. The liquid PTM provide true hydrostatic environment. However, many fluid media crystallize as pressure increases; thus a media that works well at lower pressure may crystallize and introduce error at high pressures. After the crystallization point of PTM the compression can be called only quasi-hydrostatic.

The principle scheme of DAC construction is presented in Figure II.1.

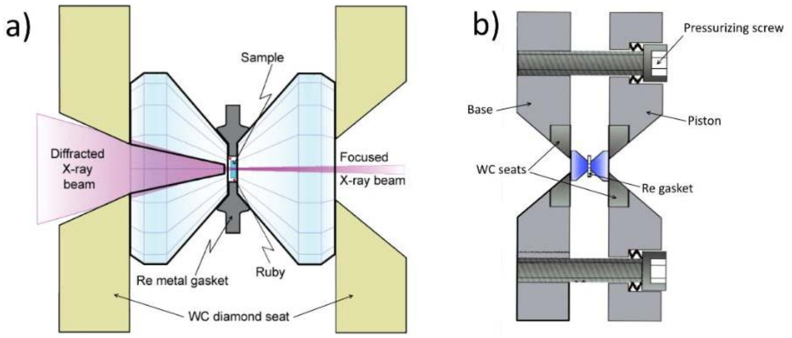

Figure II.1. DAC: a) general schematic construction; b) construction of Merrill-Bassett-type Diamond Cell, the main parts of the cell are marked.

Cell designs are as diverse as the types of experiments that are conducted in them. There are cells specialized for room temperature, cryogenic or heated experiments, ultra-high pressure, radial or axial diffraction, spectroscopic studies, fluid studies, etc.

3.2.1 Generating high pressures

There are a plenty of pressurizing mechanisms and therefore a plenty kinds of DACs (see [170]). In our studies only membrane diamond anvil cells (MDAC) have been used. It means that metallic toroidal membrane inflated with helium pushes on the piston (see Figure II.2.).

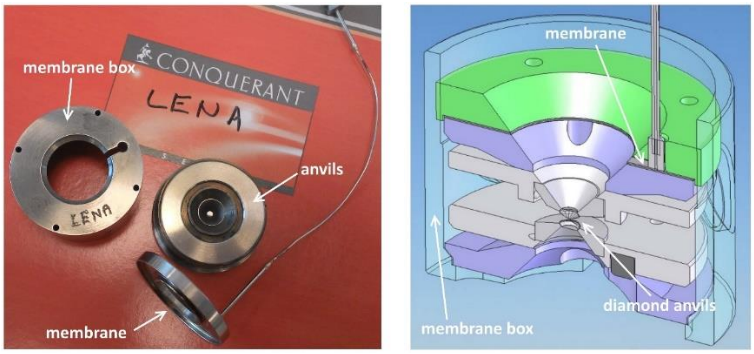

Figure II.2. Schematic view of MDAC.

Membrane generates axial force, which is therefore homogeneously extended over all the piston, permitting a precise control of the pressure. The membrane is linked by a metallic capillary to a He bottle through a pressure pneumatic drive system (PDS). By using MDAC, pressure on the sample can be easily tuned without touching or displacing the cell. This is a great advantage of the MDACs concerning to *in situ* synchrotron measurements. Using of micro-valves also permits to “keep” an obtained pressure and meanwhile to disconnect the cell from PDS for transportation or keeping it independently.

In present study, only rhenium and stainless steel have been used as gasket materials (gasket thickness ≈ 200 µm). He and Ne have been used as PTM.

3.2.2 Measuring high pressures

Although in theory, one should be able to calculate the pressure in the DAC by knowing the force applied to the support side, the area of the support side and the area of the cutlet, nobody knows the amount of force which is dissipated by flow in the gasket and the sample. Thus, an internal pressure standard is required.

The majority of DAC studies utilize one of two strategies for pressure measurement:

- measuring the unit cell size of a material whose equation of state (EoS) is well known;
- measuring the position of the fluorescence lines of ruby (Al_2O_3 doped by Cr^{+3}) or YAG. The positions of these fluorescence lines are well known as a function of pressure. Ruby fluorescence is very commonly used for pressure measurement and actually has been generally used in present work.

Ruby is chemically inert and has strong luminescence when hit with a green laser light. There are two peaks (R1 of 6942.48 Å and R2 of 6927.0 Å) in luminescence spectrum of ruby at ambient conditions. The shift of R1 with pressure has been calibrated several times [171-175]. Up to 20 GPa it was found to be linear, whereas at higher pressure it can be determined from following equation [175]:

$$P = \frac{0.274 \cdot \lambda_{R1}(0)}{B}\left[\left(\frac{\lambda_{R1}(P)}{\lambda_{R1}(0)}\right)^{B} - 1\right] \qquad (II.2),$$

where B is a parameter related to the degree of hydrostaticity on the sample: B = 5 for non-hydrostatic conditions and B = 7.665 for conditions close to hydrostaticity. As the pressure increases both components of the R1, R2 doublet broaden until there is a complete overlap at a pressure which depends on the quality of the hydrostatic conditions on the sample. The signal to noise ratio decreases with increasing pressure, making precise high pressure measurement more difficult. The position of the R1 peak is also dependent on temperature [176]. When ruby is heated, its luminescence peaks broaden and decrease in intensity to a point just above 400°C where their position can no longer be measured. Despite this, for HP experiments in DACs below 200ºC ruby is the best pressure marker.

Another strategy for pressure measurement is to use XRD to measure the lattice spacing of a material for which the EoS is known as a function both pressure and temperature. This technique can be used at high temperature as well as low temperature. It is potentially more precise than using fluorescence methods to determine pressure. The disadvantage of using an EoS is that it requires access to an X-ray source, and measurement time.

3.3 Paris-Edinburgh press

The Paris-Edinburgh press (PEP) is a large volume device with two opposed anvils. Its design is not fundamentally different from the DAC one. PEP was initially designed for high pressure neutron diffraction studies [177] being later adapted to synchrotron ADXRD experiments [178]. The general schematic view of PEP and its anvils one can find in Figure II.3 *a*. In present work we provided a few experimental sessions using PEP installed in PSICHE beamline at synchrotron SOLEIL (see Figure II.3 *b*).

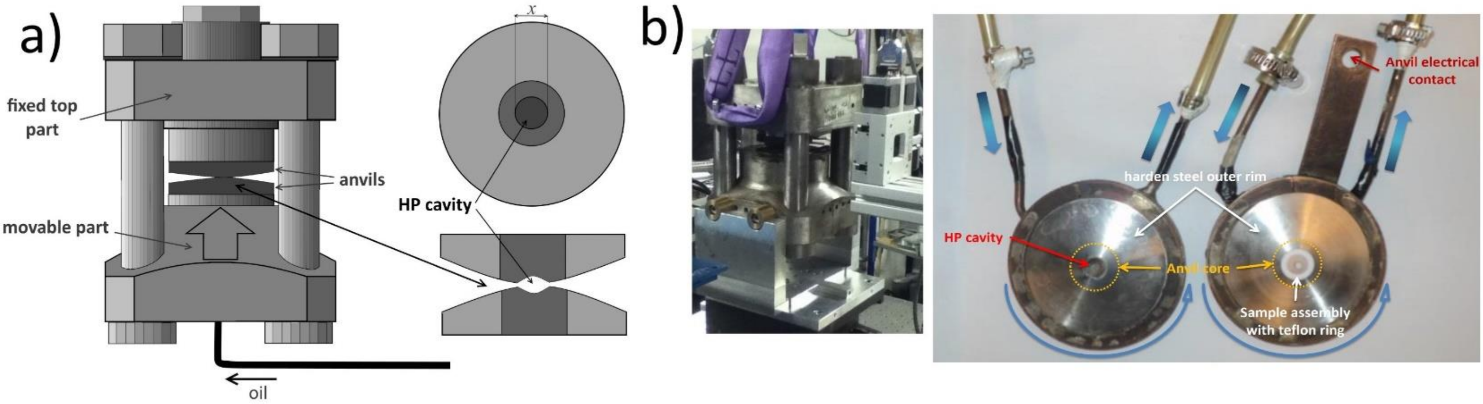

Figure II.3. a) Schematic view of PEP and its anvils; b) the PEP in PSICHE beamline and its anvils; all anvils parts are signed, the direction of the water cooling flow inside the copper cooling system is shown by the blue arrows.

As one can see from Figure II.3 PEP is easy to handle, its weight does not exceed 50-60 kg. It makes the press highly portable, which is one of the big advantages of this HP apparatus. The top part of PEP is fixed and compression is performed by means of movable bottom part (piston). The loading force of 250 tons is generated by a hydraulic jack. A hydraulic pressure of oil is exerted on a piston by means of a hand pump or an automatic one (up to ~250 MPa capacity), which is connected to the press by a flexible tube.

The most important part of the PEP are the anvils. They can be replaced with another ones, permitting to provide HP-HT experiments in different pressure ranges. The anvil has a circular shape with a quasi-conical profile (with opening angle up to 15°) and consists of two parts: the harden steel outer rim and the anvil core made from some hard material (see Figure II.3 *b*). Usually, anvils core is prepared from WC-Co alloy, but for reaching the higher pressures a sintered diamond (SD) can be used. The anvil core has a special HP cavity dedicated for sample assembly. The surface of the HP cavity determines a pressure on the sample. The ratio of its surface to those of the piston is ~0.01, thus the hydraulic pressure is increased by a factor of 100 at the sample chamber. Consequently, by changing a HP cavity dimensions (in other words, x value in Figure II.3 *a*) one can vary a maximum reachable pressure: the smaller HP cavity is (or the smaller x is), the higher pressure on the sample might be obtained. So, for instance, the x values of 5, 7, 10 and 12 mm correspond to the possible maximum reachable pressures of 17, 10, 8 and 6 GPa respectively. In our work the anvils with only x = 7 and 10 mm have been used. The HP cavity shape is also of great importance, as it has to generate the conditions that are close to hydrostaticity and to minimize the gasket deformation, in order to keep the access to the sample for the X-rays.

The sample assembly requires a special consideration. Basically it consists of: the gasket, sample capsule, heater and electrical current providers. Depending on the certain experiment needs these details can be prepared from different materials, moreover some details can be either eliminated or added. Herein we will provide the description of sample assemblies that have been used in our experiments (e.g. for the HP-HT studies of B-Se system). The detailed scheme of the sample assembly is presented in Figure II.4.

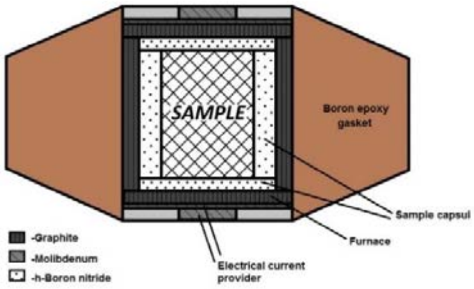

Figure II.4. Arrangement of PEP assembly, the main parts are undersigned.

Gaskets. Pyrophyllite and special boron-epoxy (BE) ceramic have been used as materials for PEP gaskets. Pyrophyllite is very popular material for the gaskets in many types of LVPs due to its high deformability, high melting temperature, low thermal conductivity, etc. Nevertheless, its chemical bruto-formula is $Al_2[Si_4O_{10}]\ (OH)_2$, which can be rather "heavy" compound in terms of XRD, leading to decrease signal to background ratio. BE is a fortunate alternative to pyrophyllite for *in situ* XRD measurements of the samples with low *Z*-numbers. The main component of this ceramic is amorphous boron, which is almost "transparent" for X-rays. Sometimes an additional Teflon (or PEEK) rings can be placed around the gasket in order to reduce gasket flow under compression (see Figure II.3 *b*).

Furnaces and electrical current providers. Only resistive heating of sample can be provided in case of LVP. Electrical current is provided to the furnace through the anvils and the electrical current contacts. As one can see from Figure II.4 the furnace is a simple sleeve with very thin wall. There are two main categories of the furnaces: high current-low voltage and low current-high voltage. The heaters of the first group include graphite and metal foils (Mo, Re). Low current-high voltage heaters include semiconductors, e.g. $LaCrO_3$, which can also be used for thermal insulation around high current-low voltage heaters in low P range. In our work only graphite furnaces have been used taking into account simplicity of their preparation, using and price. They allow to reach the temperatures up to 2300 K. The graphite disks are usually placed on the top and the bottom of furnace in order to provide an uniform heating.

Graphite is also the best heater for *in situ* XRD measurements due to its transparency for X-rays. However, the conversion of graphite to diamond, or possibly to lonsdaleite usually takes place above 10 GPa and at temperatures >1500°C. Thus, a metal-insulator transition occurs along with mechanical collapse of the sample chamber area.

Sample capsule. It is not necessarily to use. Usually capsule is used to prevent direct contact between sample and furnace material (in case of electrical conductive sample, it is of course a problem) and probable undesired chemical reaction. However, using of the sample capsule may cause of decrease of sample heating. Thus the sample capsule material must be good thermal conductor. Hexagonal BN (*h*-BN) is the most popular material, whereas Al_2O_3 or MgO might be used as alternatives to boron nitride. For the biggest assemblies the sample volume may reach 80 mm^3.

3.3.1 Generating high pressures and temperatures

As it has been written above HP in PEP is generated by the principle of hydraulic jack. The hand pump connected to the press could be complemented by automatic one. For our measurements an automatic pump of ST (Sanchez Technologies), delivering a stable oil pressure up to 2000 bars, has been used. This kind of pump does not provide high compressing rates in the beginning of compression but ensures stability of the pressure value. For instance, in our measurements pressure deviations from the set pressure value did not exceed 2 bars. Each new pair of anvils requires individual calibration (sample pressure (GPa)-hydraulic oil pressure (bars)), as even a slight variations of anvil core diameter may lead to significant differences in final pressure.

The high temperatures are generated by a power supply. Electrical cables are connected to the anvils. Thus anvils are the electrical contacts/providers. During HP-HT experiments the anvils might considerably warm up, which can lead to their breakage. To decrease the anvil's heating a water cooling system is usually used. Basically the cooling system is presented by the coper tubes which go around the side of the anvils (see Figure II.3 *b*).

3.3.2 Measuring high pressures and temperatures

The pressure generated in HP cavity is rather reproducible, so it might be enough for rough estimation. An opaque PMT and sample assembly prevent using the rubis for *in situ* pressure determination. For more precise pressure determination a pressure standard/callibrant with well known EoS (e.g. NaCl [179,180], Au [181]) is needed. In case of very small assemblies (e.g. x=5 mm) and very little samples volumes, EoS of *h*-BN capsule can be used [182]. In present work we used the internal pressure markers (e.g. *h*-BN) in *in situ* XRD measurements. For *ex situ* experiments only sample pressure - oil pressure calibration can be exploited.

Temperature measurements can be done using thermocouples, power-temperature calibration curves or internal calibrants. The thermocouples have a lot of drawbacks as for example: high risk of the assembly blow out, rupture of thermocouple wire, destruction of the furnace, temperature gradients, etc. Moreover the thermocouples do not guarantee reproducible temperature values. Thus we did not use them in our work. The power of power supply source can be regarded to phase transitions (including melting) of some etalon material. Thus a calibration curve power *versus* temperature can be plotted. Although this way of temperature determination is the easiest one and rather reproducible, it is not perfect. It happens because of variation of furnace dimensions and all other assembly details in general.

The presence of standards inside the assembly is the most desirable and effective. Fortunately, the pressure internal standards mentioned above (NaCl, Au or *h*-BN) can be also applied for temperature determination. Obviously, an internal standard allows to calibrate only one of the two P,T variables, so that the second must be known. The measurement of volume variations of two internal standards was proposed in Ref. 183. Ideally the chosen materials should have well determined and contrasting thermoelastic properties. Good choices could be Au/NCl or *h*-BN/Pt couples. It is important to choose materials whose Bragg peaks used for the determination of the volume variation do not overlap.

However it should be underlined that the method of using only the thermoelastic properties of well characterized materials, is theoretically limited by the quality diffraction patterns. Also one should note that X-ray spot should have the smallest possible dimensions in order to reduce thermal and pressure gradient effects.

3.4 Toroid type press

A toroid type press (TTP) is one more representative of the group of HP devices with two opposed anvils and has a long history of application in HP science [184]. In present work the TTP has been employed as a basic device for HP-HT *ex situ* synthesis. The press is installed at LSPM-CNRS, university Paris-Nord.

TTP construction does not dramatically differ from one of PEP and is presented in Figure II.5. As well as PEP it consists of the ram with fixed top anvil and movable bottom anvil (piston). The loading force is around 1200 tons, which is almost three times higher than those of PEP. An electric compressor is employed for hydraulic pressure generation.

There is almost no difference between TTP and PEP. However, traditionally, TTP anvils have WC-Co hard alloy anvil core with toroidal HP cavity. The toroidal HP cavities are also available for the PEP anvils, but are not so wide spread as in case of TTP. The schematic view of TTP anvils are presented in Figure II.5. The toroidal shape of the HP cavity is dedicated for additional supporting ring around the gasket, which permits to reach rather high pressures (up to 10 GPa) at considerably big sample volumes (30-500 mm^3). The sample volumes up to 500 mm^3 is the main advantage of this press, especially taking into account, that pressure and temperature gradients in the sample assembly were found to be very low.

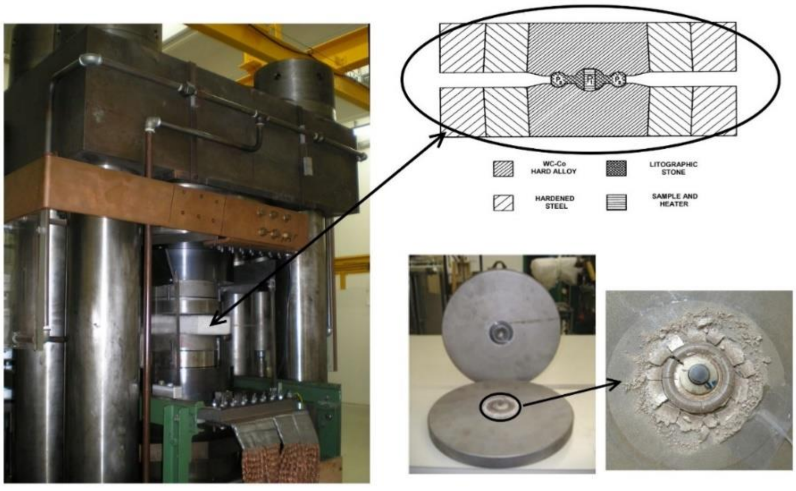

Figure II.5. TTP installed in LSPM-CNRS, university Paris-Nord. On the right, the TTP anvils with toroidal HP cavity are presented.

One may expect that decrease of the HP cavity diameter will lead to increase of the maximum reachable pressure. However, changing of the HP cavity requires recalculation of the supporting ring dimensions, which is rather sophisticated and expensive. The cheaper way to increase the highest pressure is to put an additional WC-Co harden alloy or steel tablet on the top and bottom of the assembly.

The standard sample assembly of TTP is considerably bigger than that of PEP. Depending on the experiment aims an arrangement of the sample assembly can be varied. The scheme of the basic TTP sample assembly is shown in Figure II.6.

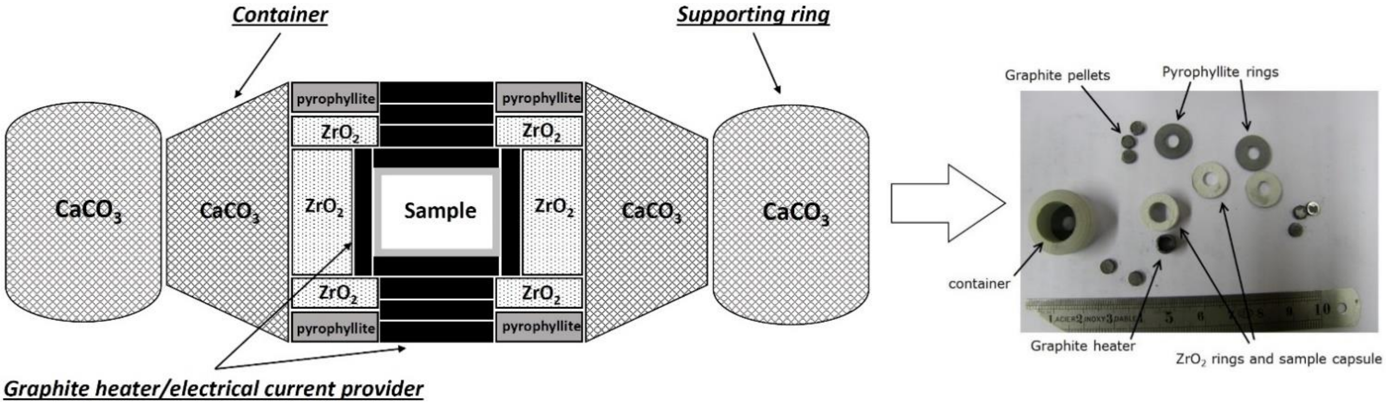

Figure II.6. The arrangement of TTP assembly; the main parts are undersigned.

Gaskets. A TTP gasket consists of two parts: container and supporting ring. The container material is limestone ($CaCO_3$). As one can see from Figure II.6 the containers are rather big (diameter of the hole is either 11 or 12 mm). The supporting ring is made from limestone as well. Together these parts create a barrier layer during compression (see Figure II.7). This very barrier layer helps to compress the samples of large volumes up to 8 GPa and heat them up to ~2500 K.

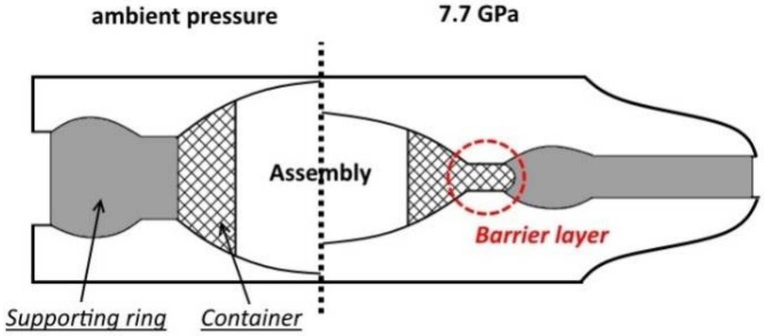

Figure II.7. A barrier layer of TTP assembly.

Furnaces and electrical current providers. The resistive heating is applied in TTP. Electrical current generated by a power supply is provided through the anvils as well as in PEP. Graphite is an universal material for the furnace and electrical providers in TTP assembly (see Figure II.6). The furnace is a sleeve with a thicker walls than in PEP heater. In combination with graphite pellets which work both as heaters and electrical contacts the furnace provides rather uniform heating. Using of Re or $LaCrO_3$ as the alternative materials for the furnace (however more expensive) is also possible, taking into account the drawback of the graphite furnaces in P-T range of graphite-diamond conversion.

Sample capsule and sleeve. Sample capsule might have internal hole of the different diameters, depending on sample size, etc. The main purpose of the sample capsule (usually made from *h*-BN) is to preserve a sample from direct chemical interaction with the heater. In HP-HT experiments the isolation of $CaCO_3$ container from furnace is also necessary. The basic material of this sleeve is pressed ZrO_2-Y_2O_3, which is an excellent temperature insulator. The choice of the materials for sample capsule and sleeve can be explained by their thermal transporting properties, high chemical inertness and low cost. It should be also underlined, that sample capsule made from one piece of *h*-BN requires a special tooling, whereas the details pressed from powder of ZrO_2-Y_2O_3 do not need any special equipment for their preparing.

3.4.1 Generating high pressures and temperature

The pressure generation in case of TTP is executed by electric compressor, which permits to reach high compression/decompression rates (initial rate up to 2 GPa/min). For instance, the compression up to 4.2 GPa takes only 2 min, whereas the decompression from 7.7 GPa takes 10 min. This can be considered as an advantage of TTP. However, TTP does not ensure the pressure stability during long time experiments (oil pressure degradation up to 25 bars). Each pair of anvils needs a calibration (pressure (GPa)-hydraulic oil pressure (bars)) as well as for PEP anvils.

High temperatures are generated by computerized direct-current IPM 30 Kempower heating system. Electrical cables are connected to the anvils. The temperature can be stepwise increased with a heating rate of 200 K/min. Duration of heating at required temperature is usually from 2-3 min at 2500 K to 60 min at 1000 K. Then samples can be rapidly quenched (~500 K/s) by switching off the power. The problem of warming up of the anvils in TTP during the HP-HT experiments might be solved by using huge steel outer rims (see Figure II.5). Despite this in long HP-HT experiments the anvils can be considerably heated, which can lead to the WC harden alloy breakage. Another problem of the HP-HT experiments is a chemical interaction between WC-Co alloy and graphite heater at high temperatures. This interaction results in damage of HP cavity. To preserve WC-Co from graphite, a thin nickel foil is placed on the bottom of HP cavity. At very high temperatures (~2500 K) and pressures around 7 GPa nickel foil can catalyze a formation the diamond, leading to decrease of the sample heating. In such case, nickel foil should be replaced by a molybdenum's one.

3.4.2 *Measuring high pressures and temperature*

As it has been mentioned above TTP is used only for *ex situ* experiments. Consequently, only external pressure and temperature determinations are available. Sample pressure as a function of hydraulic oil pressure or press load can be calibrated using room-temperature phase transitions in Bi (Bi $_{\text{I-II}}$ at 2.55 GPa and Bi $_{\text{III-V}}$ at 7.7 GPa), PbSe (4.2 GPa) and PbTe (5.2 GPa). By measuring an electrical current through the pressure standard (or electrical resistance of the sample) one can precisely discriminate a phase transition. An example of the pressure calibration curves for different pairs of anvils of TTP installed in LSPM-CNRS is presented in Figure II.8.

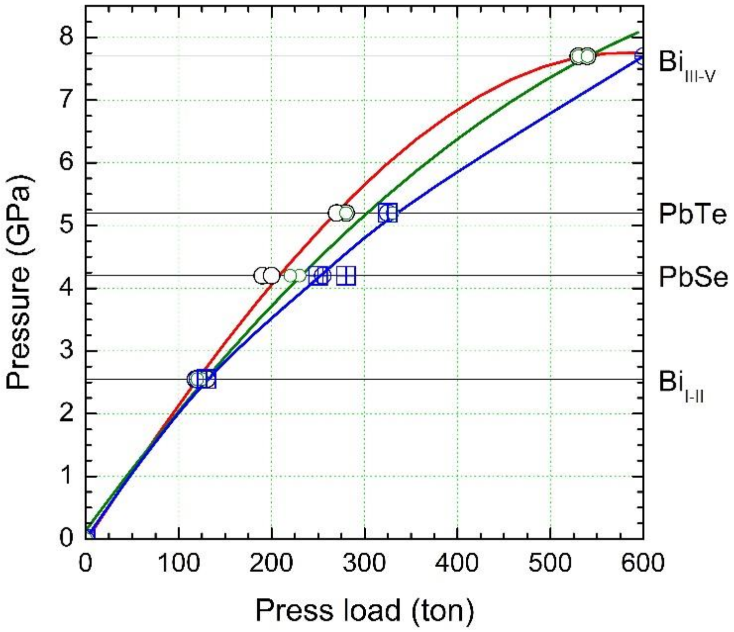

Figure II.8. Pressure calibrations curves of the different pairs of anvils of the TTP in LSPM-CNRS.

The temperature calibration under pressure can be done using Pt/Pt-10%Rh and chromel-alumel thermocouples, as well as by using well-established reference points: melting of Si, NaCl, CsCl, Pt, Rh, Al_2O_3 and Ni-Mn-C ternary eutectic. In the case of Pt, Rh, and Al_2O_3, the melting points can be found in series of quenching experiments from the change of shape and microstructure of the reference material pressed into a cylinder of *h*-BN, while in the other cases the melting temperature can be fixed *in situ* from the electrical resistance jump in the cell. In this case, an important condition is that the reference material should be in a direct contact with a heater. It should be noted, that according to *in situ* T calibrations performed for the high-temperature assembly presented in Figure II.6, the temperature gradients usually do not exceed the 20 K/mm in the sample area. The use of thermocouples is not always suitable because of frequent blow outs. In the present work, the experimental temperature was determined only by previous power-temperature calibration curves.

3.5 Multi-anvil press

A multi-anvil press (MAP) presents the next group of LVP – HP devices with another geometry of anvils. Among all of the LVPs the MAP can reach the highest pressures of ~30 GPa [185] and ~90-95 GPa [186] for WC-Co hard alloy and SD anvils respectively. Using of the several equivalent anvils results in significantly higher hydrostaticity of the compression compared to DAC, PEP and TTP. MAP can be divided on two stages: the 6 anvils of the first stage and 8 anvils of the second stage. Thanks to such two stages construction, the uniaxial compression of vertical hydraulic ram finally transforms to almost homogeneous compression of 8 anvils of second stage.

The multi-anvil apparatus was first introduced by Kawai and Endo in 1970 [187]. They used a split steel sphere suspended in pressurized oil. Later the sphere was replaced by the hydraulic ram [188]. In 1990, Walker *et al.* [189] simplified the first compression stage by introducing the removable hatbox design, allowing ordinary machine presses to be converted into multi-anvil systems. Such type of MAP module is called Walker's module. Apart from Walker's module construction, there is another MAP module - DIA module, which was first designed in 1964 [190] and has been later modified. The difference between two MAP module types is shown in Figure II.9. For a history of LVP, please see the Ref. 191.

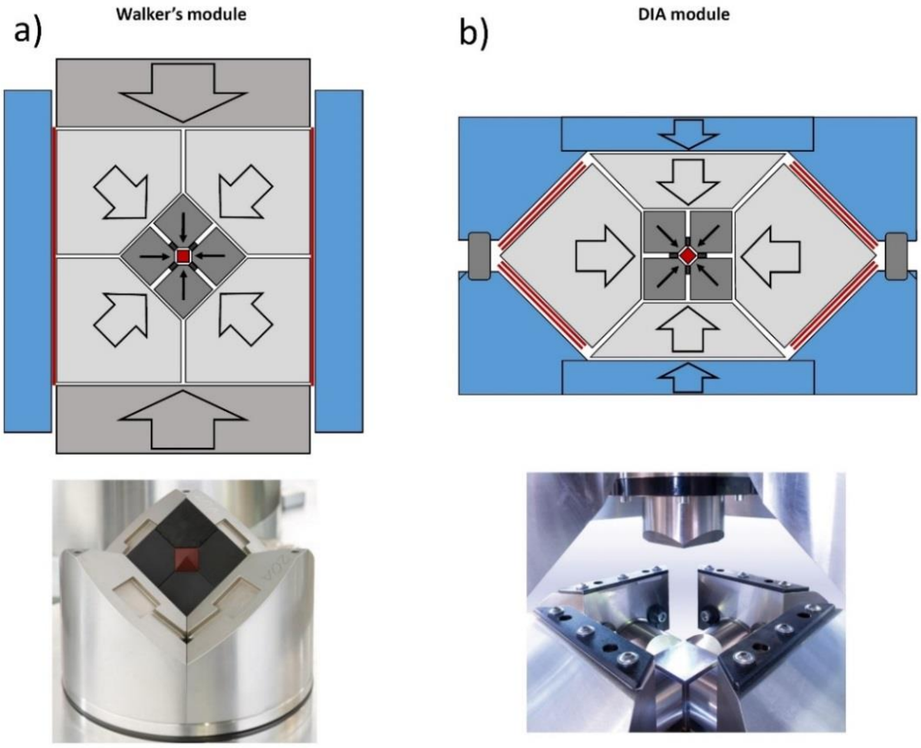

Figure II.9. Schematic view of the MAP module types: a) Walker's module; b) DIA module. The transformation of uniaxial hydraulic ram compression to homogeneous hydrostatic one is shown by the arrows. The photos in bottom row were taken from *http://www.voggenreiter-gmbh.de*.

In frames of current work, we used the Walker's module at LSPM (University Paris Nord) for the HP-HT synthesis of *r*-BS.

Three main parts of MAP should be distinguished: vertical hydraulic ram, MAP module (primary anvils and secondary anvils) and sample assembly.

Hydraulic ram. The MAPs usually use the pumps to pressurize oil, which drives a vertical hydraulic ram to compress a module. Any vertical hydraulic ram with enough loading force (>1000 tons) might be used. The loading force should be rather high to provide effective compression of both anvil stages.

MAP module. As it has been mentioned above there are two main designs of MAP modules: Walker's and DIA modules (see Figure II.9). Both have double anvils stage arrangement: primary and secondary anvils. There are different ways to count the anvil stages in MAPs. Herein we will count the stages from "outside", which means that the outer six steel anvils will be called primary anvils, whereas next eight cubes are secondary anvils. The Walker's module has a cylindrical cavity (see Figure II.9 *a*), usually covered by Kapton sheet to reduce a friction between metallic parts. The cavity is filled with six steel primary anvils, three facing up and three facing down, which form a new cavity of cubic form. In its turn, this cubic cavity is dedicated for the secondary anvils. The primary anvils are driven by uniaxial compression of a piston. The 1st stage of DIA module consists of four independent moveable equatorial anvils and fixed bottom and top anvils. As well as in case of Walker's module, in DIA module the uniaxial compression transforms to multiaxial due to construction of the top and bottom module parts. Nevertheless, the compression extent of the secondary anvils can be varied by using different lubricants (machine oil, molycot) and filling gaskets (Kapton, etc.) (see Figure II.10).

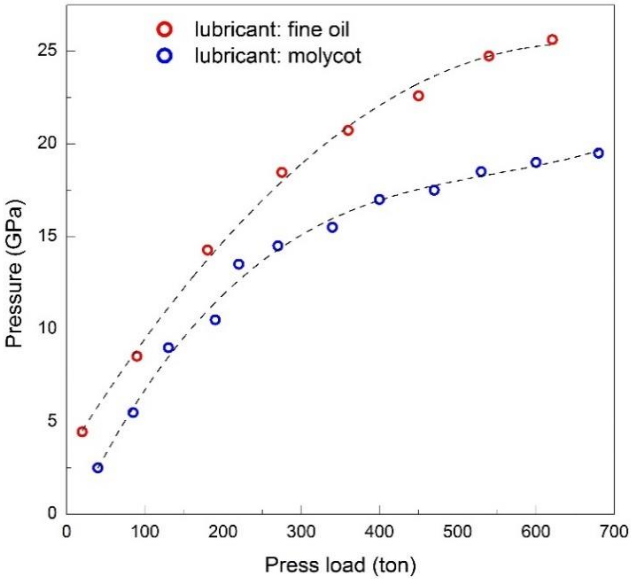

Figure II.10. Pressure calibrations of DIA module at room temperature at PSICHE beamline, synchrotron SOLEIL. Pressure determined from MgO equation of state is related to press load.

DIA design seems to be a little bit more complicated than Walker's one as it consists of two heavy module parts (the top is better to be fixed) and requires more precise alignment of the primary anvils (selection of the filling gaskets and lubricants). However in some cases, as for example, synchrotron *in situ* measurements DIA design is the most preferable: four equatorial anvils of the first stage can have a horizontal groove dedicated to incoming and outgoing X-ray beams. Due to differences in primary anvils location the geometry of the second stage anvils can be considered as (111) and (100) for Walker's module and DIA module respectively.

The secondary anvils are the set of eight cubes with truncated interior corners (see Figure II.11). These truncations form an octahedral HP assembly cavity. Usual material of the cubes is WC-Co hard alloy, although the use of *c*-BN or sintered diamond (SD) cubes is also possible, although more expensive. The harder secondary anvils are, the higher reachable pressure on the sample is. Evidently, the hardness of secondary anvils should be higher than that of primary anvils. In the present work, only WC-Co hard alloy secondary anvils have been used. The cube truncation edge length (TEL) is crucial characteristic of the secondary anvils. Evidently, the smaller TEMs result in higher attainable pressures. The standard TELs sizes are: 3 (up to ~30 GPa for WC-Co), 4 (up to ~24 GPa for WC-Co), 5 (up to ~19 GPa for WC-Co), 8 (up to ~14 GPa for WC-Co), 12, and 15 mm.

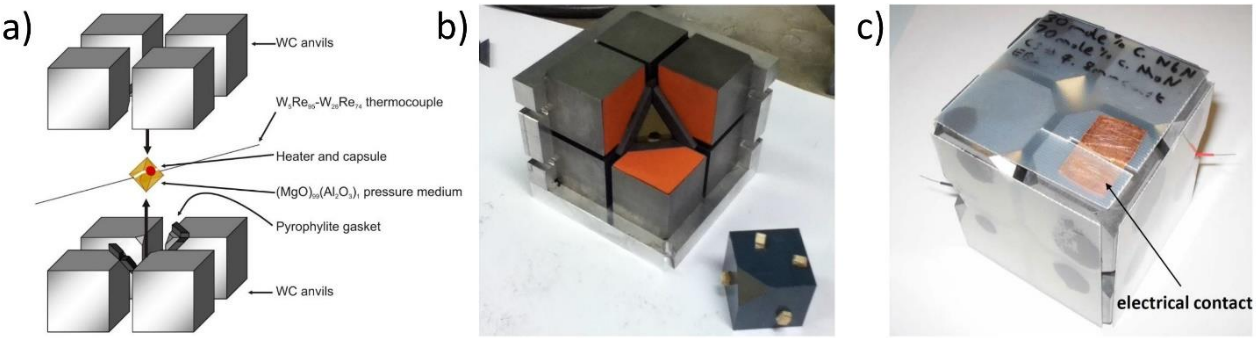

Figure II.11. A view of the MAP secondary anvils: a) schematic arrangement of the secondary anvils; b) building of the secondary anvils "cubic" set; c) "cube" fixed by plastic-glass sheets, one of two coper electrical contacts/providers is marked.

In present work, the secondary anvils with 2, 2.5, 3, 4, 5 and 8 mm of TEL have been employed. The secondary anvils are fixed by the plastic-glass sheets (see Figure II.11 *c*). The plastic-glass sheets may have various grooves intended for thermocouples wires and electrical providers in case of HP-HT experiments. The life rate of secondary anvils is sensitive to any distortions in the "cube". Consequently, the secondary anvils preparation requires high accuracy of experimenter.

Sample assembly. The sample assembly as well as secondary anvils is uniform for all types of MAP modules. It has an octahedral shape. The usual octahedron material is MgO with additions of Al_2O_3, Cr_2O_3, talk, etc. Before using the octahedron in HP experiments it is fired above 900°C during a few hours. This procedure results in harder octahedra, permitting to reach the higher pressures. In case of octahedrons consisting of MgO and Al_2O_3, a HT treatment at 1500°C leads to partial formation of harder spinel [192]. The hole dedicated for the sample, furnace, thermocouple and other details usually passes through two opposite faces of octahedron. The octahedron body may have other additional notches intended for thermocouple wires, X-ray "windows", etc. X-ray "windows" are the special holes placed perpendicular to the sample hole. These "windows" are filled by the pellets prepared from material which is more transparent for X-rays than MgO. Usually, the B-epoxy ceramics (the same as for gaskets of PEP) is used. The octahedron edge lengths (ELs) are internationally uniformed characteristics. Each EL corresponds to the TEL and can be written in the form EL/TEL, e.g.: 8/3 (sample volume ≤ 1 mm^3), 10/4 (sample volume ~ 2 mm^3), 10/5 (sample volume ~ 4 mm^3), 14/8 (sample volume ~ 9 mm^3), 18/12 and 25/15. In present work only the 14/8 assembly has been used.

The general schemes of a few MAP sample assemblies are presented in Figure II.12.

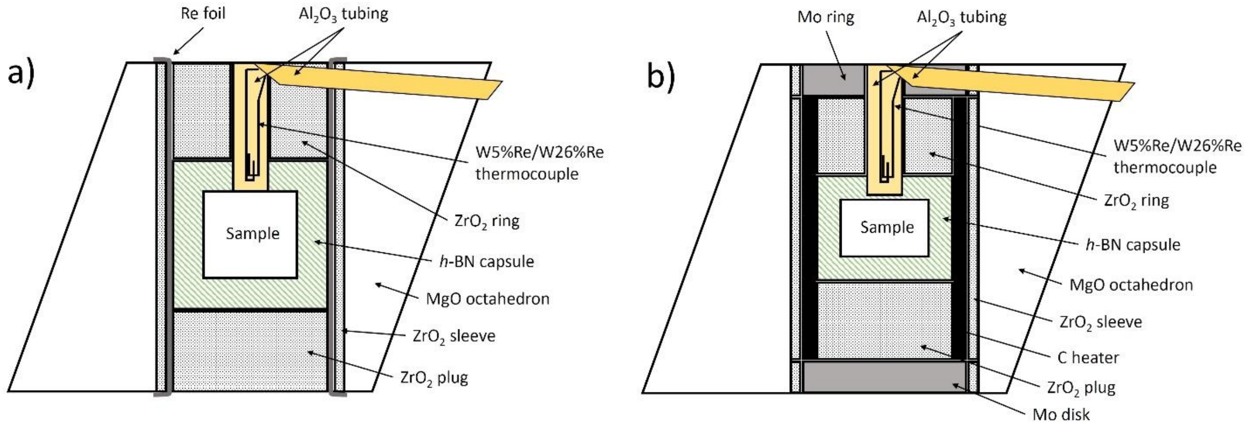

Figure II.12. Two MAP assembly arrangements: a) the scheme of the assembly arrangement with use of foil type furnace; b) the scheme of the assembly arrangement with use of sleeve type furnace.

The isolating ZrO_2 sleeve over the entire length of the sample hole is usually used, in order to preserve the MgO octahedron from overheating at contact with a furnace (which may cause the heating of the gaskets and therefore blowout). Then, the ZrO_2 sleeve is followed by the furnace. The furnace materials are the same as for PEP assembly: graphite, $LaCrO_3$, Re foil, etc. To provide heating, the both furnace ends must be in contact with secondary anvils. Usually, the foil heaters do not need a special electrical contact/provider (see Figure II.12 *a*), whereas in case of sleeve furnaces the molybdenum (or other metal) rings or disks are applied (see Figure II.12 *b*). Graphite furnace is the most popular one, due to its low cost, transparency for X-rays and high attainable temperatures. However, the formation of diamond already at ≤ 12 GPa and ~2500 K [193] forces the experimenters to use $LaCrO_3$ or Re for reaching the highest pressures and temperatures. On other hand, these furnaces absorb the X-rays, thus they pose the problems at *in situ* XRD measurements. One of the possible ways to solve this problem is to use a vanadium foil heater. V is more transparent for X-rays, than Re or $LaCrO_3$, it does not undergo any phase transition in wide pressure and temperature ranges and may be used as reliable pressure marker at the same time. Another possibility is the alternative geometry of the sample assembly presented in Figure II.13.

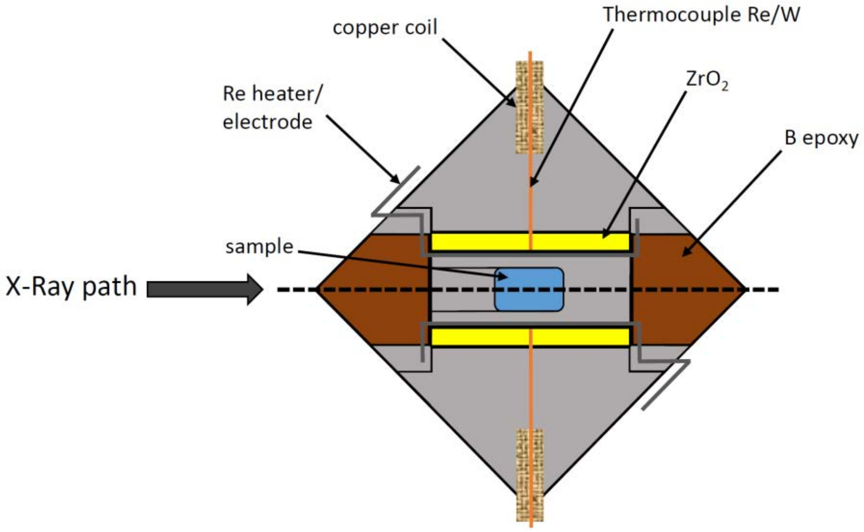

Figure II.13. The "horizontal" geometry of the MAP assembly dedicated to *in situ* XRD measurements.

In (100) geometry of DIA module the octahedron can be placed in manner to match the sample hole with a beam. Almost transparent for X-rays boron epoxy plugs are used to close the sample hole from both sides. The "horizontal" orientation of the sample along the beam has an evident advantage as compared to the conventional one: such large absorbing heater materials as Re or $LaCrO_3$ can be used without any difficulties. On other hand, in case of "horizontal" sample hole the blowout is more likely, due to the fact, that sample hole is not "closed" by the secondary anvils as in case of conventional assembly geometry.

The sample capsule is placed in the center and usually is made of *h*-BN, Al_2O_3 or MgO. These chemically inert materials provide the best thermal conduction. In terms of *in situ* XRD measurements the *h*-BN seems more preferable as it consists of the low *Z* elements. The sample capsule is sandwiched between two ZrO_2 plugs on the top and bottom in order to keep the high temperatures only in a sample area. Using of these plugs also prevents the secondary anvils overheating.

The gaskets in MAP assembly are glued around the truncations on the four out of eight secondary anvils (see Figure II.14 *a*). The gaskets situate along the octahedron edges. The gaskets in combination with MgO octahedron serve as PTM. During compression, the PMT squeezes out into the spaces between the anvils (Figure II.14 *b*). The friction between the pressure media and the secondary anvils should be equal to the pressure generated inside the sample assembly. To increase this friction a special paper sheets are glued behind the gaskets (Figure II.14 *a*).

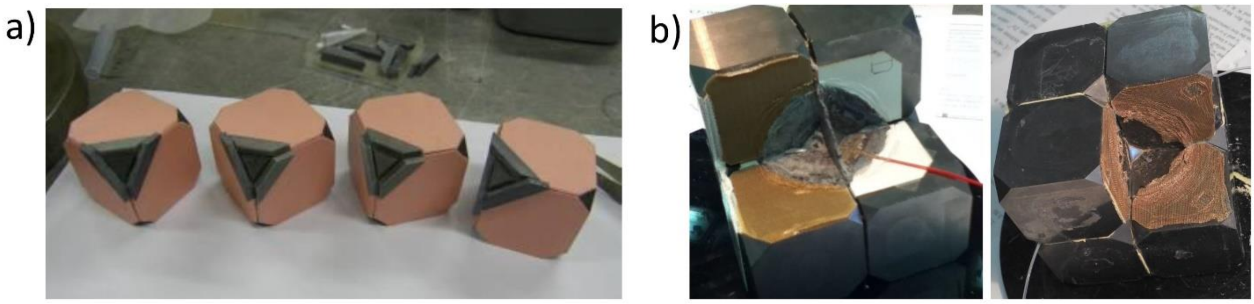

Figure II.14. The gaskets of the MAP assembly: a) the gaskets and paper support glued around truncations of four out eight cubes of the second stage anvil; b) the PMT after HP experiment.

Thus the PMT must be soft enough to flow at room temperature but not so soft that it completely squeezes out between the anvils. The most commonly used materials are boron epoxy, mullite ($2Al_2O_3 \cdot SiO_2$) and pyrophyllite ($Al_2Si_4O_{10}(OH)_2$). Another function of the PMT is to provide electrical insulation between the secondary anvils and sample assembly details (thermocouple, heater and etc.). In present work only pyrophyllite gaskets have been used, as they revealed the best homogeneous flow under compression (for the HP-HT synthesis of *r*-BS). However, for some *in situ* XRD experiments, the B-epoxy "windows" or even the whole B-epoxy gaskets have been implemented. Naturally, the positions of B-epoxy "windows" in the gaskets and in the octahedron must coincide.

3.5.1 Generating high pressures and temperature

The MAP modules require rather high loading forces (~1200 tons), comparable with those of TTP. In this work, the loading forces of the hydraulic rams applied to the Walker's and DIA modules are 1500 and 1200 tons respectively. Due to this only automated electric compressors can be applied for pressure generation. Unlike TTP and PEP, the MAP compression/decompression rate is considerably slower. Actually the secondary WC-Co or SD anvils are very sensitive to the heating and loading stresses. Thus, slow compression helps to avoid breakage of the secondary anvils. Thanks to use of automated compressors the high pressure stability during long HP-HT experiments can be guaranteed.

The resistive heating in MAP significantly differs from one in PEP or in TTP. Herein the power supply is connected to the top and bottom parts of the module. Then the electrical current passes primary and secondary anvils. The plastic-glass sheets of "cubic" secondary anvils set isolate it from the primary anvils. Only two of eight cubes in the second stage anvils have electrical contacts with primary anvils (see Figure II.11). These cubes are located diagonally opposite to each other and are in contact with furnace ends or with the electrical providers of the assembly. They must be electrically insulated from each other, in order to ensure that the electrical current runs only through the furnace. In order to prevent some random contact between second stage anvils, the special scotch and paper are glued on the internal sides of the cubes.

3.5.2 Measuring high pressure and temperature

Temperature and pressure measurements for MAP are fundamentally the same as for the PEP or TTP. Due to wide use of MAP in *in situ* XRD experiments, the pressure and the temperature can be easily determined with help of thermoelastic equation (TEE) and EoS of standard materials as, for instance *h*-BN, Al_2O_3, MgO, etc. An example of the temperature calibrations for MAP installed at PSICHE beamline with using of EoS of MgO, *h*-BN and thermocouples is shown in Figure II.15.

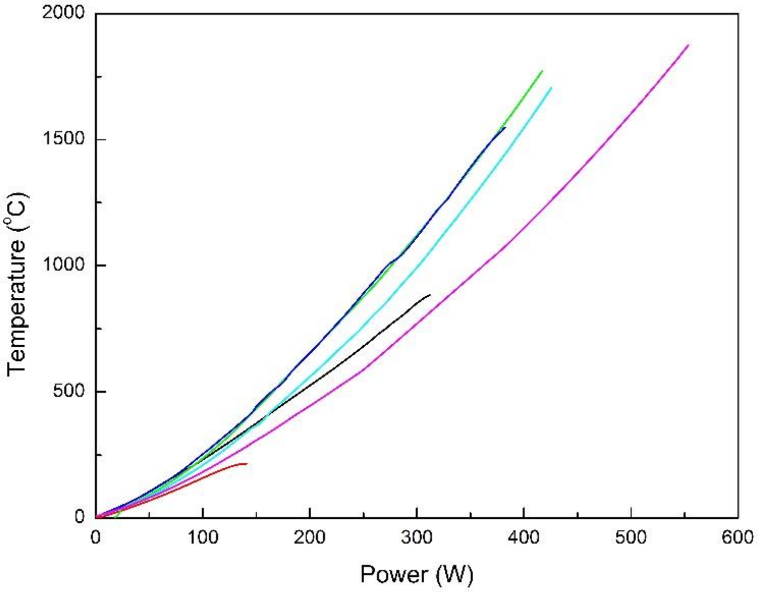

Figure II.15. *In situ* temperature measurements in MAP at PSICHE beamline. Sample: MgO; standard 7/3 assemblies with "horizontal" sample hole geometry; Re heater, W/Re thermocouple, MgO sample capsule and B-epoxy plugs.

The pressure in *ex situ* experiments can be estimated only with help of calibration curves: sample pressure as a function of applied loading force of the ram/hydraulic oil pressure. These calibration curves might be constructed in the same manner as for PEP or TTP, basing on the well-studied phase transitions of the standard compounds.

Unlike to other LVPs with opposed anvils design, the MAP allows more reliable using of thermocouples (TC) at high pressures (up to 30 GPa). The W_5Re_{95}-$W_{26}Re_{74}$ TCs (the indexes mean the percentage of the Re and W in TC wire) are usually applied. The TC insertion does not lead to the big number of blowouts, thanks to almost homogeneous compression of the sample assembly and consequently less pressure gradients. The TC must be as close as possible to the sample in order to make the reliable measurement of the temperature. There are a few ways to provide the TC inside the octahedron assembly; two of the most common ways are presented in the Figure II.16.

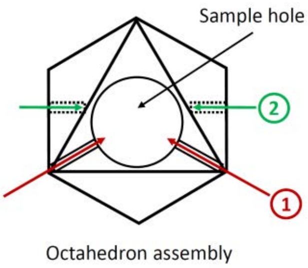

Figure II.16. Two the most common ways of TC providing into sample assembly; the paths of TC wires are marked by the arrows and numbers.

The most popular and easy way is that marked by **1** in the Figure II.16 - from the top through the hole of the sample (see also Figure II.12). Inside the assembly the TC junction and the wires are protected by Al_2O_3 tubes. This material has a very high melting temperature and is very good heat conductor and electrical insulator. Then the Al_2O_3 tubes are followed by copper coils. This kind of protection ensures that even at slight tear of TC wire, there will be an electrical contact and TC will work. Of course, all these protections do not absolutely guarantee the TC safe and the TC tears happen rather often. However, TC remains very powerful and useful option in HP-HT experiments in MAPs and is widely used.

4 Spectroscopy techniques

Raman and infra-red (IR) spectroscopy techniques have been used in present work. The IR and Raman spectroscopies enable the compound characterization on the molecular scale (short and average distances). All of these spectroscopy techniques are well suited to the measurements of solids both at ambient and extreme conditions. Moreover, these analytical techniques are non-destructive and are able to work with tiny samples (micro- or even nano-sample). In this part we will provide short review of the Raman and IR spectroscopies used in our experiments.

4.1 Raman spectroscopy

The Raman measurements have been executed on the basis of LSPM (Université Paris Nord) and IMPMC (UPMC). Both Raman installations were designed to allow measurements at normal and extreme conditions. At IMPMC, the Raman spectra were recorded in back-scattering geometry with a Horiba Jobin Yvon HR460 Raman spectrometer equipped with ×10 and ×20 objectives. The 514.5 nm line of a Ar^+ laser (5 µm beam spot) has been used to measure the samples. At LSPM, back-scattering geometry Horiba Jobin Yvon HR800 Raman spectrometer equipped with ×10 and ×20 objectives was used. Raman spectra were excited with the 632.8 nm line of a He-Ne laser (10 μm beam spot). Both spectrometers were calibrated using the single crystal of cubic Si at room temperature.

It should be noted that only DACs permit to provide *in situ* HP Raman measurements due to transparency of the diamond anvils. However, as it has been marked above, that not all the types of diamonds are suitable with Raman scattering. In present work, only the diamonds especially dedicated for Raman spectroscopy and related vibrational techniques (with N_2 content of ~$2\cdot10^3$ ppm) have been used. Indeed the use of single-crystal diamonds of other classes in DACs for *in situ* Raman measurements are also possible. In case of ordinary diamond anvils a noisy background due to fluorescence is observed. There is also a strong first-order Raman band at 1332 cm^{-1}. However, in some experiments it can be used for pressure determination instead of ruby.

4.2 Infrared absorption spectroscopy

IR absorption spectroscopy is a supplementary technique to the Raman one, which can be clearly demonstrated by example of CO_2 molecule given in Figure II.17.

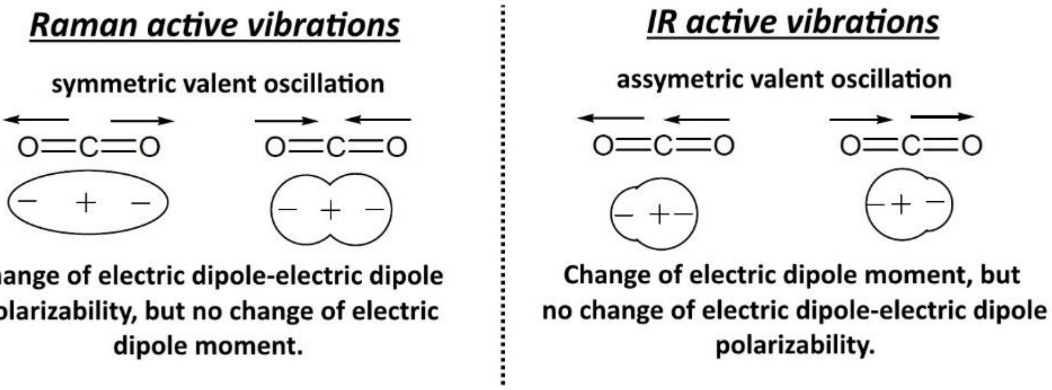

Figure II.17. Comparison of the Raman and IR oscillations of the CO_2 molecule.

The IR installation used for measuring of IR spectra at ambient conditions included: emitter of IR radiation, few lenses for focusing and collecting of IR beams, sample holder and spectrometer. In this work the Fourier transform IR spectrometer Bruker IFS 125HR has been used. The main particularity of this type spectrometer is Michelson interferometer. This device divides the IR rays after the sample on two beams and makes them interfere with each other. The detector records interferogram where intensity is a function of the wavelength difference between two beams. Finally, the interferogram transforms in conventional IR spectrum (Int.(λ^{-1})) by means of Fourier transformation. The Fourier transform spectrometers revealed better quality of the IR spectra at less times of spectrum acquisition.

In situ HP IR measurements as well as *in situ* Raman measurements can be provided only in DACs. However the type of diamonds suitable for HP Raman is not good for IR spectroscopy, as ~1 ppm of N_2 content is needed. Thus, in present work no HP IR measurements have been provided.

5 X-ray diffraction

X-ray diffraction (XRD) is non-destructive analytical technique which reveals information about the crystal structure and some physical properties of the solids. XRD is schematically shown in the Figure II.18.

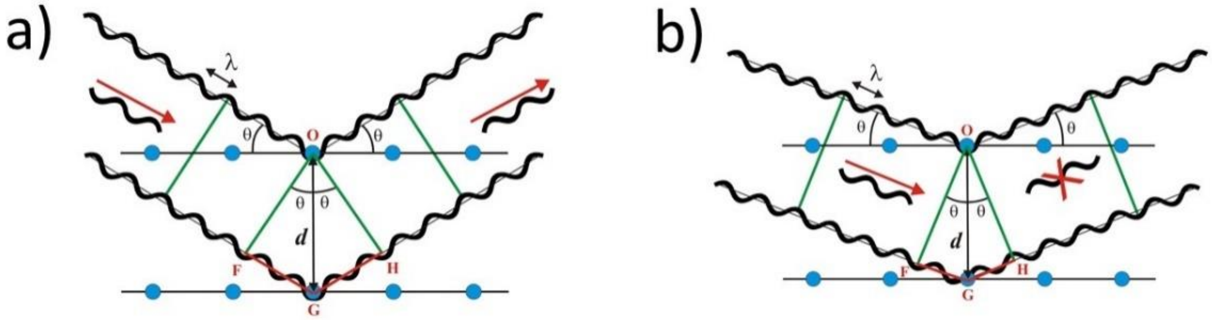

Figure II.18. The scheme of diffraction of the monochromatic X-ray wave on the regular array of “scatters” in the crystal: a) reflected waves are in phase; b) reflected waves have opposite phase.

The core of XRD phenomena is the elastic scattering of the electro-magnetic wave on the electron shells of the atoms in the crystal. The electric field of the incident electro-magnetic wave forces to oscillate shell electron with the same frequency, forcing them to emit a secondary electro-magnetic wave with the same frequency as that of incident one. A regular array of the atoms (or “scatters”) produces a regular array of secondary waves of the same frequency. The Bragg’s law (*II.3*) describes the interference of these waves and conditions of interference maximums:

$$n\lambda = 2d_{hkl}\sin\theta \qquad (II.3),$$

where λ is a wavelength of the X-ray wave, d_{hkl} (further it will be marked only d) is a spacing between two planes of the scatters, θ is the angle of incidence and reflection, n is an integer number.

There are few consequences from the formula (*II.3*):

1) If someone adds new additional planes with the same “scatters” in the middle between already existing *hkl* planes in Figure II.18 *a*, there will be scattering and interference of the X-rays from the new planes but with the phase shift of π. This will lead to the total disappearing of the XRD due to interference between diffracted beams from the “old” and ”new” atomic planes (see Figure II.18 *b*).
2) If the d-spacing is less than $\lambda/2$, there won’t be any XRD on the crystal. It happens because $\sin\theta$ cannot be more than 1. Thus there is a condition at which the XRD is still possible: $d_{min} \geq \lambda/2$.
3) At polychromatic radiation and fixed θ angle there might be the interference between the reflections not from the nearest atomic planes, but from the ones, which are located a few planes from each other. Such kind reflections concern to the higher reflection order $n > 1$.

They can be observed at wavelengths λ/n if these wavelengths are in the polychromatic spectrum. This is called the overlapping of the harmonics and leads to overlapping of the peaks (n order overlapping) in diffraction pattern, which therefore interferes to the precise determination of d value.

The Bragg's law allows to determine the structure of the unit cell through the d value determination and the lattice planes relative position. However, this information is not sufficient to know the space group, i.e. the symmetrical relationship between atoms in the unit cell. This problem can be solved by looking at the relative intensity of the peaks. For the reflection, the diffracted wave amplitude is:

$$F_{hkl}(\bar{h}) = \sum_i f_{at,i}(\bar{h}) e^{(-2i\pi\,\bar{h}\cdot\bar{r}_i)} \qquad (II.4a),$$

$$\text{where } f_{at,i}(\mathrm{Q}) = \int_V^0 dV\,\rho_e(\bar{r}) e^{(-2i\pi\,\mathrm{Q}\cdot\bar{r}_i)} \qquad (II.4b).$$

Herein, vector $\bar{h}$ connects two nodes of the reciprocal lattice, $\rho_e(\overline{r_i})$ is the local electron density, F_{hkl} is structure factor, $f_{at,i}$ is atomic form factor, Q = k−k' is the momentum, k and k' are the wave vectors of the incident and diffused radiation respectively. In its turn, the structure factor contains the information relative to the atomic positions and widely used for atomic position refinement.

Basing on the law of interference maximums of the scattered X-rays on the crystal proposed by Bragg and Wulf two main XRD techniques have been developed in 20th century: angle-dispersive XRD (ADXRD or ADX) and energy-dispersive XRD (EDXRD or EDX). Both these techniques will be described below.

5.1 Angle-dispersive X-ray diffraction

The ADX is an analytical technique for characterizing materials. Historically it arose the first. Herein we will use the Bragg's law to consider the ADX. ADX can be used only at monochromatic incident X-ray beam.

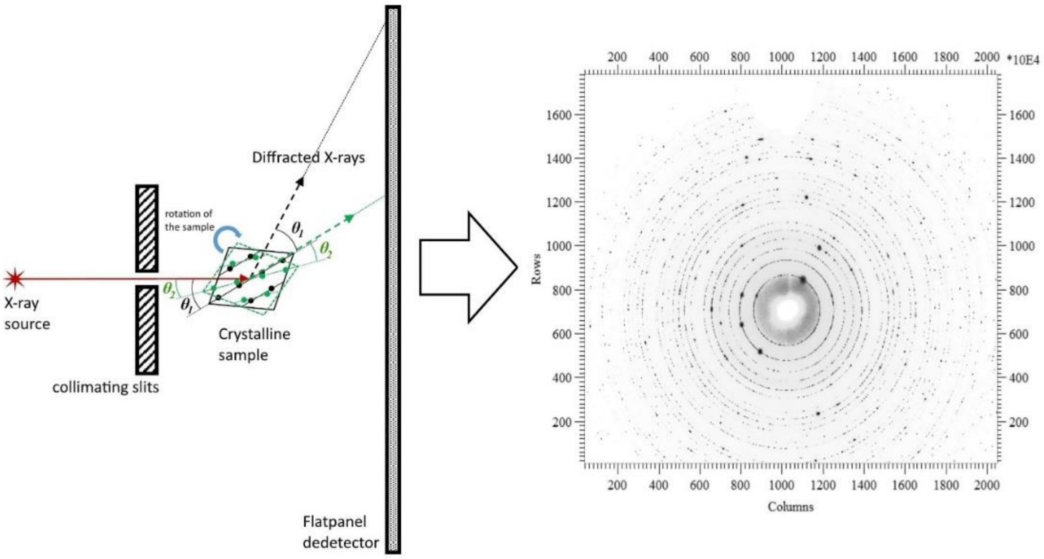

Figure II.19. The scheme of ADX (on the left) and an example of ADX pattern of polycrystalline LaB_6.

Figure II.19 presents schematically the ADX installation: source of X-rays, the sample placed on the goniometer and flatpanel detector. As it has been mentioned above, the X-rays scatter on the arrays of atoms (scatters) in the crystal. The interference of the diffracted X-ray waves leads to mutual damping, except a few specific directions, which are defined by the formula (*II.3*). These specific directions are registered by the flatpanel detector and appear as spots on the diffraction pattern (reflections). Unlike monocrystal, the ADX of polycrystalline sample represents the "rings" consisting of reflections set from randomly orientated monocrystals (see Figure II.19). During ADX acquisition, the sample (usually crystalline or polycrystalline) is rotated and therefore the X-rays incident angle θ changes. At constant value of λ, the θ angle and d are the variables in the formula (*II.3*), and, thus the ADX pattern presents a diffraction intensity concerning different d as a function of θ angle. Thus, ADX in combination with flatpanel detector can be considered as 2D ADX, as an experimenter sees the whole projection of cone of diffracted X-rays (see Figure II.19).

The recorded series of ADX patterns, each corresponding to a different crystal orientation, is converted into a 3D model of the electron density by means of the mathematical technique of Fourier transforms. Each spot or reflection corresponds to a different type of variation in the electron density. It is necessary to determine which variation corresponds to which reflection, the relative strengths of the reflections in different images and how the variations should be combined to yield the total electron density. In present work, all the 2D ADX patterns have been converted in conventional form (intensity *versus* 2θ) by means of Fit2D software [194], whereas the data treatment have been done with help of FullProf software [195-197]. The ADX patterns usually employs the 2θ scale, although the d-spacing (d value) or F_{hkl} scales can also be used.

The high precision/quality crystallographic data (*d*-spacing, space group, coordinates of atoms, polycrystals preferential orientation, etc.) can be yielded from the 2D ADX measurements. Hence, the 2D ADX technique is the main tool of experimentalist for study sample structure. However, the 2D ADX has some drawbacks, which can limit its application, for instance: rather long time of acquisition (compared to EDX) and necessity of high spatial accessibility.

5.2 Energy-dispersive X-ray diffraction

A development of the X-rays sources (e.g. synchrotrons) and creation of the new semiconductor detectors with good energy resolution in the second part of 20th century gave rise to creation of the EDX technique, which has been proposed for the first time in 1968 [198]. EDX technique is used at polychromatic X-ray radiation of polycrystalline samples and is usually operated at a fixed angle ($2\theta_0$). Using the Plank's equation $\lambda = 12.398/\varepsilon$, where λ in [Å] ε in [keV], the Bragg's law can be converted in:

$$\varepsilon = \frac{6.199}{d \cdot sin\theta} \qquad (II.5).$$

From the equation (II.*5*) one can conclude that for the given energy/or wavelength range ($\lambda_1 \ldots \lambda_i$) there is a set of d values, giving a reflections, which can be observed at a fixed angle. During the EDX measurements, a white collimated X-ray beam is scattered by the sample through a $2\theta_0$ angle and the energy distribution of the scattered photons is analyzed by an energy-dispersive detector (EDD). The measured energy distribution of the scattered X-rays shows distinct peaks, providing the required information for structural studies of materials.

EDX technique dramatically differs from 2D ADX one. The first, it should be underlined, that unlike 2D ADX, in case of EDX only a part of cone of diffracted X-rays is observed through the fixed $2\theta_0$ angle (the blue stripe in Figure II.20).

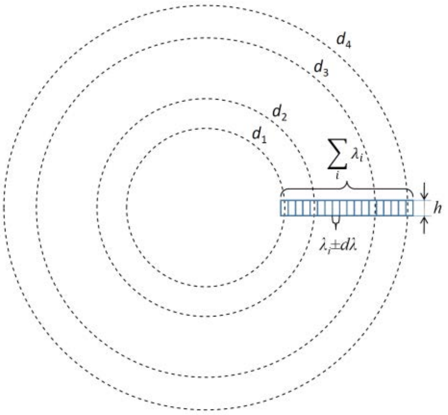

Figure II.20. The schematic representation of diffraction patterns acquired by ADX and EDX techniques.

As one can see from Figure II.20, each monochromatic component of white beam ($\lambda_i \pm d\lambda$) refers to the *d* value. The summing of all ($\lambda_i \pm d\lambda$) gives the entire energy-dispersive spectrum. As far as height *h* of the "stripe" of energy-dispersive data is negligible with respect to the whole 2D pattern, the EDX technique presented in Figure II.20 can be considered as 1D. 1D EDX cannot provide the same data quality as angle-dispersive diffraction and is almost inconvenient for detailed sample structure refinement (Rietveld refinement). Another reasons of low 1D EDX data quality are: the presence of fluorescence peaks, limitation of input count rate by EDD, presence of the background in energy spectrum of incident X-ray radiation (especially at synchrotron) and few orders less peak resolution than in ADX. However the resolution can be slightly improved by reduction of *h* value (by closing of vertical collimating slits). On other side, diminution of *h* is limited by input count rate of EDD.

However, energy-dispersive method has some advantages compared to 2D ADX technique. EDD is usually connected to multichannel pulse height analyzer (each channel refers to separate ε_i or λ_i). Hence, measurement of energies of all scattered photons happens simultaneously. The summing of all channels into whole EDX spectrum takes some μs or *p*s. It makes EDX the powerful tool for rapid structural analysis (e.g. the samples, which are unstable or exist for a short period of time) and allows to study structure changes over time. It should be also noted, that $2\theta_0$ angle variation may change the position of the diffraction peaks, distances between them and even change their quantity in the diffraction pattern. The important advantage of EDX is the opportunity to obtain diffraction patterns without the use of any goniometer. Fixed scattering angle permits to use the collimators for diffracted X-rays in order to define the detected area (see Figure II.21), leading to suppressing of the undesirable peaks in the sample EDX pattern. Hence, a large spatial accessibility to the sample is not required and EDX can be applied for *in situ* experiments with significantly limited access to the sample.

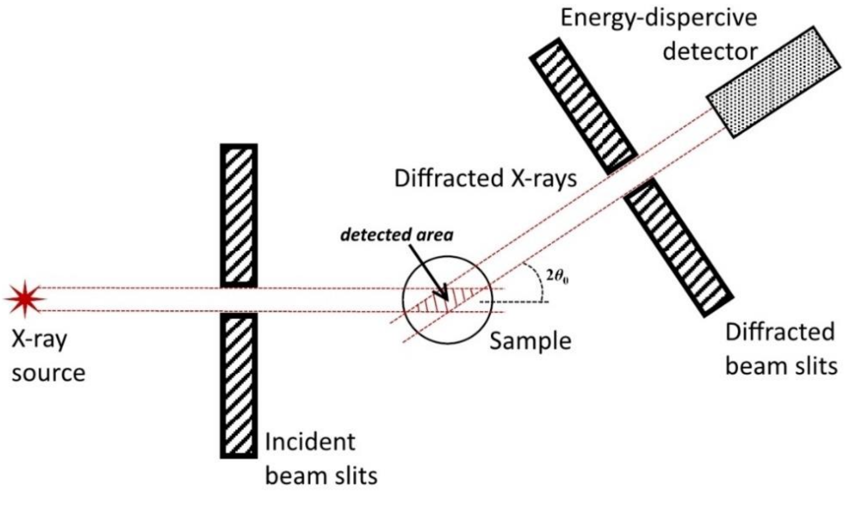

Figure II.21. The scheme of EDX technique.

The collimating system presented in Figure II.21 does not require very high flux of X-ray source, as the whole energy photon spectrum is used. Such a collimating system cannot be applied in monochromatic mode because of the 2-dimensional nature of the detection. In order to measure high quality diffraction data in *in situ* experiments with limited access to the sample, a collimator with multiple channels (Soller slits) can be used. The Soller slits system consists of two blocks of slits: inner and outer with a radial alignment. Although the Soller slits suppress effectively all waste peaks and strong background, it should be noted, that it loses about 80% of diffracted X-rays. Hence, to provide high quality and express 2D ADX *in situ* measurements, the X-ray source with high flux is necessary.

So we can conclude, that 2D ADX is powerful tool for providing XRD measurements of high data quality. However, *in situ* 2D ADX experiments require the X-ray sources of high brightness. Unlike 2D ADX, the quality of energy-dispersive data does not permit to provide Rietveld refinement, but is rather sufficient for *in situ* XRD measurements with use of X-ray sources with lower spectral brightness. Thus, EDX and ADX can be considered to be complimentary techniques and might be applied depending on the aims of experiment, type of X-ray source and the sample nature. In the present work we used the both techniques.

6 Synchrotron radiation

A photon radiation occurred in bending magnet of the synchrotron storage ring due to electrons deflecting is called *synchrotron radiation*. Classical synchrotron radiation is magnetic bremsstrahlung electromagnetic radiation. It can be obtained not only from the bending magnets but from other insertion devices as well (e.g. wigglers and undulators). It dramatically differs from conventional radiation from X-ray tube. The following features of synchrotron radiation compared to ordinary one can be underlined:

- spectral continuity over a range from infrared to X-rays;
- weak divergence of emission in the vertical plane;
- flux and luminance billions of times greater than those of classic sources of X-rays;
- polarization in the horizontal plane;
- temporal structure in pulses;
- certain spatial and temporal coherence.

Thanks to these qualities the synchrotron radiation is particular useful tool for providing *in situ* experiments especially under extreme conditions. In present work a great part of scientific results has been obtained from *in situ* measurements under extreme conditions at PSICHE beamline at synchrotron SOLEIL and at ID27 at ESRF. A high brilliance of the X-ray sources and modern synchrotron X-ray optics installed in these beamlines ensured high XRD data quality. Thus, in this part, first of all, the general description of synchrotron and comparison of ESRF and SOLEIL will be given. Then it will be followed by description of main synchrotron characteristics. Two different X-ray sources (wiggler and undulator) will be compared on the example of PSICHE and ID27 beamlines. Finally, the detailed description of PSICHE beamline as a fortunate example of modern beamline dedicated for various *in situ* experiments under extreme conditions will be done.

6.1 General description of synchrotron

Synchrotron is an accelerator of elementary particles, more often of electrons. The synchrotrons can be divided on several specialized types, but in this work we will review only a synchrotron light source type. Further, we will call it as "synchrotron" although this is technically incorrect. The general scheme of synchrotron construction is presented in Figure II.22.

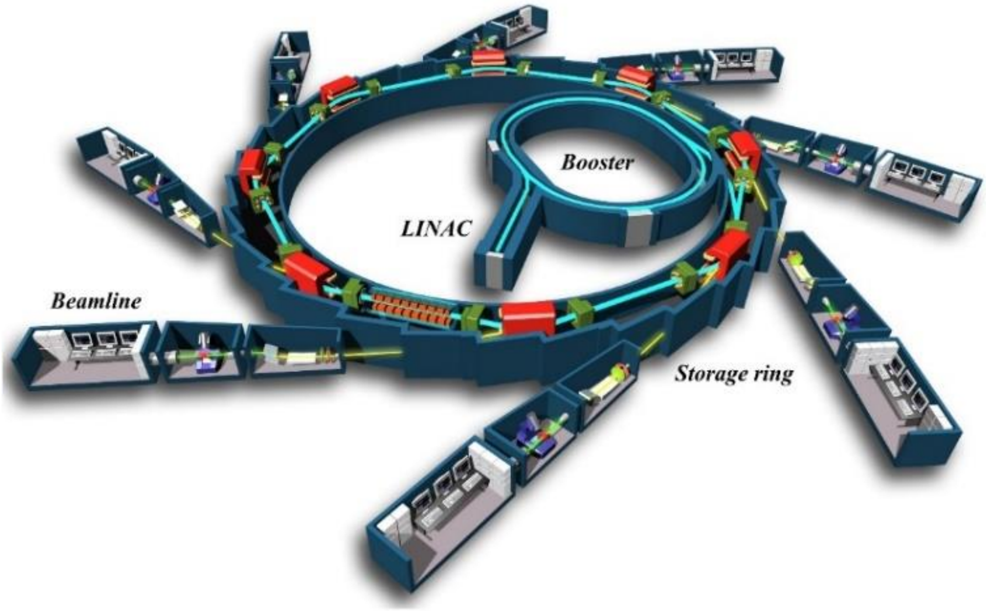

Figure II.22. General arrangement of synchrotron of 3^d generation.

A synchrotron can be divided on three main parts: **Lin**ear particle **ac**celator (LINAC); booster and storage ring with beamlines. The electrons produced and initially accelerated in LINAC are injected to the booster where they are pre-accelerated up to GeV energy values in synchrotron mode. Finally the electrons are injected into storage ring where their circulation becomes stable in time and the electron energy reaches the "working value" (usually it is from 2 to 8 GeV).

The synchrotrons SOLEIL and ESRF are the examples of the synchrotrons of the 3^{rd} generation. Nonetheless, they are significantly different. Their main storage ring parameters are presented in Table 1.

Characteristic	ESRF	SOLEIL
Storage ring circumference, m	844.4	354.1
Bending magnets (BM)	64	22
Insertion devices (ID)	65	25
Energy, GeV	6.0	2.75
Maximum curent, mA	200	~500
Horizontal emittance, nm	4.0	3.9
Revolution frequency, MHz	0.36	0.85
Number of bunches	1 - 992	1 - 516

Table 1. The main storage ring parameters of ESRF and SOLEIL synchrotrons.

6.2 Main characteristics of synchrotron radiation

There is a plenty of various synchrotron sources which deliver the radiation of different quality. In order to compare the synchrotron radiation of the different sources some uniform international characteristics were proposed. Herein only a few of them (basically those, which will be used further) are listed.

Spectral brightness, spectral brilliance and critical energy.

A spectral brightness or photon flux per solid angle is defined as the number of photons emitted per second, in a spectral bandwidth $\Delta\lambda/\lambda = 0.1\%$, into a unit solid angle. Spectral brightness standard unit is [photon/s/mrad^2/0.1% $\delta\lambda/\lambda$]. From the brightness, the photon flux impinging on a sample may be easily evaluated using simple geometrical considerations.

A spectral brilliance can be defined as the number of photons emitted per second, in a spectral bandwidth $\Delta\lambda/\lambda = 0.1$ by an unit source area and per unit of solid angle. Its standard unit is [photon/s/mrad^2/mm^2/0.1% $\delta\lambda/\lambda$]. This characteristic can be used for comparison of sources with same spectral brightness and other properties. The advantage of these characteristics is in their independence from distance between observer and the source, as well as from divergence of the beam.

Another important synchrotron characteristic is a critical energy, which can be found from following expression:

$$\varepsilon_c = BE^2 \qquad (II.6),$$

where B is magnetic induction [T]; E – electron energy [GeV]. It should be noted, that knowledge of this characteristic permits to determine other ones, as for example critical wavelength, critical frequency, etc.

6.2.1 Insertion devices (ID). PSICHE and ID27 beamlines

As it has been mentioned above, the great part of experimental work has been done at PSICHE and ID27 beamlines. The both beamlines are dedicated for *in situ* XRD measurements at ambient and extreme conditions. Nevertheless, it should be marked, that the beamlines deliver the beams from two different X-ray sources: wiggler (in case of PSICHE) and undulator (in case of ID27).

Wiggler and undulator are insertion devices (ID) with periodic magnetic structures in the synchrotron storage ring. In fact their constructions are very close to each other. These magnetic structures, made up of a complex array of small magnets, force the electrons to follow an undulating, or wavy, trajectory (Figure II.23). The magnetic bremsstrahlung electromagnetic radiation is emitted at each consecutive bend. Consequently, the total quantity of emittances from one electron is significantly higher than in bending magnet. Thus, the both IDs deliver increased spectral brilliance with respect to that achievable with bending magnets (see Figure II.23).

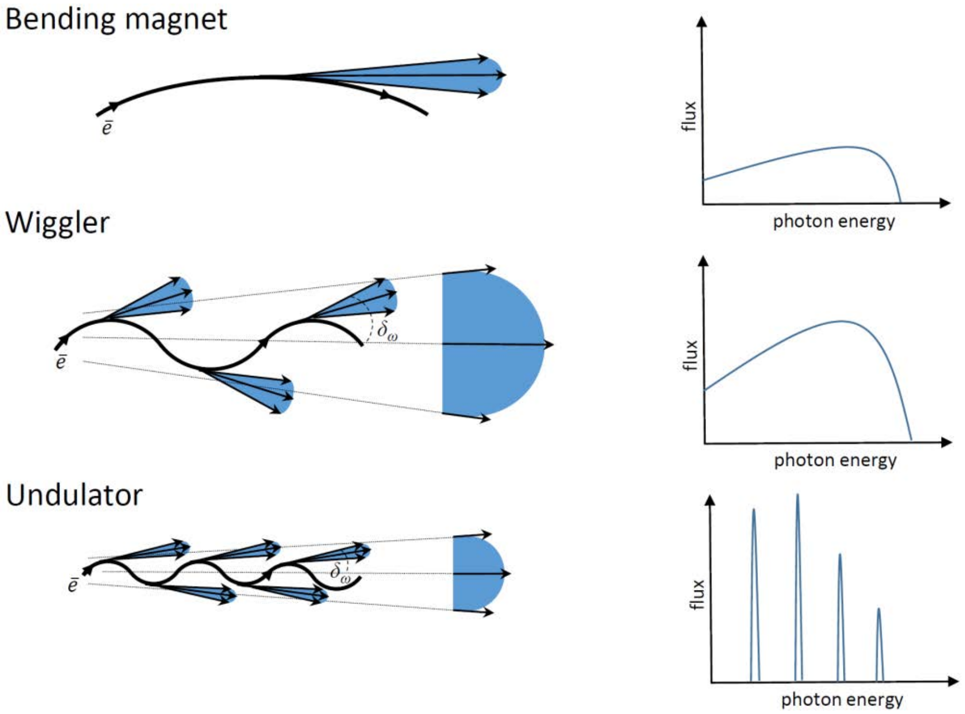

Figure II.23. Different synchrotron radiation features; where δ_ω is a maximum deviation of electron bunch from main trajectory.

Nevertheless, there is a difference between radiation emitted by wigglers and undulators. In the case of undulators, due to relatively weak magnet dipoles are used in ID periodic structure, the electrons are only slightly deviated from their trajectory (a small value of δ_ω). An interference occurs between the radiations emitted by the same electron at different points along the trajectory. Due to interference at low δ_ω value and overlapping of emitted light, the flux of undulator radiation is dramatically higher than in all other IDs. It should be noted, that the emitted photons are concentrated at certain energies (called harmonics, see Figure II.23). By varying the gap between the rows of magnets the quantity and relative intensities of harmonics can be changed.

The wigglers contain the less quantity of magnet dipoles but have considerably stronger periodic magnetic field. Because of this fact, the electron deviations are significantly larger (rather big δ_ω value), the interference effects between the emissions from the different poles can be neglected and the overall intensity is obtained by summing the contribution of the individual poles. The flux of such radiation is lower than that from undulator. At big δ_ω value, total harmonics number and their width increase, leading to continuous photon spectrum (the same as from bending magnet). Unlike undulator, wiggler delivers white beam. It should be marked, that wiggler radiation flux is few time higher than one from the bending magnet.

Using of wiggler and undulator at PSICHE and ID27 respectively, leads to the different sets of experiments possible to provide at these beamlines. The *in situ* measurements at ID27 are available in 20-90 keV energy range with the high flux. The beamline provides the experimental techniques only for monochromatic beam mode: powder diffraction, XRD, X-ray fluorescence (XRF) and X-ray Raman scattering. Due to high beam flux, ID27 can easily use the Soller slits without any risk to lose data quality. PSICHE beamline proposes continuous photon spectrum from 15 to 80 keV with comparatively rather lower flux. Thus, the using of Soller slits is impossible. Thanks to wiggler source, a monochromatic, white beam and pink beam modes can be delivered. Unlike ID27, such experimental techniques as EDX and pink beam tomography are disposable. More detailed description of PSICHE beamline will be presented in the next part.

7 PSICHE beamline

7.1 Line description

PSICHE (**P**ressure, **S**tructure and **I**maging by **C**ontrast at **H**igh **E**nergy) beamline is dedicated to tomography techniques and *in situ* material research under regular and high pressures using hard X-ray diffraction at room or high temperatures.

High energy photons are produced by an in-vacuum multipole wiggler WS 50 (see Figure II.24).

Figure II.24. Wiggler WS 50 of PSICHE beamline at synchrotron SOLEIL.

Due to the intrinsic properties of the wiggler as insertion device ($B_{\max}$ = 2.1 T, period 50 mm, 38 periods) and of X-ray optics installed, the beamline can deliver three different beam modes: white beam mode (15-80 keV), pink beam mode (filtered white; 25-70 keV) and monochromatic beam mode (20-50 keV). The PSICHE beamline has the highest photon energy spectrum of SOLEIL, a maximum flux close to 25-35 keV. The photon energy spectrum from WS 50 WS 50 is presented below (see Figure II.25). The beam flux on the exit from the WS 50 is close to$\cdot 10^{16}$ photon/s/mrad^2/0.1% $\delta\lambda/\lambda$. It should be noted that, when the wiggler operates at low energy (<10 keV), an "undulator" structure of photon spectrum is observed (with distinct harmonics). At higher energies, harmonics overlap and spectrum looks like more like a continuous background ("wiggler" structure).

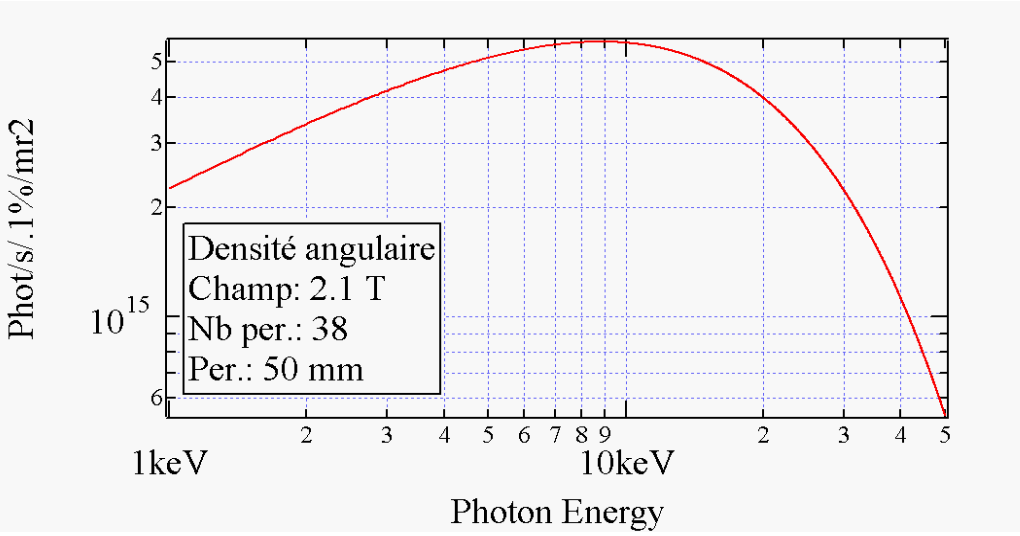

Figure II.25. The flux of WS 50 wiggler of PSICHE beamline.

After the Wiggler beam passes water cooled 300 µm CVD filter, which removes a radiation below 5 keV. The diamond is ideal candidate for these purposes, as it has low *Z*-number, is a highly resistant material and good thermoconductor. Thus in combination with water cooling there is no risk to damage it by the beam. The beam flux after CVD filter is ~$3.5\cdot 10^{14}$ photon/s/mrad^2/0.1% $\delta\lambda/\lambda$. The CVD filter is followed by 100 µm CVD window, which is also used like a filter and closes the front end, which is kept under deep vacuum. As in case of CVD filter, CVD window is kept under water cooling. The beam flux after CVD window is almost equal to that after CVD filter. After CVD, the beam passes the cascade of SiC filters, which remove a radiation below 15 keV. Due to SiC is less resistant and more sensitive to the heating than diamond, it must be installed only after CVD filters. It should be noted that initially the Al filters were intended to be used. The white beam brilliance values after Al filters of the thickness of 150, 200 and 400 µm have been calculated to be ~2.5·, ~2· and ~$1.6\cdot 10^{14}$ photon/s/mrad^2/0.1% $\delta\lambda/\lambda$ respectively. Taking into account, that the absorption properties of the Al and SiC are rather close one can expect the same brilliance values after the SiC filters of the corresponding thicknesses. The power absorption after CVD and SiC filters is around 66% of the total power [199]. The beam flux can be varied by changing of number of SiC filters. For instance, to protect the "sensitive" samples from high energetic white beam the additional SiC filter can be installed before the sample.

The beamline can be changed especially for concrete experiment needs by removing/changing the settings of all X-ray optics and high pressure and tomography equipment. In Figure II.26 one can find a schematic plan of the PSICHE beamline.

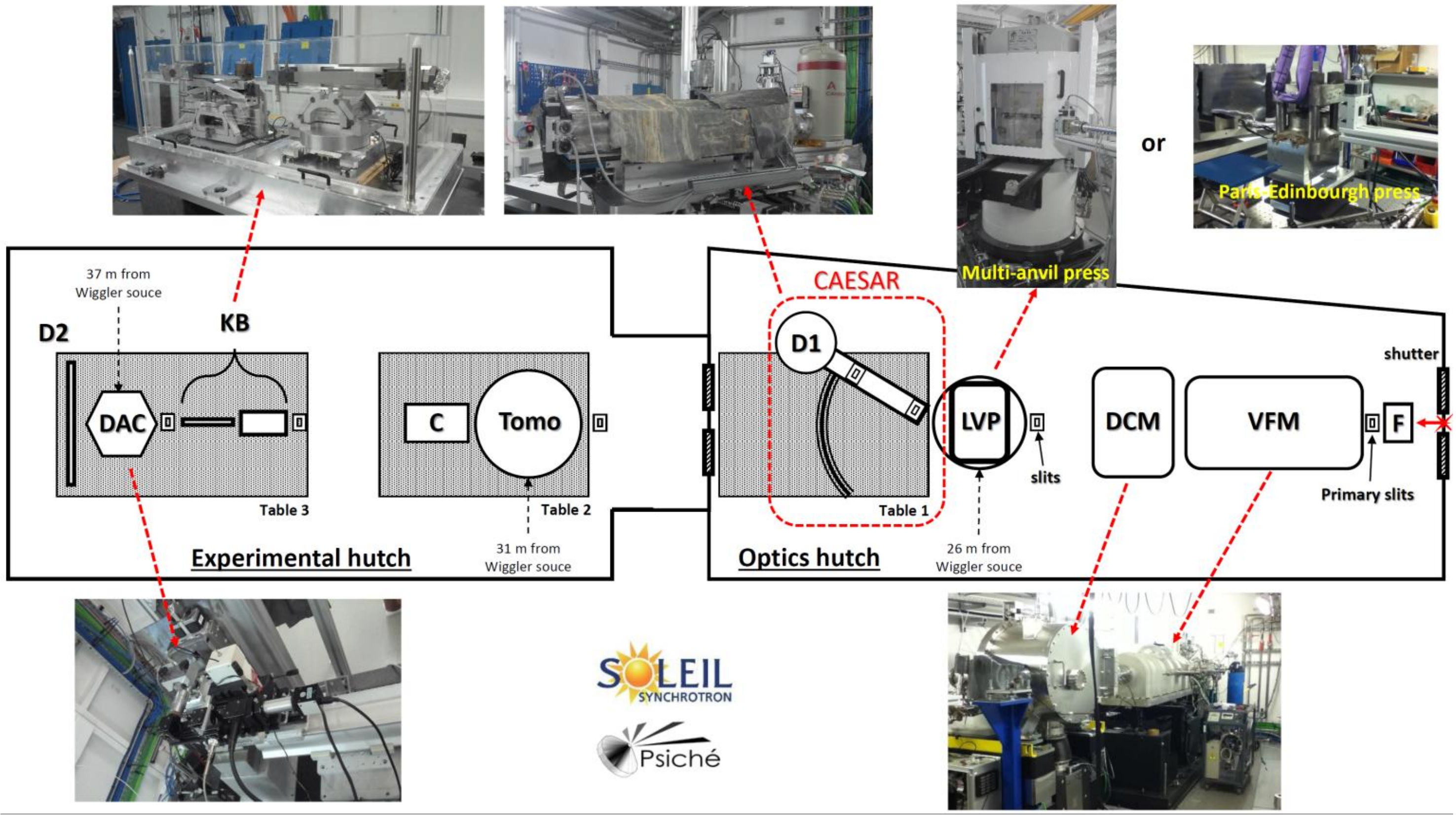

Figure II.26. The scheme of PSICHE beamline at synchrotron SOLEIL. The abbreviations meaning: F – CVD and SiC filters, VFM – vertical focusing mirror, DCM - Bragg-Bragg fixed exit double crystal monochromator, LVP – large volume presses, D1 – EDX Ge solid-state detector (SSD), Tomo – tomograph with rotation stage, C – camera/tomograph detector, KB - Kirkpatrick-Baez micro-focusing optics, DAC – diamond anvil cell, D2 – PerkinElmer flatpanel detector or CCD rayonix 165 detector.

The beamline is divided onto two hutches: optics hutch and experimental hutch. The main X-ray optics features of the optics hutch are: the cascade of CVD and SiC filters, vertical focusing mirror (VFM) and Bragg-Bragg fixed exit double crystal monochromator (DCM). VFM can be applied for two purposes: to focus the beam in vertical direction (or to make it denser in order to control the vertical divergence) and to use it like a filter for rejection of high-energy photons [199]. The dimensions of profile of the beam coming to VFM are defined by the primary slits. Vertical beam condensing may lead to increase of flux density, as it has the effect of increasing the effective source size in vertical direction. Such beam condensation may increase the flux by the factor ~40 [199]. From another side, VFM is an important part of combination of filters and scintillator materials at pink beam mode creation. VFM is followed by DCM, which contains two sets of flat Si crystals: Si 111 and Si 311. One of the Si 311 crystals can bend in order to focus the beam. Actually only set of Si 111 crystals has been used. DCM energy resolution is $\Delta E/E \sim 10^{-3}$. The DCM is cryogenically cooled with a closed-loop circuit of nitrogen in order to absorb the beam power and to reduce thermal deformations. The experimental hutch contains only Kirkpatrick-Baez micro-focusing mirrors on the 3rd experimental table. The maximum possible focusing of the monochromatic beam at micro-focusing is 6×6 μm^2, although a focalization of 12×12 μm^2 is more usual. The maximum beam size at the sample position is approximately 12×3.5 mm^2 in the optics hutch, and 15×4.5 mm^2 in the experimental hutch. If the VFM is used, the maximum beam height is 2.5 mm in the optics hutch, or 3 mm in the experimental hutch. Depending on beam mode and which X-ray optics is used, different beam flux on the sample can be obtained:

- 3×10^{15} Ph/s for 12×3.5 mm^2 unfocused white beam mode (1st table, 26 m from Wiggler source);
- 4×10^{11} Ph/s in 0.1×0.1 mm^2 spot at 30 keV for monochromatic beam mode using VFM and DCM (Si 311) (at 31 m from Wiggler source, 2nd table);
- $\sim10^{13}$ Ph/s in a 16.8×5.9 mm^2 spot at 30 keV for unfocused monochromatic beam mode using DCM (Si 111) (2nd table, 31 m from Wiggler source);
- 10^{10} Ph/s in 10×10 μm^2 spot at 30 keV for monochromatic beam mode after VFM, DCM (Si 111) and KB mirrors (3rd table, 37 m from Wiggler source).

PSICHE beamline permits to provide different experiments using various combinations of X-ray optics and HP and tomography equipment. All the possible experimental installations for each experimental table are listed below:

1) The 1st experimental table. All beam modes (white, pink, monochromatic) are available. Basically, the setup of this table is intended for EDX measurements in LVPs: Paris-Edinburgh press (PEP) and multi-anvil press (MAP). A white (or sometimes pink) beam might be either focused (50 μm in vertical direction) or not. For all EDX measurements rotating Ge solid-state detector as a part of CAESAR system is used (detector energy resolution $\Delta E/E$ of $\sim 10^{-2}$ is a limiting resolution at this operating mode). There are also three collimating slits: one is installed before LVP and two others are placed between LVP and Ge SSD. Apart from EDX, the fast imaging tomography (FIT) is also available at white and pink beam modes. Other tomography techniques for phases or grains mapping are preferably to be used with monochromatic beam mode. However, in some particular cases, because the flux of monochromatic beam is low, the scan times become very long for small pixel sizes, and using a pink beam mode for such techniques as diffraction contrast

tomography (DCT) or 3D XRD is advantageous. Due to easy beamline adaptability for concrete experiment the tomograph can replace the LVP in optics hutch.

2) The 2nd experimental table. Only monochromatic beam (parallel or focused by VFM) is available. Generally, this table is dedicated to various tomography techniques (which do not require very short scan times): DCT, 3D XRD, quantitative imaging, high quality phase contrast imaging, imaging with large pixel sizes and diffraction tomography. As the parallel monochromatic beams can be produced with sizes up to 15×3 mm^2 the maximum sample dimension can be ~25 – 30 mm. The incident beam size can be easily changed by collimating slits which are installed before the tomograph. Some ADX measurements in diamond anvil cells (DACs) with use of PerkinElmer flatpanel detector and a CCD rayonix 165 detector might be also provided. However, taking into account not enough focusing of the monochromatic beam, the 3d experimental table is more preferable for *in situ* measurements in DACs.
3) The 3rd experimental table. The monochromatic micro-focused beam is available. Kirkpatrick-Baez micro-focusing mirrors (KB) and a pinhole (virtual point source of light) might deliver a high flux focused beam (~6×6 μm^2). The experimental setup is perfectly suitable with *in situ* ADX measurements in DACs at different temperatures. On the detection side there are PerkinElmer flatpanel detector and a CCD rayonix 165 detector. At present time, only room temperature and low temperature (4.2 K, liquid He) experiments in DACs are available in PSICHE beamline. However, the 3rd experimental table is planned to be used for installation of laser heating setups, covering wide temperature ranges (up to 2000 K).

7.2 Combined Angle- and Energy-dispersive Structural Analysis and Refinement (CAESAR) system

PSICHE beamline (synchrotron SOLEIL) has been equipped with combined angle- and energy-dispersive structural analysis and refinement (CAESAR) in frames of the ANR Grant No. ANR-2011-BS08-018 ("Synthesis of Novel High-Pressure Phases in the B–C–N–O–P System"). The CAESAR system proposed by Wang et al. [200] is based on Ge solid-state rotating detector and is installed in optics hutch of PSICHE beamline. The detector is coupled to a multi-channel analyzer, allowing to count the number of events at a given energy. Based on ADX and EDX techniques, the CAESAR system is a highly powerful tool for *in situ* HP-HT experiments (Figure II.27). In combination with LVPs the CAESAR system is a unique installation in Europe.

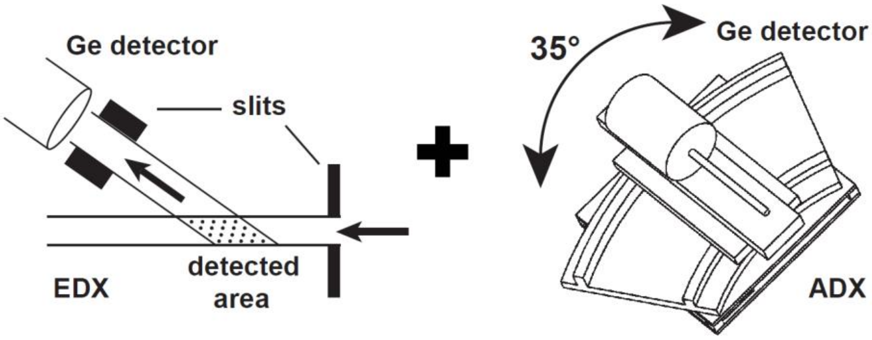

Figure II.27. A combination of EDX and ADX techniques in CAESAR system.

HP-HT *in situ* experiments in LVP imply some particularities in X-ray diffraction measurements, as for example: sample environment signal (gasket, heater, sleeves, etc.) or limited aperture. Hence, the EDX techniques are more preferable for *in situ* measurements in LVP, thanks to their high speed of signal acquisition, efficiency in removing background and waste signals and most importantly a possibility of working with limited volume of sample/limited aperture. On the other hand, as it has been mentioned above, there are significant drawbacks of EDX as low resolution of the Ge SSD, the detector artifacts and the complex corrections necessary for intensities determination to perform Rietveld powder diffraction refinement. 1D ADX technique usually used for *in situ* angle-dispersive measurements does not have these drawbacks, but requires comparatively long acquisition time. The combination of ADX and EDX in one system overcomes their drawbacks.

Experimental

A general view of CAESAR system in optics hutch in PSICHE beamline is presented in Figure II.28.

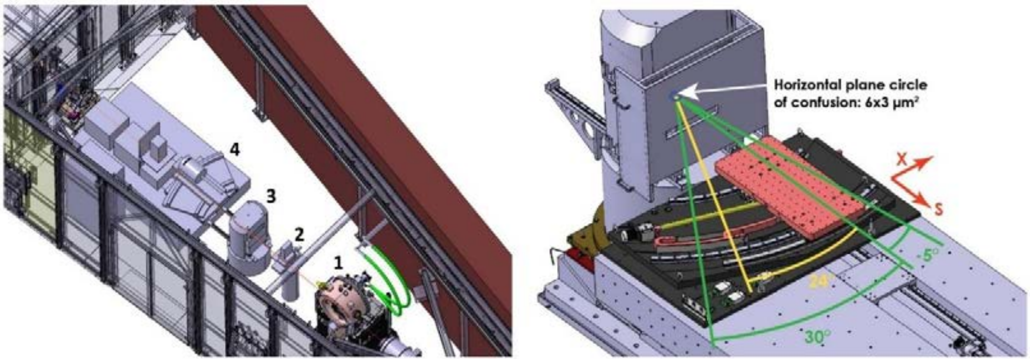

Figure II.28. CAESAR system in PSICHE beamline. On the left: the general plan of optics hutch at PSICHE, the monochromator, input collimating slits, MAP and CEASAR system are indexed by 1, 2, 3 and 4 respectively. On the right: detailed scheme of CEASAR system.

There are three pairs of collimating slits in CAESAR installation. One pair of slits is situated in front of LVP in order to define an incident beam profile size. This pair is called input slits. Other two pairs of slits placed behind LVP move together with Ge solid-state detector. These are output slits. As it has been already noted, the change of vertical gap of output slits varies slightly beam flux and therefore diffraction peaks resolution. However it does not influence on the pattern quality dramatically, as effect of gap change in vertical direction is limited by the resolution of EDD. Unlike vertical gap, the horizontal gap of output slits plays an important role in CAESAR measurements. Change of the horizontal gap of output slits defines the 2θ angle as well as EDD angular resolution. As it has been noted in review of EDX technique, the system of input and output slits allows to define detected area (see Figure II.21), which therefore leads to suppressing of background signal.

During CAESAR measurements mode the Ge SSD moves through the 2θ scan range and collects series of one dimensional energy-dispersive data (intensity versus energy) as function of 2θ. The CAESAR system allows the diffraction angle to be varied between 0 and 30°. SSD rotation mechanism cannot be physically attached to the rotation axes, which leads to large circle of confusion on the position of this axes. To minimize the circle of confusion, the translation corrections has been done at each angle step. Finally, the circle of confusion has been reduced up to 3×6 μm^2, allowing to provide studies of very small objects. At each 2θ step (up to 0.01°) an EDX pattern is acquired, consisting of several thousand channels covering a range of photon energies (up to ~100 keV; 1CH ~ 0.04 keV). The entire data set consists of all 2θ steps from 0° to 30° and forms a two-dimensional array (2D diagram): Int.(E,2θ). These intensity data can be then regrouped according to photon energies, giving a great number of angle-dispersive (intensity *versus* 2θ) data sets, each of which corresponds to a given photon energy. An example of data presentation of CEASAR system is shown in Figure II.29.

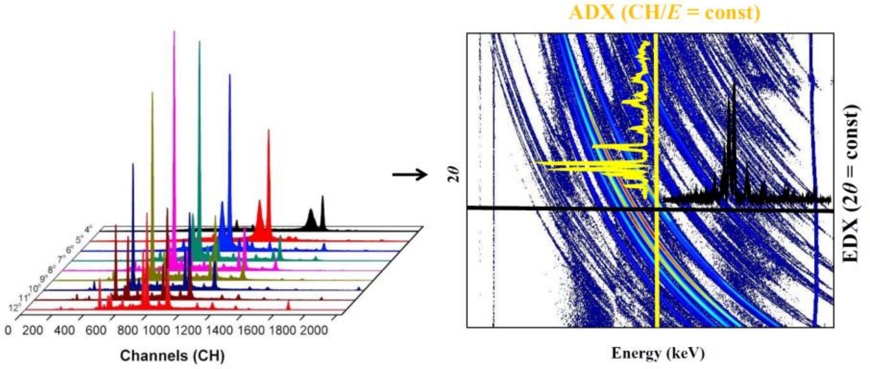

Figure II.29. Representation of the set of EDX patterns in the form of 2D diagram: the function of 2θ for angle range from 4° to 12°.

Data treatment

Such way of data presentation in CAESAR system provides various opportunities in further data treatment. The 2D diagram yields a great number of ADX patterns. The key point of this CAESAR particularity is that using considerably faster EDX acquisition mode a vast set of ADX patterns can be obtained in whole energy range (at PSICHE beamline it is from 15-80 keV). The number of ADX patterns is actually equal to the number of channels. Thus the entire data set, selected subsets or composite scans can be used for multiple data set Rietveld refinement. Nonetheless, one should keep in mind, that data collected with the CAESAR system are sensitive to sample homogeneity and preferential orientation. It happens due to the data are acquired only in the horizontal plane and the volume, even if it is kept constant by adjusting the horizontal gap of input and output slits, changes in shape with the 2θ angle.

One of the most outstanding features of the CAESAR system is binning of a set of ADX patterns in order to increase effective 2θ coverage and to improve counting statistics at chosen energy (channel). Hence angular scan steps can be significantly increased and thus this technique can be significantly less time consuming than a traditional step-scan monochromatic diffraction measurement. The idea of binning is based on Bragg's law. By differentiating of Bragg's formula and taking into account tiny change of energy, and therefore wavelength (λ), one can obtain:

$$2d = \frac{\partial\lambda}{cos\theta\partial\theta} \cong \frac{\Delta\lambda}{cos\theta\Delta\theta} \qquad (II.7).$$

In combination with Bragg's formula one can retrieve:

$$\Delta\theta = tg\theta\frac{\Delta\lambda}{\lambda} \qquad (II.8).$$

where $\Delta\lambda$ is the difference between the two wavelengths. This equation can be used to convert observations at various energies to a specific wavelength. The $\Delta\lambda/\lambda$ is a constant value for a certain channel, hence $\Delta\theta$ depends on and changes only with θ. The binning process is schematically presented in Figure II.30.

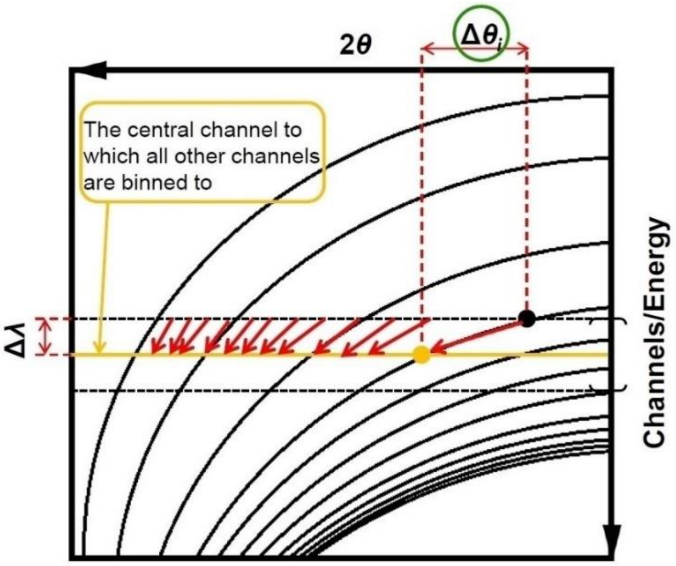

Figure II.30. Schematic representation of CAESAR binning option, herein $\Delta\theta_i$ refers to $\Delta\theta$ in formula (*II.17*); b) ADX spectrum, showing increasing of data density after application of the binning option.

The Figure II.31 clearly demonstrates the gain with the binning option. Data from various EDX spectra perfectly fall into a smooth peak profile. It should be noted that increasing of the angle step of Ge SSD (e.g. from 0.1° to 0.2°) does not lead to deterioration of data quality, as can be compensated by taking wider energy range [200]. Actually, the energy binning limits can be up to $\Delta E/E \sim \pm 10\%$ without significant affecting on data quality. On another hand, there is no sense to increase binning energy range as it does not result in considerable amelioration of counting statistics. On the contrary, at the larger $\Delta E/E$ values variations in background become more important.

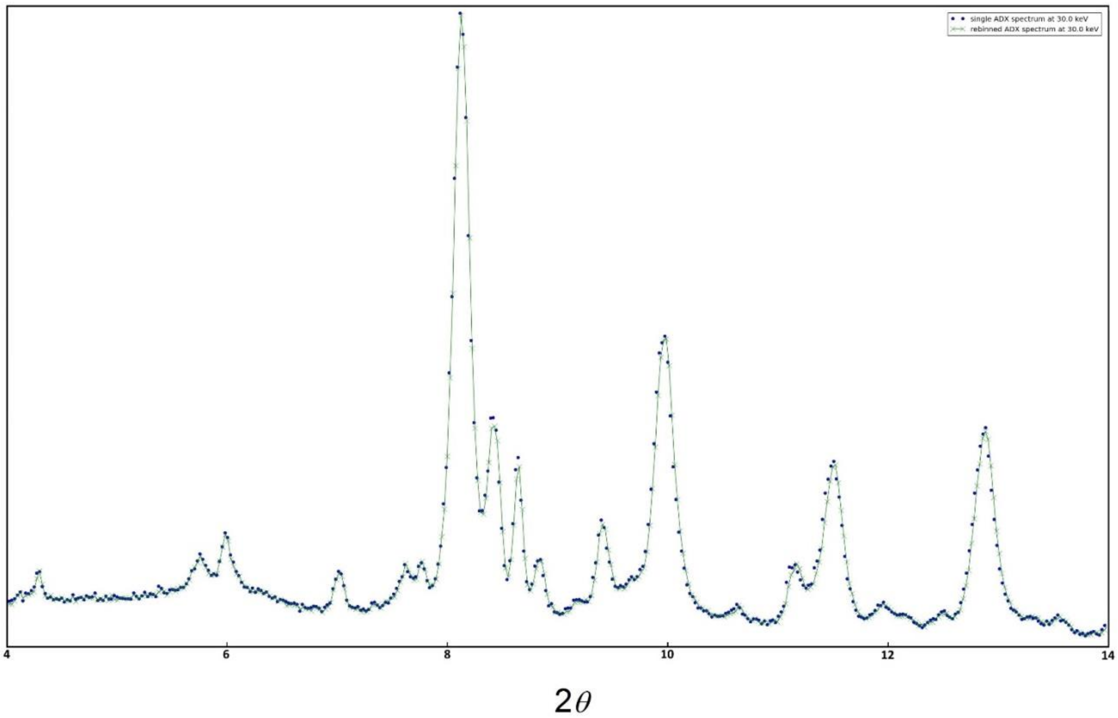

Figure II.31. ADX spectrum of CaB_6 at 30 keV, showing increasing of data density after application of the binning option (the angle step 0.025°). The single ADX pattern is marked by blue dots, rebinned ADX spectrum is marked by the green crosses.

As it has been already mentioned above, the whole data set can be used for Rietveld refinement. Nevertheless for these purposes, it is better to transform the energy axis (in keV) of a 2D diagram to *d*-spacing one (in Å) (Int.(d,2θ)). From this transformed 2D diagram a classical diffraction spectrum can be retrieved (with *d* scale). Such spectrum gathers all of the data obtained at every angle and every energy from binning range (see Figure II.32).

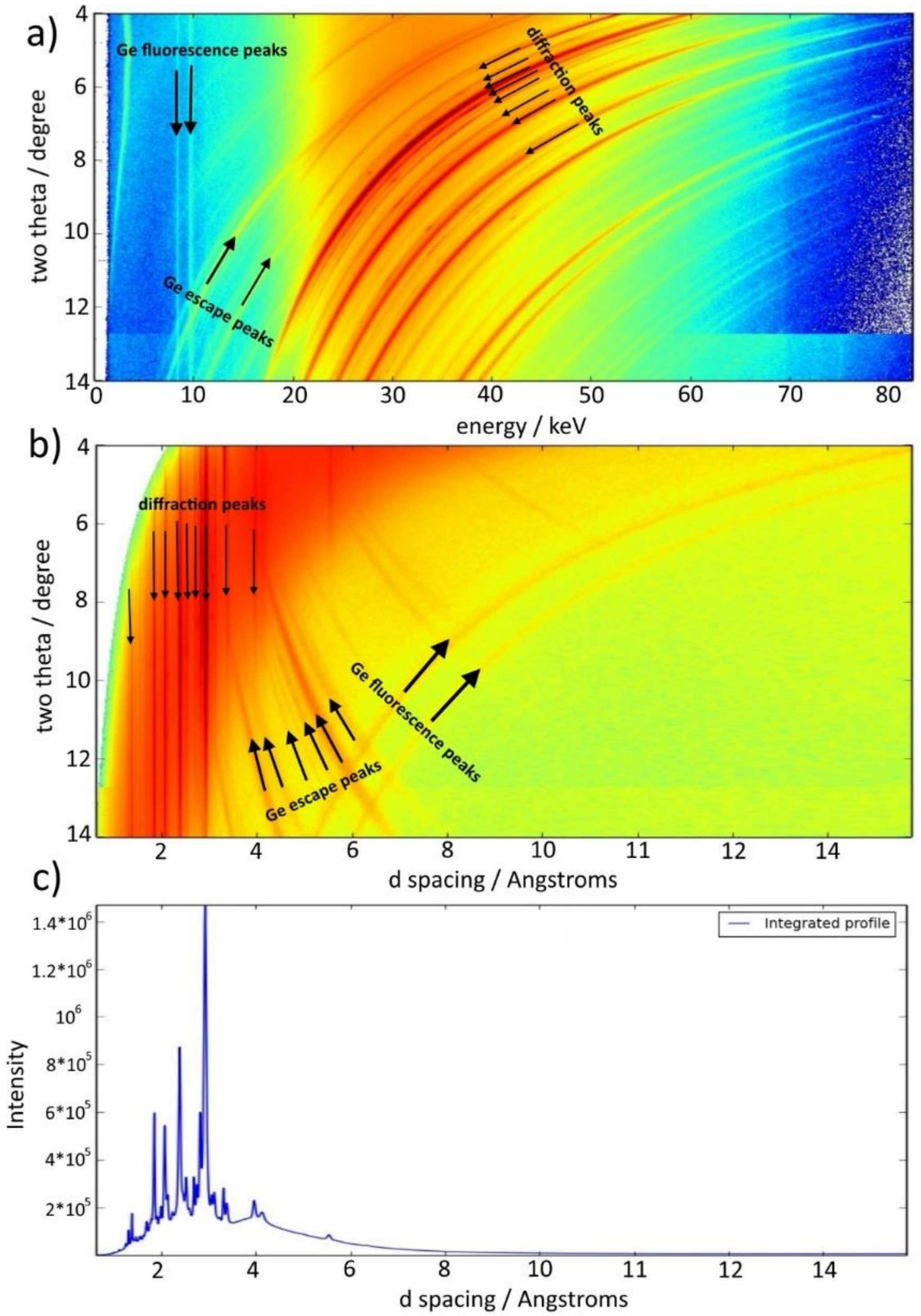

Figure II.32. CAESAR scan of CaB_6/B at 1400°C and ~5 GPa in 4° to 14° 2θ range (angular step = 0.025°; 401 images): a) 2D diagram Int.$(E,2\theta)$ in logarithmic scale, revealing waste signals as escape and fluorescence peaks; b) 2D diagram Int.$(d,2\theta)$ in logarithmic scale, for both diagrams the arrows show the diffraction peaks of CaB_6, Ge fluorescence peaks and Ge escape peaks; c) diffraction spectrum of CaB_6 Int.(d).

As one can see from the Figure II.32 even on the level of 2D diagram Int.$(d,2\theta)$ all the "contaminations" in diffraction pattern, as detector material fluorescence and escape peaks can be discriminated: the sample diffraction peaks are the straight lines, whereas all other peaks are presented by bended lines. It can be easily explained: any diffraction line of the sample should follow the Bragg's law and consequently should become a straight at Int.(E,2θ)→Int.(d,2θ) transformation; the lines, which do not follow it concern to non-diffraction peaks. Using the general EDX pattern (see Figure II.32 *c*)), intensity dependence on the photon energy or beam spectrum could be considered and correction of background could be implemented.

The CAESAR system is widely used by beamline users. For instance, very recently a chemical interaction between Mg and C at high temperatures (~1500 K) and high pressures (~8 GPa) has been provided in PEP [201]. The chemical interaction and formation of a new Mg_2C_3 polymorph was observed in rapid EDX measurements mode ($\theta = 8^o$), whereas after crystallization of a new phase, CAESAR system was used to collect structural data of high quality ($\Delta E/E$ <5%). Basing on this CAESAR measurements Rietveld refinement was implemented and the structure of new β-Mg_2C_3 has been determined.

Moreover the scientific group of J. Chantel et al. has provided successful *in situ* measurements of liquid basalt at 2.7 GPa and 1200 K. The data were obtained with help of CAESAR system which permitted to subtract background on each EDX. The background was estimated by integrating the whole dataset in angle. Due to this a profile of the wiggler emission, the various filtering and absorptions were obtained. After such treatment the liquid scattered signal became clearly visible. This work is still in progress but it showed the possibility of using CAESAR system for *in situ* study of liquids and melts under extreme conditions.

8 *Ab initio calculations*

The theoretical description of material helps to verify experimentally measured properties. Moreover, some properties might be difficult to obtain experimentally, so in this case the quantum mechanics (QM) has a great value. Thus, the QM calculations complement information about material under investigation. In this work we have used the theoretical calculations in order to estimate the properties of studied compounds.

The time independent Schrödinger equation is used in QM to find eigenfunctions (Φ) and eigenvalues (E) of Hamiltonian ($\hat{H}$):

$$\hat{H}\Phi = E\Phi \qquad (II.9).$$

To solve this equation number of approximations should be applied. The first is Born-Oppenheimer or adiabatic approximation. Due to large mass difference between electrons and nuclei, the motion of electrons can be considered separately from nuclei motion. The second approximation is one electron approximation. The N-electron wave function (Φ) is approximated by a Slater determinant constructed from the one-electron wave functions (φ_i).

To find one-electron functions (φ_i), the self-consistent field (SCF) or Hatree-Fock (HF) method is used. The one-electron wave functions are determined from variational principle. The one-electron wave functions should satisfy the system of equations:

$$\hat{F}\varphi_i = \epsilon_i\varphi_i \qquad (II.10),$$

where $\hat{F}$ is the HF operator:

$$F_{HF} = T + U_c + J + X \qquad (II.11),$$

which includes kinetic energy contribution (T), electron-nuclei Coulomb interaction (U_c), electron-electron Coulomb interaction (J) and HF exchange operator (X).

Another approach to the solution of the Schrödinger equation also exists and is called the density functional theory (DFT). It deals with electron densities and is based on the Hohenberg-Kohn (HK) theorems [202,203] and Kohn-Sham equations [204]. The first HK theorem states that the one-to-one mapping between the ground state electron density, and the ground state wave function of a many particle system exist. The second HK theorem proves that the ground state density minimizes the total electronic energy of the system.

The difference between HF and DFT approaches is that in DFT electronic exchange ($X(\rho)$) and correlation ($C(\rho)$) interactions are additionally taken into account. Therefore, the Fockian operator in the KS theory is:

$$F_{KS} = T + U_c + J + X(\rho) + C(\rho) \qquad (II.12),$$

However, the calculation of these interactions is not a trivial task, because the exact functional forms are not known within the KS DFT.

The hybrid HF-DFT functionals, which include a part of the HF exchange were introduced and successfully applied in quantum mechanical calculations of solids [205]. The use of these functionals in the calculations allows one to increase accuracy for the obtained parameters such as optical band gap, atomic structure and vibrational frequencies [205].

For the heavy elements the number of basis functions necessary for their description is large due to large number of electrons. This leads to the high computational cost. The fact that the core electrons do not participate significantly in the chemical bonding allows one to separate description of core and valence electrons. The core electrons are described by one-particle potential (pseudopotential), and the valence electrons are described by effective core potential [205]. The division to the core and valence electrons should be chosen depending on concrete system and type of calculations. Large and small core approximations are available [206]. Usually, the small core approximation is used for compounds with *d*- and *f*-elements [205].

The CRYSTAL09 code [207] allows one to obtain many useful properties of the material such as the electronic band structure and the band gap value, the density of electronic states (DOS), charges on atoms and orbital occupancy, electronic density maps and atomization energy. The relaxation of atomic structure following to the minimum energy criterion is also possible. Bulk modulus, phonon frequencies and phonon dispersion curves can be calculated as well.

The bulk modules were calculated using the Murnaghan EoS [208]:

$$E(V) = E_0 + B_0 V_0 \left(\frac{1}{B_0'(B_0' - 1)} \left(\frac{V}{V_0} \right)^{1-B_0'} + \frac{V}{B_0' V_0} - \frac{1}{B_0' - 1} \right) \qquad (II.13),$$

where V_0 is the equilibrium volume, B_0 is the zero-pressure bulk modulus, B_0' is the pressure derivative of the bulk modulus at ambient pressure, and E_0 is the equilibrium energy. The $E(V)$ dependence is calculated by varying unit cell parameters for few percent close to the equilibrium structure, thus simulating the effect of hydrostatic pressure. Next, the $E(V)$ dependence is fitted by Eq. (*II.*13), having four adjustable parameters (E_0, V_0, B_0, B_0').

The vibrational frequencies were calculated in the harmonic approximation using the "frozen-phonon" approach [209]. In the "frozen-phonon" approach [210] the phonon energy is determined as the difference in the energies of the distorted and equilibrium crystalline lattices for a particular atom displacement.

Chapter III

9 *Studies in B-O binary system*

As it has been already mentioned in Chapter I, the B-O system is already well studied, first of all, due to the great interest drawn to boron suboxide $B_{12}O_{2-x}B_x$ ($0 \leq x \leq 1$) and boron oxide B_2O_3. According to the literature data [103,106-110], a vast number of attempts to investigate new phases in B-O system have been done so far; however, up to now, there are no confident and reproducible results. Thus, in our current work we rejected any attempts to obtain a new phase/phases under extreme conditions in binary B-O system.

Although B-O system is considered to be well studied, some properties of its already known compounds have not been still entirely described. For instance, the phonon properties of the high-pressure phase of B_2O_3 (β-B_2O_3) are still very poorly studied. On another hand, we have already shown that precise EoS of β-B_2O_3 (and therefore bulk modulus determination) requires an additional experiment due to an absence of complete confident results on it.

In this chapter we will present a description of our XRD measurements of β-B_2O_3 under high pressure in order to refine its EoS. It will be followed by the phonon studies of β-B_2O_3 at ambient and under high pressures. Thanks to *ab initio* LCAO calculations performed on β-B_2O_3 the obtained experimental data have been verified and supplemented.

9.1 Equation of state of β-B_2O_3

9.1.1 Experimental techniques

Synthesis details

Polycrystalline β-B_2O_3 has been synthesized by the method described in Ref. [93]. Vitreous boron (III) oxide has been produced by decomposing metaboric acid HBO_2 at ~670°C in a nickel crucible and subsequent re-melting in order to remove air bubbles. The diffraction pattern of *g*-B_2O_3 sample exhibited two characteristic wide halos with *d* values around 2.0 and 3.5 Å. The high-pressure phase of B_2O_3 has been synthesized from remelted *g*-B_2O_3 in TTP at 5.3 GPa and ~1000°C. Boron nitride (grade AX05, Saint-Gobain) capsule was used to isolate the reaction mixture from the graphite heater.

X-ray diffraction measurements at ambient conditions

The X-ray diffraction provided with G3000 TEXT Inel diffractometer (Cu Kα1 radiation) at ambient conditions showed that the sample is highly crystalline β-B_2O_3 with small quantity of impurities of foreign phases (for instance, *h*-BN, the sample capsule material). The XRD pattern is presented in Figure III.1.

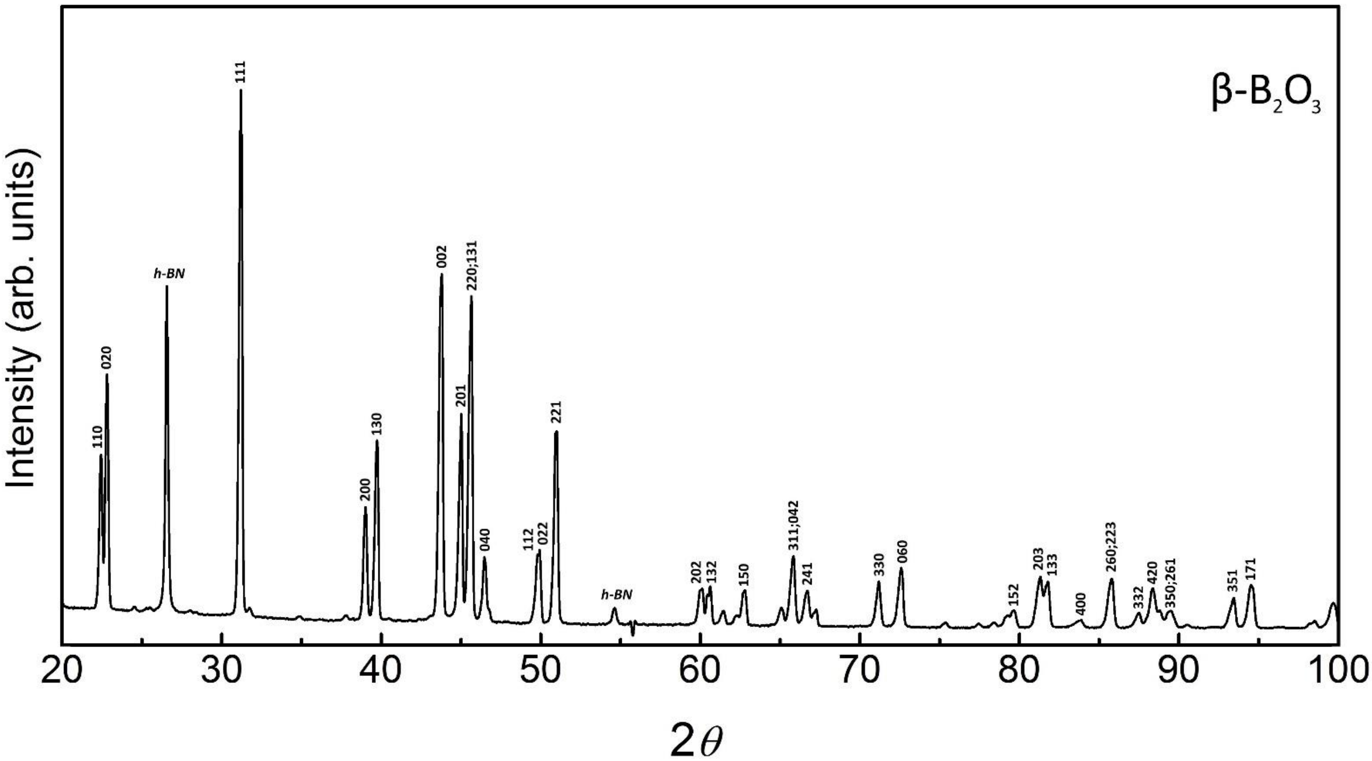

Figure III.1. XRD pattern (λ=1.5406 Å) of our synthesized β-B_2O_3 at ambient conditions. The most intensive peaks of β-B_2O_3 are marked by the *hkl* Miller indexes; the peaks of *h*-BN are also indicated.

The lattice parameters of β-B_2O_3 (a = 4.611(5) Å, b = 7.804(5) Å, c = 4.132(3) Å) are close to those published in Ref. 124 (a = 4.613(1) Å, b = 7.803(2) Å, c = 4.129(1) Å). The β-B_2O_3 unit cell volume of 148.7 Å^3 is also rather close to the values reported before: 148.6 Å^3 [124] and 149.3 Å^3 [111].

High-pressure X-ray diffraction measurements

High-pressure XRD experiments were carried out in a Chervin type membrane diamond anvil cell (MDAC) [211] of 300 μm culet anvils. The polycrystalline sample (55 μm) was loaded into a 100 μm hole drilled in a rhenium gasket pre-indented down to ~25 μm. Neon gas was used as a pressure transmitting medium. Pressure in MDAC was *in situ* determined from the calibrated shift of the ruby R1 fluorescent line [171,212] and equation of state of neon [213,214]. The pressure values according to the both pressure gauges are presented in Table 1. Up to 22 GPa both pressure gauges (ruby, neon) indicated very close pressure values with less than 0.5 GPa difference, this fact indicates negligible strains and stresses and also very low pressure gradients all over the cell. Thus, one can suppose that there were the quasi-hydrostatic conditions during the measurement up to the highest pressure in MDAC. Further, only experimental data with the ruby pressure scale has been used, as they cover the whole pressure range. Pressure in the DAC was measured before and after each ADXRD measurement. Further we used the mean value of these two pressures. The pressure drift during measurement did not exceed 0.5 GPa in the 0-22 GPa pressure range. In order to get rather dense data coverage in the whole pressure range, the intervals between the pressure points did not exceed ~2.2 GPa.

HP XRD measurements were performed at ESRF ID27 beamline. The collection of XRD patterns was implemented in angle-dispersive mode with a focused monochromatic beam. The beam wavelength was selected to 0.3738 Å. Beamline X-ray optics delivered a pencil beam spot of 9 μm^2. The XRD data acquisition was implemented by MAR 345 image plate detector with an exposure time of 10 seconds. Laue diffraction patterns obtained during the measurements were treated by fit2D software [194]. During the compression of the β-B_2O_3 the expected monotonous shift of the diffraction peaks towards the higher 2θ values was observed (see Figure III.2).

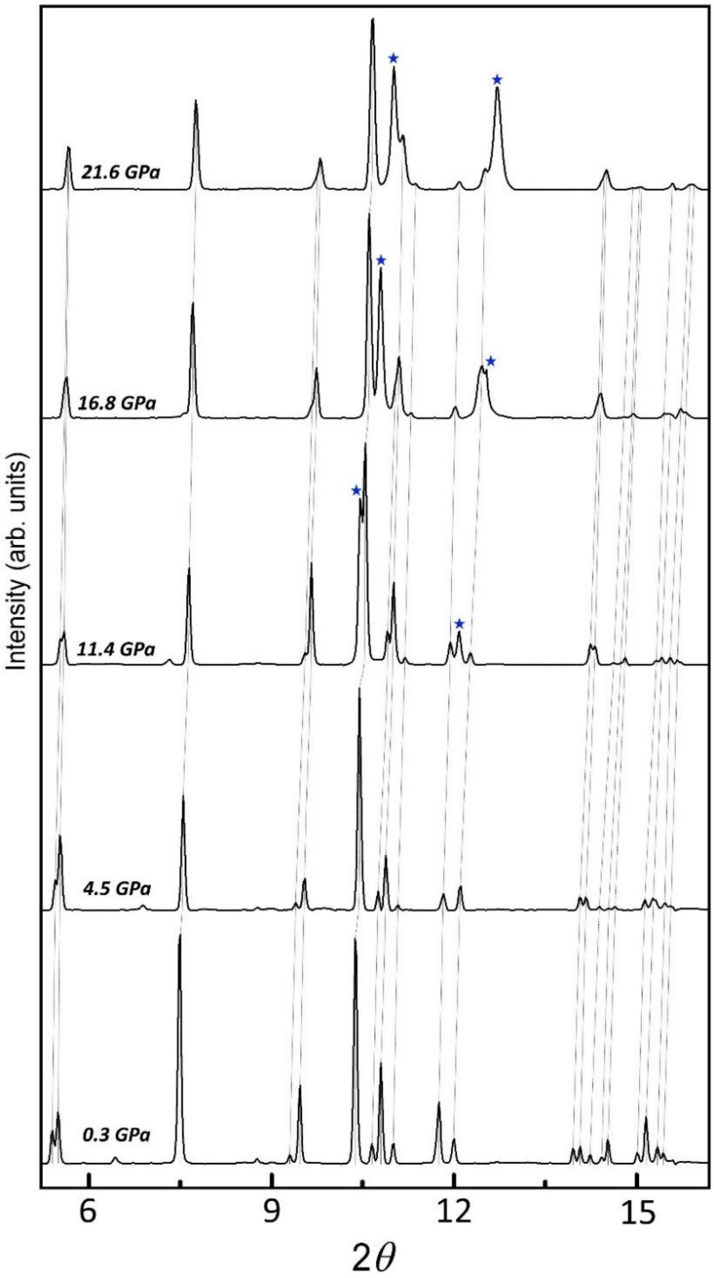

Figure III.2. ADXRD patterns of β-B_2O_3 taken at different pressures; the beam wavelength is 0.3738 Å. The shifts of each β-B_2O_3 peak under compression are traced by the dashed lines; the solid Ne peaks are marked by the blue stars.

The lattice parameters and unit cell volume at each pressure point were refined by using DICVOL04 and WinPLOTR packages in FullProf software [195-197] and are presented in Table 1.

Pressure, GPa		*a*, Å	*b*, Å	*c*, Å	Volume, Å^3
Ne scale	Ruby scale				
-	0.0	4.611(5)	7.804(5)	4.132(3)	148.7
-	0.3	4.607(1)	7.798(1)	4.129(1)	148.3
-	0.5	4.606(1)	7.796(1)	4.128(1)	148.2
-	1.2	4.599(1)	7.787(1)	4.122(1)	147.6
-	2.1	4.589(1)	7.776(1)	4.117(1)	146.9
-	3.2	4.577(1)	7.762(2)	4.112(1)	146.1
-	4.5	4.561(1)	7.741(1)	4.101(1)	144.8
-	5.7	4.548(1)	7.724(2)	4.097(2)	143.9
7.2	7.3	4.532(1)	7.706(3)	4.088(2)	142.8
8.7	8.9	4.514(2)	7.697(3)	4.081(1)	141.8
10.5	10.5	4.496(1)	7.670(1)	4.072(1)	140.4
11.3	11.4	4.486(1)	7.656(1)	4.067(1)	139.7
12.7	12.8	4.473(1)	7.640(1)	4.059(1)	138.7
14.6	14.6	4.455(1)	7.615(2)	4.048(2)	137.3
16.5	16.8	4.431(1)	7.589(3)	4.036(3)	135.7
18.8	18.6	4.418(2)	7.572(3)	4.029(2)	134.8
20.3	20.2	4.398(5)	7.563(10)	4.025(5)	133.9
22.3	21.6	4.394(2)	7.541(4)	4.022(3)	133.3

Table 1. Lattice parameters and volume of the unit cell of β-B_2O_3 as a function of pressure to 22 GPa at room temperature. The numbers in parentheses are the fitting standard deviations (95% confidence interval) on the last or last two digits.

Calculations details

In the present work, β-B_2O_3 has been studied with first principles LCAO calculations performed using the CRYSTAL09 code [207]. The optimized (in earlier calculations) all-electron basis sets for boron [215] and oxygen [216] atoms have been used. In the CRYSTAL09 code [207], the accuracy in evaluating the Coulomb series and the exchange series is controlled by a set of tolerances, which were taken to be (10^{-8}, 10^{-8}, 10^{-8}, 10^{-8}, 10^{-16}). The Monkhorst-Pack scheme [217] for an 8 x 8 x 8 k-point mesh in the Brillouin zone was applied. Self-consistent field calculations were performed for hybrid DFT–HF WCGGA–PBE-16% [218] functional. The percentages 16% define the Hartree–Fock admixture in the exchange part of DFT functional.

We performed the full β-B_2O_3 structure optimization procedure according to the energy minima criterion. The lattice parameters (*a*, *b*, and *c*) and the unit cell volume (V_0) are 4.645(12) Å, 7.873(8) Å, 4.139(6) Å and 151.4 Å^3 respectively. The theoretically calculated lattice parameters have been found to be slightly larger than experimentally determined ones. The deviations of the calculated a, b, c parameters from the experimental ones are 0.74%, 0.88% and 0.17% respectively. The unit cell volume deviation does not exceed 2%. Although the boron isotope content in β-B_2O_3 is 20% ^{10}B - 80% ^{11}B, all *ab initio* calculations have been performed for boron isotope content of 100% ^{11}B (further it will be marked as β-$^{11}B_2O_3$*).

The β-$^{11}B_2O_3$* equation of state parameters (bulk modulus B_0 and its first pressure derivative B_0') have been estimated using routine implemented in the CRYSTAL09 code. In order to obtain E(V) dependence, the unit cell volume was varied from 89.9% to 109.9% of the equilibrium volume (V_0). The structure optimization was performed at each volume. Obtained E(V) dependence has been fitted to the Murnaghan equation of state [208] taking $V_0 = 151.4$ Å^3 and $E_0 = -29.9$ keV (Eq. *II*.13). In order to estimate the P(V) dependence the Murnaghan equation (Eq. *III*.1) has been used:

$$P(V) = \frac{B_0}{B_0'}\left[\left(\frac{V}{V_0}\right)^{B_0'} - 1\right] \qquad (III.1).$$

It should be noted here, that electron structure optimization did not converge at highly reduced unit cell volume (P > 22 GPa). Hence, all the pressure dependencies of β-$^{11}B_2O_3$* unit cell parameters (a, b, c, V_0, etc.) will be given only up to 21 GPa. The possible reason of this divergence might be noticeable changes of the electronic structure for the unit cell with reduced volume. Therefore the chosen set of the calculation parameters and all-electron basis sets might become not optimal at the highly deformed unit cell.

9.1.2 Results and discussion

The lattice parameters of β-B_2O_3 have been determined over the whole pressure range and their pressure dependencies are plotted in Figure III.3.

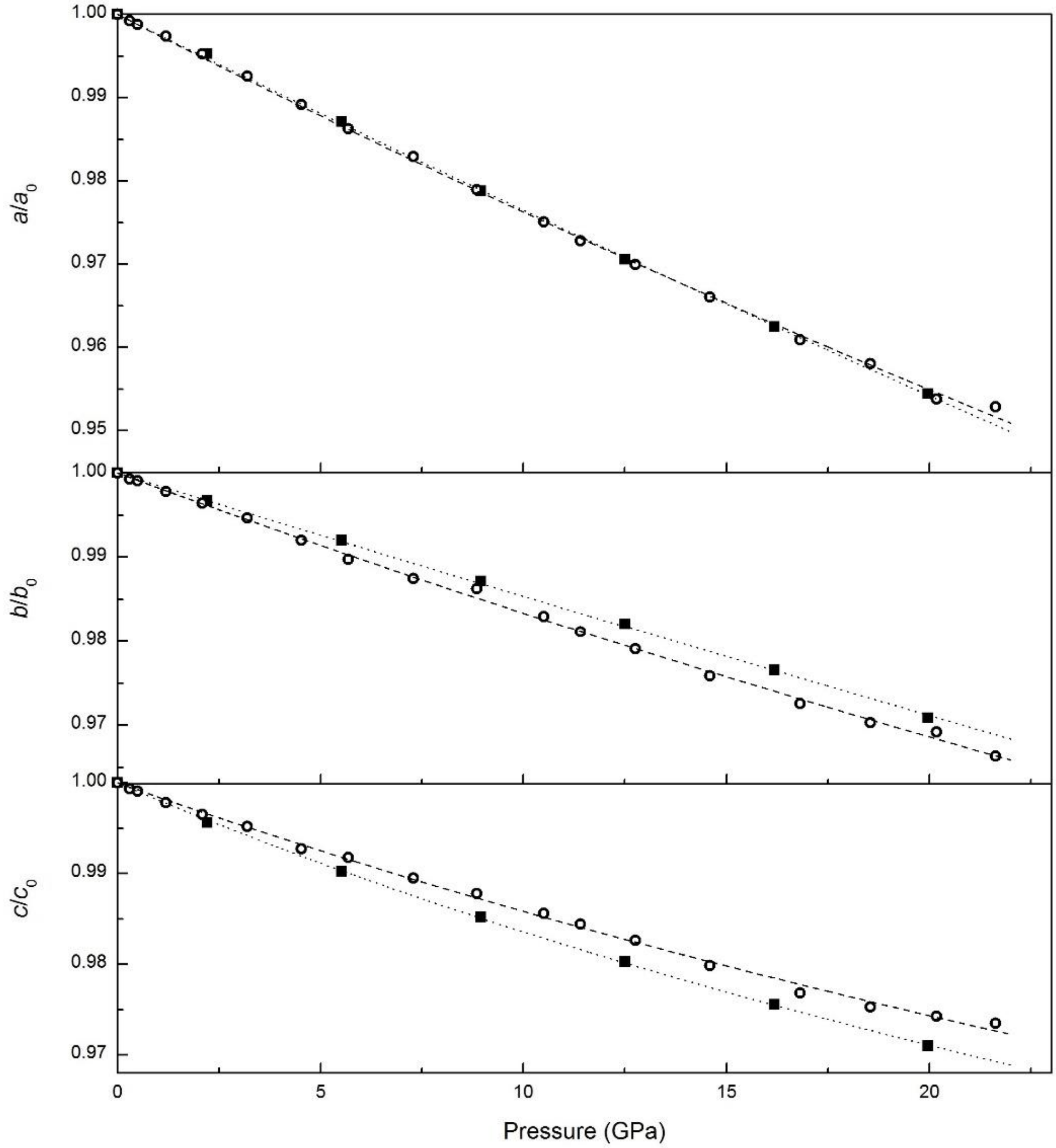

Figure III.3. Normalized lattice parameters of β-B_2O_3 *versus* pressure. Open circles and solid squares represent experimental and theoretical data respectively. The dashed and dotted lines represent the fit of one-dimensional analog of the Murnaghan equation of state to the experimental and theoretical data respectively; the pressure values are given by the ruby gauge.

According to Figure III.3 the most significant compression undergoes along *a* axis. We used the one-dimensional analog of the Murnaghan equation of state (Eq. *III*.2), to approximate the relationship between the lattice parameters and pressure, as well as it has been done in Ref. 219:

$$r = r_0\left[1 + P\left(\frac{\beta_0'}{\beta_0}\right)\right]^{-\frac{1}{\beta_0'}} \qquad (III.2).$$

Here r is the lattice parameter (index 0 refers to ambient pressure); β_0 is the axial modulus and β_0' is the pressure derivative of β_0. The $\beta_{0,a}$, $\beta_{0,b}$ and $\beta_{0,c}$ axis moduli values are 398.6±6.7, 562.4±13.2 and 627.7±18.6 GPa respectively. Using the (Eq. *III*.3) and the axial modulus values, the linear compressibility (k_r) along each direction in the unit cell can be determined:

$$k_r = \beta_{0,r}^{-1} = \left(\frac{d\ln(r)}{d\,P}\right)_{P=0} \qquad (III.3).$$

The k_r values found for a, b and c directions are $(2.51\pm0.05)\times10^{-3}$, $(1.78\pm0.04)\times10^{-3}$ and $(1.59\pm0.05)\times10^{-3}$ GPa^{-1} respectively. The ratios k_a/k_b and $k_b/k_c > 1$ clearly indicate, that β-B_2O_3 is more compressible along the b axis than along the c axis, whereas the compression along the a axis is maximal. According to theoretical data also illustrated in Figure III.3, the pressure dependency of a parameter perfectly fits with experimental one, while the compression along c axis is bigger than one along the b axis. The $\beta^*_{0,a}$, $\beta^*_{0,b}$ and $\beta^*_{0,c}$ parameters concerning the one-dimensional analog of the Murnaghan equation of state approximation of the LCAO data are 414.6±6.7, 671.2±3.3 and 519.3±9.7 GPa respectively. Hence, using (Eq. *III*.3) the k_r* values found for a, b and c directions are $(2.41\pm0.05)\times10^{-3}$, $(1.49\pm0.01)\times10^{-3}$ and $(1.93\pm0.04)\times10^{-3}$ GPa^{-1} respectively. All β_0 and k_r values calculated for theoretical and experimental data, as well as lattice parameters are collected in Table 2.

	Experimental data	Theoretical calculations
a, Å	4.611(5)	4.645(12)
b, Å	7.804(5)	7.873(8)
c, Å	4.132(3)	4.139(6)
$\beta_{0,a}$, GPa	398.6±6.7	414.6±6.7
$\beta_{0,b}$, GPa	562.4±13.2	671.2±3.3
$\beta_{0,c}$, GPa	627.7±18.6	519.3±9.7
k_a ×10^{-3} GPa^{-1}	2.51±0.05	2.41±0.05
k_b ×10^{-3} GPa^{-1}	1.78±0.02	1.49±0.01
k_c ×10^{-3} GPa^{-1}	1.59±0.05	1.93±0.04

Table 2. Lattice parameters at ambient conditions, axial moduli and linear compressibility obtained from theoretical and experimental studies.

As one can see, the experimentally measured linear compressibility values reduce in the following row: $\beta_{0,a} < \beta_{0,b} < \beta_{0,c}$. Basing on the simple logic one might expect the same order of the calculated compressibility values. However, according to theoretical calculations the row of the linear compressibility values is: $\beta^*_{0,a} < \beta^*_{0,c} < \beta^*_{0,b}$. Thus, one can see that the *ab initio* prediction of the unit cell compression along a, b and c axis is not the perfect. On other hand the maximum deviation of the theoretically estimated lattice parameters at high pressure from the corresponding experimental values is lower than 1.5%. Hence, the *ab initio* calculations performed using

CRYSTAL09 revealed rather reasonable values and hence can be used for quick and coarse estimations.

The parameters of β-$^{11}B_2O_3$* equation of state have been estimated using the E(V) dependence obtained from LCAO calculations (Figure III.4 *a*). The isothermal bulk modulus value (B_0) has been found to be 175.3±1 GPa. Its first pressure derivative B_0` is 1.4±0.3.

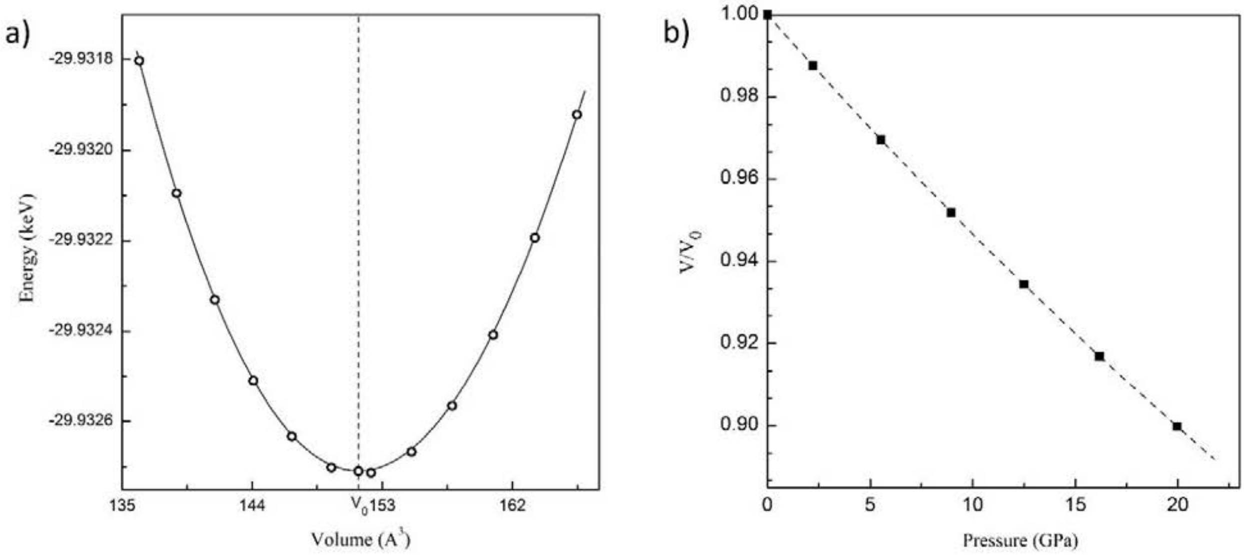

Figure III.4. a) Energy of the β-$^{11}B_2O_3$* unit cell *versus* volume (Murnaghan fit – solid line). The position of V_0 is indicated by dashed line; b) equation of state of β-$^{11}B_2O_3$*. The dashed line presents the Murnaghan fit to the theoretical data.

This bulk modulus value is close to that (B_0 = 169.9 GPa) obtained in [111] by fitting the experimental data by Vinet equation of state [220]. Volume dependence V(P) of the theoretical data fitted by the Murnaghan equation of state is shown in Figure III.4 *b*.

The experimentally observed unit cell volume change under compression is plotted in Figure III.5.

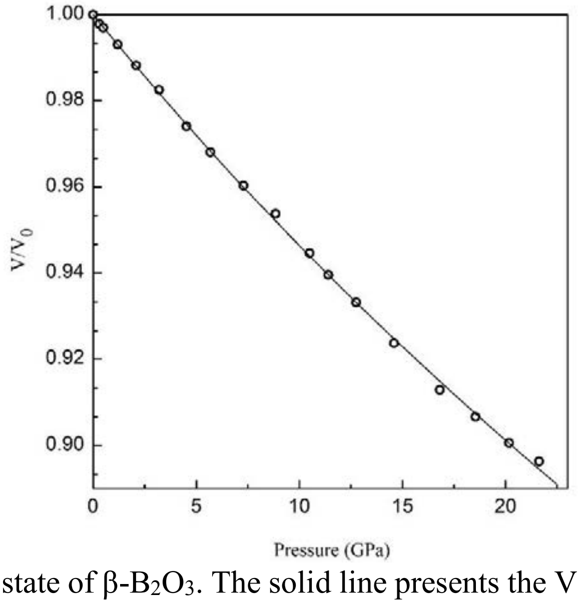

Figure III.5. Equation of state of β-B_2O_3. The solid line presents the Vinet fit to the experimental dataset; the pressure values are given by the ruby gauge.

We implemented the Murnaghan (Eq. *III*.1) [208], third order Birch-Murnaghan (Eq. *III*.4) and Vinet (Eq. *III*.5) [219] formulations of equation of state for data fitting:

$$P(V) = \frac{3B_0}{2}\left[\left(\frac{V_0}{V}\right)^{\frac{7}{3}} - \left(\frac{V_0}{V}\right)^{\frac{5}{3}}\right]\left\{1 + \frac{3}{4}(B_0' - 4)\left[\left(\frac{V_0}{V}\right)^{\frac{2}{3}} - 1\right]\right\} \qquad (III.4),$$

$$P(V) = 3B_0\frac{(1-X)}{X^2}e^{\left(1.5(B_0'-1)(1-X)\right)} \qquad (III.5),$$

where $X = \sqrt[3]{V/_{V_0}}$, V_0 is unit cell volume at ambient pressure.

The obtained bulk modulus B_0 and its first pressure derivative B_0' values are presented in Table 3.

EoS	Parameters	[111]	χ^2	Current study	χ^2	Total dataset	χ^2
V	B_0, GPa	169.5±10	0.55	169.9±3	0.06	168.7±4	0.86
	B_0'	2.6±0.7		2.4±0.4		2.6±0.3	
B-M	B_0, GPa	167.4±8	0.41	169.4±3	0.07	167.5±3	0.48
	B_0'	2.8±0.5		2.6±0.3		2.8±0.2	
M	B_0, GPa	172.1±8	0.39	170.6±3	0.06	170.6±3	0.48
	B_0'	2.3±0.6		2.3±0.3		2.3±0.3	

Table 3. Parameters for the equation of state of β-B_2O_3. Murnaghan (*M*) and Vinet (*V*) formulations have been used for fitting the current experimental data, data of *Nieto-Sanz et al* [111] and combined total dataset based on the both datasets. χ^2 is an indication of the quality of the fit (lower for a better fit).

As one can see from the Table 3 the B_0 values calculated using Vinet, Birch-Murnaghan, Murnaghan EoS formulations and our experimental data are very close to those of [111] and to our theoretical estimation (175.3 GPa, 1.4). Such close B_0 values for three independent datasets are a strong ground to state that B_0 value reported in [121] (90±15 GPa) is incorrect. The lower χ^2 parameters for dataset in our experiment indicate the better accuracy of our measurements compared to [111].

In the Figure III.6 we plotted the combined data on β-B_2O_3 equation of state obtained in Ref. 111 and in our study. One can note that P(V) curves plotted on the basis of two independent experimental datasets match almost perfectly (except one point at 19.6 GPa in the study [111]). Consequently, we supposed, that all the points in Figure III.6 might be reviewed as the whole dataset and be fitted by the same formulations of equation of state. The results of this fitting are listed in Table 3.

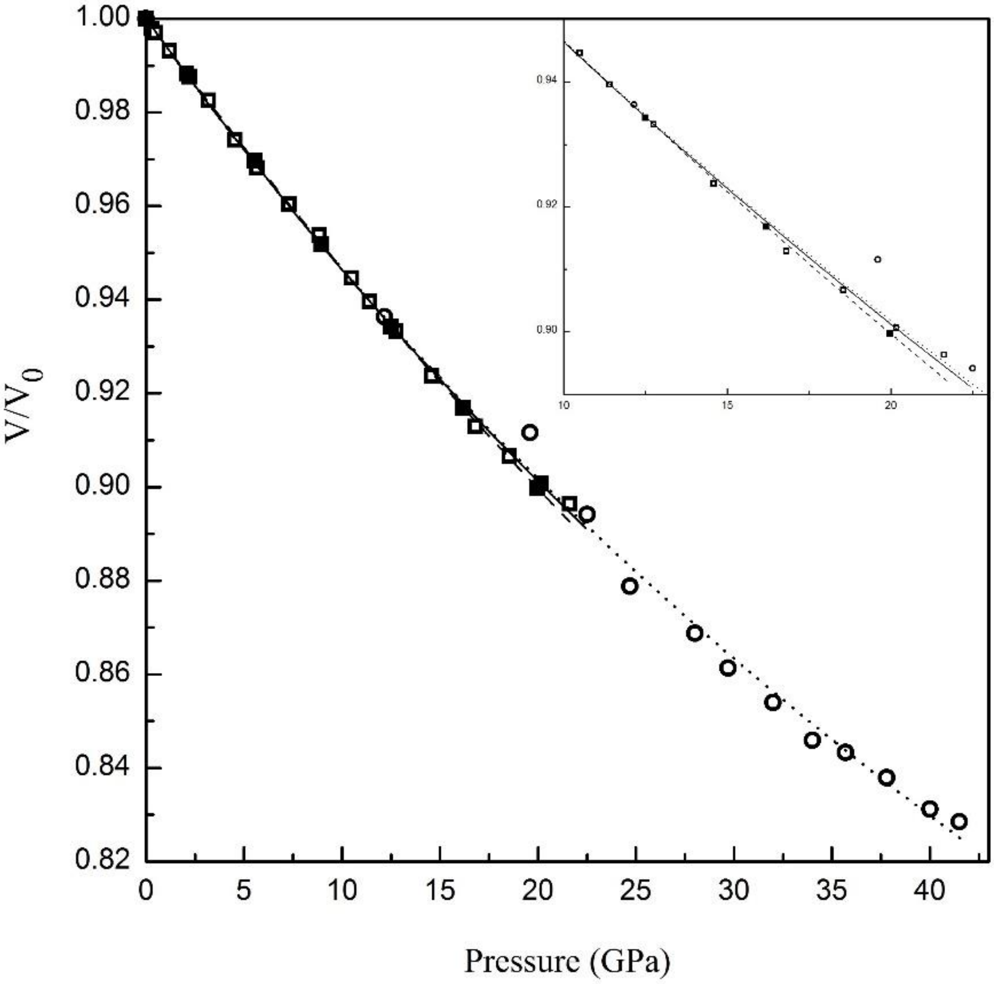

Figure III.6. Equation of state of β-B_2O_3. The open squares and circles represent the current experimental data and experimental data of [111] respectively. The solid squares represent theoretical data. The solid and dotted lines present the Vinet fit to the current study experimental dataset and to dataset of [111] respectively; the dashed line presents the Murnaghan fit to the theoretical data; the pressure values are given by the ruby gauge.

The B_0^t values of total dataset are slightly lower than ones determined on basis of our study and study of *Nieto-Sanz et al* [111], meanwhile $B_0^{t}{}'$ values are very close to those obtained in our study and in Ref. 111. In spite of the fact that the χ^2 values for total dataset are higher than those found for separate datasets, they are still rather low. Thus, the obtained B_0^t and $B_0^{t}{}'$ values can be considered as rather precise and confident ones. According to χ^2 values found for both formulations of equation of state, the Murnaghan formulation has been found to be a better choice for fitting the experimental P(V) data. Summing up all the facts stated above, there are strong grounds to suppose that the experimental points of the present research complement those of Ref. 111 and the whole dataset might be considered.

One should note, that the differences between bulk modulus values of total and two separate datasets ($\Delta B_0 = B_0 - B_0^t$) vary from 0.5 to 1.9 GPa for different formulations of equation of state. This fact demonstrates the importance of the low-pressure range in equation of state measurements.

As it has been written in Chapter I, β-B_2O_3 is constructed from BO_4 tetrahedra, which form the 6- and 8-membered rings (see Figure III.7). Due to this, we put in Table 4 the β-B_2O_3 lattice parameters, the B-O bond lengths and B-O-B angles values of the distorted BO_4 tetrahedron obtained in our research. Since there is a perfect coincidence of the lattice parameters found in our work with those reported before [124] we used the atoms positions determined in [124]. It should be underlined that Table 4 contains the structure information about β-B_2O_3 enriched by ^{10}B isotope (enrichment ≈95%). For convenience the isotope enriched boron (III) oxide will be further marked as β-$^{10}B_2O_3$. The details of its synthesis, phase purity and etc. will be given in the next part.

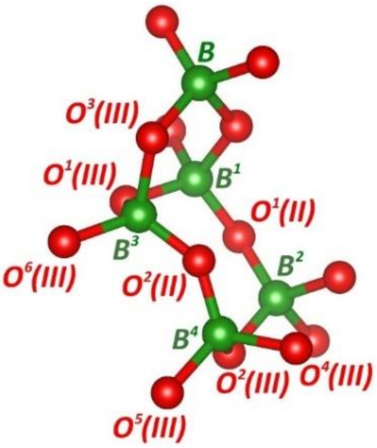

Figure III.7. The structural fragment of β-B_2O_3: six- and eight-membered rings (the superscript index defines atom number, the number in brackets defines coordination of O atom: two- or three-coordinated).

Parameter	β-B_2O_3	β-$^{10}B_2O_3$	β-B_2O_3 [124]	β-$^{11}B_2O_3$*
a, Å	4.611(3)	4.626(3)	4.613(2)	4.645(12)
b, Å	7.804(4)	7.824(3)	7.803(4)	7.873(8)
c, Å	4.132(3)	4.147(4)	4.129(4)	4.139(6)
V_0, Å^3	148.66	150.11	148.62	151.37
B^3-O^2(II), Å	1.373(3)	1.377(4)	1.373(3)	1.385(2)
B^3-O^1(III), Å	1.512(4)	1.517(3)	1.512(2)	1.522(2)
B^3-O^3(III), Å	1.508(2)	1.512(5)	1.507(2)	1.518(4)
B^3-O^6(III), Å	1.507(5)	1.512(6)	1.506(3)	1.510(4)
O^2(II)-B^3-O^1(III), °	113.110	113.104	113.125	113.199
O^2(II)-B^3-O^3(III), °	110.204	110.167	110.194	110.347
O^2(II)-B^3-O^6(III), °	115.824	115.822	115.825	115.840
O^1(III)-B^3-O^3(III), °	104.868	104.881	104.910	104.970
O^1(III)-B^3-O^6(III), °	104.686	104.699	104.656	104.508
O^3(III)-B^3-O^6(III), °	107.389	107.415	107.373	107.199

Table 4. Cell parameters, bond lengths and angles of β-B_2O_3, β-$^{10}B_2O_3$, β-B_2O_3 [124] and β-$^{11}B_2O_3$* (theoretically calculated) at ambient conditions.

According to the structural data presented in Table 4 the BO_4 tetrahedra in β-B_2O_3 are significantly distorted. As it has been mentioned before [124], the structure of β-B_2O_3 consists of a network of corner-linked BO_4 tetrahedra. Three corners of BO_4 are connected to two other BO_4, whereas the fourth corner is linked with only one tetrahedron. Consequently there are two types of oxygen atoms in β-B_2O_3 structure: two- and three-coordinated (in Figure III.7 they are marked O(II) and O(III) respectively). As one can see from Table 4, the oxygen atoms shared between only two tetrahedra relate to the shortest B-O distance, while the other three oxygen atoms shared between three BO_4 tetrahedra relate to the longer B-O distances.

The EXAFS and XANES *in situ* measurements could be used for the determination of the interatomic distances and angles changes under compression. However, in the case of β-B_2O_3 the low energy edges of boron (0.2 keV) and oxygen (0.5 keV) are not compatible with direct high pressure experiments in the DACs as the soft X-rays would be absorbed by the diamond anvils. The direct HP measurements in DACs are only possible by inelastic X-ray Raman scattering (XRS) using hard X-rays [221], but the available energy range would rather limited to draw some information/conclusions about the interatomic distances and angles. That is why in present work in order to show the pressure dependencies of the all four B-O bonds in distorted BO_4 tetrahedron up to 22 GPa we used the structural data obtained in our HP XRD measurements (Figure III.8), assuming that the atoms positions are fixed. Actually we employed the B and O positions refined before [124].

	x	***y***	***z***
B	0.1606(4)	0.1646(3)	0.4335(9)
O(1)	0.2475(3)	0	0.5
O(2)	0.3698(3)	0.2911(1)	0.5802(8)

The error bars of the obtained interatomic distances and angles are determined by the corresponding error bars of the lattice parameters (<0.3%) and atoms positions (<0.2%). The pressure dependencies of the interatomic distances estimated using the data obtained from LCAO *ab initio* calculations are also plotted in Figure III.8. It should be underlined that in LCAO structure optimization according to energy minima criterion the lattice parameters as well as atoms coordinates (in the given space group) have been varied.

During β-B_2O_3 compression, a significant change of B-O bonds was observed. For instance, the most long B^3-O^1(III) bond becomes the most short among all B-O(III) bonds, hence B^3-O^1(III) bond has been found to be the most compressible. The compressibility values of all B-O bonds are collected in Table 5. According to Figure III.8 and Table 5 the B-O bonds compressibilities in 0-

22 GPa pressure range reduces in the following order: B^3-O^1(III) > B^3-O^3(III) > B^3-O^2(II) > B^3-O^6(III). The decreasing order of B-O(III) compressibilities has been found to be the same to decreasing order of B-O(III) bond lengths (see Table 4).

	Parameters	B^3-O^2(II)	B^3-O^1(III)	B^3-O^3(III)	B^3-O^6(III)
exp.	β_0, GPa	559.6±11.6	419.5±6.4	469.4±7.2	594.0±18.5
	k_r ×10^{-3}, GPa^{-1}	1.79±0.04	2.38±0.04	2.13±0.03	1.68±0.05
theor.	β_0, GPa	648.5±4.2	428.7±3.3	533.5±3.7	527.4±9.2
	k_r ×10^{-3}, GPa^{-1}	1.54±0.01	2.33±0.02	1.87±0.01	1.90±0.03

Table 5. The axial moduli and linear compressibilities of the B-O bonds in β-B_2O_3 obtained from theoretical and experimental data.

It should be also noted, that in pressure range from 13 to 22 GPa the relative changes of B-O distances (l/l_0) are very close to each other and, hence, the compressibility of all B-O bonds can be considered as uniform. However one should note, that BO_4 tetrahedron remains distorted in whole pressure range. The experimental data were compared with theoretical ones. In spite of the fact that theoretically predicted B-O bonds compressions follow the main tendencies of the experimental ones (see Figure III.8), the bonds compressibility values are rather different and reduce in the following row: B^3-O^1(III) > B^3-O^6(III) > B^3-O^3(III) > B^3-O^2(II)). Thus, according to *ab initio* calculations B^3-O^2(II) bond is the least compressible in BO_4 unit. The decreasing order of B-O(III) compressibilities has been found to be not the same to decreasing order of B-O(III) bond lengths estimated from the calculations (see Table 4). The difference between experimentally determined and theoretically estimated compressibilities of the B-O bonds in β-B_2O_3 is not a surprising, since, as it has been marked above, the theoretical prediction of the compression along *b* and *c* directions differs from experimental observations.

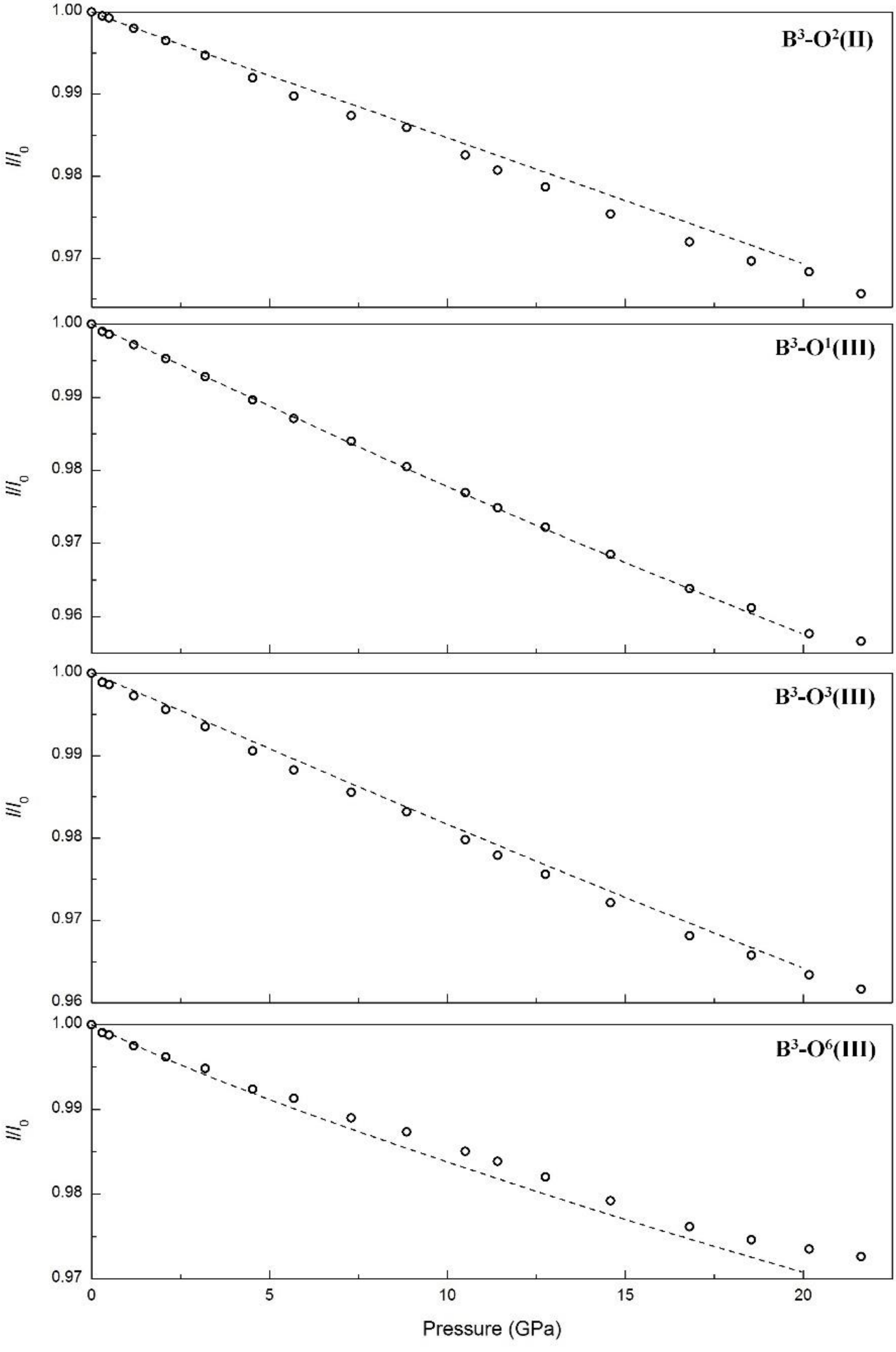

Figure III.8. Normalized changes of B-O distances in BO_4 (l/l_0) *versus* pressure. The open circles indicate experimental data, dashed lines indicate theoretical data.

We also plotted the pressure dependencies of all O-B-O angles in BO$_4$ unit up to 22 GPa (see Figure III.9).

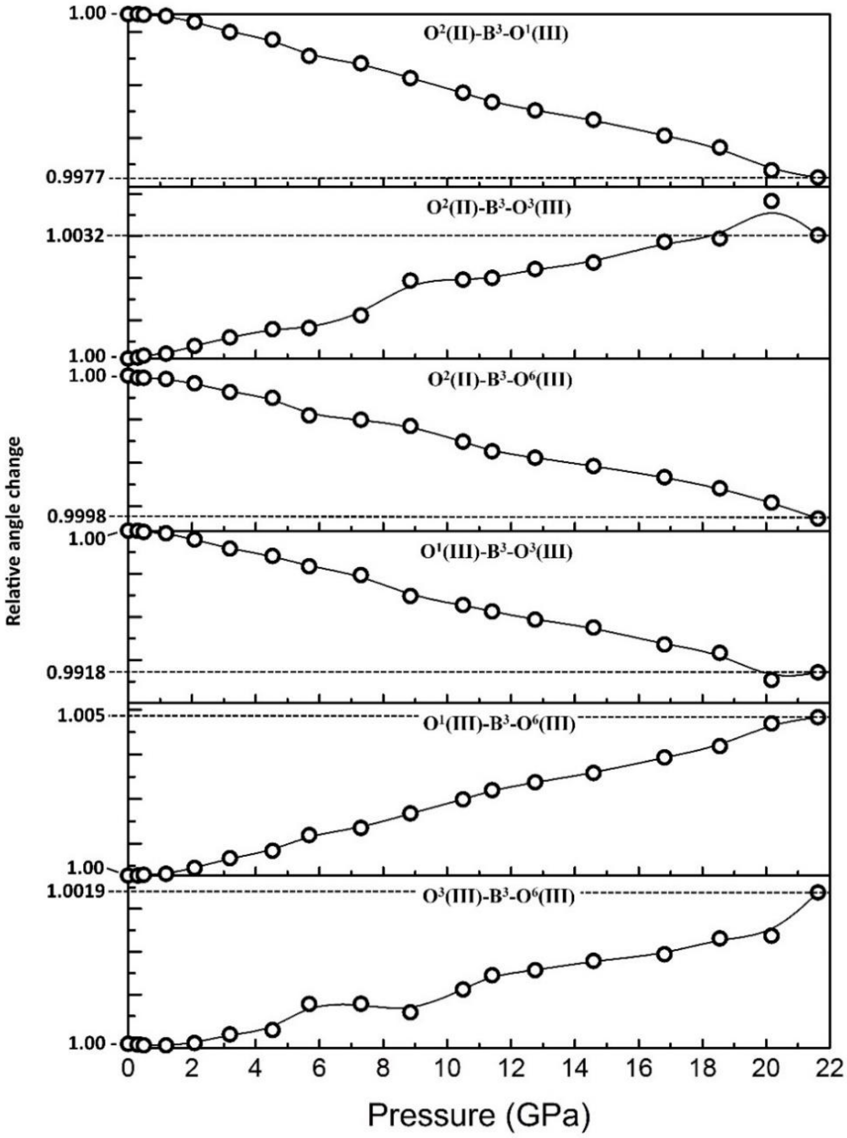

Figure III.9. Relative O-B-O angle changes *versus* pressure.

As one can see from Figure III.9 the O-B-O angles have not changed a lot during compression (the maximum angle change is 0.8% for O^1(III)-B^3-O^3(III)). The smallest angle change of 0.02% has been observed for O^1(II)-B^3-O^6(III). Based on the Figure III.8 and Figure III.9 one can conclude that a B-O bond compressibility influences on the O-B-O angle change. So, the angles between the less compressible B-O bonds reveal the less change under compression. On the contrary, the biggest O-B-O angle changes correspond to the most compressible B-O bonds.

According to the data presented in Figure III.3, 8 and 9 one can conclude that the compression of β-B$_2$O$_3$ is not identical/monotonous. The lattice parameters, B-O distances and O-B-O angles change in a different way. It should be noted, that during compression the structure of β-B$_2$O$_3$ does not become less distorted. This fact will further contribute to the understanding of the β-B$_2$O$_3$ phonons behavior under compression.

9.2 Phonon study of β-B_2O_3

9.2.1 *Experimental techniques*

Synthesis details

The synthesis of polycrystalline β-B_2O_3 has been described in details in a previous section of this chapter. However, in order to investigate an isotope substitution effect in Raman spectra of β-B_2O_3, we synthesized β-B_2O_3 enriched by ^{10}B isotope, by consequent thermal decompression of commercial $^{10}H_3BO_3$ (Aldrich Chem. Co., 99.9%, enrichment by $^{10}B \approx 95\%$) to HBO_2 and then to B_2O_3. As it has been marked above, for convenience, we will mark the boron (III) oxide with natural B isotope distribution (80% ^{11}B and 20% ^{10}B) as β-B_2O_3 and the enriched by ^{10}B isotope as β-$^{10}B_2O_3$. Waterless $^{10}B_2O_3$ melt was obtained during annealing inside graphite heater cup in a closed corundum crucible. β-$^{10}B_2O_3$ was obtained by compressing up to 7.7 GPa at 800°C during 5 min in TTP, followed by a decrease of the temperature down to 400°C during 5 min and subsequent quenching.

XRD measurements

The X-ray diffraction of β-$^{10}B_2O_3$ has been provided with G3000 TEXT Inel diffractometer (Cu Kα1 radiation) at ambient conditions. The sample was found to be highly crystalline with some quantity of impurities (as in case of synthesis of β-B_2O_3, *h*-BN, the sample capsule material). The XRD pattern of β-$^{10}B_2O_3$ is presented in Figure III.10.

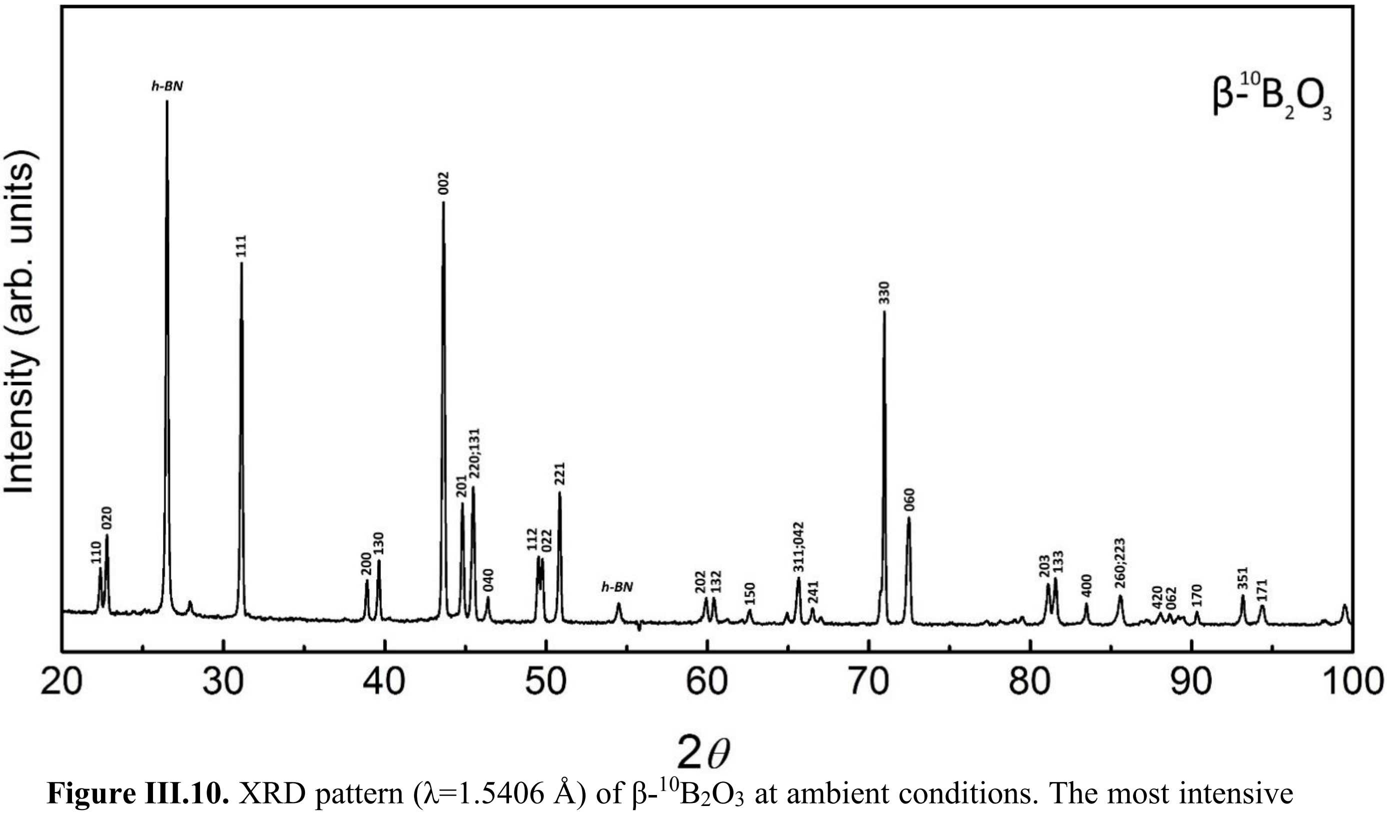

Figure III.10. XRD pattern (λ=1.5406 Å) of β-$^{10}B_2O_3$ at ambient conditions. The most intensive peaks of β-B_2O_3 are marked by the *hkl* Miller indexes; the peaks of *h*-BN are signed.

The lattice parameters and unit cell volume of β-$^{10}B_2O_3$ have been obtained from the structure refinement using Le Bail method (see Table 4). The β-$^{10}B_2O_3$ lattice parameters are rather close to those obtained for β-B_2O_3 in our work and in Ref. 124. Taking this into account we used the interatomic distances found previously [124] and the β-$^{10}B_2O_3$ lattice parameters to find the B-O distances and B-O-B angles. They are listed in Table 4 and compared with those of β-B_2O_3.

Raman and IR measurements at ambient conditions

Raman spectra of β-B_2O_3 and β-$^{10}B_2O_3$ at ambient pressure have been measured using Horiba Jobin Yvon HR800 Raman spectrometer (in the 200-2000 cm^{-1} range). The 632.8 nm line of a He-Ne laser (10 μm beam spot) has been used for excitation (the laser power is less than 30 mW). A single crystal of cubic Si has been used for spectrometer calibration at room temperature. The Raman study of β-$^{10}B_2O_3$ has been performed only at ambient conditions in order to observe the phonons influenced by the isotopic substitution.

The Fourier transform infrared (FTIR) absorption spectra in mid-infrared (450-4000 cm^{-1}) and far-infrared (10-600 cm^{-1}) ranges were recorded using a Bruker IFS 125HR spectrometer. The β-B_2O_3 was uniformly mixed with KBr (for mid-infrared range) and polyethylene (for far-infrared range) powders and pressed in pellets.

High pressure Raman measurements

High-pressure Raman measurements have been performed in a MDAC [222] with 300 μm culets. β-B_2O_3 sample has been placed into a 50 μm hole drilled in a rhenium gasket pre-indented down to 20 μm thickness. In these measurements neon pressure transmitting medium has been used. Pressure in the DAC was determined by the ruby luminescence technique [171] using the calibration proposed in [212]. The pressure has been measured before and after each run and the mean value has been used; drift during single run did not exceed 0.4 GPa in the whole studied pressure range.

The 514.5 nm line of Ar^+ laser (5 μm beam spot) has been used to measure β-B_2O_3 Raman spectra. Raman spectra have been recorded in the 200-2000 cm^{-1} range using Horiba Jobin Yvon HR460 Raman spectrometer. The spectrometer was calibrated using a single crystal of cubic Si at room temperature. The laser power at the sample was estimated to be less than 10 mW. No effect due to laser heating of the sample has been observed. Raman spectra of β-B_2O_3 have been measured within 19 pressure points from 0.25 to 46.4 GPa at room temperature.

Calculation details

The β-B_2O_3 phonon properties at ambient pressure and under compression (up to 20 GPa) have been studied using first principles LCAO calculations performed using the CRYSTAL09 code [207]. The phonon frequencies for β-B_2O_3 containing 100% ^{10}B (β-$^{10}B_2O_3$*) and 100% ^{11}B (β-$^{11}B_2O_3$*) have been calculated using the direct (frozen-phonon) method [207,223]. For the phonon modes calculations under compression we employed already performed calculations of β-B_2O_3 equation of state. The phonon frequencies at selected pressure points up to 21 GPa have been calculated using optimized geometries for corresponding reduced volume unit cells. As it has been already noted above, all the pressure dependencies of the phonon frequencies of β-$^{11}B_2O_3$* are available only up to 21 GPa, because of divergence of the parameters of electron structure optimization at highly reduced unit cell volume (P > 22 GPa).

9.2.2 Results and discussion

A careful analysis of structural data presented in Table 4 has revealed that the isotope substitution content affects the bond nature (and therefore the interatomic angles). In our study we observed, that *a*, *b* and *c* lattice parameters of β-$^{10}B_2O_3$ are larger than those of β-B_2O_3 on 0.32, 0.26 and 0.36% respectively (the deviations of *a*, *b* and *c* of β-$^{10}B_2O_3$ and β-B_2O_3 are larger than the error bars of the corresponding lattice parameters of β-$^{10}B_2O_3$ and β-B_2O_3). The B-O-B angles in BO_4 tetrahedron in β-$^{10}B_2O_3$ differ as well. Actually the same effect isotope substitution in H_2O/D_2O was observed by *A.K. Soper et al.* [224]. However, it should be marked that according to our *ab initio* calculations there is no difference between structure optimization procedures and therefore for the obtained lattice parameters and interatomic distances of β-$^{10}B_2O_3$* and β-$^{11}B_2O_3$*.

β-B_2O_3 has 10 atoms in the unit cell, thus, 30 normal modes of vibration at the Brillouin zone center. They are described by the irreducible representation of the C_{2v} point group:

$$\Gamma = 8\mathrm{A}_1 + 7\mathrm{A}_2 + 7\mathrm{B}_1 + 8\mathrm{B}_2 \qquad (III.6)$$

Three modes among 30 are acoustic: $A_1 + B_1 + B_2$. The 20 optical modes $7A_1 + 6B_1 + 7B_2$ are both IR and Raman active, whereas $7A_2$ are only Raman active, thus one can expect the 27 non-degenerate Raman active modes in Raman spectrum.

Raman spectrum of β-B_2O_3 at ambient conditions has been measured previously [225]. However only the phonon frequencies of the observed Raman bands has been described. In current work we provided more detailed and complete investigation of β-B_2O_3 Raman spectrum at ambient conditions. Raman spectrum was investigated in the 100-2500 cm^{-1} frequency range, however all bands were observed in 200-1200 cm^{-1} range. For β-B_2O_3 only 12 bands were observed, whereas the Raman spectrum of β-$^{10}B_2O_3$ contains 6 (repeating the bands of β-B_2O_3) (Figure III.11). The frequencies of all phonon modes for β-B_2O_3 and β-$^{10}B_2O_3$ are collected in Table 5. According to relative intensity, the Raman bands can be divided on three main groups: strong, medium and weak (are marked as superscripts to the wavenumbers).

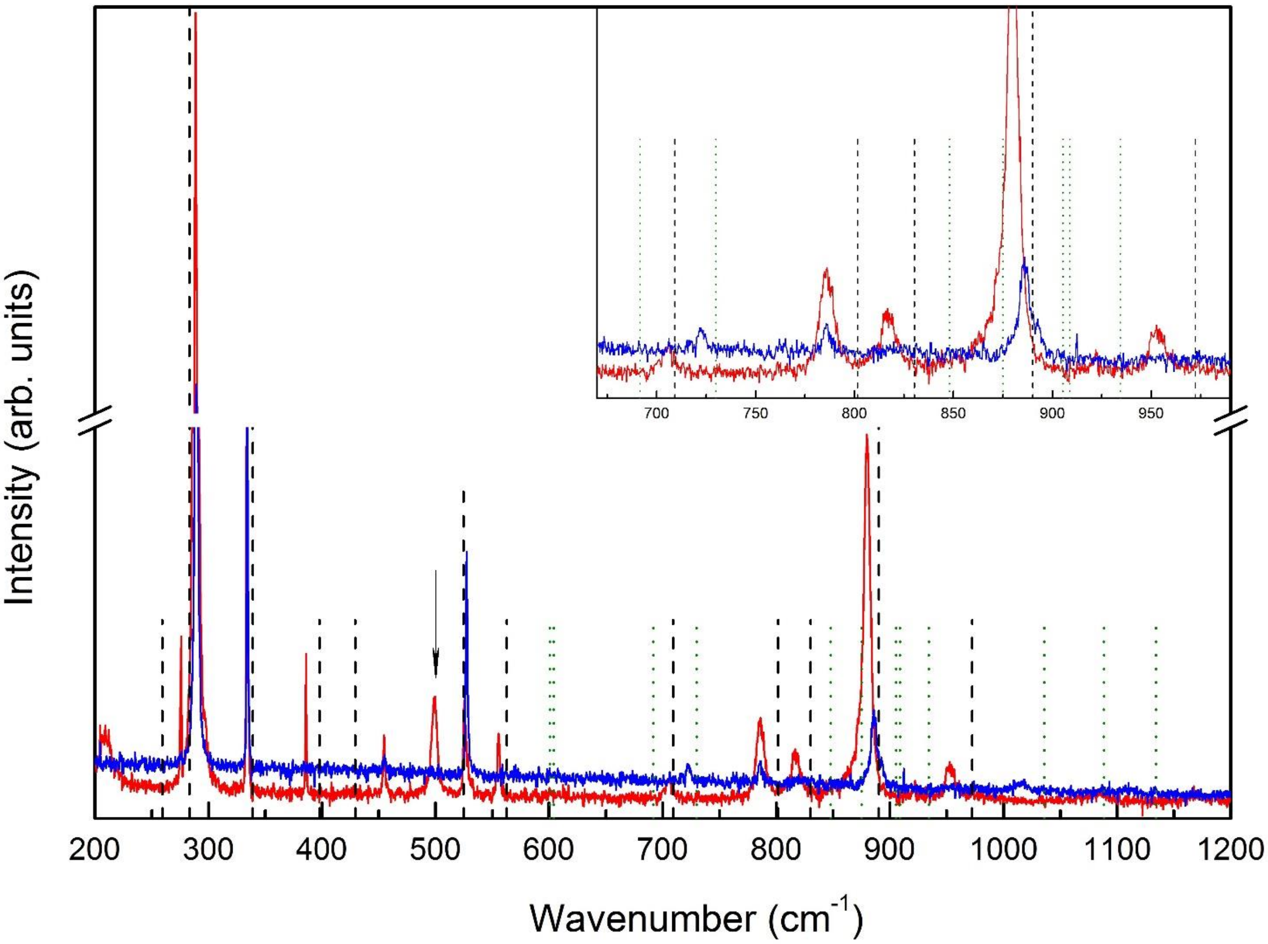

Figure III.11. Experimentally observed Raman bands in β-B_2O_3 (red) and β-$^{10}B_2O_3$ (blue) at ambient conditions. The positions of the phonons predicted by LCAO calculations are marked by the lines: the black dashed lines correspond to the phonons observed in the measurements, the green dot lines correspond to the non-experimentally observed phonons. Inset: magnification of the 670-990 cm^{-1} region. The arrow indicates the Raman peak presumably concerning to the metal borate contamination.

It is well known, that the atomic oscillations can be described with harmonic and anharmonic oscillator models. At the consideration of the simplest model of the harmonic oscillator for two-atomic molecule (m_1, m_2 are atoms masses), in which atoms are connected by the no weight elastic spring with the force constant K, one can obtain the following expression for frequency:

$$\omega = \frac{1}{2\pi}\sqrt{K\frac{m_1 m_2}{m_1 + m_2}} \qquad (III.7),$$

where ω is frequency. One can see from the (Eq. *III*.7), that the resonant frequency is related to the strength of the bond and the mass of the atoms at either end of it. Consequently, the isotope substitution influences on the ω value. As far as the ^{10}B isotope is lighter than ^{11}B, the isotope substitution in β-B_2O_3 must lead to Raman bands shift toward high frequencies.

One can easily observe such isotope shift in Figure III.11. We evaluated it using the following expression:

$$\Delta\omega = \omega\,(\beta\text{-}^{10}B_2O_3) - \omega\,(\beta\text{-}B_2O_3) \qquad (III.8).$$

The isotope shifts vary in 0.3-15.8 cm^{-1} range (Table 6). The theoretically predicted isotope shifts vary in 0.1-4.6 cm^{-1} range (Table 6). As one can see the order of magnitude of the experimentally observed and the theoretically predicted isotope shifts is the same. However, the quality of the theoretical prediction still remains not perfect. Taking into account that there are less observed bands and they have low signal-to-noise ratio in β-$^{10}B_2O_3$ Raman spectrum, in the discussion below we will basically consider the Raman spectra of β-B_2O_3, keeping in mind that all conclusions will be true for β-$^{10}B_2O_3$ too. For more convenience we will number all the observed Raman bands: #1, #2, #3, etc.

№	Modes	Wavenumber (cm^{-1})						
		Experiment				LCAO		
		ω_0 (β-B_2O_3) [225]	ω_0 (β-B_2O_3)	ω_0 (β-$^{10}B_2O_3$)	$\Delta\omega$	ω_t (β-$^{11}B_2O_3$*)	ω_t (β-$^{10}B_2O_3$*)	$\Delta\omega$
(#1)	A_1	-	275.9^{m}	-	-	259.4	259.6	0.2
(#2)	B_1	288	288.6^{s}	289.3^{s}	0.7	283.2	283.3	0.1
(#3)	A_1	333	333.5^{m}	334.1^{s}	0.6	338.9	339.3	0.4
(#4)	A_2	385	385.7^{m}	-	-	397.8	398.9	1.1
(#5)	B_1	454	454.6^{w}	-	-	429.4	429.5	0.1
(#6)	A_1	525	525.3^{m}	527.5^{s}	2.2	524.7	525.6	0.9
(#7)	A_2	557	555.7^{w}	-	-	562.8	565.2	2.4
(#8)	A_1	704	706.2^{w}	722.0^{w}	15.8	709.2	713.8	4.6
(#9)	A_1	784	786.0^{m}	786.3^{w}	0.3	801.5	803.7	2.2
(#10)	B_2	817	816.7^{w}	-	-	830.3	833.9	3.6
(#11)	A_2	879	879.5^{s}	885.9^{m}	6.4	890.1	894.4	4.3
(#12)	B_1	952	952.7^{w}	-	-	934.4	935.9	1.5

Table 6. The phonon frequencies of β-B_2O_3 and β-$^{10}B_2O_3$ (ω_0) experimentally observed by Raman spectroscopy in current study and in [225] and β-$^{11}B_2O_3$* and β-$^{10}B_2O_3$* phonon frequencies (ω_t) theoretically predicted by LCAO calculations. The superscripts to the experimental wavenumbers (^{w}, ^{m}, ^{s}) indicate the relative intensity of the Raman bands. Isotope shifts of observed Raman bands are presented.

IR spectra of β-B_2O_3 (Figure III.12) have been also observed for a first time. They were recorded in the 10-600 cm^{-1} and 450-4000 cm^{-1} frequency ranges and contain a vast quantity of bands and shoulders. The most intense bands in the 1300-4000 cm^{-1} range can be explained by the presence of organic impurities (two bands at ~2850 cm^{-1} and ~2920 cm^{-1} referring to C-H stretching oscillations) and adsorbed water (broad band and shoulder at ~3210 cm^{-1} and ~3380 cm^{-1}). On the basis of LCAO theoretical prediction we referred 6 bands (or shoulders) in far-infrared region and 10 bands in mid infrared region to β-B_2O_3 (see Table 7). As well as in case of Raman bands, we marked the observed IR bands by the numbers: #1, #2, #3, etc.

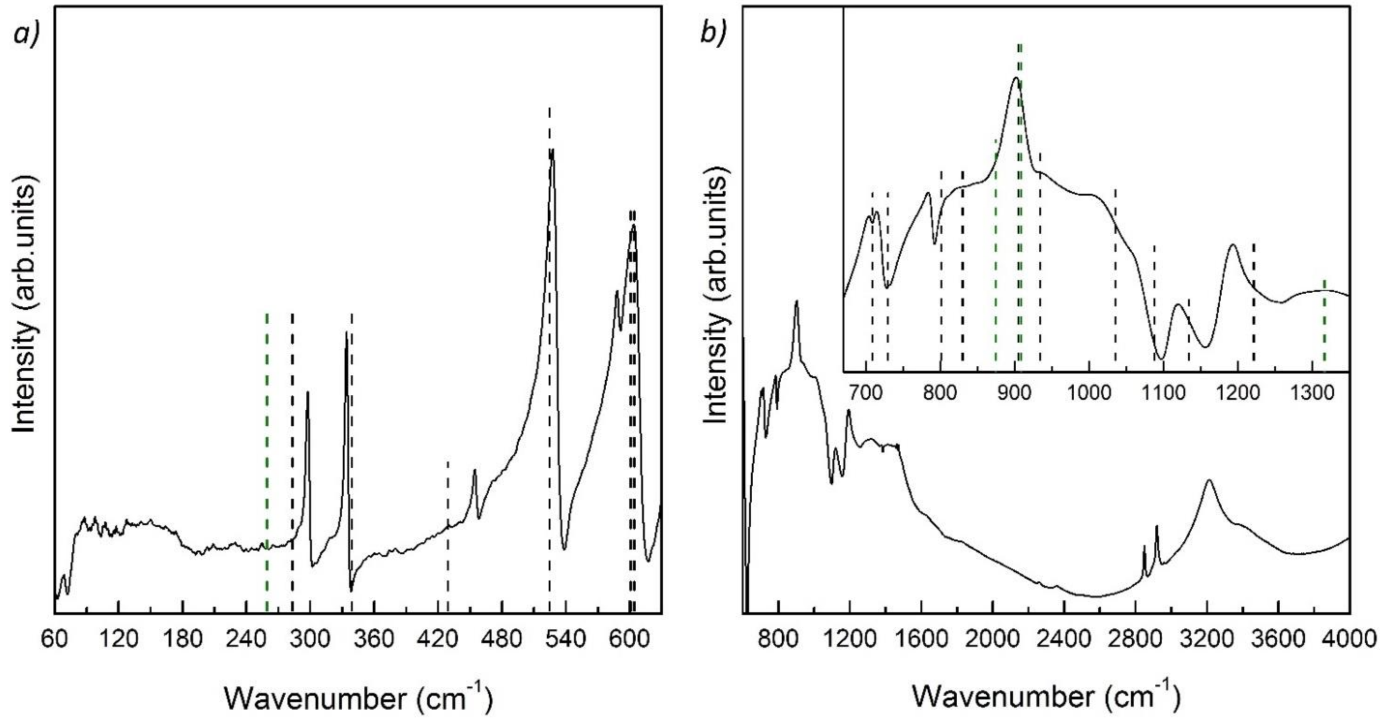

Figure III.12. Experimentally observed phonons of β-B_2O_3 in: *a*) far-infrared and *b*) mid-infrared regions (inset: magnification of the 640-1350 cm^{-1} region) at ambient conditions. The positions of the phonons predicted by LCAO calculations are marked by the lines: the black dashed lines correspond to the phonons observed in the measurements, the green dashed lines correspond to the non-experimentally observed phonons.

№	Modes	Wavenumber (cm^{-1})		№	Modes	Wavenumber (cm^{-1})	
		Experiment	LCAO			Experiment	LCAO
		ω_0 (β-B_2O_3)	ω_t (β-$^{11}B_2O_3$*)			ω_0 (β-B_2O_3)	ω_t (β-$^{11}B_2O_3$*)
(#1)	B_1	297.6	283.2	(#9)	A_1	783.9	801.5
(#2)	A_1	333.9	338.9	(#10)	B_2	819.9	830.3
(#3)	B_1	454.5	429.4	(#11)	A_1	901.9	905.4
(#4)	A_1	527.4	524.7	(#12)	B_1	939.2	934.4
(#5)	B_1	588.2	600.7	(#13)	B_2	1017.6	1035.9
(#6)	B_2	603.9	604.2	(#14)	B_1	1059.1	1088.4
(#7)	A_1	704.2	709.2	(#15)	B_1	1119.5	1134.4
(#8)	B_2	714.8	729.9	(#16)	A_1	1193.7	1221.7

Table 7. The phonon frequencies of β-B_2O_3 experimentally (ω_0) observed by IR spectroscopy and theoretically predicted (ω_t) by LCAO calculations.

The assignment of the experimentally observed phonon modes has been performed basing on LCAO calculations for β-B_2O_3. The calculated phonon frequencies of β-B_2O_3 have been found to be in good agreement with the experimentally observed bands positions (Table 6,7). The deviation of calculated Raman and IR modes from experimentally observed ones did not exceed 6% and 5% respectively. As one can see from Table 6 the Raman band at ~499 cm^{-1} (marked by the arrow in Figure III.11) cannot be attributed to B_2O_3 high pressure form. However, according to the literature review of the Raman studies on different metals borates, this Raman mode is a ”typical” band for metal borates [226-235].

The results obtained from LCAO *ab initio* calculations have been further used for computer modeling and visualization of the vibrational modes by means of MolDraw software. Thus it became possible to link the Raman and IR bands to the oscillations/vibrations in β-B_2O_3 structure fragment presented in Figure III.7. One should note that the superscript index defines an atom number, whereas the number in brackets defines a coordination of oxygen atoms: two- (II) or three-coordinated (III). The Tables 8 and 9 present the description of the oscillations assigned to the all phonon modes observed in Raman and IR spectra respectively. We used the following abbreviations: oscillation – osc., stretching – str., scissoring – sci., torsion – tor., wagging – wag., rocking – roc., twisting – twi., parasol – par. So, for example the “in phase scissoring oscillation” will be marked as “in phase sci. osc.”.

№	Modes	Wavenumbers, cm^{-1}	Assignment
(#1)	A_1	275.9	in phase B-O(II)-B sci. osc.
(#2)	B_1	288.6	in phase tetrahedra tor. osc.
(#3)	A_1	333.5	in phase B^1-O^1(III)-B^3, B^2-O^2(III)-B^4 sci. osc. and out of phase O(II) wag. osc.
(#4)	A_2	385.7	in phase O^1(III)-O^2(III) and O^5(III)-O^6(III) wag. osc.
(#5)	B_1	454.6	out of phase B-O(II)-B sci. osc.
(#6)	A_1	525.3	in phase O^1(II)-B^1-O^1(III), O^1(II)-B^2-O^2(III) and O(II) sci./wag. osc.
(#7)	A_2	555.7	out of phase O^1(III)-B^1-O^1(II)-B^2-O^2(III) and O^6(III)-B^3-O^2(II)-B^4-O^5(III) sci./wag./str. osc.
(#8)	A_1	706.2	in phase B^3O^1(III)O^2(II)O^6(III) and B^4O^2(III)O^2(II)O^5(III) par. osc.
(#9)	A_1	786.0	in phase B^3-O^1(III) and B^4-O^2(III) str. osc.
(#10)	B_2	816.7	out of phase B^3-O^1(III) and B^4-O^2(III) str. osc.
(#11)	A_2	879.5	out of phase O^6(III)-B^3-O^1(III)-B^1 and O^5(III)-B^4-O^2(III)-B^2 str. osc.
(#12)	A_2	952.7	out of phase B^1-O^1(III)-B^3, B^2-O^2(III)-B^4 and B^3-O^6(III), B^4-O^5(III) str. osc.

Table 8. An assignment of the phonon modes observed in β-B_2O_3 Raman spectrum at ambient conditions.

№	Modes	Wavenumbers, cm^{-1}	Assignment
(#1)	B_1	297.6	in phase tetrahedra tor. osc.
(#2)	A_1	333.9	in phase B^1-O^1(III)-B^3, B^2-O^2(III)-B^4 sci. osc. and out of phase O(II) wag. osc.
(#3)	B_1	454.5	out of phase B-O(II)-B sci. osc.
(#4)	A_1	527.4	in phase O^1(II)-B^1-O^1(III), O^1(II)-B^2-O^2(III) sci. osc. and O(II) wag. osc.
(#5)	B_1	588.2	in phase O^2(II)-B^3-O^1(III) and O^2(II)-B^4-O^2(III) sci. osc.
(#6)	B_2	603.9	in phase O^1(III)-B^1-O^1(II)-B^2-O^2(III) and O^6(III)-B^3-O^2(II)-B^4-O^5(III) roc./str. osc.
(#7)	A_1	704.2	in phase B^3O^1(III)O^2(II)O^6(III) and B^4O^2(III)O^2(II)O^5(III) par. osc.
(#8)	B_2	714.82	in phase O^1(III), O^2(III),O^5(III), O^6(III) wag. osc.
(#9)	A_1	783.92	in phase B^3-O^1(III) and B^4-O^2(III) str. osc.
(#10)	B_2	819.9	out of phase B^3-O^1(III) and B^4-O^2(III) str. osc.
(#11)	A_1	901.9	in phase B^1-O^1(III), B^2-O^2(III), B^3-O^6(III), B^4-O^5(III) str. osc.
(#12)	B_1	939.2	in phase O^1(III)-B^3-O^6(III), O^2(III)-B^4-O^5(III) sci. osc. and B^1-O^1(III), B^2-O^2(III) str. osc.
(#13)	B_2	1017.6	out of phase B^3O^1(III)O^2(II)O^6(III) & B^4O^2(III)O^2(II)O^5(III) par. osc.
(#14)	B_1	1059.1	out of phase B^1-O^1(III)-B^3, B^2-O^2(III)-B^4 sci. osc.
(#15)	B_1	1119.5	out of phase B-O(II)-B str. osc.
(#16)	A_1	1193.7	in phase B-O(II)-B and B^1-O^1(III)-B^3-O^6(III), B^2-O^2(III)-B^4-O^5(III) str. osc.

Table 9. An assignment of the phonon modes observed in β-B_2O_3 IR spectra at ambient conditions.

First, it should be underlined that an assignment of the phonon modes to the concrete type of vibrations is rather nominal due to the complicated structure of β-B_2O_3 part presented in Figure III.7. We distinguished the most pronounced vibrations. For instance, the mode referred to scissoring vibrations may have a little contribution of stretching oscillation, but in the Tables 8 and 9 it will be referred only to scissoring oscillation. As it has been expected, there are almost no separate oscillations of B-O bonds. Due to the fact that boron and oxygen atoms in β-B_2O_3 are linked by strong ionic-covalent bonds, almost every phonon is referred to a vibration of structural part or to the group of structural parts, for instance: BO_3, BO_4, B-O-B, B-O-B-O, B-O-B-O-B, etc. The same observations have been done in Raman studies of some metal borates [228-231].

According to (Eq. *III*.7) the phonon mode frequencies (ω) depends on the force of the interatomic interaction (in terms of (Eq. *III*.7) on K values). The stronger interatomic interaction result in bigger ω values. On other hand the stronger interatomic forces usually correspond to the shorter interatomic distances. In case of β-B_2O_3 one might expect, that the vibrations of the structural parts containing the shortest B-O(II) bond will correspond to the higher frequencies, than those without B-O(II). However, in Table 8 and 9 there are a lot of phonon modes in the low frequency range, which can be attributed to the vibrations containing B-O(II) oscillation, for example: A_1 (~275 cm^{-1}), B_1 (~455 cm^{-1}), A_1 (~525 cm^{-1}), A_2 (~555 cm^{-1}), etc. Thus, one can conclude that presence of B-O(II) in structural part does not influence dramatically on the oscillation frequency.

The distribution of the vibration types should be also noticed. The majority of stretching oscillations have been expectedly turned out to be in the high frequency range. This phenomenon can be easily explained, considering the influence of the bond length on Raman shift given above. During the stretching vibration the oscillations happen along the bonds and two atoms come near each other. The bond length changes, which in its turn results in the higher phonon frequency values. At scissoring vibrations the interatomic distances do not change as much as at stretching ones, so majority of corresponding Raman bands are placed in low frequency range. Unlike scissoring oscillations, the parasol vibrations can be referred to the simultaneous movements of the bigger number of atoms in one direction, leading to the comparatively higher phonon frequencies.

One can note, that there is also a slight difference between in phase and out of phase oscillations. For example, the modes referring to in phase vibrations are tending to be in low frequency range, whereas the ones concerning out of phase vibrations are in high frequency range (e.g. the parasol oscillations of $B^3O^1(III)O^2(II)O^6(III)$ see Table 7). One of the possible reasons of such “symmetry division” of the phonon modes may be that the non-symmetric vibrations lead to the greater structure distortion, which, therefore, results in the higher frequency values.

The pressure dependence of the vibrational modes has been measured in β-B_2O_3 up to 46 GPa. Some of the observed Raman spectra are presented in Figure III.13.

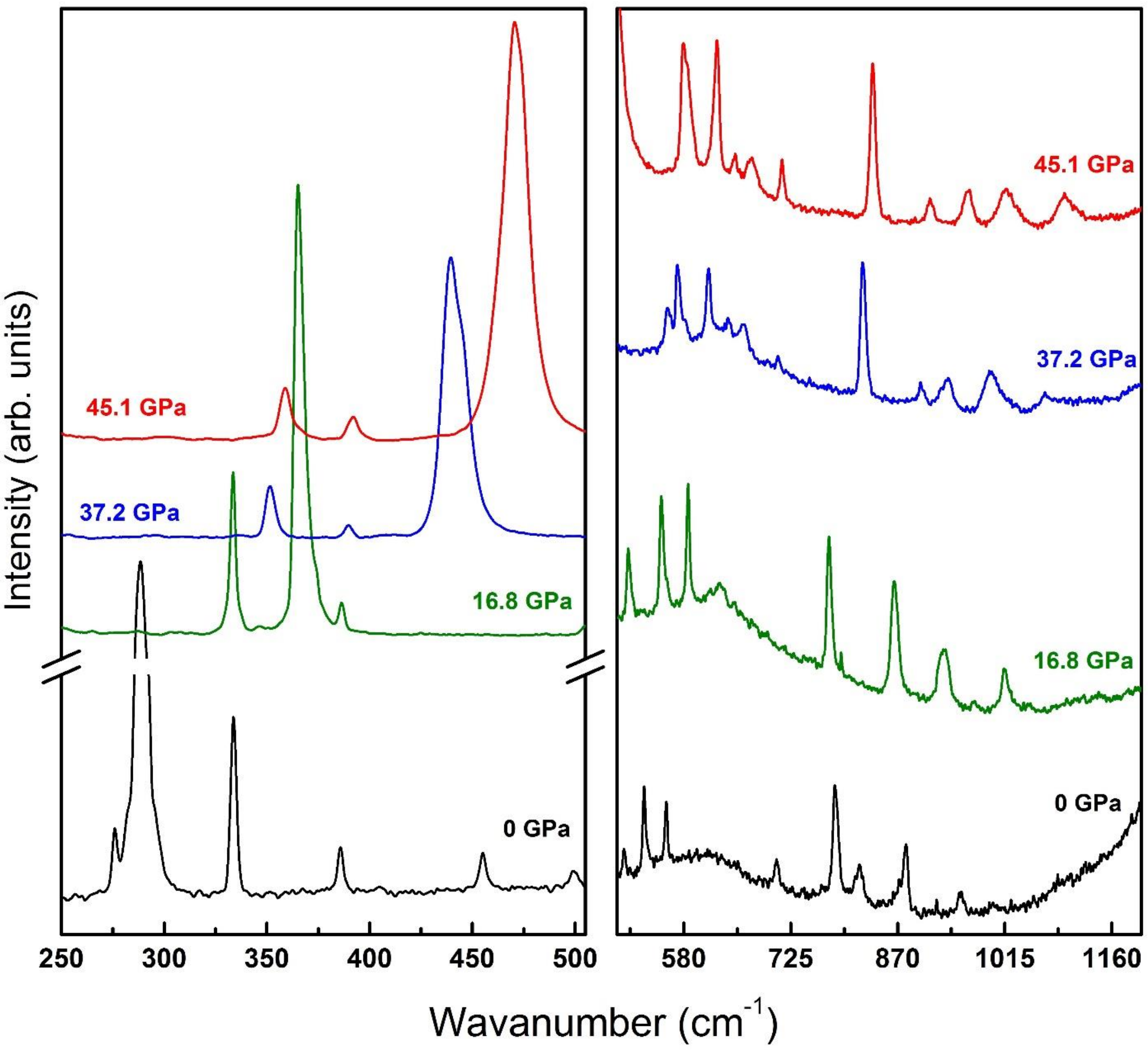

Figure III.13. Raman spectra of β-B_2O_3 at different pressures and room temperature.

During compression all Raman bands expectedly shifted toward higher frequencies and revealed rather strong phonon shift (Figure III.14). For more convenience we also numbered all observed Raman bands. However, it should be noted that numbering herein differs from that in Table 8 due to three bands which appeared at higher pressures.

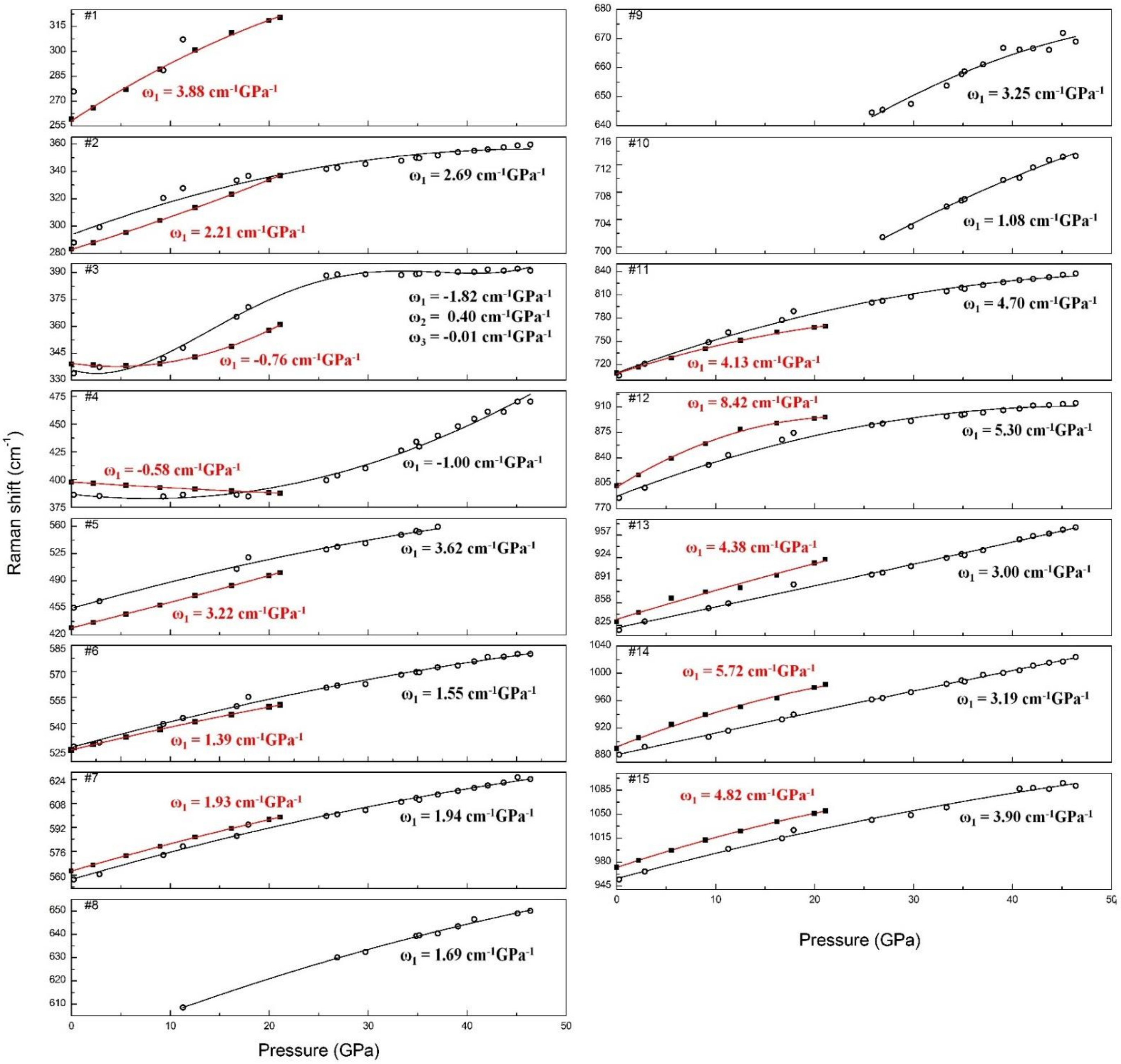

Figure III.14. Pressure dependencies of the phonon mode frequencies experimentally observed (open circles) and theoretically calculated (solid squares). The lines are quadratic least squares fits ($R^2 > 0.95$) to the experimental data (black) and to the theoretical data (red); the ω_1 parameters of (Eq. *III.*9) are listed.

Three new bands appeared during compression: (#8) 608.6 cm^{-1} at 11.3 GPa, (#9) 644.6 at 25.8 GPa and (#10) 701.4 cm^{-1} at 26.9 GPa. It should be also noted, that Raman band related to the metal borate contamination of β-B_2O_3 was observable only up to 11.3 GPa. Moreover, (#1) and (#5) Raman bands of β-B_2O_3 observed at 275.9 cm^{-1} and 455.1 cm^{-1} in spectrum at ambient conditions disappeared during compression at 11.3 GPa and 37.0 GPa respectively. We exclude the possibility of any phase transition, as according to the previous reports on phase stability of the high-pressure form of B_2O_3: there has not been observed any phase transition in 0-42 GPa pressure range at room temperature [111,115,236]. Taking into account the modes assignment made on the basis of LCAO calculations, all the new peaks appeared during compression can be attributed to the β-B_2O_3 phase. So (#8), (#9) and (#10) might be assigned to B_1, B_2 and A_2 respectively. It should be also noted, that these phonon modes have not been observed before [225]. We assume, that the possible reason of the appearance of the new modes might be the change of orientation of the micro-monocrystals of B_2O_3 polycrystalline sample due to non-hydrostatic compression and the pressure gradients in the DAC. However, we should note that the assignment of (#8), (#9) and (#10) to the phonon modes is suppositional and in order support it an additional high-pressure *in situ* phonon measurement of the β-B_2O_3 monocrystal is needed.

One of the important characteristics of the solid materials is the Grüneisen parameter. This parameter describes the effect that changing the volume of the crystal lattice has on its vibrational properties, and, as consequence, the effect that changing temperature has on the size of or dynamics of the lattice. As one can see from the definition given above, the Grüneisen parameter can be found from *in situ* HP measurements of vibrational properties, and, hence, from *in situ* HP Raman measurements.

In order to calculate the Grüneisen parameters of observed Raman modes the fitting of Raman modes pressure dependencies by the same equation as in [237] has been performed:

$$\omega = \omega_0 \cdot \left(1 + P \cdot \frac{\delta_0}{\delta'}\right)^{\delta'}, \text{ where } \delta_0 = \left(\frac{d\, ln\omega}{dP}\right)_{P=0} \text{ and } \delta' = \delta_0^2 \left(\frac{d^2\, ln\omega}{d\,P^2}\right)_{P=0} \qquad (III.9).$$

A least-squares fit of (Eq. *III*.9) to the experimental data yields the values of first-order parameters (δ_0) for all 12 observed Raman modes. We defined the Grüneisen parameters $\gamma_G = B_0 \times \delta_0$ for the bulk modulus value (B_0 = 165.4 GPa) obtained from *in situ* HP XRD measurements described in previous part. All γ_G values are collected in Table 10.

№	ω_1, $cm^{-1}GPa^{-1}$		γ_G	№	ω_1, $cm^{-1}GPa^{-1}$		γ_G
	Experimental	LCAO			Experimental	LCAO	
(#1)	-	3.88	-	(#9)	3.25	-	-
(#2)	2.69	2.21	3.887	(#10)	1.08	-	-
(#3)	-1.82	-0.76	1.392	(#11)	4.70	4.13	1.628
(#4)	-1.00	-0.58	0.577	(#12)	5.30	8.42	1.813
(#5)	3.62	3.22	1.388	(#13)	3.00	4.38	0.656
(#6)	1.55	1.39	0.504	(#14)	3.19	5.72	0.599
(#7)	1.94	1.93	0.618	(#15)	3.90	4.82	0.742
(#8)	1.69	-	-				

Table 10. The Grüneisen parameters (γ_G) and ω_1 values determined for theoretical and experimental data presented in Figure III.14.

It should be underlined that as the modes (#8), (#9) and (#10) have not been observed at ambient pressure (and thus their frequencies are unknown), it is impossible to know their ω_0 values and hence to determine their Grüneisen parameters.

As one can see from Figure III.14, a majority of *ab initio* calculated phonon frequencies under compression are close to experimentally obtained data. In order to express the extension of the phonons shifts toward high frequency range, the quadratic equation has been employed for fitting of experimental and theoretical data (Figure III.14):

$$\omega = \omega_0 + \omega_1 \cdot P + \omega_2 \cdot P^2 \qquad (III.10).$$

The parameters ω_1 used in (Eq. *III*.10) are listed in Table 9. It should be noted that the pressure dependency of (#3) Raman mode could be satisfactorily fitted only by the polynomial of the 4th order. The ω_1, ω_2 and ω_3 are presented in Figure III.14, meanwhile the ω_4 parameter has not been listed because of its negligible value ($<10^{-4}$). The big variation of the ω_1 values might be explained by the fact that compression of the distorted BO_4 tetrahedron (the building block of β-B_2O_3) undergoes not uniformly. It should be also underlined that the ω_1 values well correlate with the extent of bonds shrinking under compression: the higher ω_1 values are observed at larger bonds compression.

A careful analysis of data presented in Table 8 and 10 permitted us to make some general notes. Looking on Table 8 one can roughly divided it onto two parts: the top part containing the phonon modes concerning the angular oscillations (scissoring and parasol) and the bottom part with the stretching oscillations (along the B-O bond). The out of phase scissoring oscillation (#5) has been found to be rather more pressure dependent (higher ω_1 value), than in phase scissoring vibrations. However, the in phase stretching vibration (#12) (ω_1 value is 5.30 $cm^{-1}GPa^{-1}$) is much more pressure dependent than out of phase stretching vibration (#13) (ω_1 value is 3.00 $cm^{-1}GPa^{-1}$). It should be noted, that (#12) and (#13) modes are related to the stretching vibration of the same structural fragment, B^3-O^1(III). This observation clearly demonstrates that in phase and out of phase oscillations of the same structure parts depend on compression differently.

There are also two unexpected phonon mode pressure dependencies in Figure III.14: (#3) and (#4). The (#3) curve has two bends and the phonon mode does not significantly depend on pressure in 0-5 and 25-46 GPa pressure ranges. According to modes assignment this mode is referred to angular oscillations of 8-membered ring (see Figure III.7). There is no explanation yet for so strange mode behavior under compression. The (#4) mode completely differs from other modes. In 0-15 GPa pressure range its Raman band slightly moves towards low frequencies. The LCAO *ab initio* calculations predict the same mode behavior in this pressure range. However, after

15 GPa the Raman band reveals a constant positive Raman shift. As well as in case of (#3) mode, we cannot yet explain the phenomenon observed for (#4) mode.

Figure III.14 presents a nice coincidence of the slopes and the shapes of the frequency *versus* pressure curves for theoretical and experimental datasets. Nonetheless, the theoretical and experimental ω_1 values of last four high frequency phonon modes (#12,#13,#14,#15) significantly differ. Taking this into account, for the further consideration of the frequency pressure dependences only the experimentally determined ω_1 values will be employed.

Using of data of B-O bonds and O-B-O angles changes under compression presented in Figure III.8 and 9, the behavior of some phonon modes under high pressure (and therefore explanation of ω_1 values) can be explained. We will use a simple assumption model of harmonic oscillator. According to this model we can assume that the greater B-O distance and O-B-O angle changes during compression lead to the higher ω_1 values. We also supposed that complicated oscillation of the huge structure fragment can be considered in first approximation as a combination of the more simple vibrations, corresponding to the smaller structure parts.

According to Table 8, the (#7) mode is referred to the out of phase O^6(III)-B^3-O^2(II)-B^4-O^5(III) vibration. As one can note it contains O^6(III)-B^3-O^2(II) fragment. As it is known from Figure III.8, the B^3-O^2(II) and B^3-O^6(III) bonds are the most resistant to compression, leading to the low ω_1 values. Due to the O^6(III)-B^3-O^2(II) fragment is rather huge, it significantly influences on the vibration of the whole structural part. We suppose that it can be the main reason of low ω_1 value of (#7) mode, 1.94 $cm^{-1}GPa^{-1}$.

Unlike the mode (#7), the modes (#12), (#13) and (#14) have the bigger ω_1 values. All of these modes are attributed to the oscillations containing the B^3-O^1(III) vibration. As it follows from Figure III.8, the B^3-O^1(III) is the most pressure dependent bond, that is why the large ω_1 values for (#12), (#13) and (#14) are rather expected. However, the ω_1 value of mode (#12) is significantly bigger than those of (#13) and (#14). It mostly happens due to the oscillation corresponding to (#12) mode does not have a contribution of B^3-O^6(III) vibration, whereas the modes (#13) and (#14) do.

The mode (#15) referring to the stretching oscillations of B^3-O^6(III) and B^1-O^1(III)-B^3 structural parts, has ω_1 value of 3.90 $cm^{-1}GPa^{-1}$. Herein we assume, that rather big ω_1 value is a result of two contributions: a positive one coming from the “easy compressible” B^3-O^1(III) fragment, and a negative one coming from “resistant” B^3-O^6(III) fragment.

According to Table 8, the mode (#11) can be assigned to the parasol oscillation of B^3O^1(III)O^2(II)O^6(III) part. Assuming that O^3(III) atom does not move, one may divide the “parasol” oscillation of B^3O^1(III)O^2(II)O^6(III) part on three scissoring oscillations: O^2(II)-B^3-O^3(III), O^1(III)-B^3-O^3(III) and O^6(III)-B^3-O^3(III). As one can see from Figure III.9, all of these three O-B-O angles are highly pressure dependent, which leads to the high ω_1 value (4.70 $cm^{-1}GPa^{-1}$).

9.3 Conclusions

As it has been underlined in the introduction of this chapter, an investigation of binary compounds of B-O system is very difficult because of low Z numbers of boron and oxygen, necessity of high brilliance X-ray sources, modern analytical equipment of high precision, etc. The high pressure phase of B_2O_3 has been chosen as subject of our investigations due to its outstanding mechanical properties (first of all, the hardness) and poor information about other properties. In this chapter we measured the equation of state of β-B_2O_3 in the pressure range from 0 to 22 GPa and studied the phonon modes at ambient and under high pressures (up to 46 GPa).

Thanks to our studies on equation of state we obtained a new bulk modulus (B_0) and its first pressure derivative (B_0`) values, which slightly differed from ones reported before [111]. The advantage of our EOS measurements towards those done in Ref. 111 consists in the following: in our work we provided the direct XRD measurements of powder of β-B_2O_3, meanwhile in Ref. 111 the HP phase of boron (III) oxide was obtained during HP-HT reaction and EOS was measured during DAC decompression. It should be emphasized that according to the obtained χ^2 parameter our measurements have been found to be significantly more precise than in Ref. 111. The B_0 and B_0` values estimated by means of *ab initio* LCAO calculations are rather close to the experimental values (the bulk modulus deviation < 3%). Despite a slight deviation between bulk modulus and its first pressure derivative values obtained in our work and in Ref. 111, the experimental datasets of our study and of [111] are rather close. By using of these two datasets as the whole one, we calculated the bulk modulus value of β-B_2O_3 in 0-42 GPa pressure range. Also, the pressure dependencies of the lattice parameters have been plotted and discussed.

In order to get the pressure dependencies of the B-O interatomic distances and O-B-O angles in β-B_2O_3 the following hypothesis has been applied: we assumed that the atoms do not change dramatically their positions during the unit cell compression. Thus, in order to describe the changes of the interatomic distances and angles, the atoms positions of B and O can be considered to be fixed (herein we used the atoms positions at ambient conditions refined in Ref. 124) and hence only the pressure dependencies of the lattice parameter of β-B_2O_3 are required. Thanks to this hypothesis the bonds compressibility values have been obtained.

A phonon study of β-B_2O_3 by means of Raman and IR spectroscopies at ambient pressure and room temperature have been done for the first time. Thanks to the *ab initio* calculations of the phonon mode frequencies and modes visualization, the assignment of all experimentally observed bands to the phonon modes has been provided for the first time. The isotope substitution effect of

^{10}B in β-B_2O_3 Raman spectrum has been observed for the first time and discussed. The phonon properties of β-B_2O_3 have been also studied at room temperature and under high pressure up to 46 GPa by means of Raman spectroscopy. Basing on the *ab initio* calculations of the phonon frequencies for the reduced unit cell volumes, modes assignment and pressure dependencies of the B-O bonds and O-B-O angles, some explanations of the phonon modes behavior under compression have been proposed. As a result, the Grüneisen parameters of all Raman-active phonon modes have been calculated for the first time.

Chapter IV

10 Studies in B-S binary system

Since the chemical properties of sulfur and oxygen are not the same, the number and properties of binary compounds in B-S and B-O systems consequently differ. Actually, the sulfur can form a larger number of binary compounds with boron than oxygen does. Unlike B-O system, the binary compounds of B-S system have not revealed the unusual hardness, mechanical resistance, etc. However these compounds possess other interesting physical properties, like semiconductivity, high thermal conductivity, etc. As it has been mentioned in Chapter I, there were not detailed studies on these compounds under extreme conditions. The regions of phase stability of already discovered compounds have not been studied neither.

Rhombohedral boron monosulfide (*r*-BS) is one of the best known representatives of the B-S system with promising physical properties (e.g. the influence of the anisotropic layered structure on the physical properties and therefore the possibility to vary them by applying for example the pressure). *r*-BS belongs to the $A^{III}B^{VI}$ layered semiconductors family. It should be noted that the main representatives of the $A^{III}B^{VI}$ semiconductors (GaS, GaSe, InS and InSe) were found to be promising materials for solar cells, nonlinear optics, photovoltaic energy converters, radiation detectors, photoresistors and solid-state batteries [238-240], due, among other things, to the high anisotropy of their physical properties. Although *r*-BS has been obtained a decade ago as in 2001 [154], it still remains very poorly studied due to the low Z number of boron and therefore difficulties of studying it by conventional laboratory XRD measurements.

In this chapter we will describe our *in situ* HP XRD measurements of *r*-BS with high brilliance synchrotron radiation. The equation of state of *r*-BS has been measured for the first time and the bulk modulus and its first pressure derivative have been obtained. A phase transition of *r*-BS was observed around 42 GPa at room temperature. A new high-pressure phase of BS has been obtained and studied. This part will be followed by a description of our phonon studies of *r*-BS at ambient and under high pressures. The *r*-BS phonons have been assigned to the vibrational modes for the first time thanks to *ab initio* LCAO calculations.

10.1 Equation of state of *r*-BS

10.1.1 Experimental techniques

Synthesis details

r-BS was synthesized at 7.5 GPa and ~1900°C from amorphous boron (Johnson Matthey, 99%) and sulfur (Johnson Matthey, spectrographic grade) powders mixed in the 1:1 molar ratio using a toroid-type press (TTP) with specially designed high-temperature cell (see Chapter II

(Figure II.6) and [241]). Boron nitride (grade AX05, Saint-Gobain) capsules were used to isolate the reaction mixture from the graphite heater. Finally, a yellow-green polycrystalline sample (with rather strong H_2S smell) was obtained.

r-BS was also synthesized using MAP installed at LSPM-CNRS, university Paris-Nord. In Figure II.12 one can find the scheme of the MAP assembly used in HP-HT synthesis. The uniform compression of eight secondary WC-Co anvils have been provided in the Walker's module. MgO octahedron with EL of 14 mm and WC-Co secondary anvils with TEL of 8 mm have been used. The mixture of fine powders of B and S was placed into *h*-BN sample capsule. The graphite heater provided the resistive heating. During the synthesis the temperature was controlled *in situ* with help of W5%Re/W26%Re thermocouple. Experiment has been conducted at pressure of 3 GPa and temperatures ranging ~1200-1800°C with reaction time of ~25 min, after which the sample was quenched by the switching off the power and decompressed. The recovered polycrystalline sample was identical to that obtained from the HP-HT synthesis in TTP.

X-ray diffraction measurements at ambient conditions

The X-ray diffraction provided with G3000 TEXT Inel diffractometer (Cu Kα1 radiation) at ambient conditions confirmed high phase purity of polycrystalline sample of *r*-BS, however with some amounts of *h*-BN capsule. The XRD pattern is presented in Figure IV.1.

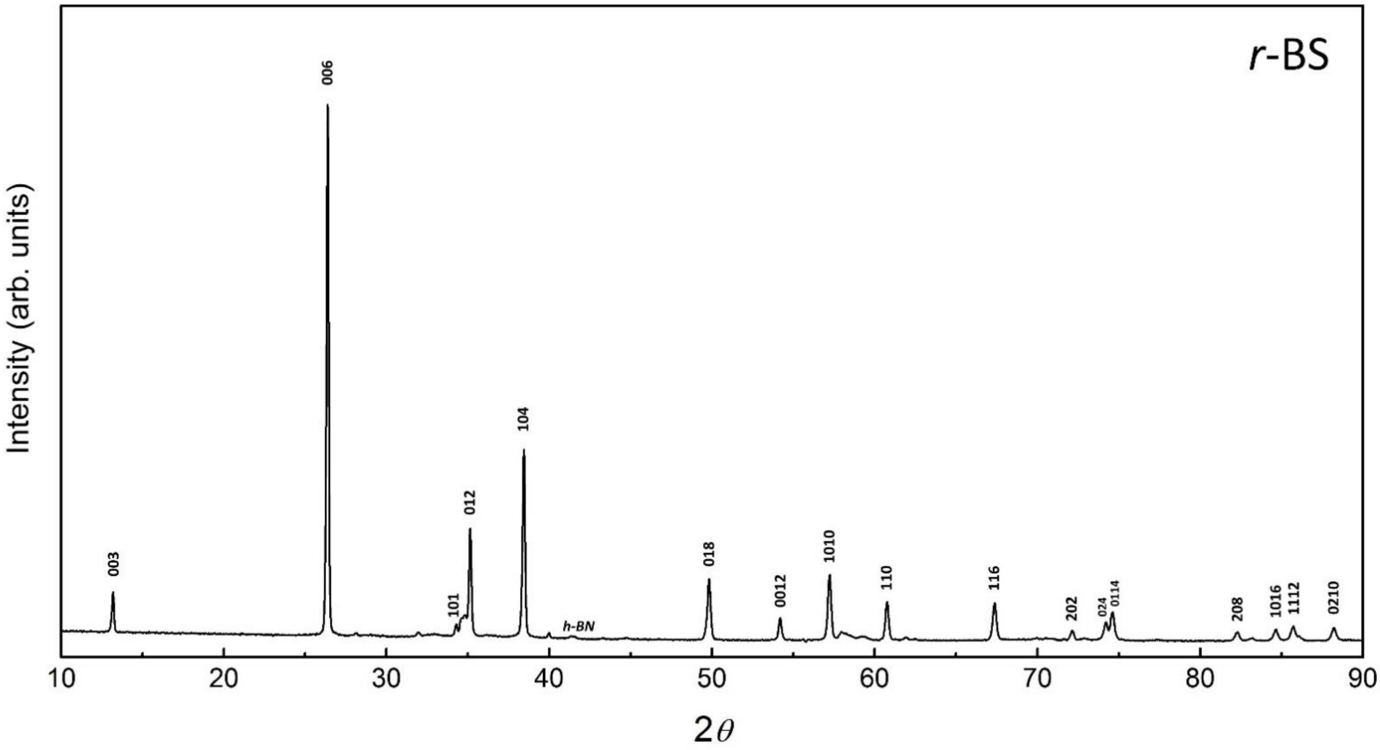

Figure IV.1. XRD pattern (λ=1.5406 Å) of *r*-BS at ambient conditions. The most intensive peaks of r-BS are marked by the *hkl* Miller indexes.

The lattice parameters of *r*-BS (*a*,*b* = 3.054(1) Å, *c* = 20.482(2) Å) are close to those published previously (*a*,*b* = 3.052(2) Å, *c* = 20.411(9) Å) [154].

High pressure X-ray diffraction measurements

High-pressure XRD measurements were carried out at room temperature in a Le Toullec type MDAC [242] with 300 µm culet anvils. *r*-BS powder was loaded into a 110 µm hole drilled in a rhenium gasket pre-indented down to ~30 µm. Neon pressure transmitting medium was used. Pressure determination was implemented by the ruby luminescence technique using the calibration of Mao et al. [212]. The pressure values are presented in Table 1. The pressures were measured before and after each ADXRD measurement; further the mean pressure value was used. The pressure drift during measurement did not exceed 1 GPa in the 0-42 GPa pressure range.

Pressure, GPa	*a=b,* Å	*c*, Å	Volume, Å^3	Pressure, GPa	*a=b,* Å	*c*, Å	Volume, Å^3
0.0	3.054(1)	20.482(2)	165.5	20.6	2.943(1)	17.689(10)	132.7
2.6	3.033(1)	19.512(5)	155.5	21.4	2.944(2)	17.630(4)	132.3
3.8	3.028(0)	19.340(1)	153.6	22.1	2.936(2)	17.592(13)	131.3
4.4	3.024(1)	19.186(1)	151.9	24.1	2.929(1)	17.516(12)	130.1
6.7	3.009(2)	18.854(3)	147.9	25.3	2.924(1)	17.442(11)	129.2
8.4	3.002(1)	18.681(2)	145.8	26.0	2.922(1)	17.407(11)	128.7
10.2	2.991(1)	18.487(3)	143.4	26.1	2.921(3)	17.323(4)	128.0
11.5	2.986(1)	18.384(1)	141.9	27.9	2.910(2)	17.292(13)	126.8
12.4	2.980(1)	18.295(4)	140.7	29.4	2.899(1)	17.241(11)	125.5
13.1	2.977(1)	18.247(2)	140.1	31.1	2.899(1)	17.138(5)	124.8
14.2	2.971(1)	18.141(6)	138.7	31.4	2.894(1)	17.215(7)	124.8
16.1	2.965(1)	17.979(6)	136.9	38.0	2.873(2)	17.005(16)	121.6
16.5	2.962(1)	17.954(5)	136.4	38.3	2.876(3)	16.948(11)	121.4
17.2	2.957(1)	17.909(9)	135.6	42.0	2.858(6)	16.940(17)	119.8
18.0	2.955(1)	17.838(13)	134.9				

Table 1. Lattice parameters and volume of the unit cell of *r*-BS *versus* pressure up to 42 GPa at room temperature measured at ID27 and PSICHE beamline. The numbers in brackets are the fitting standard deviations (95% confidence interval) on the last or last two digits.

HP XRD measurements were performed at ESRF ID27 beamline and at synchrotron SOLEIL PSICHE beamline. At both beamlines the collection of XRD patterns was measured in angle-dispersive mode with a focused monochromatic beam. The selected beam wavelength was equal to 0.3738 Å. The X-ray optics of ID27 and PSICHE beamline delivered a focused beam spot of 9 µm^2 and 15 µm^2 respectively. The XRD data were acquired using a MAR 345 image plate detector with an exposure time of 10 seconds (at ID27) and a PerkinElmer XRD 1621 image plate detector with an exposure time of 15 seconds (at PSICHE beamline). Laue diffraction patterns obtained during the measurements were treated by fit2D software [194]. The lattice parameters and unit cell volume at each pressure point were refined by using DICVOL04 and WinPLOTR packages in FullProf software [195-197] and are presented in Table 1.

Calculation details

As well as for β-B_2O_3, first principles LCAO calculations have been made for study of *r*-BS. The calculations were performed using the CRYSTAL09 code [207]. For the boron atoms, we used the all-electron basis set, which was optimized in earlier calculations [215]. The core electrons of the sulfur atom were excluded from consideration using the effective small-core pseudopotential (ECP) and the corresponding atomic basis set [243], which excludes any diffuse Gaussian-type orbitals with the exponents less than 0.1. In the CRYSTAL09 code [207], the accuracy in evaluating the Coulomb series and the exchange series is controlled by a set of tolerances, which were taken to be (10^{-8}, 10^{-8}, 10^{-8}, 10^{-8}, 10^{-16}). The Monkhorst-Pack scheme [217] for an 8 x 8 x 8 k-point mesh in the Brillouin zone was applied. Self-consistent field calculations were performed for hybrid DFT–HF WCGGA–PBE-16% [218] functional. The percentages 16% define the Hartree–Fock admixture in the exchange part of DFT functional.

The full *r*-BS structure optimization procedure was performed according to the energy minima criterion. The lattice parameters (*a* and *c*) and the unit cell volume (V_0) for the primitive hexagonal cell are 3.114(7) Å, 20.749(6) Å and 174.3 Å^3, respectively. Like in *ab initio* calculations for β-B_2O_3, the calculated lattice parameters of *r*-BS are slightly larger than experimentally determined values. The deviations of the calculated lattice parameters from the experimental ones are 1.96% and 1.30% respectively. The unit cell volume deviation is equal to 5.36%. In spite of the fact that the boron isotope content of *r*-BS used in experiments is 20% ^{10}B - 80% ^{11}B, all *ab initio* calculations have been performed for boron isotope content of 100% ^{11}B (which will be further marked as *r*-^{11}BS*).

The equation of state parameters of *r*-^{11}BS* (bulk modulus B_0 and its first pressure derivative B_0') have been estimated by the same routine implemented in the CRYSTAL09 code as for β-$^{11}B_2O_3$*. In order to obtain the E(V) dependence, the unit cell volume was varied from 76% to 100% of the equilibrium volume (V_0). The structure optimization was performed at each volume. Obtained E(V) dependence has been fitted to the Murnaghan equation of state [208] taking V_0 = 174.3 Å^3 and E_0 = -5.7 keV (Eq. *II*.13). In order to estimate the P(V) dependence the (Eq. *III*.1) has been used.

The electron structure optimization did not converge at highly reduced unit cell volume (P > 34 GPa). Like for *ab initio* calculations for β-B_2O_3 in Chapter III the possible reasons of this divergence might be noticeable changes of the electronic structure for the unit cell with reduced volume. Therefore the chosen set of the calculation parameters and all-electron basis sets might become not optimal at the highly deformed unit cell. Hence, all the pressure dependencies of *r*-^{11}BS* unit cell parameters (*a*, *c*, V_0, etc.) will be given only up to 34 GPa.

10.1.2 Results and discussion

During the compression the diffraction peaks of the *r*-BS monotonously moved towards the larger 2θ values. For instance, the ADXRD spectra of *r*-BS at intermediate pressures (2.6, 14.2 and 26.2 GPa) are presented in the Fig. IV.2.

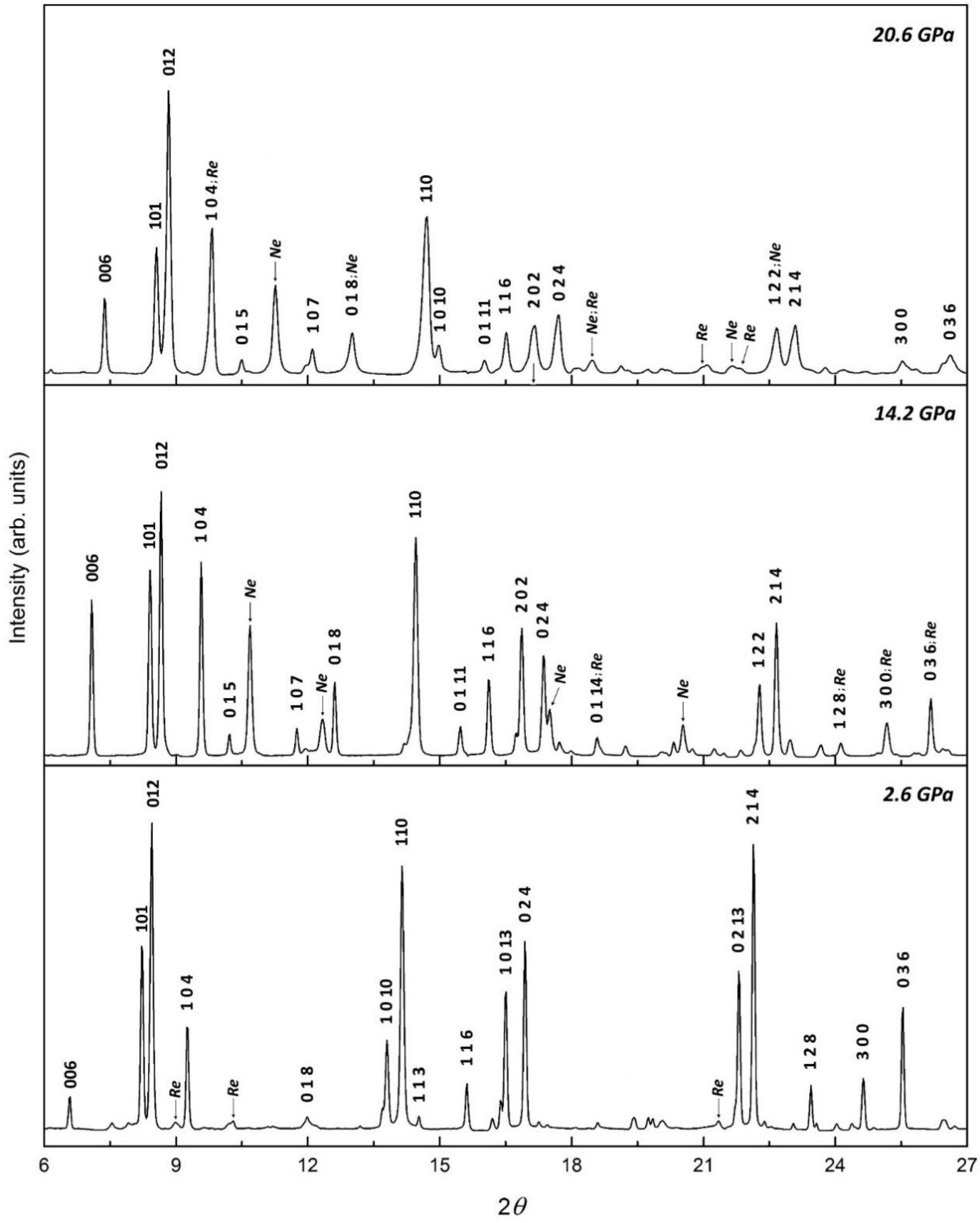

Figure IV.2. X-ray diffraction patterns of *r*-BS taken at different pressures (ID27, ESRF; λ = 0.3738 Å). The most intense *r*-BS reflections are marked by Miller indexes; the diffraction peaks of Re (gasket) and solid Ne (pressure medium) are indicated.

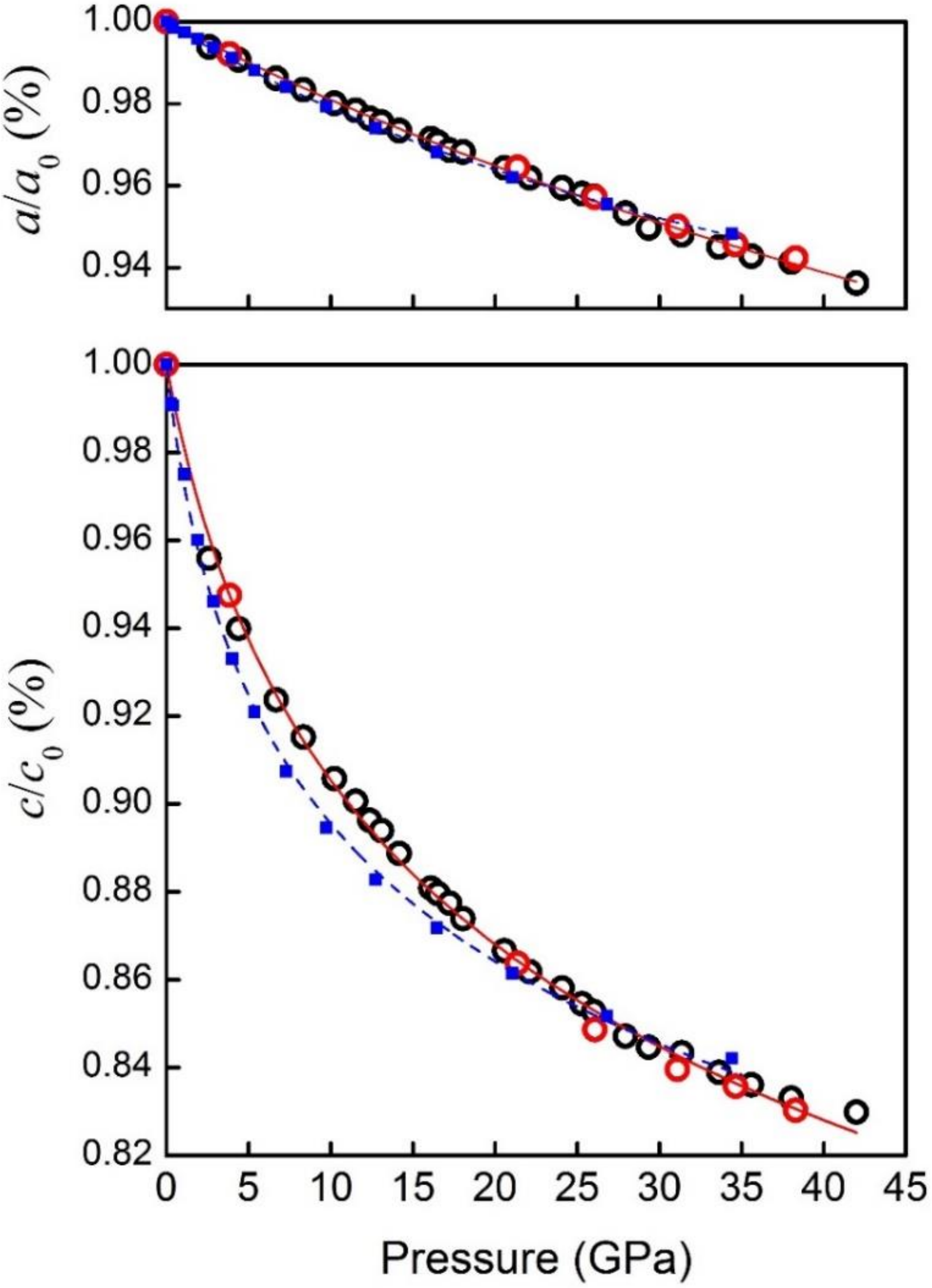

Figure IV.3. Relative lattice parameters changes of *r*-BS *versus* pressure. Open circles represent experimental data obtained at ID27 (black circles) and at PSICHE beamline (red circles). Blue solid squares represent theoretical data. The solid red and dashed blue lines represent the fit of one-dimensional analog of the Murnaghan equation of state to the experimental and theoretical data respectively.

As mentioned in Chapter I, *r*-BS has a layered structure with two types of bonds: weak interlayer van-der-Waals and strong intralayer ionic-covalent bonds. The Figure IV.3 presents the obtained results of *r*-BS lattice compression along the different unit cell axis. One can see that the compression along the *c* axis is more significant than along the *a* axis. In other words, the compressibility in the layer is dramatically lower compared to the compressibility between the layers. In order to approximate the pressure dependence of the lattice parameters and to determine the axial modulus values, we used the one-dimensional analog of the Murnaghan equation of state (Eq. *III*.2). The $\beta_{0,a}$ and $\beta_{0,c}$ axial moduli values are 476.9±8.6 GPa and 49.4±1.2 GPa respectively. Similarly to boron (III) oxide, we calculated the linear compressibility (k_r) values using the (Eq. *III*.3). The k_r values found for *a* and *c* directions are $(2.09\pm0.04)\times10^{-3}$ GPa^{-1} and $(2.02\pm0.05)\times10^{-2}$ GPa^{-1}respectively differing by one order of magnitude, which clearly demonstrates and proves the layered character of *r*-BS, and its similarity to the other compounds of the III-VI family.

According to Figure IV.3, the theoretical pressure dependence of the *a* parameter almost perfectly fits with experimental one. On the contrary, there is a deviation between the experimental and theoretical values along the *c* axis. Applying the one-dimensional analog of the Murnaghan equation of state to the LCAO data, we found $\beta^*_{0,a}$ and $\beta^*_{0,c}$ parameters equal to 388.4±6.9 GPa and 30.1±1.1 GPa respectively. Hence, using (Eq. *III*.3) the k_r* values found for *a* and *c* directions are $(2.58\pm0.05)\times10^{-3}$ GPa^{-1} and $(3.32\pm0.12)\times10^{-2}$ GPa^{-1} respectively. All β_0 and k_r values calculated for theoretical and experimental data, as well as lattice parameters are presented in Table 2.

	Experimental data	Theoretical data
a, Å	3.054(1)	3.114(7)
c, Å	20.482(2)	20.749(7)
$\beta_{0,a}$, GPa	476.9±8.6	388.4±6.9
$\beta_{0,c}$, GPa	49.4±1.2	30.1±1.1
$k_a\times10^{-3}$, GPa^{-1}	2.09±0.04	2.58±0.05
$k_c\times10^{-2}$, GPa^{-1}	2.02±0.05	3.32±0.12

Table 2. Lattice parameters, axial moduli and linear compressibilities obtained from theoretical and experimental data.

In spite of the fact that the order of β^*_0 and k_r* values match with experimental ones, there is a considerable difference between experimental and theoretical compressibilities along *a* and *c* axis (see Table 2). We assume that the observed difference between LCAO and experimental k_a values can be due to a slight theoretical overestimation of the *a* lattice parameter. On other hand, a dramatic difference between theoretical and experimental k_c values can be due to the lack by CRYSTAL09 of some part of interlayer interactions. According to the reports on the other $A^{III}B^{VI}$ layered semiconductors (GaSe, GaS, InSe) which can be considered as structural analogs of *r*-BS, the nature of interlayer interaction is rather complicated and apart from van-der-Waals bonds there is a ionic-covalent contribution [238,240].

We compared the k_r values of *r*-BS with the linear compressibility values of GaS, GaSe and InSe determined previously (see Table 3).

Compound	k_a ×10^{-3}, GPa^{-1}	k_c ×10^{-2}, GPa^{-1}	Reference
r-BS	2.09±0.04	2.02±0.05	Current study
GaS	3.27	2.52	[244]
	4.5±1.3	2.30±0.36	[245]
	5.1±0.1	2.39±0.04	[247]
GaSe	5.2±0.5	2.56±0.18	[245]
	5.73±0.04	2.70±0.06	[246]
	5.05±0.25	2.27±0.11	[248]
InSe	3.3±1.9	2.22±0.71	[245]
	3.85	2.31	[249]
	6.74±1.14	2.86±0.12	[250]

Table 3. Linear compressibilities (k_r) of *r*-BS, GaS, GaSe and InSe.

According to Table 3 *r*-BS has the smallest k_a value among all $A^{III}B^{VI}$ compounds, and the largest ratio between k_a and k_c. We assume that this phenomenon can be simply explained by the fact that the B-B and B-S bonds are significantly shorter and therefore more rigid than Ga-Ga, In-In, Ga-S(Se) and In-Se (due to small radii of electron shells of boron and sulfur atoms). Thus, the smallest k_a value of *r*-BS compared to other $A^{III}B^{VI}$ compounds seems logical and predictable.

The linear compressibilities of $A^{III}B^{VI}$ semiconductors along the *c* axis are one order of magnitude greater than those along the *a* axis. It should be noted, that unlike k_a values, all k_c values are rather close to each other. It is not also an unexpected result, as the large compressibility along *c* is mainly due to the weak van-der-Waals interlayer interactions. However, the linear compressibility along the *c* axis increases in *r*-BS < GaS ≤ GaSe < InSe row if the k_c value of InSe reported in Ref. 250 is considered as correct. The higher k_c value of InSe results in more remarkable volume diminution during compression. This observation matches with one made in Ref. 251, stating that InSe is less ionic than GaS and therefore the interlayer interaction in InSe is closer to the van-der-Waals type, which leads to the bigger initial compressibility along *c* axis. Thus, one can conclude that the k_c values of InSe reported in Ref. 245,249 have been measured not precisely. Using the statement, that the contribution of the forces/interactions different from van-der-Waals one to the interlayer interactions in the $A^{III}B^{VI}$ compounds leads to the smaller k_c values one can draw a rather surprising conclusion. Based on the k_r values presented in Table 3, one can say that the contributions of forces different from van-der-Waals one to the interlayer interaction (and consequently, according to [251] the ionicity of $A^{III}B^{VI}$ compounds) decrease in following row: *r*-BS > GaS ≥ GaSe > InSe. Thus, according this simple logic *r*-BS have been concluded to be the most ionic $A^{III}B^{VI}$ layered compound. This conclusion does not contradict the well-known empirical rule that the AB compounds with the bigger electron shells are considered to be more ionic, as herein the term “ionicity” regards to the whole compound, including intralayer and interlayer interactions.

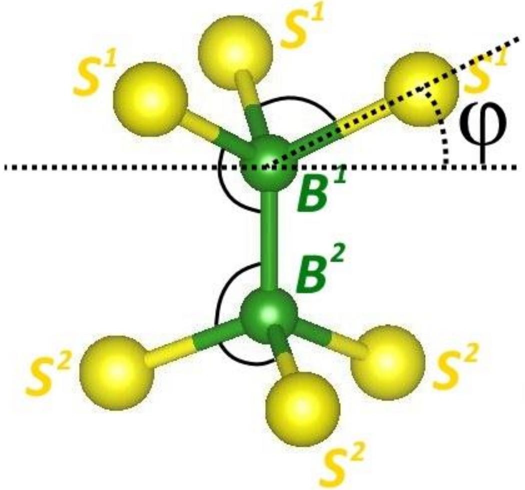

Figure IV.4. S_3B-BS_3 structural fragment of *r*-BS.

As previously mentioned in Chapter I one layer of *r*-BS consists of the B-B pairs aligned along the *c* axis and sandwiched between two hexagonal layers of S atoms. Thus, one can consider the S_3B-BS_3 trigonal antiprism (see Figure IV.4) as the main “building block” of one layer in *r*-BS. It should be underlined that according to our XRD data and that in Ref. 154, the S_3B-BS_3 unit is slightly distorted. The B^1-S^1 bond lengths are not equal to the B^2-S^2 ones, as well as S^1-B^1-S^1, S^2-B^2-S^2, B^2-B^1-S^1 and B^1-B^2-S^2 angles values. The lattice parameters, bond lengths, angles of S_3B-BS_3 structure and interlayer and intralayer distances (d_{inter} and d_{intra} respectively) are listed in Table 4.

Parameter	*r*-BS	*r*-^{10}BS	*r*-^{11}BS*	*r*-BS [154]
a=*b*, Å	3.054(1)	3.055(5)	3.114(7)	3.052(2)
c, Å	20.482(2)	20.348(4)	20.749(7)	20.411(9)
V_0, Å^3	165.5	164.5	174.3	164.7
B^1-B^2, Å	1.700(3)	1.689(5)	1.722(2)	1.694(2)
B^1-S^1, Å	1.993(4)	1.990(3)	2.029(4)	1.990(3)
B^2-S^2, Å	1.913(3)	1.912(3)	1.949(3)	1.911(3)
d_{intra}, Å	3.384(2)	3.359(2)	3.366(2)	3.372(2)
d_{inter}, Å	3.433(1)	3.433(1)	3.535(3)	3.433(3)
S^1-B^1-S^1, °	100.041	100.244	100.233	100.125
S^2-B^2-S^2, °	105.918	106.075	106.066	105.983
B^1-B^2-S^2, °	117.771	117.609	117.618	117.704
B^2-B^1-S^1, °	112.826	112.685	112.693	112.768

Table 4. Cell parameters, bond lengths and angles in S_3B-BS_3 structure fragment of *r*-BS, *r*-^{10}BS, *r*-BS [154] and *r*-^{11}BS*.

As one can see from Table 4, *ab initio* calculations give almost the same parameters for the S_3B-BS_3 unit as the measured ones. However, like in the case of the lattice parameters, the theoretical B-B and B-S distances and B-B-S and S-B-S angles are larger than experimental ones. It should be marked that the Rietveld structure refinement of *r*-BS performed in Ref. 154 did not give the confident results due to the preferred orientation and the small charge density of boron. Due to this fact, in the present we employed the atoms positions refined previously [154].

	x	***y***	***z***
B(1)	0	0	0.538(4)
B(2)	0	0	0.455(4)
S(1)	0	0	0.2500
S(2)	0	0	0.7521(8)

The description of the interatomic distances and angles changes in $A^{III}B^{VI}$ layered compounds (e.g. GaSe, InSe and GaS) was performed using EXAFS, XANES measurements [240,252] or XRD single crystal measurements [253]. However, the application of these techniques for the description of the S_3B-BS_3 unit structure under compression is almost impossible. The HT-HP synthesis of *r*-BS monocrystal is rather challenging due to the possible presence of stacking faults and other structural defects. Due to this fact the HP XRD measurements of *r*-BS single crystal were not practiced in our work. The HP XAFS measurements of sulfur at the S K_α edge is still under development [254].The direct HP XAFS measurements of boron are on other hand impossible due to its low energy edge (0.2 keV). The direct HP measurements of *r*-BS in DACs are only possible by XRS technique using hard X-rays [221]. However, the available energy range would rather limited to draw some information/conclusions about the interatomic distances and angles.

Regarding all the facts given above, for the description of interatomic distances under high pressure we used only the data on the lattice parameters at the different pressures, assuming that the atoms positions are constant during compression. The error bars of the obtained interatomic distances and angles can be estimated by means of the corresponding error bars of the lattice parameters (<0.4%) and atoms positions (<0.9%).

The changes of normalized bond lengths (B^1-B^2, B^1-S^1, B^2-S^2) and the B-B-S and S-B-S angles in S_3B-BS_3 unit up to 42 GPa are presented Figure IV.5 and IV.6 respectively. In Figure IV.5 we employed the same analog of Murnaghan equation of state, which has been used previously in Ref. 240,252 for the data approximation fitting (the solid lines). The local isothermal bulk moduli

B_{0,B^1-B^2}, B_{0,B^1-S^1} and B_{0,B^2-S^2} obtained from this fit are 16.0±0.4, 87.0±1.1 and 101.5±1.0 GPa respectively (B_0' was fixed to 5, as well as in Ref. 240). The linear compressibility values (k_r=1/3$B_{0,r}$=1/$\beta_{0,r}$) for B^1-B^2, B^1-S^1 and B^2-S^2 are $(2.08\pm0.05)\times10^{-2}$, $(3.83\pm0.05)\times10^{-3}$ and $(3.28\pm0.04)\times10^{-3}$ GPa^{-1} respectively.

The B-B bond in the layer of *r*-BS has been found to be significantly more compressible than B-S ones, like for example, in γ-InSe where the change of In-In under compression is bigger compared to the change of In-Se [252]. One can also notice that the linear compressibility of the B-S bonds is greater than that of the *a* axis in contrast to other $A^{III}B^{VI}$ layered compounds [240,252]. Moreover, unlike other $A^{III}B^{VI}$ compounds the compressibilities of the B-S bonds in the "top" and in the "bottom" of the layer have been found to be different. Based on the compressibility values of the B^1-S^1 and B^2-S^2 bonds, one can conclude that the "bottom" part of S_3B-BS_3 unit is less compressible than the "top" part.

Considering the more rigid "bottom" part of S_3B-BS_3 one can find that the axial module of B-S bond is slightly larger compared to those of Ga-Se (92±6 GPa) and In-Se (116±20 GPa) reported in Ref 240 (herein it should be underlined that we consider $B_{0,B^2-S^2} > B_{0,In\text{-}Se}$ taking into account the big error bar of local bulk modulus of InSe). This observation proves our suggestion that the high relative rigidity of *r*-BS perpendicular to the *c*-axis can be explained by the short and stiff B-S bonds.

We also estimated the B-B and B-S pressure dependencies obtained from our *ab initio* calculations. The results of this estimation are presented in Figure IV.5. One can see that the theoretically estimated bonds compressions are rather close to the experimental values. The local isothermal bulk moduli of B^1-B^2, B^1-S^1 and B^2-S^2 are 10.0±0.4, 68.9±2.4 and 83.4±2.4 GPa (again B_0' was fixed to 5). The deviation of the calculated B_0^* values of B-S bonds from experimentally determined ones are similar to the deviation of $\beta_{0,a}^*$ from $\beta_{0,a}$ ~20%.

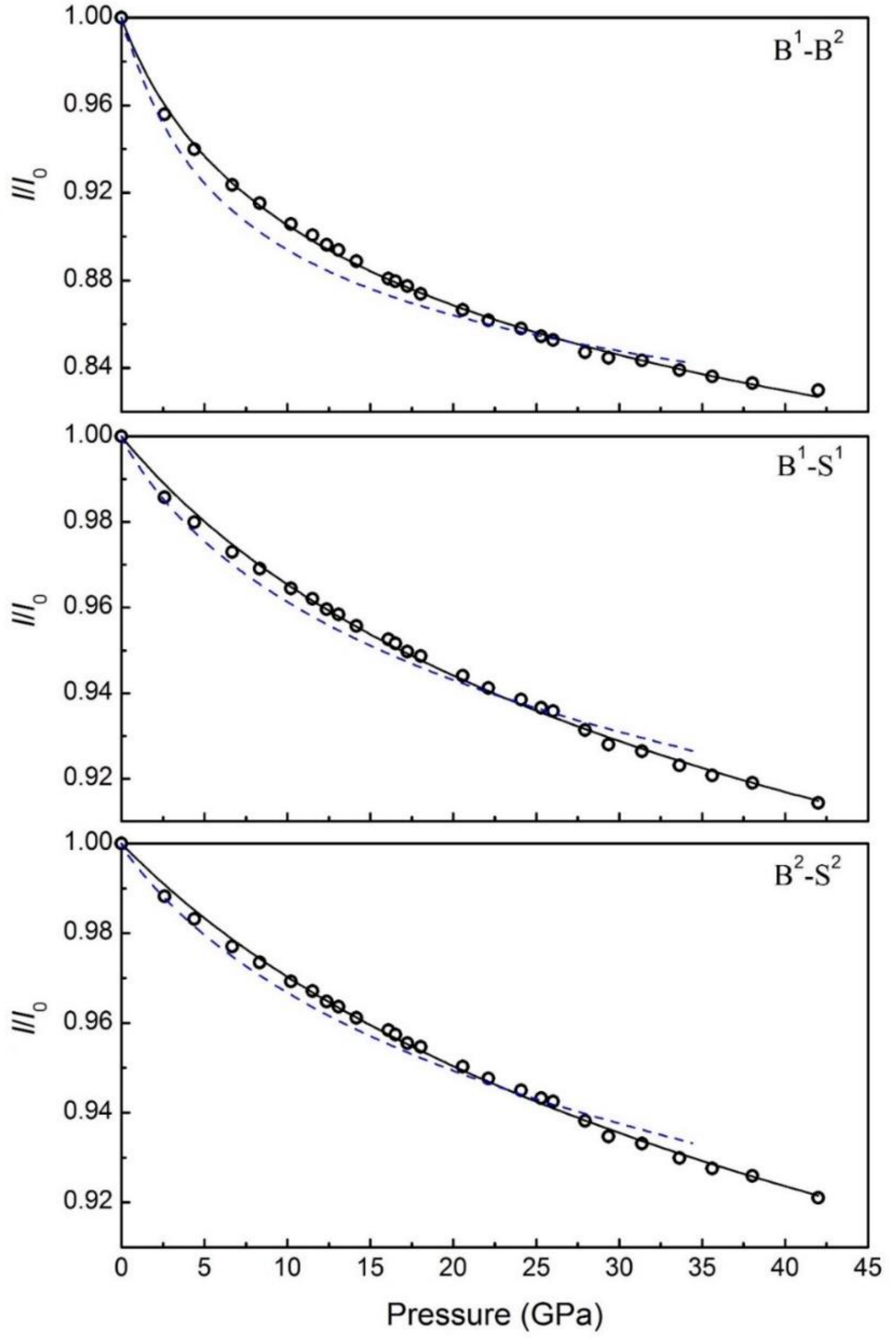

Figure IV.5. Relative changes of B-B and B-S distances (l/l_0) in S_3B-BS_3 unit *versus* pressure. The open circles indicate experimental data, the solid black lines indicate the fit of analog of Murnaghan equation of state to the experimental data, the blue dashed lines represent the theoretical estimations.

Thus one can conclude that CRYSTAL09 estimates *r*-BS intralayer structure changes with some nearly constant error. However, based on the similarity of the shapes of the pressure dependence curves presented in Figure IV.5 and the same orders of magnitude of B_0^* values, one can conclude that our model/approach proposed above for the *r*-BS intralayer structural description matches with the *ab initio* predictions. It should be underlined that during LCAO structure optimization according to energy minima criterion the lattice parameters as well as atoms coordinates (in the given space group) have been varied, whereas in our model of interpretation of the experimental XRD data the atoms positions have been fixed. Thus, we can conclude that the atoms position change in the layer during compression is negligible, which makes our model of *r*-BS layer compression more confident, but still not completely correct.

According to the proposed model of intralayer compression we estimated the changes of angles in S_3B-BS_3 (see Figure IV.6). As expected, the $B^1B^2S^2$ and $B^2B^1S^1$ angles slightly decrease (~2.5%) under high pressures. On the contrary, the $S^1B^1S^1$ and $S^2B^2S^2$ angles increase during compression. A few remarks can be made concerning Figure IV.6. First of all, the angles become simultaneously less pressure dependent above ~27 GPa. We supposed that the further small change of the angles and therefore a stop of moving of the atoms might be an indirect evidence of *r*-BS structure transformation (which has been further confirmed).

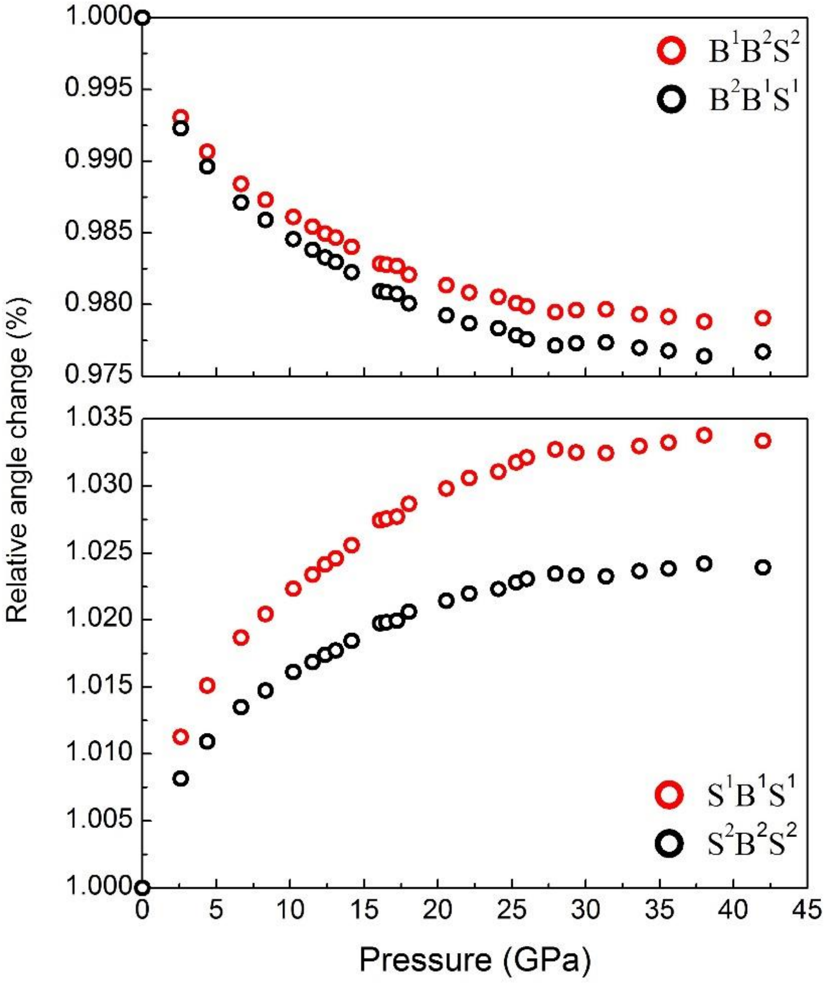

Figure IV.6. Relative changes of B-B-S and S-B-S angles in S_3B-BS_3 unit under compression.

One can note that the smaller change of $B^1B^2S^2$ angle expectedly corresponds to the bigger $S^1B^1S^1$ change and vice versa for $B^2B^1S^1$ and $S^2B^2S^2$. Moreover, the difference between changes of $S^1B^1S^1$ and $S^2B^2S^2$ is more significant than for $B^1B^2S^2$ and $B^2B^1S^1$. A change of $S^1B^1S^1$ angle of the more compressible "top" part of S_3B-BS_3 is greater than that of $S^2B^2S^2$ of the stiffer "bottom" part. However, we do not have an explanation of this phenomenon.

Of course the changes of the angles in S_3B-BS_3 during compression influence on the compressibility values in the layer perpendicular to *c* axis. In Ref. 240, the angle φ (see Figure IV.4) was proposed to reconcile the compressibilities of the B-S bonds and *a* lattice parameters:

$$\frac{a}{2} = d_{B-S} cos\varphi \cdot cos30° \qquad (IV.1).$$

In the case of GaSe [240] and InSe [252] the φ angles increased during compression up to 16 GPa by 1.4° and up to 10 GPa by 2.7° respectively. Unlike these compounds, *r*-BS revealed the constant decrease of the φ angle at high pressures. Due to the difference of the "top" and "bottom" parts of S_3B-BS_3 the corresponding φ angles (φ_1 and φ_2) are different too. In 0-42 GPa pressure range the φ_1 angle decreases from 22.83° to 20.41°, meanwhile the φ_2 angle changes from 27.77° to 24.96°.

Using simple geometric considerations, φ_1 and φ_2 angles, B^1-B^2, B^1-S^1 and B^2-S^2 bonds lengths (*l*) the height (*H*) and the width (*W*) of the S_3B-BS_3 unit can be easily determined:

$$H = l(\mathrm{B}^1 - \mathrm{B}^2) + l(\mathrm{B}^1 - \mathrm{S}^1) \cdot sin\varphi_1 + l(\mathrm{B}^2 - \mathrm{S}^2) \cdot sin\varphi_2 \qquad (IV.2),$$

$$W = l(\mathrm{B}^1 - \mathrm{S}^1) \cdot cos\varphi_1 + l(\mathrm{B}^2 - \mathrm{S}^2) \cdot cos\varphi_2 \qquad (IV.3).$$

The pressure dependencies of the *H* and *W* are presented in Figure IV.7.

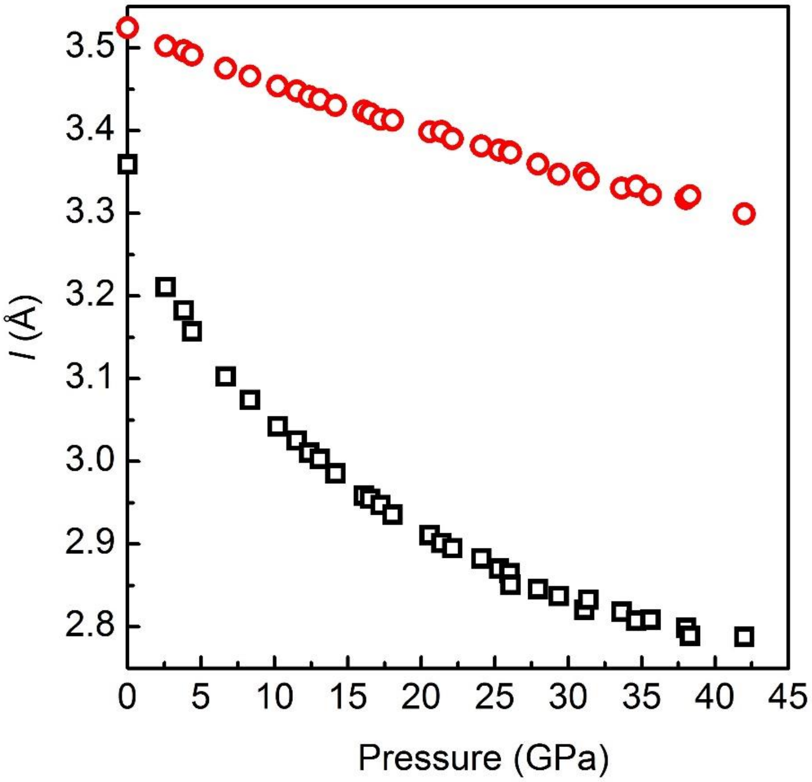

Figure IV.7. The changes of the width (*W*) (red circles) and the height (*H*) (black squares) of S_3B-BS_3 unit under compression.

Thus, we can conclude that *r*-BS layer compression is not isotropic, which is typical for other $A^{III}B^{VI}$ layered semiconductors.

The isothermal bulk modulus of *r*-^{11}BS* B_0 = 31.2 GPa and its first derivative B_0\` = 8.4 have been estimated using the E(V) dependence obtained from the LCAO calculations (Figure IV.8 *a*). Unlike β-$^{11}B_2O_3$*, the E(V) dependence of *r*-^{11}BS* was obtained by varying the equilibrium unit cell volume (V_0) from 100 to 76%. In other words, the parabola of E(V) curve in Figure IV.8 *a* misses the right part. Indeed, in the 100-130% range of V_0 the unit cell energy remains almost constant. In terms of the real structure, this can be interpreted as moving away of the S-B-B-S layers from each other without (almost without) changing their intralayer distances. This makes the determination of the local minimum energy (E_0) rather uncertain, leading to the big dispersion of the B_0 and B_0\` values. Due to the impossibility of the accurate energy minimum determination we considered the E_0 at 100% of V_0 (see Figure IV.8 *a*).

The pressure dependence of normalized volume V/V_0 fitted to the Murnaghan equation of state is shown in Figure IV.8 *b*. The band gap value E_g = 3.5 eV found from LCAO calculations is in good agreement with the estimation made in Ref. 154 (~3.4 eV).

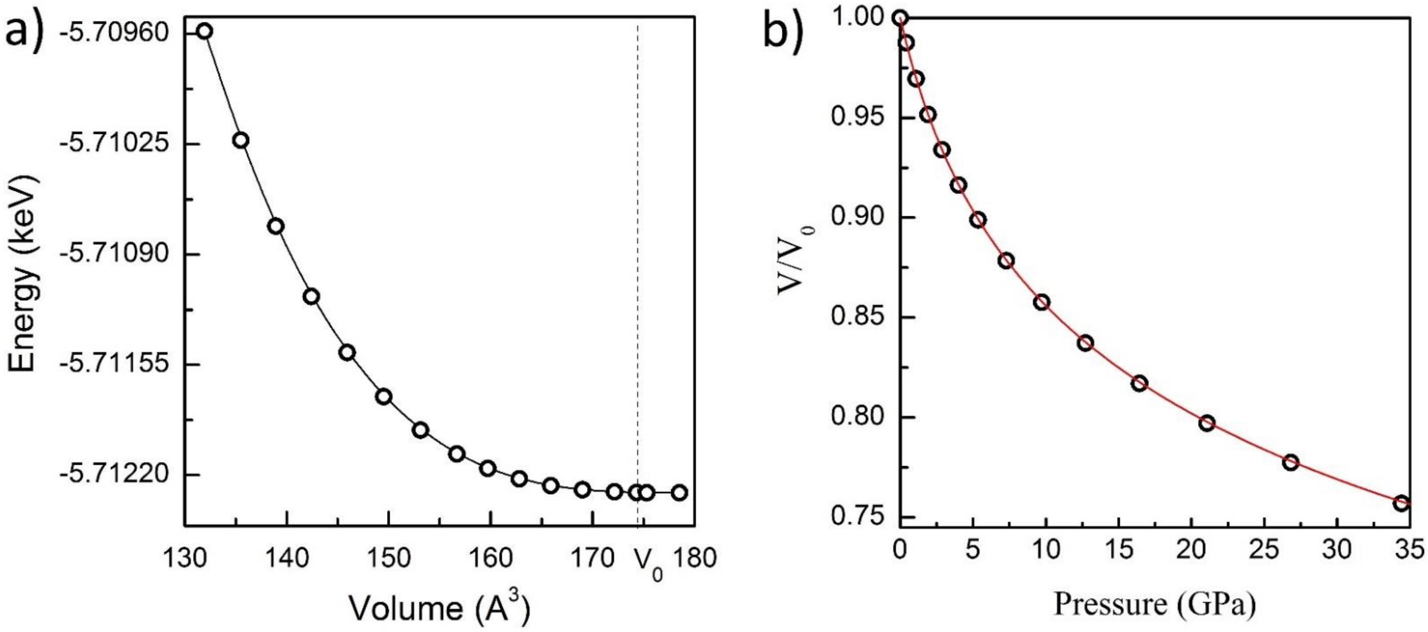

Figure IV.8. a) Energy variation of the *r*-^{11}BS* unit cell *versus* volume (Murnaghan fit – solid line). The position of V_0 is indicated by dashed line; b) equation of state of *r*-^{11}BS*. The red line presents the Murnaghan fit to the theoretical data.

The pressure dependence of the normalized unit cell volume up to 42 GPa measured by XRD at ID27 and PSICHE beamlines is presented in Figure IV.9. One can see that the experimental data obtained in two different runs match very well. Hence we provided a fitting of the whole dataset by a Murnaghan equation of state [208]. The bulk modulus B_0 value was found to be 48.4±1 GPa, whereas its first derivative B_0' is 5.5±0.2. The χ^2 is 0.54. We also approximated the experimental data by a Vinet and Birch-Murnaghan equations of state (Eq. *III*.4, Eq. *III*.5). The obtained bulk modulus and its first pressure derivative are 46.7±1 GPa and 6.7±0.2 with χ^2=0.42 for Vinet EoS formulation and 47.1±1 GPa and 6.6±0.2 with χ^2=0.44 for Birch-Murnaghan EoS formulation. So, all of the formulations of equation of state give rather close B_0 and B_0' values. The low χ^2 parameters obtained using Vinet and Birch-Murnaghan equations of state indicate that these EoS formulations are more suitable for the fitting of the experimental data than Murnaghan equation of state. The rather high value of B_0' is evidently due to the huge anisotropy of the *r*-BS structure similarly to graphite (for which $B_0' = 8.9$) [255], hexagonal graphite-like boron nitride ($B_0' = 5.6$) [256] and turbostratic BN ($B_0' = 11.4$) [257].

It should be noted that B_0 and B_0' values obtained from our theoretical estimations differ from the experimental ones. We suppose that the main reason of this discrepancy is due to the deviation of the theoretical and experimental compressibilities along the *c* axis. As it has been mentioned above, the CRYSTAL09 code does not take into account some contributions to the interlayer interactions, which make *r*-BS stiffer along the *c* axis. To avoid this calculation imperfection, we used $B_0'= 5.5$ for the fitting of the theoretically calculated points to the Murnaghan equation. The new B_0 value is 42.1±1 GPa, which is rather close to the experimentally obtained one.

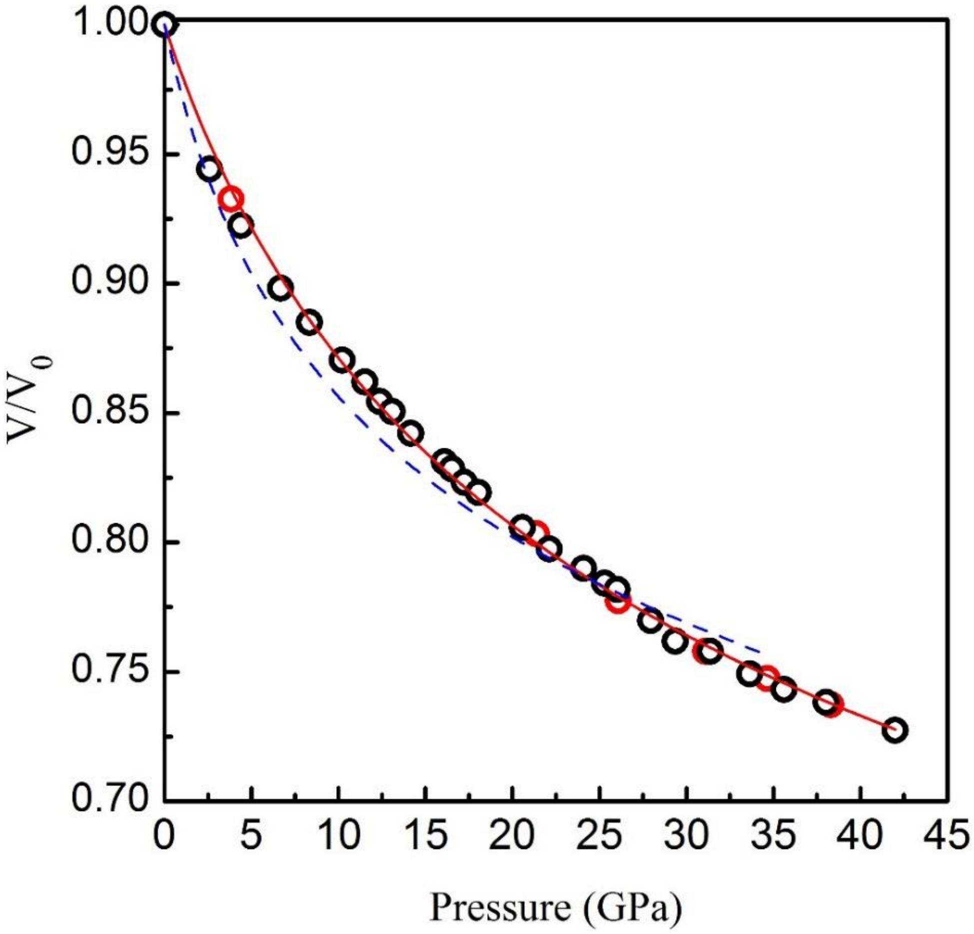

Figure IV.9. Equation of state of *r*-BS. The open circles and squares represent high-pressure experimental data obtained at ID27 (ESRF) and at PSICHÉ beamline (SOLEIL) respectively. The solid red line represents the Murnaghan fit to the whole experimental data set; the blue dashed line represents the theoretical estimation of equation of state of *r*-^{11}BS*.

According to the literature, *r*-BS has the highest experimentally measured bulk modulus value among $A^{III}B^{VI}$ layered compounds (see Table 5).

Compound	B_0, GPa	B_0'	Ref.
β-GaS	37.2(2) (exp.)	5.2	[251]
ε-GaSe	34(2) (exp.)	6.4(5)	[248]
β-GaSe	48.9 (theor.)	4.60	[239]
ε-GaSe	49.6 (theor.)	4.55	
ε-GaSe	28.6 (exp.)	-	[258]
	28.4 (theor.)	-	
ε-GaSe	27.1 (theor.)	-	[238]
	26.9 (theor.)	-	
ε-GaSe	26.4 (theor).	-	[259]
ε-GaSe	28.3 (theor.)	-	[260]
ε-GaSe	27.7 (exp.)	-	[245]
ε-GaSe	28.7 (exp.)	-	[261]
γ-InSe	24(3) (exp.)	8.6(8)	[251,240]

Table 5. Bulk modulus and its first pressure derivative of some $A^{III}B^{VI}$ compounds obtained from experimental (exp.) and theoretical (theor.) studies.

One can see that like *r*-BS, other $A^{III}B^{VI}$ compounds present rather considerable difference between theoretical and experimental B_0 values. Also, the general conclusion is that the selenides are less hard than the sulfides. It has been already mentioned that the most important part of the unit cell diminution in $A^{III}B^{VI}$ compound under compression derives from the interlayer space diminution (due to the weak van-der-Waals interactions). As it has been found that *r*-BS has the largest ionic-covalent contribution to the interlayer interactions among the III-VI compounds, its high B_0 values was rather expected and reasonable.

Thanks to our *in situ* XRD measurements the compression of *r*-BS has been found to be highly anisotropic due to presence of the different types of bonds: intralayer ionic-covalent bonds and interlayer van-der-Waals bonds. Among all $A^{III}B^{VI}$ semiconductors *r*-BS has been turned out to be the most rigid in all directions (*a*, *c*) and hence with the highest B_0 value. The detailed investigation of the *r*-BS layer structure under high pressure showed that its compression is not isotropic. In spite of the fact that under compression *r*-BS generally behaves like other $A^{III}B^{VI}$ compounds, it however has some particularities, e.g. decreasing φ angle.

10.2 New high pressure phase of BS

10.2.1 Results and discussion

The new high pressure phase of BS has been observed during XRD measurements in MDACs at ID27 (ESRF) and at PSICHE beamline (SOLEIL). New diffraction peaks appeared around 28 GPa (stars in Figure IV.10).

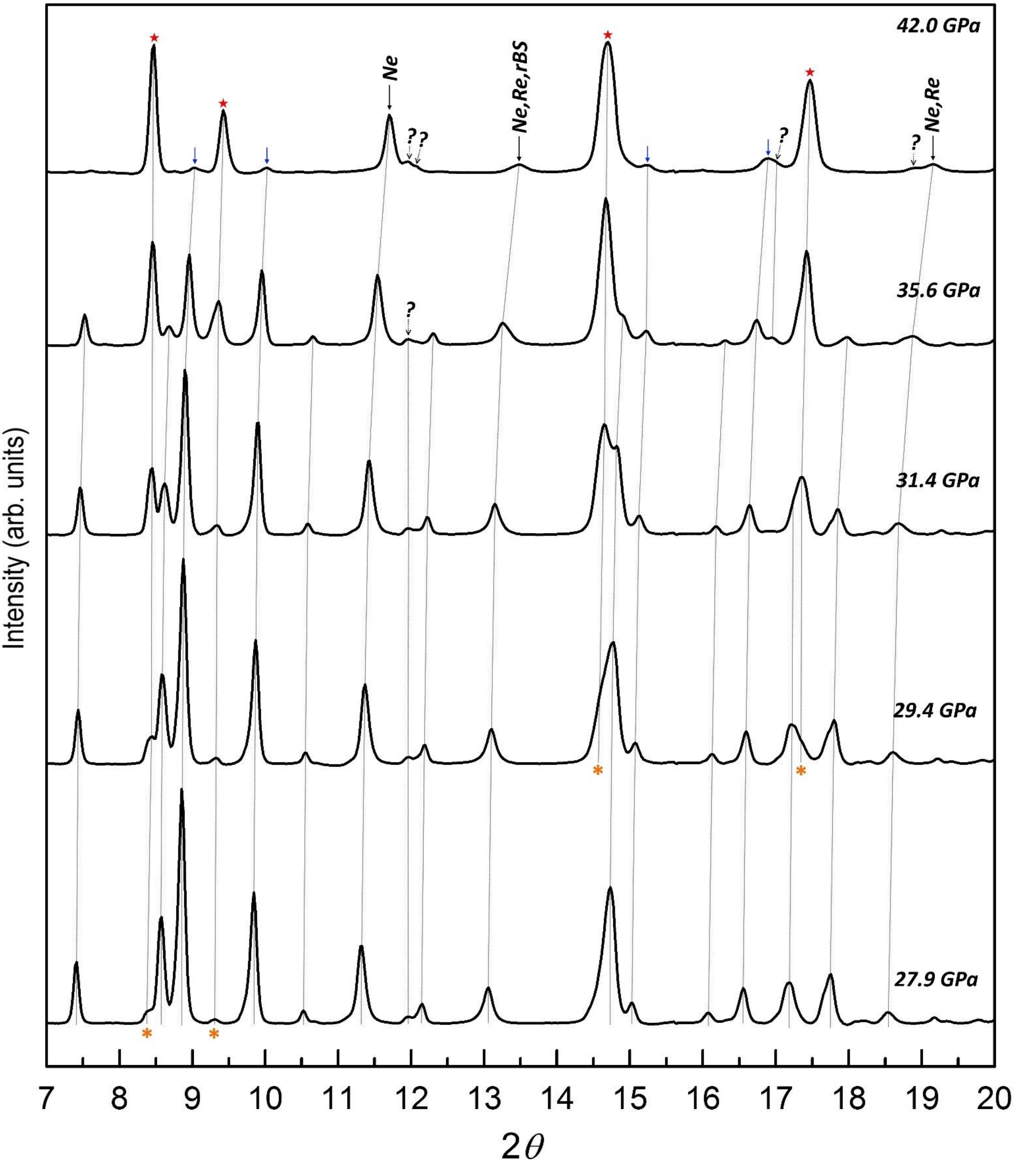

Figure IV.10. XRD patterns (λ=0.3738 Å) of *r*-BS at room temperature and in pressure range 27.9-42 GPa. The shifts of the most intense diffraction peaks under compression are traced by dashed lines; the Re and solid Ne peaks are indicated; the blue arrows indicate the *r*-BS peaks; the peaks of the new BS high pressure phase marked by the red stars (their first appearance by the orange stars) the peaks which might be attributed to the new BS high pressure phase are marked by the question marks.

As shown in Figure IV.10, at pressure of 42 GPa there remain very weak diffraction peaks of *r*-BS and four/five (?) intense peaks of the new high pressure (HP) phase. Figure IV.11 presents an example of the 2D ADX diffraction pattern acquired at 42 GPa using flatpanel detector. The reflections of *r*-BS are almost invisible, whereas the reflections of the new phase are apparent. The HP phase turned out to be unstable during the decompression. The phase transformation is hence reversible.

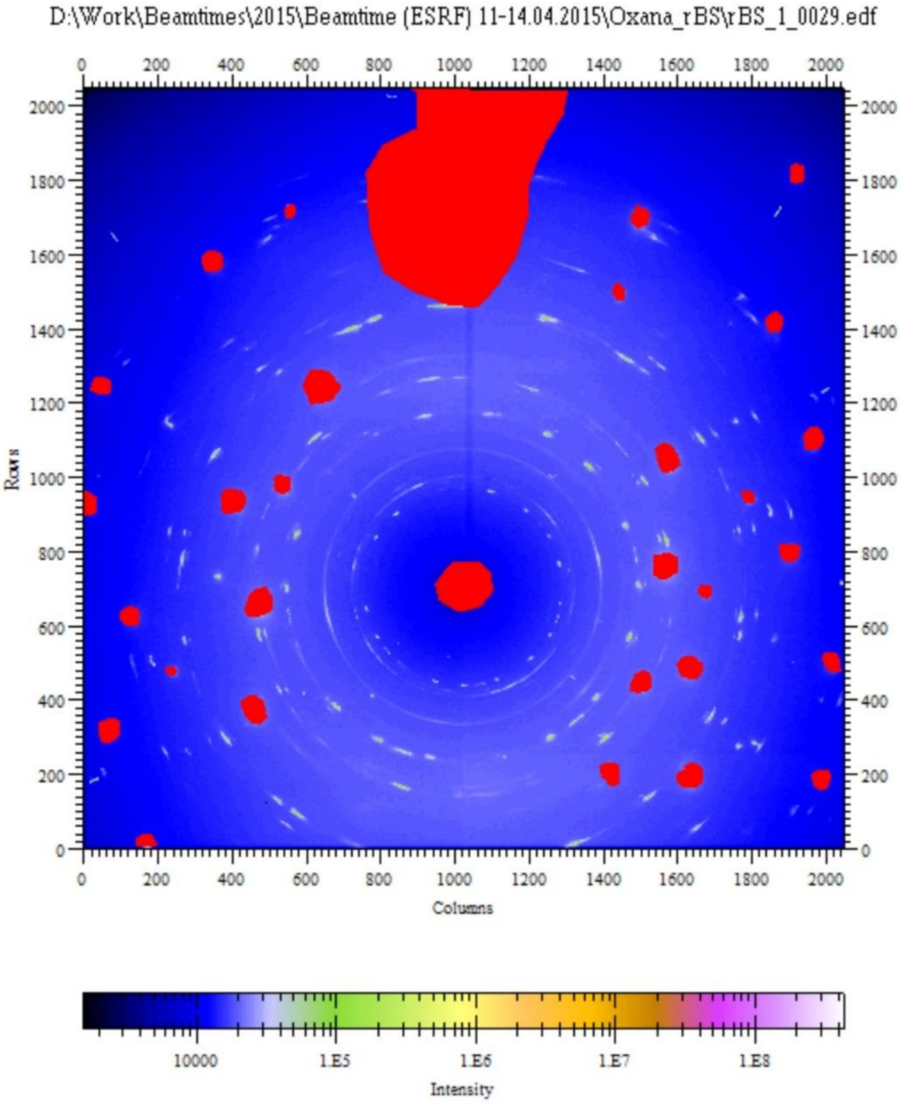

**

Figure IV.11. 2D ADX diffraction pattern (λ=0.3738 Å) of *r*-BS acquired at room temperature and 42 GPa. The reflections of diamond anvils and beamstop are "masked" by red areas. The colored logarithmic intensity gauge is given below. The reflections of BS (rhombohedral and new high-pressure phases) are presented by white dots (circles).

Structure of HP BS phase

Due to the fact that the new BS phase has been observed only at high pressures, its diffraction peaks were rather broaden. The number and the quality of the peaks make a structure refinement (e.g. Rietveld refinement) impossible. However, according to the refinement of the crystal symmetry and the lattice parameters, we can say that the HP phase structure likely belongs to the cubic symmetry. There are two most probable structure motives: rock-salt or CsCl with a lattice parameter of 5.086(1) Å (at pressure of 29.4 GPa). However, considering the $Fm\overline{3}m$ (225) space group, the second and the fourth diffraction peaks present in the diffraction pattern (Figure IV.10) are not expected. Unlike NaCl structure motive, an assignment of all new observed diffraction peaks by the *hkl* indexes can be done (200, 210, 220(?), 222 and 322) in the case of CsCl ($Pm\overline{3}m$ (221)). Nonetheless, rather intense 111 peak is expected for the NaCl structure, whereas CsCl structure implies 100, 110 and 111 diffraction peaks, which have not been observed in our XRD measurements (Figure IV.12).

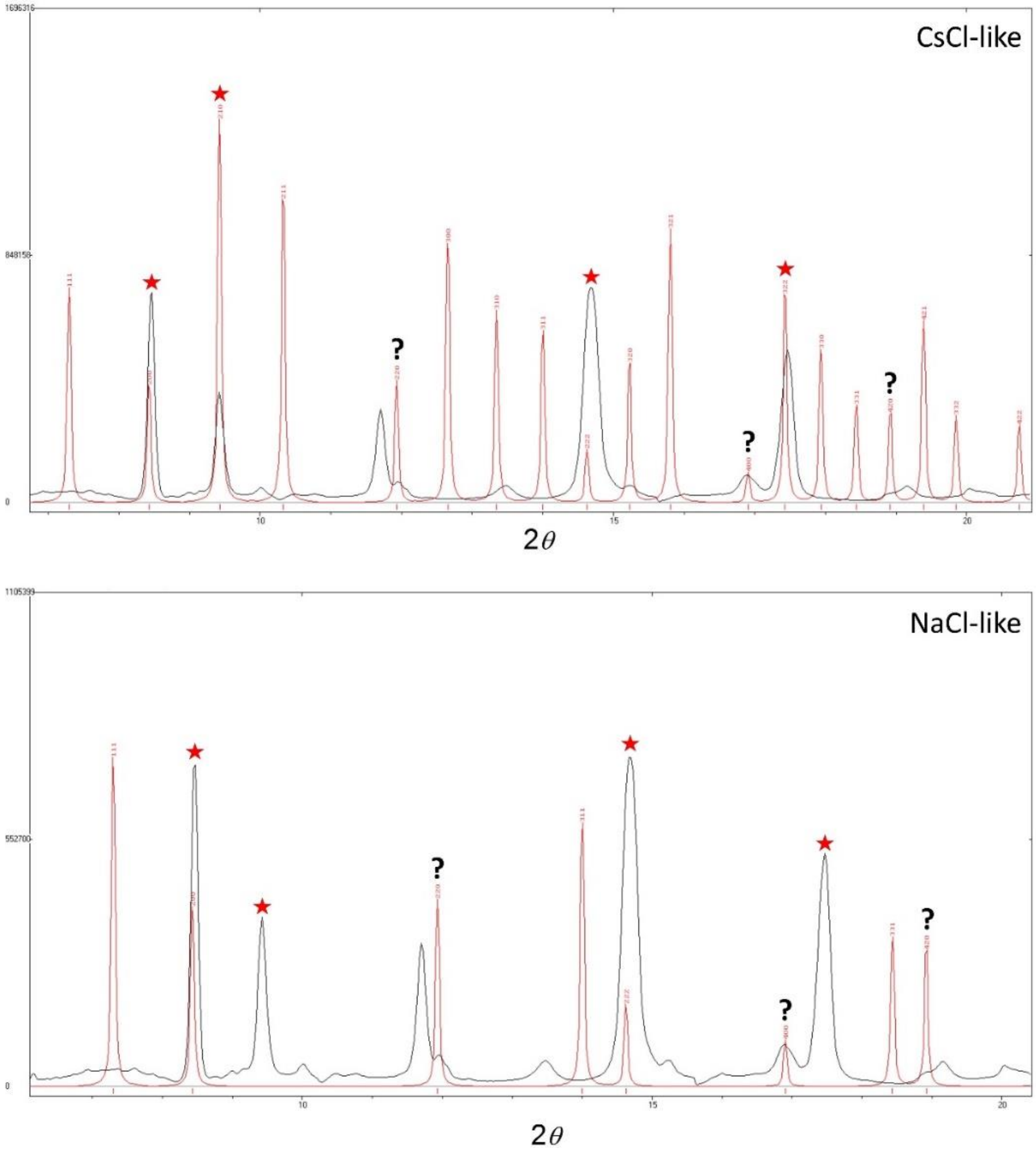

Figure IV.12. The simulations of NaCl and CsCl structural motives applied to the new BS high pressure phase XRD pattern acquired at 42 GPa. The peaks of the new BS high pressure phase marked by the red stars, the peaks which might be attributed to the new BS high pressure phase are marked by the question marks.

We also considered the volume change at the phase transition. It is well known that during HP phase transition the unit cell volume per structure unit (in our case it is BS) should become smaller. In the case of CsCl structure the volume per structure unit becomes larger than that of *r*-BS at 29.4 GPa, which is not probable. Unlike CsCl structure, the rock-salt structure completely reveals an expected volume per structure unit diminution (~50%, which is close to the data presented in Ref. 248).

According to the literature data, the phase transition over 20 GPa is rather typical for $A^{III}B^{VI}$ layered compounds. However, it should be noted that different polytypes of $A^{III}B^{VI}$ compounds have phase transitions at different pressures. For instance, for four known polytypes of GaSe (β-, γ-, δ- and ε-; different number and sequence of the layers [239]) only for two (β- and ε-) HP phase transitions have been reported (see Table 6).

Compound	$P_{(\text{phase transition})}$, GPa	HP phase structure	Reference
β-GaS	19-75	NaCl	[262]
GaS-II	21	?	[251]
γ-InSe	7.5-13.2	?	[251]
γ-InSe	7.1-12.6	NaCl	[252]
ε-GaSe	16-25	?	[240]
ε-GaSe	22.8-27.8	NaCl	[248]
β-GaSe	17.06	NaCl	[239]
ε-GaSe	17.74		
ε-GaSe	25	NaCl	[263]
ε-GaSe	29.2	NaCl	[264]

Table 6. The pressures of the phase transitions of different $A^{III}B^{VI}$ compounds. The most probable structure is indicated.

However, there are no experimental study in which the structure of the new HP phase of GaSe has been well refined [248,263,264]. According to the authors of these reports the quality of the obtained X-ray diffraction patterns did not permit to perform a refinement. The *ab initio* calculations seem to be the only way to confidently sort out the structure of the new HP phase. In Ref. 239 four possible HP structures of GaSe have been tested: NaCl, CsCl, zinc blende and wurtzite. However, only the NaCl-like structure was found to be suitable as it nicely matches with experimental data. The results of Ref. 239 are in good agreement with Ref. 240. The authors of Ref. 240 provided the detailed and accurate HP XAFS study of GaSe. According to this study, during the phase transition Ga changes its coordination from 4 to 6 and only NaCl-like structure satisfies to this new coordination number. On other hand, it contradicts an empirical rule, that a high pressure stable phase structure for a two elements compound (of general formula AB) has usually a CsCl structure [262]. It should be also noticed that according to Ref. 263, a diffraction pattern of HP phase of GaSe looks like those of HP phases of Ga_2Se_3. Thus, based on the example of ε-GaSe we can conclude that the structures of HP phases of $A^{III}B^{VI}$ compounds have presumably a cubic unit cell, however they are not well refined and raise the doubts.

In order to interpret the *r*-BS phase transition, one can mention an idea proposed previously [240,252]: from ~28 GPa on, the interlayer distance in *r*-BS is rather small, leading to more active interaction of the S atoms of adjacent layers. At the same time, the B-B bonds weaken, which results in a whole structure destabilization. Then the B-B bond breaks and one B "jumps" to the interlayer space, where it has an octahedral coordination. Thus, the S-B-B-S layer sequence transforms to S-B-S-B one.

Equation of state of HP BS phase

A change of the unit cell volume of the HP phase of BS in 29.4-42 GPa pressure range has been observed. We calculated the B (where B is a bulk modulus at a given pressure) and B_0' values (389.7±18 GPa and 7.80±1.22) at 29.4 GPa from fitting of the six experimental points to a Murnaghan equation of state. As it follows from the formulation of Murnaghan equation of state, the B_0' value is a constant for the whole pressure range. We used the formula for bulk modulus definition (Eq. *IV*.4) in order to estimate the B_0 of the new HP phase at ambient pressure.

$$\mathrm{B} = \mathrm{B}_0 + \mathrm{P}\mathrm{B}_0' \qquad (IV.4).$$

Thus, B_0 value (the bulk modulus at zero pressure) of HP BS is equal to 160.7±18 GPa. Taking this B_0 value into account, the V_0 at ambient pressure has been estimated to be 156.3±2.2 $Å^3$. The obtained HP BS bulk modulus value at 29.4 GPa is of same order of magnitude as bulk modulus of NaCl-like GaSe 380(30) GPa [248]. Based on the similarity of the *r*-BS and ε-GaSe, the same order of the bulk moduli (B) of HP phases and theoretically predicted physical properties of NaCl-like GaSe, one can suppose that the same physical properties might be expected for HP BS as well, for example a metallic behavior [239].

10.3 Phonon study of *r*-BS

10.3.1 Experimental techniques

Synthesis details

We synthesized *r*-BS enriched by ^{10}B-isotope in order to investigate an isotope substitution effect in Raman spectra. Amorphous ^{10}B (enrichment > 95%) and S (Johnson Matthey, spectrographic grade) powders have been mixed in 1:1 molar ratio and compressed up to 7.5 GPa at ~1900ºC in the TTP high-temperature cell described above. For convenience, further we will indicate the rhombohedral boron monosulfide enriched by ^{10}B isotope as *r*-^{10}BS.

X-Ray Diffraction measurements at ambient conditions

The X-ray diffraction of *r*-^{10}BS has been provided again with G3000 TEXT Inel diffractometer (Cu Kα1 radiation) at ambient conditions. The sample was found to be highly crystalline with negligible admixtures of the *h*-BN. The XRD pattern of r-^{10}BS is presented in Figure IV.13.

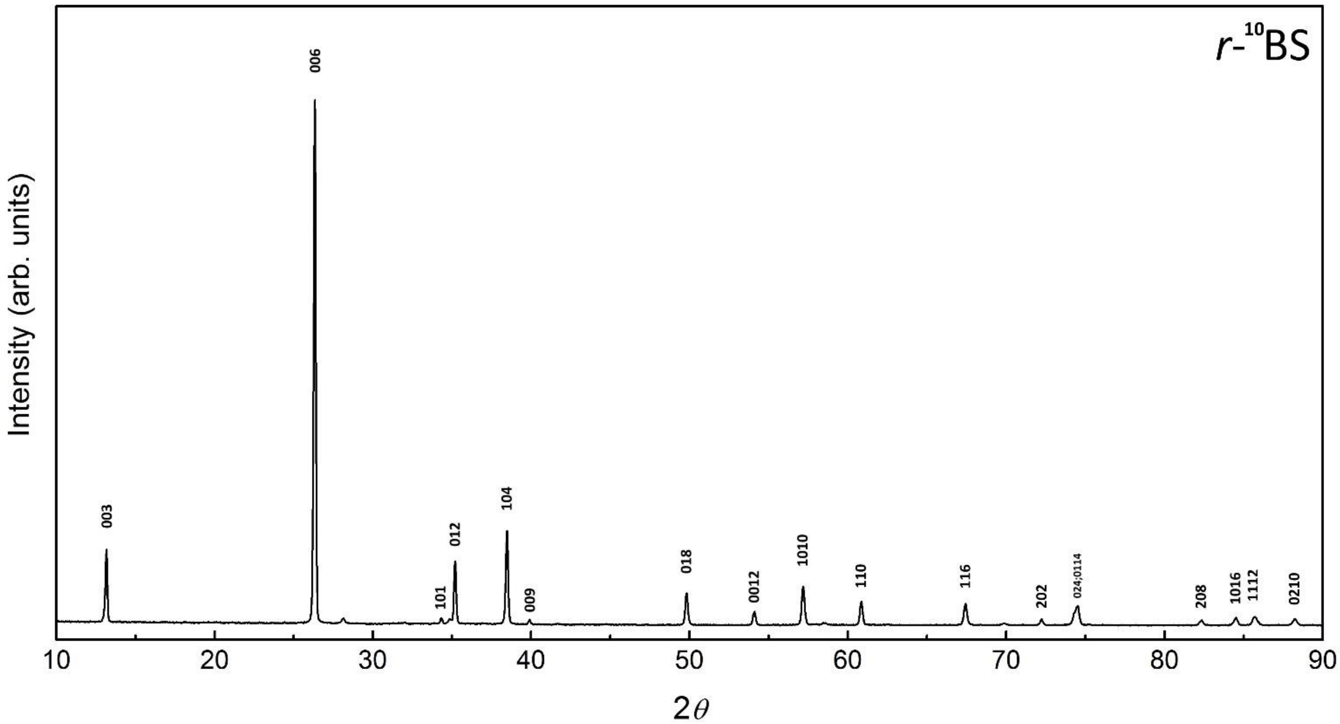

Figure IV.13. XRD pattern (λ=1.5406 Å) of *r*-^{10}BS at ambient conditions. The most intensive peaks of *r*-^{10}BS are marked by the *hkl* Miller indexes.

The lattice parameters, unit cell volume, bond lengths and bond angles of *r*-^{10}BS have been refined and are listed in Table 4. Like in the case of β-$^{10}B_2O_3$, we observed a difference between the unit cell volumes of *r*-BS and *r*-^{10}BS (deviation of ~0.56%).

Raman and IR measurements at ambient conditions

Raman spectra of *r*-BS and *r*-^{10}BS at ambient pressure have been measured using Horiba Jobin Yvon HR800 Raman spectrometer (in the 200-2000 cm^{-1} range). The 632.8 nm line of a He-Ne laser (10 μm beam spot) has been used for excitation (the laser power is less than 30 mW). A single crystal of cubic Si has been used for spectrometer calibration at room temperature. The Raman study of *r*-^{10}BS has been performed at ambient conditions in order to observe the isotope substitution effect in phonon modes.

Fourier transform infrared (FTIR) absorption spectra in mid-infrared range (450-4000 cm^{-1}) were recorded using a Bruker IFS 125HR spectrometer. Samples were uniformly mixed with KBr powder and pressed into pellets. It should be noted, that *r*-^{10}BS has not been studied by IR spectroscopy.

High pressure Raman measurements

High-pressure Raman measurements have been performed in a MDAC [265] with 300 μm culets. *r*-BS sample has been putted into a 50 μm hole drilled in a rhenium gasket pre-indented down to 25 μm thickness. In these measurements neon pressure transmitting medium has been used. Pressure in the MDAC was determined by the ruby luminescence technique [171] using the calibration proposed in Ref. 212. The pressure has been measured before and after each run; drift during single run did not exceed 0.4 GPa in the 0-34 GPa pressure range.

Raman spectra were excited with the 632.8 nm line of a He-Ne laser (10 μm beam spot) and recorded in the 200-2000 cm^{-1} range using Horiba Jobin Yvon HR800 Raman spectrometer. The spectrometer was calibrated using a single crystal of cubic Si at room temperature. A laser power at the sample was estimated to be less than 30 mW. No effect due to laser heating of the sample was observed. Raman spectra of *r*-BS were measured in 23 pressure points from 1.8 to 34.0 GPa at room temperature.

Calculation details

The phonon properties of *r*-BS at ambient conditions and under pressure (up to 34 GPa) have been studied using first principles LCAO calculations performed using the CRYSTAL09 code [207]. The phonon frequencies of *r*-^{11}BS* and *r*-^{10}BS*at ambient conditions have been calculated using the direct (frozen-phonon) method [207,223]. For the phonon calculation under compression, we employed already performed calculations of *r*-^{11}BS* equation of state. The phonon frequencies at selected pressures up to 34 GPa have been calculated using optimized geometries for corresponding reduced volume unit cells. The pressure dependence of the phonon frequencies of *r*-^{11}BS* are available only up to 34 GPa, because of divergence of the parameters of electron structure optimization at highly reduced unit cell volume (P > 34 GPa).

10.3.2 Results and discussion

According to the structural data presented in Table 5, lattice parameters of *r*-BS enriched by ^{10}B isotope differ from those of *r*-BS: *r*-^{10}BS has the smaller unit cell volume as compared to that of *r*-BS. Nonetheless, it should be also underlined that *a* lattice parameter of *r*-^{10}BS is equal to that of *r*-BS. Hence, the main contribution to the volume difference of *r*-BS and *r*-^{10}BS is due to the difference between the *c* lattice parameters. As shown in Table 5, in spite of the fact that the bond lengths in S_3B-BS_3 unit of *r*-^{10}BS (herein the atoms positions refined in Ref. 154 have been used) and *r*-BS are very close to each other, the layer thicknesses are different by 0.025 Å. On other hand, the interlayer distances are the same. Thus, we can conclude, that the isotope substitution does not change the interlayer interactions (it does not affect the Van-der-Waals bonds), while it influences the intralayer ionic-covalent bonds.

r-BS can be considered in both rhombohedral and hexagonal primitive cells (or in other words in rhombohedral and hexagonal settings). In hexagonal setting it has three layers with A-B-C stacking motive, whereas in rhombohedral setting there is only one layer.

In layered crystals, the vibration modes may be separated in the modes of the isolated layer (internal modes in molecular crystals), and the whole crystal modes. Thus, considering the hexagonal primitive cell, since each layer contains the same number of atoms, the number of modes from isolated layer should be multiplied by the number of layers in the primitive unit cell. That gives rise to "rigid layer modes" (similar to the external modes in molecular crystals) and "Davydov multiplets". However, the Raman studies on the $A^{III}B^{VI}$ polytypes [247,265-270] have proved that the layer modes are not dependent on the number of layers.

r-BS has 4 atoms in the unit cell in rhombohedral setting. Thus, 12 normal modes of vibration at the zone center are described by the irreducible representation of the C_{3v} point group:

$$\Gamma = 4\mathrm{A}_1 + 4\mathrm{E} \qquad (IV.5)$$

where the E modes are doubly degenerate. All the optic modes are both infrared and Raman active and thus there should be 6 non-degenerate Raman active modes, since $A_1(1)$ and E(1) modes are the acoustic ones. Speaking about the phonon properties of *r*-BS we should stress that, as in γ-InSe, the vibrational spectra and all corresponding discussion will concern the vibrations in one layer.

At ambient conditions *r*-BS Raman spectra have been investigated in the 200-2500 cm^{-1} frequency range. Five Raman active modes have been observed in the 200-1200 cm^{-1} range (Figure IV.14). In the case of isotope enriched *r*-^{10}BS, only four bands have been observed in the same frequency domain. No peak was observed above 1200 cm^{-1} for both compounds.

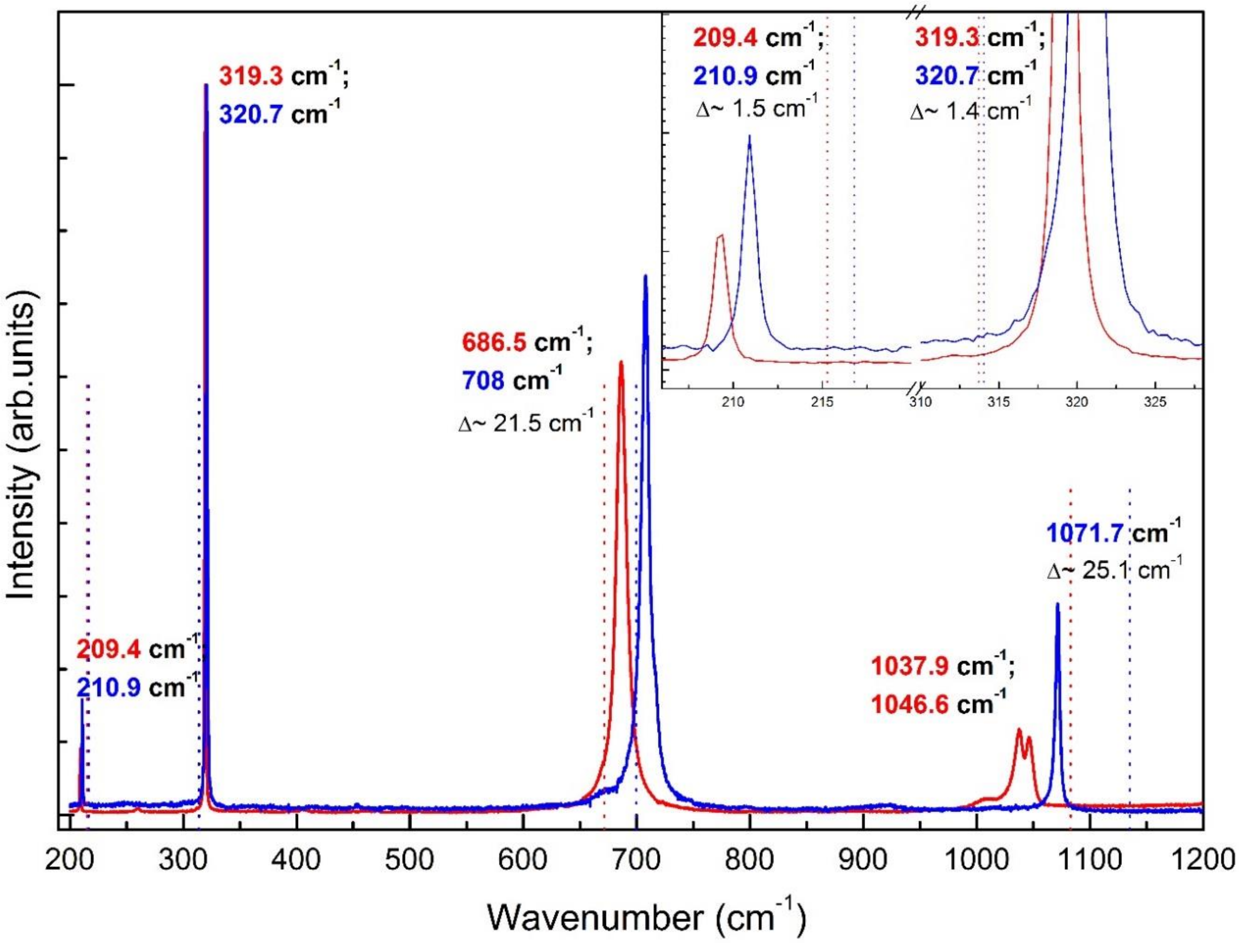

Figure IV.14. Experimentally observed Raman bands in *r*-BS (red) and *r*-^{10}BS (blue) at ambient conditions. The positions of the phonons predicted for *r*-^{11}BS* and *r*-^{10}BS* by LCAO calculations are marked by the red and blue dotted lines respectively. Inset: magnification of the 200-330 cm^{-1} region. Frequency values of experimentally observed modes and the isotope shift values ($\Delta\omega = \omega$ (*r*-^{10}BS) - ω (*r*-BS)) are indicated.

As one can easily see from the Figure IV.14 the Raman spectra of *r*-BS and *r*-^{10}BS contain less than the six bands predicted from the irreducible representation of non-degenerate Raman modes. The frequencies of all modes for *r*-^{10}BS and *r*-BS are presented in Table 7.

Modes	Wavenumber (cm^{-1})							
	[268]	LCAO	Experiment			LCAO		
	ω_0(γ-GaSe)	ω_t(γ-GaSe*)	ω_0(*r*-BS)	ω_0(*r*-^{10}BS)	$\Delta\omega$	ω_t(*r*-^{11}BS*)	ω_t(*r*-^{10}BS*)	$\Delta\omega$
E(3)	59.4	62	209.4	210.9	1.5	215.3	216.8	1.5
A_1(3)	135	143	319.3	320.7	1.4	313.7	314.1	0.4
E(4)	211	236	686.5	708	21.5	671.7	699.8	28.1
?	-	-	1037.9	-	-	-	-	-
A_1(4)	309.5	338	1046.6	1071.7	25.1	1083.2	1135.3	52.1

Table 7. The phonon frequencies of *r*-BS, *r*-^{10}BS and γ-GaSe (ω_0) experimentally observed by Raman spectroscopy and *r*-^{10}BS*, *r*-^{11}BS* and γ-GaSe* phonon frequencies (ω_t) theoretically predicted by LCAO calculations. Isotope shifts ($\Delta\omega$) of observed Raman bands are presented.

Like in the case of the isotope effect in β-B_2O_3 we used the simplest model of harmonic oscillator. The Raman bands of isotope enriched sample are expectedly shifted towards high frequencies. However, unlike β-B_2O_3, we observed an increase of the isotope shift values for the high frequency Raman bands. Isotope shift exceeds 20 cm^{-1} for the pair of high-frequency phonons while it does not exceed 2 cm^{-1} for the low-frequency ones.

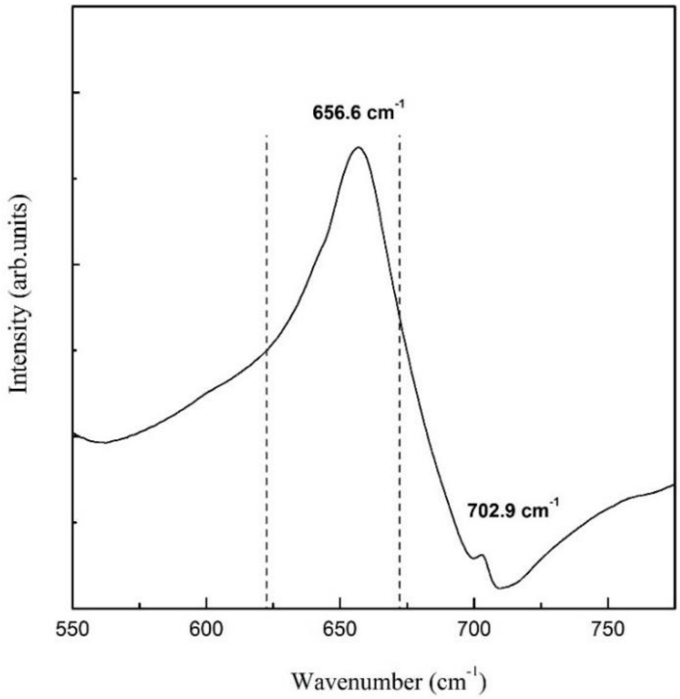

Figure IV.15. Experimentally observed phonons of *r*-BS in mid-infrared region at ambient conditions. The positions of the phonons predicted by LCAO calculations are marked by the dashed lines.

IR spectrum of *r*-BS (Figure IV.15) in the 200-4000 cm^{-1} frequency range shows many bands. Most of them can be explained by the presence of impurities and adsorbed water. However, based on the shape and relative intensities of IR spectrum of one of GaS polymorphs [271] we have characterized two bands at 656.6 cm^{-1} and 702.9 cm^{-1}, which can be supposed to be the vibrational modes of *r*-BS. Our suggestion has been later supported by the LCAO calculations (see Table 8). It should be noted that we could observe only TO vibrational modes due to the experimental conditions (use of transmission IR spectroscopy).

Modes	Wavenumber (cm^{-1})	
	Experiment	LCAO
	ω_0 (*r*-BS)	ω_t (*r*-^{11}BS*)
E(2)	656.6	622.5
A_1(2)	702.9	672.2

Table 8. The phonon frequencies of *r*-BS experimentally (ω_0) observed by IR spectroscopy and theoretically predicted (ω_t) by LCAO calculations.

The results of our LCAO calculations of the phonon modes corresponding to the lowest temperature limit (T = 0 K) agree with the experimentally observed bands wavenumbers at ambient conditions (Table 7,8). Based on LCAO calculations performed for *r*-^{11}BS* and *r*-^{10}BS*, the Raman and IR modes assignment has been performed. The deviation of calculated Raman modes from experimentally observed ones does not exceed 3.4% and 5.6% for *r*-BS and *r*-^{10}BS respectively. The deviation of the calculated IR modes from the experimentally observed bands for *r*-BS is less than 5.5%. To confirm the obtained results, we provided test calculation of phonon frequencies of γ-GaSe, which is the closest structural analog of *r*-BS with reported Raman spectra [268]. Results of these calculations presented in Table 7 indicate that the LCAO calculations in our work give rather confident data. One can see that the sequence of the modes found in Raman spectra (E(3), A1(3), E(4), A1(4)) of γ-GaSe is the same as for *r*-BS. This fact makes it clear that compounds of the same symmetry and almost similar structure exhibit the common sequence of the phonons.

The LCAO calculations have also shown that the IR intensities of the E(2) and A_1(2) modes are much higher than those of the other modes. In spite of the fact that all modes are considered to be both Raman and IR active, the modes with the highest IR intensities have not been observed in Raman spectra. Taking into account this fact, we suppose that those modes, which have not been observed in Raman spectra are observed in IR spectra.

The rather intense band at 1037.9 cm^{-1} observed in Raman spectrum of *r*-BS is not predicted by LCAO calculations. It has been observed only in the Raman spectra of *r*-BS with the natural boron isotope content. The coincidence of XRD patterns of *r*-^{10}BS and *r*-BS excludes any possibility of structural difference or systematic alternating defects. Moreover, it has been noted [268] that the vibrational frequencies are dominated by the intralayer forces and that changes in stacking sequence has no influence on the frequency of the "internal" layer modes. However, invisible for XRD technique random structural defects may occur in the polycrystalline sample and thus could lead to unpredictable bands arrangement and relative intensities or even appearance of band splitting in Raman and IR spectra. Moreover, one can notice that Raman spectra of GaSe and GaS polymorphs (structural analogs of *r*-BS) have the same doublet at high-frequency wavenumbers [268,269]. *Hoff et al.* [268] showed that some of the bands can appear as a result of combination of A(LO) – E(LO) and A(TO) – E(TO) modes. This could be an explanation of the doublet appearance, but proving this assumption requires techniques that are not available in the present work.

An irreducible representation (Eq. *IV*.1) has been assigned to the set of atomic displacement patterns in Figure IV.16, in a manner similar to that previously used [268]. We determined the directions and amplitudes of the atoms oscillations from the *ab initio* LCAO data using the

MolDraw visualizing software. In this Figure IV.16 the bracketed numbers associated with the group representations have no physical meaning and are used only as labels, whereas the arrows lengths indicate the relative amplitudes of B and S atoms.

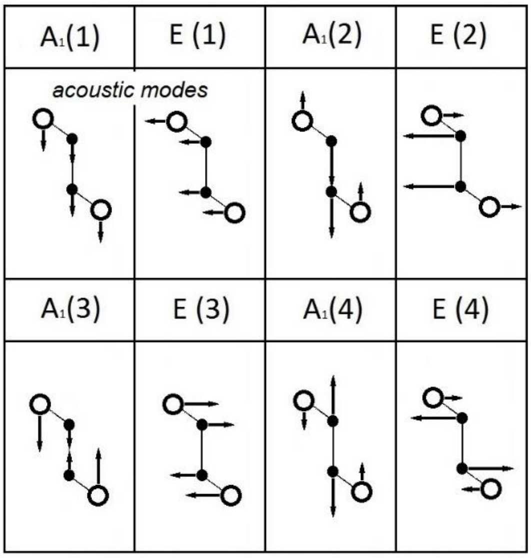

Figure IV.16. Normal vibration modes of *r*-BS. The arrows length reflects relative amplitudes of B and S atoms oscillations in the mode. The amplitudes have been estimated from LCAO calculations.

Taking into account the information presented in Table 7 and in Figure IV.16 the different isotope shift values of *r*-BS Raman bands can be explained. According to Figure IV.16, among all observed Raman bands the A1(4) and E(4) modes have the largest boron atoms displacements. Thus, considering the simplest harmonic oscillation model, it has been concluded that the frequencies of E(4) and $A_1(4)$ modes are significantly influenced by the oscillation frequencies of the boron atoms, and therefore by boron atoms mass (pure isotopic crystals).

As mentioned in Chapter III, the stronger interatomic interaction leads to the shorter bonds and greater Raman shifts. We also supposed that an oscillation of the structural part, like S-B-B-S, can be roughly divided and considered as a set of its smaller parts: S-B, B-B and B-S. Using this supposition and the information about the atoms displacements in S-B-B-S unit presented in Figure IV.16 the Raman bands arrangement in Figure IV.14 can be explained.

As described in previous part, the B-S bonds have been found to be more rigid as compared to the B-B one. In Figure IV.16 the modes $A_1(4)$ and E(4) are referred to the S-B-B-S oscillations, in which the B and S atoms are moving in opposite directions. Moreover the boron atoms displacements are the maximum among all Raman modes. Thus at these mode vibrations the rigid B-S bonds are considerably distorted and consequently have the highest frequencies. Unlike $A_1(4)$ and E(4) modes, in case of $A_1(3)$ and E(3) modes the B and S atoms move in the same directions, leading to the less B-S bonds dependent and hence resulting in lower frequencies. It should be also noted, that in low- ($A_1(3)$ and E(3)) and high frequency ($A_1(4)$ and E(4)) mode pairs the A_1 modes have the highest frequencies.

The pressure dependence of the five vibrational modes has been measured up to 34 GPa. Raman spectra at different pressures are shown in Figure IV.17, indicating rather strong phonon's shift.

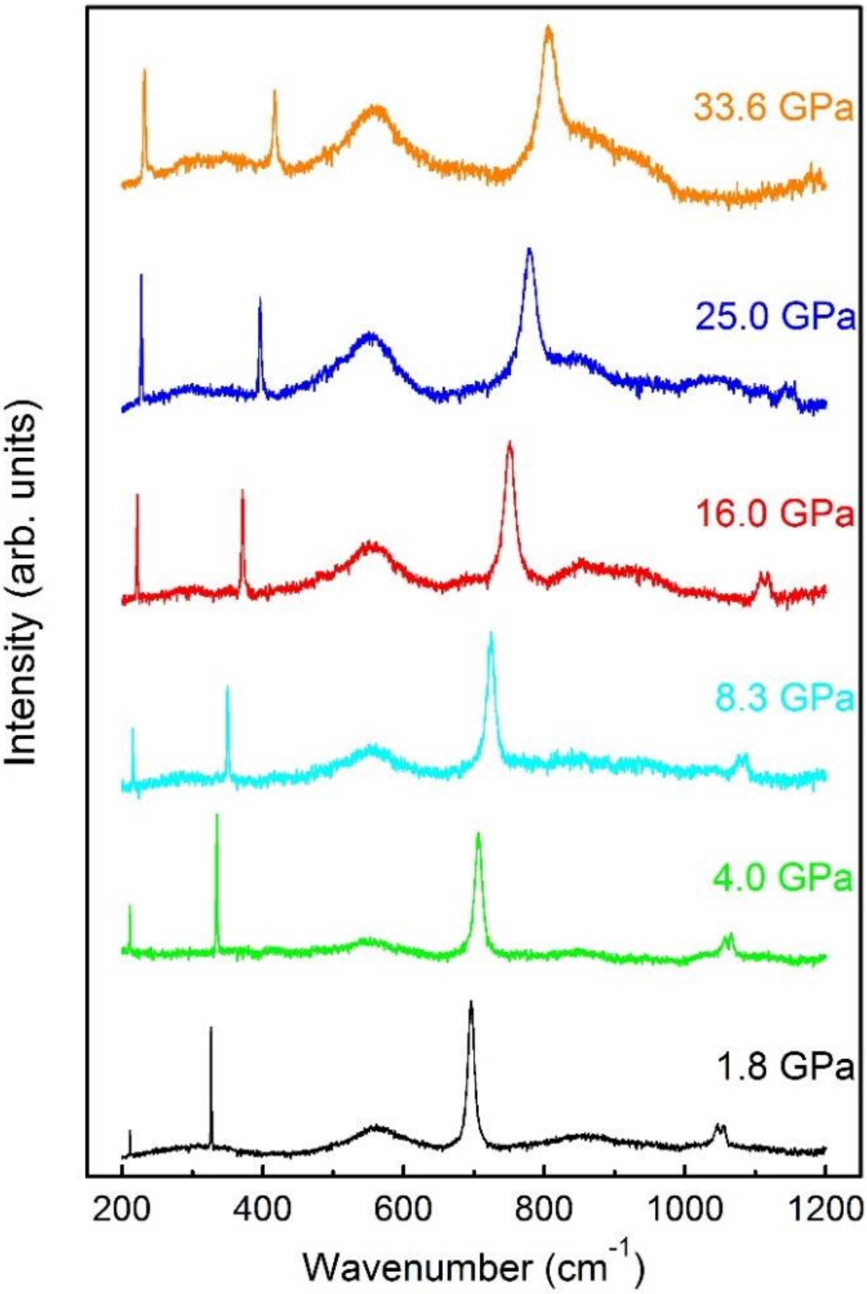

Figure IV.17. Raman spectra of *r*-BS under compression up to 34 GPa and at room temperature.

During the compression, all the lines shift monotonically toward high frequencies and no new line appeared. The LCAO *ab initio* calculations provided for the phonon modes at selected pressure points up to 34 GPa match nicely with the experimental observations and support them (Figure IV.18). Taking into account the fact that *r*-BS transforms to the HP phase already around

30 GPa at room temperature one can conclude that BS HP phase does not have the Raman bands (at least at high pressure). The absence of new Raman bands at high pressure corresponding to the new BS HP phase supports our supposition about its probable structure motives: CsCl or NaCl (which are, according to the selection rules, Raman inactive). Unlike the formation of HP phase of GaS followed by rapid disappearing of β-GaS Raman bands [270], in our HP Raman measurements we did not observe any dramatic drop of the bands intensities. It can be explained by the coexistence of the both *r*-BS and HP phases up to the highest pressures of our Raman study (see Figure IV.10).

A broad band in the 500-625 cm^{-1} range was observed, but no correlation between band intensities, frequency shifts and pressure applied to the system could be found. Thereby we have supposed that the origin of this band is connected with the non-homogeneity of the powder sample under study. Simultaneous growing of the background and bands broadening has been observed at high pressure. So, high-frequency bands at 1037.9 and 1046.6 cm^{-1} became indistinguishable above 29 GPa. It should be also noted that a monotonic pressure dependence of full width at half maximum (FWHM) of the second (~320 cm^{-1}) and third (~700 cm^{-1}) bands have been observed.

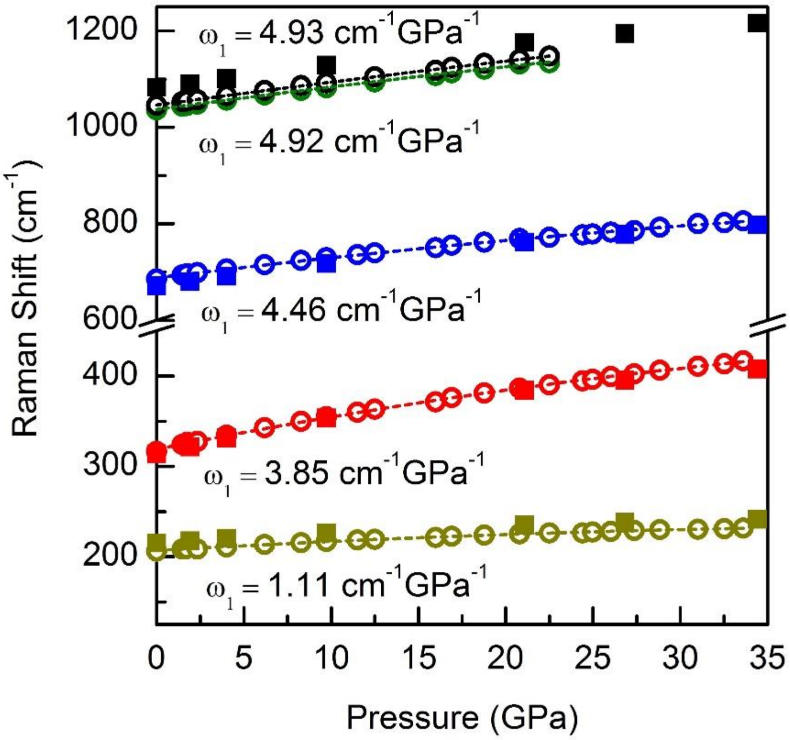

Figure IV.18. Pressure dependencies of the phonon mode frequencies experimentally observed (open circles) and theoretically calculated (solid squares). Dashed lines are quadratic least squares fits ($R^2 > 0.999$); the ω_1 parameters of (Eq. *III*.9) are listed.

We calculated the Grüneisen parameters for *r*-BS using the (Eq. *III*.8) for approximation of the phonon modes pressure dependencies. A least-squares fit of (Eq. *III*.8) to the experimental data yields the values of first-order parameters (δ_0) (see Chapter III) for all five observed Raman bands.

We defined the Grüneisen parameters $\gamma_G = B_0 \times \delta_0$ for the B_0 = 48.4 GPa (Murnaghan formulation), 47.1 GPa (Birch-Murnaghan formulation) and 46.7 GPa (Vinet formulation) obtained from *in situ* HP XRD measurements. All γ_G values are collected in Table 9.

Modes	ω_1, cm^{-1}GPa^{-1}		γ_G		
	Experimental	LCAO	*M*	*B-M*	*V*
E(3)	1.11	1.24	0.243	0.236	0.234
$A_1(3)$	3.85	4.42	0.515	0.501	0.497
E(4)	4.46	5.15	0.269	0.262	0.260
?	4.92	-	0.182	0.177	0.176
$A_1(4)$	4.93	5.07	0.182	0.177	0.176

Table 9 The Grüneisen parameters (γ_G) calculated for bulk modulus values obtained from Murnaghan (*M*) and Vinet (*V*) equation of state approximations and ω_1 values determined for theoretical and experimental data presented in Figure IV.17.

As already mentioned, all experimentally observed Raman bands shift to the high frequencies under compression, but the extension of these shifts was different. We used a quadratic equation (Eq. *III*.9) in order to fit these pressure dependencies. The ω_1 parameters used in (Eq. *III*.9) are given in Figure IV.18 and listed in Table 9. We also employed (Eq. *III*.9) for an approximation of the calculated phonons under compression. The ω_1 parameters obtained from theoretical data fitting are also listed in Table 9. Observed coefficients ω_1 and ω_2 have values typical for boron-rich compounds [272-274]: ω_1 values are not exceeding 5 cm^{-1}GPa^{-1}, while ω_2 values are slightly negative tending to zero. Besides, these coefficients are of the same order of magnitude as those of the corresponding modes in GaSe [275] and GaS [270].

Based on the information presented in Table 9 and in Figure IV.16 the different ω_1 values of $A_1(3)$, E(4) and $A_1(4)$ can be explained. As already suggested the E(4) and $A_1(4)$ phonon modes frequencies are situated in the high frequency range due to maximum boron atoms displacements in opposite directions relative to the sulfur atoms and therefore big changes/deformations of the rigid B-S bonds. There are strong grounds to expect that these large atoms displacements will be dramatically influenced by the compression, especially along *c* axis (because of high van-der-Waals bonds compressibility), and consequently the corresponding phonon modes will reveal the maximum ω_1 values. The $A_1(3)$ mode is referred to the smaller B-S bond deformations (the B-S sublayers oscillate against each other), which makes the ω_1 value lower or, in other words, has a slightly negative effect on the ω_1 value. On other side, according to Figure IV.5 the B-B pair is rather compressible, so that it is strongly affected by the compression, giving a positive effect on ω_1 value. So, the final ω_1 value of $A_1(3)$ mode is a result of summing of the negative and positive effects.

Due to anisotropic compression of *r*-BS (a high compression of interlayer space and low compression of intralayer space), one can assume that the atoms oscillations along the *c* axis are strongly influenced by HP than in case of oscillations in the layer plane. This assumption is supported by the experimental observations: the $A_1(3)$ and $A_1(4)$ modes (concerning the oscillations along *c* direction) have the higher ω_1 values in both low-frequency and high-frequency phonon mode pairs.

Unlike $A_1(3)$, E(4) and $A_1(4)$ modes, the low-frequency mode E(3) revealed unusual behavior under compression (see Table 9). According to Figure IV.16 only E(3) mode reveals the same amplitude of vibration for boron and sulfur atoms. Summing up, we can conclude the particularity of the E(3) mode with respect to the other observed modes. This mode is similar to the E mode (60 cm^{-1}) of γ-GaSe, E" mode (60 cm^{-1}) in ε-GaSe and E_{1g} mode (74 cm^{-1}) in β-GaS, because all these modes have the same displacement pattern (rigid half layer shear modes). Moreover, in these compounds, these modes have low pressure coefficients, in contrast to the other modes. In Ref. 270, the peculiar pressure coefficient of the E_{1g} mode was explained by the similarity of its displacement pattern with an edge-of-the-zone TA mode as regards the destabilizing effect of pressure upon electronic contributions to restoring forces. The pressure coefficient of the E(3) mode can be explained in the same way. It is a rigid half-layer shear mode, involving mainly B-B restoring forces, as far as vibration amplitudes for B and S atoms are the same in this mode. Since this mode does not change much the B-S distance within the same half-layer, this vibration will be viewed as a transverse acoustical (TA) mode of BS molecules, on a chain along the *c* axis. Edge-of-the-zone TA modes in 3D crystals are known to exhibit negative coefficients of the pressure dependence. Under pressure the electronic charges involved in the first neighbors bonds delocalize towards interlayer space, which soften the total restoring spring, and results in a negative pressure coefficient. We assumed that explanation given in Ref. 270 can be used also for E(3) mode. Low coefficient of the pressure dependence of E(3) mode is a result of two contributions: a positive one coming from the increase with pressure of the interlayer interaction and therefore distance decrease between the atoms, and a negative one coming from the shear motion and the TA-like character in this mode. The total may be slightly positive, zero, or slightly negative i.e. much less than for other intralayer modes.

The same explanation concerning weak pressure dependence of the low-frequency Raman band was proposed in [275]. Very small pressure coefficient of such mode can be explained by the compensation of the decrease in the B-B bond length, which leads to the frequency increase under pressure, and the charge delocalization, which tends to depopulate the B_2 radical environment and thus decrease the B-B bond strength. The same effect can be observed in diatomic molecules under the pressure (I_2, H_2 *etc.*), where the charge transfer occurs between the space towards to the intermolecular region, tending to symmetrization of the bonds and eventually leading to the same intensity of intra- and intermolecular ones. In other words, the charge density between the layers increases with the pressure because of interlayer space decrease and also of the total effective number of electrons squeezed out from intralayer space.

10.4 Conclusions

Like in the case of B-O system, an X-ray investigation of binary compounds in B-S system is rather difficult due to the low Z number of boron and related problems of detection and characterizations of these compounds. The *r*-BS has been chosen as subject of our investigations due to very poor data on the physical properties of this promising $A^{III}B^{VI}$ layered semiconductor. In this chapter we measured the equation of state and explored the stability range of *r*-BS between 0 to 42 GPa at room temperature and studied the phonon modes at ambient and under high pressures (up to 34 GPa).

As a result of our HP XRD studies, the equation of state of *r*-BS has been measured for the first time. The bulk modulus and its first pressure derivative are 46.7 GPa and 6.7 respectively (according to the Vinet formulation, revealed the lowest χ^2 value). The B_0 and B_0` values have been also estimated by *ab initio* LCAO calculations. The obtained theoretical values differ from the experimental ones, due to the calculation error in estimation of interlayer interactions. This calculation problem of the layered structures is well known and has been expected. However, the using of the experimentally determined first pressure derivative for the fitting of the theoretical E(V) data gave us the B_0 value rather close to the experimental one. The pressure dependences of the lattice parameters of *r*-BS has been plotted and compared with those of other $A^{III}B^{VI}$ layered compounds (GaSe, GaS, InSe). According to the comparative analysis of these pressure dependencies *r*-BS has been found to be the most rigid (or "resistant" to the compression in all directions) $A^{III}B^{VI}$ compound.

Taking into account the difficulties and the time required for the special XAFS and XRS measurements in order to estimate the changes of the B-B and B-S distances and angles between the atoms in one layer during compression the special hypothesis/approach has been engaged. We supposed that the atoms in the layer do not dramatically change their positions during compression. Thus, they can be considered fixed. This hypothesis allowed us to completely describe the layer structure change under compression, using our HP XRD data and the B and S atoms positions refined previously [154]. The interatomic distances under compression in the layer of *r*-BS have been also estimated with help of *ab initio* calculations (in which the atoms positions variations was permitted). Theoretically estimated bonds pressure dependencies were found to be close to the experimental ones, which leads one to the conclusion that the approach/hypothesis proposed above is rather confident. It should be noticed that the linear compressibility of the B-S bonds in *r*-BS is greater than that of the *a* axis in contrast to other $A^{III}B^{VI}$ layered compounds [240,252]. Moreover, unlike other $A^{III}B^{VI}$ compounds the compressibilities of the B-S bonds in the "top" and in the "bottom" of the layer have been found to be different.

The formation of the HP BS phase around 30 GPa has been observed and described. Due to the low quality of the diffraction pattern of the HP phase, only the preliminary refinement of the crystal symmetry and lattice parameters has been done. The unit cell of new BS phase has been proposed to be cubic with NaCl or CsCl structure (a = 5.086(1) Å at pressure of 29.4 GPa). According to arrangement of the diffraction peaks in XRD pattern the CsCl structure seems to be the most probable. On other side, only NaCl structure satisfies the condition that the unit cell volume per structure unit (in our case it is BS) must decrease at HP phase transition. The HP BS equation of state and its parameters have been estimated in 30-42 GPa pressure range. The bulk modulus value at 29.4 GPa has been found to be 389.7±18 GPa. This value has the same order of magnitude as bulk modulus values of the high pressure phases of other $A^{III}B^{VI}$ layered semiconductors studied previously. The estimated B_0 value (at zero pressure) is equal to 160.4 GPa, whereas the estimated V_0 is ~156 Å^3.

A phonon study of *r*-BS by means of Raman and IR spectroscopy techniques at ambient pressure and room temperature have been performed for the first time. Thanks to the *ab initio* calculations of the phonon mode frequencies and modes visualization, the assignment of all experimentally observed bands to the phonon modes has been provided. The ^{10}B isotope substitution effect has been studied in *r*-BS Raman spectrum. The isotope Raman shifts have been explained. The phonon properties of *r*-BS have been also studied at room temperature and under HP up to 34 GPa by means of Raman spectroscopy. Based on the *ab initio* calculations of the phonon frequencies for the reduced unit cell volumes, modes assignment and pressure dependencies of the B-S and B-B bonds, the explanation of the phonon modes under compression have been proposed. The Grüneisen parameters of all Raman-active phonon modes have been calculated. The information retrieved from the study of *r*-BS phonon properties might be a good base for the further optical *r*-BS studies.

Chapter V

11 Studies in B-Se binary system

According to the literature review presented in Chapter I, the B-Se system resembles the B-S system. However all the binary compounds of B-Se system have been synthesized only at ambient pressure. Taking into account the similarity of B-S and B-Se systems one might expect the same physical properties of the binary compounds of both systems synthesized under extreme conditions.

In this chapter we will provide a description of our preliminary studies of the new compounds in B-Se system. From our *ex situ* HP-HT studies of different ratios of boron and selenium (1:1, 2:1, 3:1, 6:1, 3:2, 13:1 respectively) in the wide pressure and temperature ranges (up to 15 GPa and 2000 K) we did not extract any reliable and confident data about new B-Se compounds. Taking this into account, the HP-HT synthesis in LVP in combination with the synchrotron radiation have been provided in order to immediately observe *in situ* the possible metastable phases. Thus, in this chapter only our *in situ* experiments and the obtained results will be described and discussed. Different B:Se stoichiometries have been studied: 1:1, 6:1 and 13:1. Based on the results of *in situ* XRD measurements and XRD and Raman measurements at ambient conditions it will be shown that we can suppose the formation of a new metastable compound with general formula $B_{1-x}Se_{1-y}$ ($x < 1$, $y < 1$). However, further detailed *in situ* and *ex situ* studies in B-Se system are necessary.

11.1 Synthesis of the new compounds in B-Se binary system

11.1.1 *Experimental techniques*

Synthesis details

The HP-HT synthesis of the new compounds in B-Se binary system have been implemented using PEP in 3-4 GPa pressure range and at temperatures above 1200°C from amorphous boron (Johnson Matthey, 99%) and selenium (Johnson Matthey, spectrographic grade) powders mixed in the 1:1, 6:1 and 13:1 molar ratios. Four *in situ* runs (Run 01, Run 02, Run 03 and Run 04 correspond to 1:1, 6:1 and 13:1 molar ratios respectively) have been performed at synchrotron SOLEIL PSICHE beamline.

The scheme of the PEP assembly used in our studies is presented in Figure II.4. The mixture of fine powders of the amorphous boron and selenium were placed in *h*-BN capsules and almost transparent for X-rays graphite heaters provided a resistive heating (up to 1800°C) of the sample area. Taking into account the low Z-number of boron, the special X-ray transparent 10 mm BE gaskets have been used. The experiments have been conducted at pressure of 3-4 GPa and temperatures ~1200-1800°C with reaction time of ~10 min. In Run 01, Run 02 and Run 03 the samples were cooled down by the slow switching off the power and decompressed, whereas in Run 04 the sample was thermally quenched and decompressed.

High pressure X-ray diffraction measurements

The *in situ* HP-HT XRD measurements have been implemented at synchrotron SOLEIL PSICHE beamline in energy-dispersive mode (white beam with energy spectrum from 15 to 80 keV) with the fixed angle between the X-ray beam and Ge solid-state detector (SSD). The selected angle was equal to 8.041°. The set of beam collimators installed in optic hutch of PSICHE beamline (see Figure II.21 and Figure II.26) delivered a required beam profile size and allowed to define the detected area and effectively remove the diffraction peaks of PTM and heater.

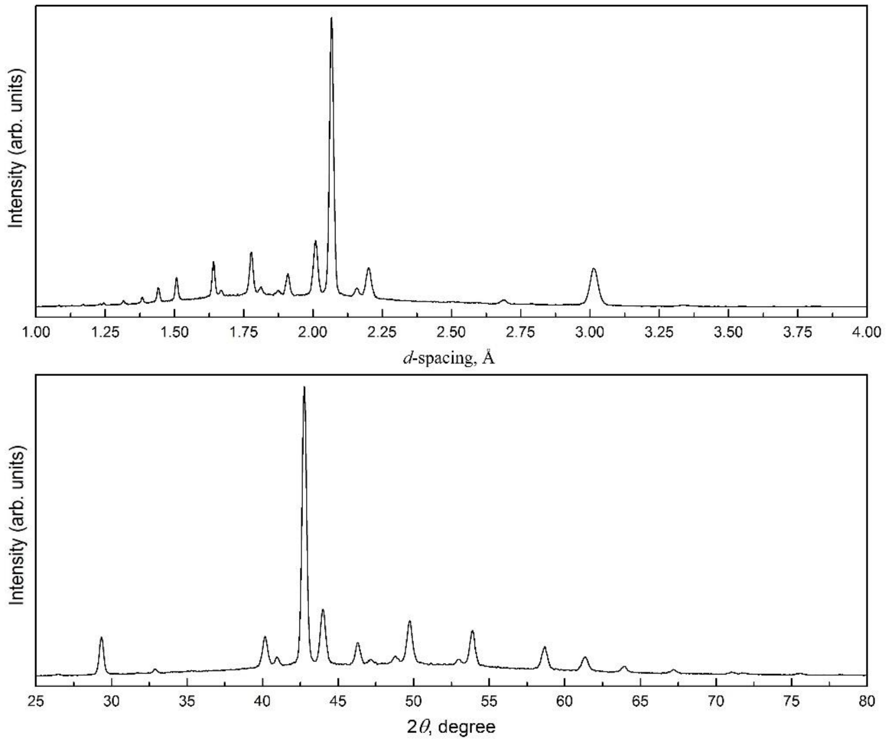

Figure V.1. The transformation of the EDX pattern (Int.(*d*-spacing)) in Run 01 to ADX pattern (Int.(2*θ*)) for Cu Kα1 radiation.

The pressure determination was implemented with help of oil pressure *versus* sample pressure calibration curve. The pressure values obtained from this “external” pressure gauge nicely matched with those determined during the experiment using *h*-BN EoS. The pressure deviation from the set pressure value did not exceed 0.05 GPa in the whole pressure range thanks to stable oil pressure of automatic pump (Sanchez Technologies). The temperature measurements have been provided using the power *versus* temperature calibration curve. Selenium has been also used as internal standard in these measurements as its melting point under compression is well known [276,277].

The XRD data acquisition was implemented by SSD with an exposure time of 60 seconds. The EDX patterns obtained during the measurements were converted (from Int.(E or *d*-spacing)) to the conventional Int.(2θ) form (for Cu Kα1 radiation) and treated by Powder Cell software. The example of such transformation of EDX to ADX pattern is presented in Figure V.1. The lattice parameters and unit cell volume of suppositional "goal" compound were determined by means of DICVOL04 and WinPLOTR packages in FullProf software [195-197].

Raman measurements at ambient conditions

Raman spectra of the obtained samples at ambient pressure have been measured using Horiba Jobin Yvon HR800 Raman spectrometer (in the 200-2000 cm^{-1} range). The 632.8 nm line of a He-Ne laser (10 μm beam spot) has been used for excitation (the laser power is less than 30 mW). A single crystal of cubic Si has been used for spectrometer calibration at room temperature.

11.1.2 Results and discussion

The *in situ* experiments in B-Se binary system provided at PSICHE beamline can be roughly divided on five main steps: (1) the compression at room temperature, (2) the heating, (3) melting of Se, (4) the chemical reaction between B and melted Se at the continuing heating and (5) finally slow decrease of temperature (except of Run 04) and pressure. For instance, the steps (1)-(4) in Run 01 are presented in Figure V.2. Due to the fact that amorphous boron is almost "invisible" for X-rays, only diffraction peaks of Se (and sometimes the peaks of some contaminations, e.g. *h*-BN) have been observed. In Figure V.2 one can see, that initial compression at room temperature led to the broadening of the Se diffraction peaks due to crystal lattice distortion (micro-strain of the Se grains). However, the further heating releases this micro-strain between the grains and the diffraction peaks become narrower and reach almost the same width right before Se melting. After melting of Se, at the continuing heating, new diffraction peaks appeared which clearly indicates that a chemical reaction underwent. Based on data presented in Ref. 277 no transitions of trigonal Se to the tetragonal or monoclinic high-pressure phases (both at > 10 GPa) should be expected at the P,T conditions reached in our experiments. Nonetheless, the synthesis conditions allowed us to expect β-B formation [29].

In Figure V.2 the new peaks which can be presumably attributed to the possible new B-Se compounds are marked by the red stars. However, except of the chemical reaction between B and Se, the processes of B and Se oxidation happened as well (due to the fact that the sample assembly was not isolated from the environment). During the measurements we registered the B_2O_3 and SeO_2 formations. According to the phase diagram of B_2O_3 and SeO_2 [123,278], orthorhombic γ-SeO_2 (*Pmc*2$_1$) and hexagonal α-B_2O_3 (*P*31) are the most probable phases at these P,T conditions. Taking this fact into account, the deviations of stoichiometric ratios of boron and selenium in synthesized new B-Se compounds from initial molar ratios (1:1, 6:1, 13:1) should be expected. It should be also marked that the formation of the new ternary B-Se-O compounds cannot be excluded.

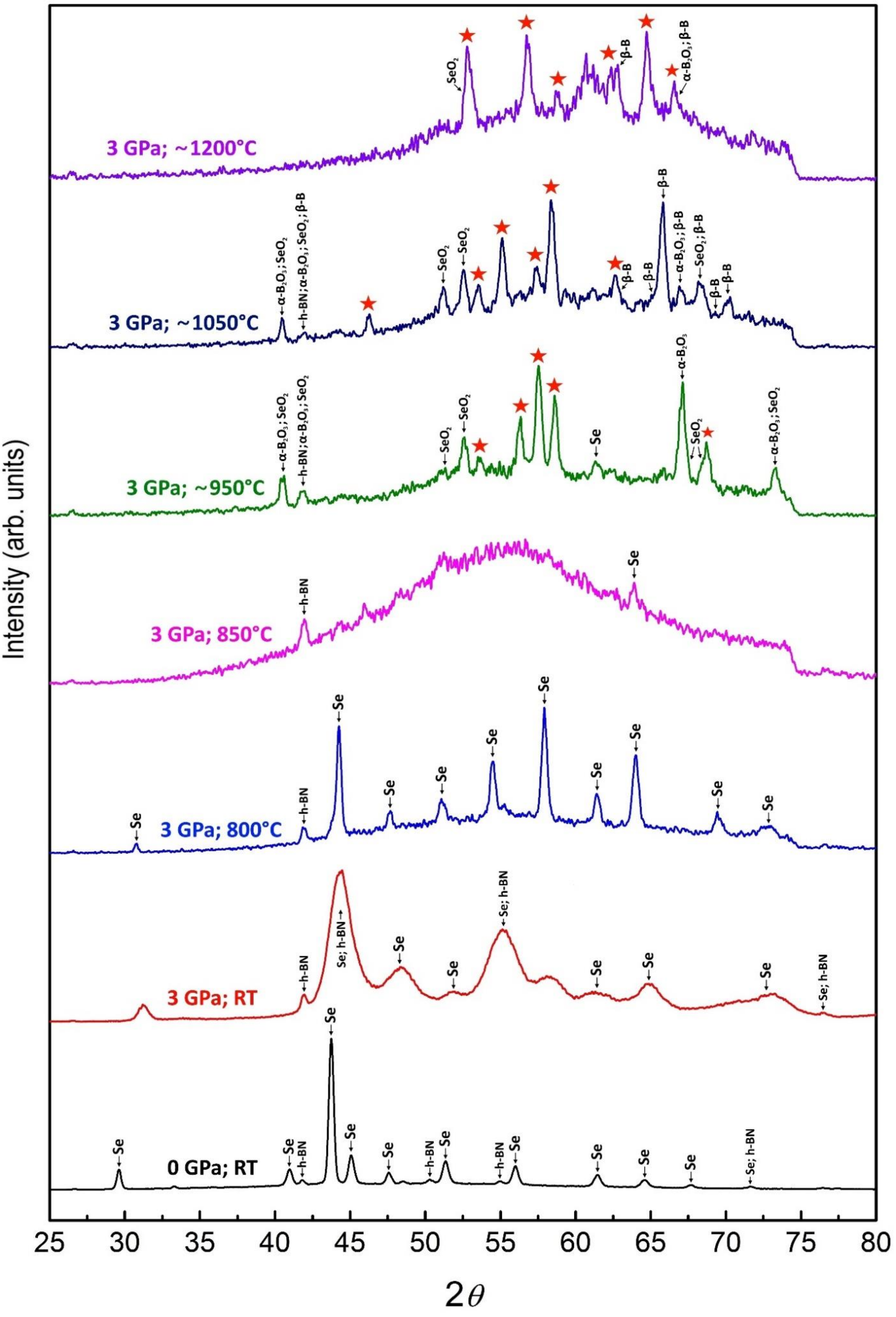

Figure V.2. X-ray diffraction patterns acquired in Run 01. The diffraction peaks of Se, β-B, *h*-BN, α-B_2O_3 and γ-SeO_2 are singed. The new peaks appeared after Se melting are marked by the red stars.

The XRD patterns acquired in all four runs at almost the same conditions are presented in Figure V.3. Apart from the diffraction peaks of the by-products, contaminations and initial reagents (α-B_2O_3, γ-SeO_2, *h*-BN, β-B and Se), there are a lot of "new" peaks. The 2θ values of all observed "new" peaks in all runs are listed in Table 1.

Run 01	Run 02	Run 03	Run 04
	31.24	**31.38**	**31.37**
	32.76	**32.88**	**32.75**
		34.40	
	37.33	**37.49**	**37.59**
			39.01
46.25			
	48.48	**48.53**	**48.58**
		52.11	
53.54	53.56		
55.11			
57.43	57.36		
58.37	**58.65**	**58.59**	
61.22	**61.41**		**61.73**
		62.20	
62.64	62.91		
		64.69	
		66.15	
	67.17	67.41	
			67.99
	68.81	**68.87**	**68.79**
	71.56		
	73.23		
			73.95

Table 1. The 2θ values of the "new" peaks appeared after Se melting in XRD patterns of Run 01-Run 04 presented in Figure V.2. The common "new" peaks for the different runs are marked by bold font.

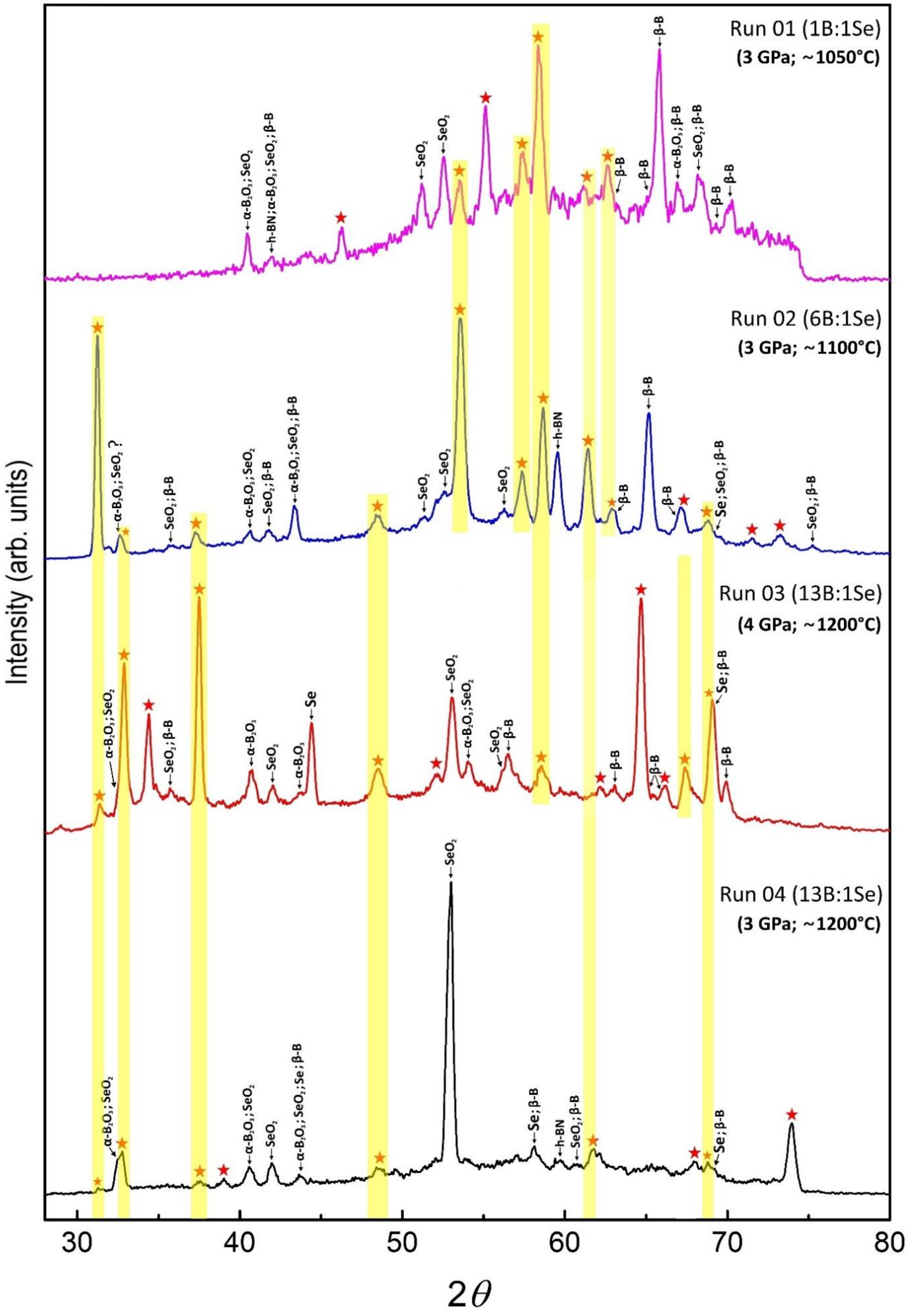

Figure V.3. XRD patterns acquired in all runs (Run 01-04) at HP-HT. The diffraction peaks of Se, β-B, *h*-BN, α-B_2O_3 and γ-SeO_2 are singed. The “new” peaks appeared after Se melting are marked by the red stars. The common peaks of XRD patterns from different experiments are highlighted by the yellow lines.

As one can see from Figure V.3 and Table 1, in spite of the fact that the XRD patterns presented in Figure V.3 are referred to the different B:Se molar ratios, some of the observed “new” peaks are common. In Table 1 and Figure V.3 they are highlighted by the bold font and yellow stripes respectively.

As it has been noted in experimental part, the samples in Run 01-Run 03 have been recovered by the slow cooling and pressure release. Unlike these experiments, in Run 04 the sample has been quenched by switching off the power, which led to the amorphization of the sample. It should be noted that the XRD spectra of the recovered samples in Run 01-Run 03 completely differ from ones acquired at HP-HT (see Figure V.4,5,6.). The XRD spectra measured at the ambient conditions also contain the diffraction peaks of α-B_2O_3, γ-SeO_2, *h*-BN, β-B and Se, but the positions and the relative intensities of the “new” peaks are different from those observed in XRD patterns presented in Figure V.3. Thus, we can do the rough supposition that the “new” diffraction peaks observed at ambient and under extreme conditions correspond to the different phases or even to the different compounds.

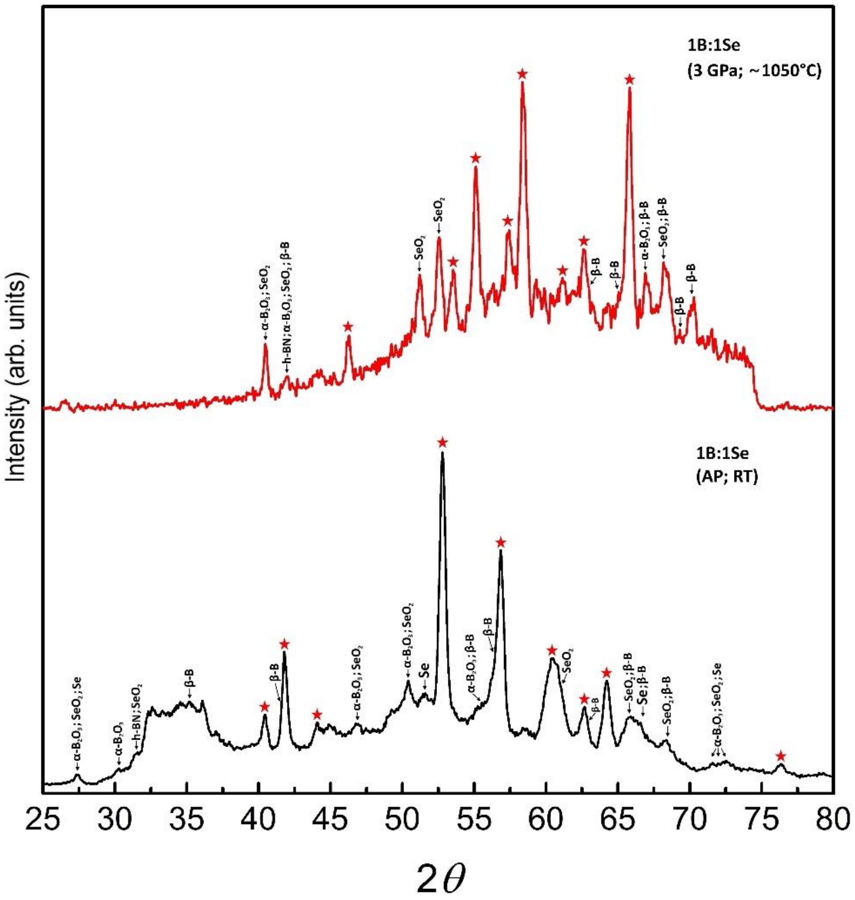

Figure V.4. XRD patterns acquired under extreme and ambient conditions (AP,RT) in Run 01. The diffraction peaks of Se, β-B, *h*-BN, α-B_2O_3 and γ-SeO_2 are singed. The “new” peaks appeared after Se melting are marked by the red stars.

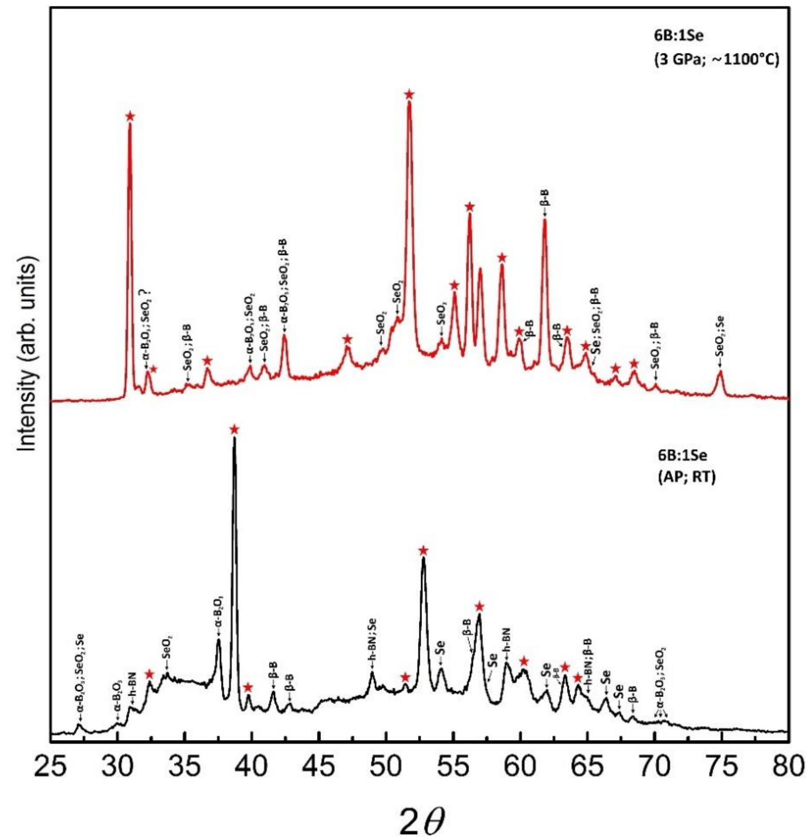

Figure V.5. XRD patterns acquired under extreme and ambient conditions (AP,RT) in Run 02. The diffraction peaks of Se, β-B, *h*-BN, α-B_2O_3 and γ-SeO_2 are singed. The "new" peaks appeared after Se melting are marked by the red stars.

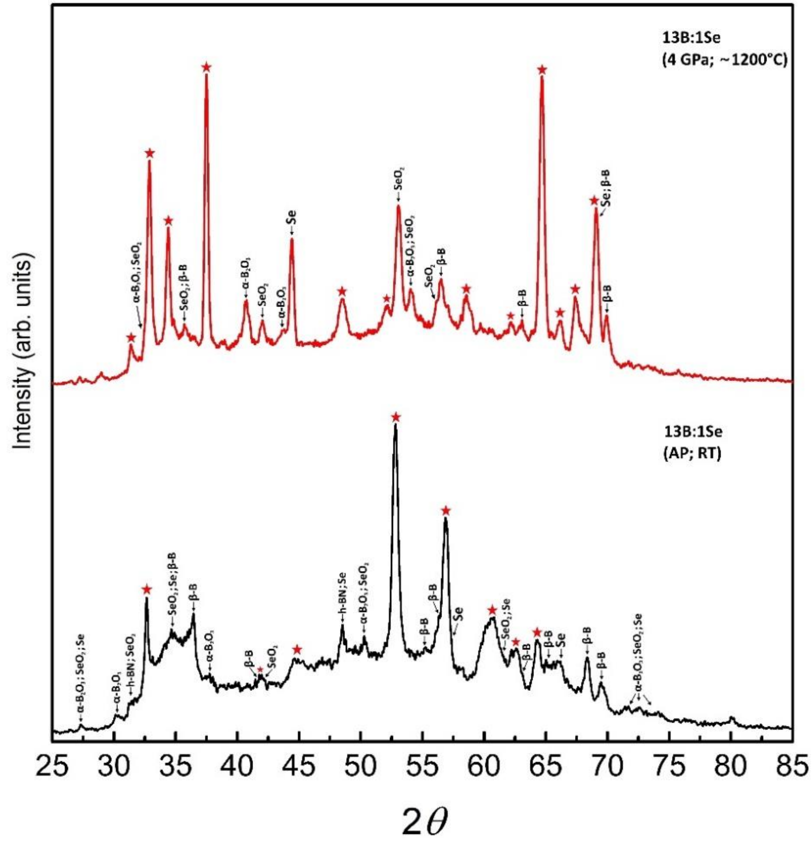

Figure V.6. XRD patterns acquired under extreme and ambient conditions (AP,RT) in Run 03. The diffraction peaks of Se, β-B, *h*-BN, α-B_2O_3 and γ-SeO_2 are singed. The "new" peaks appeared after Se melting are marked by the red stars.

We also compared the XRD patterns measured at ambient conditions in order to find the common "new" peaks (see Figure V.7).

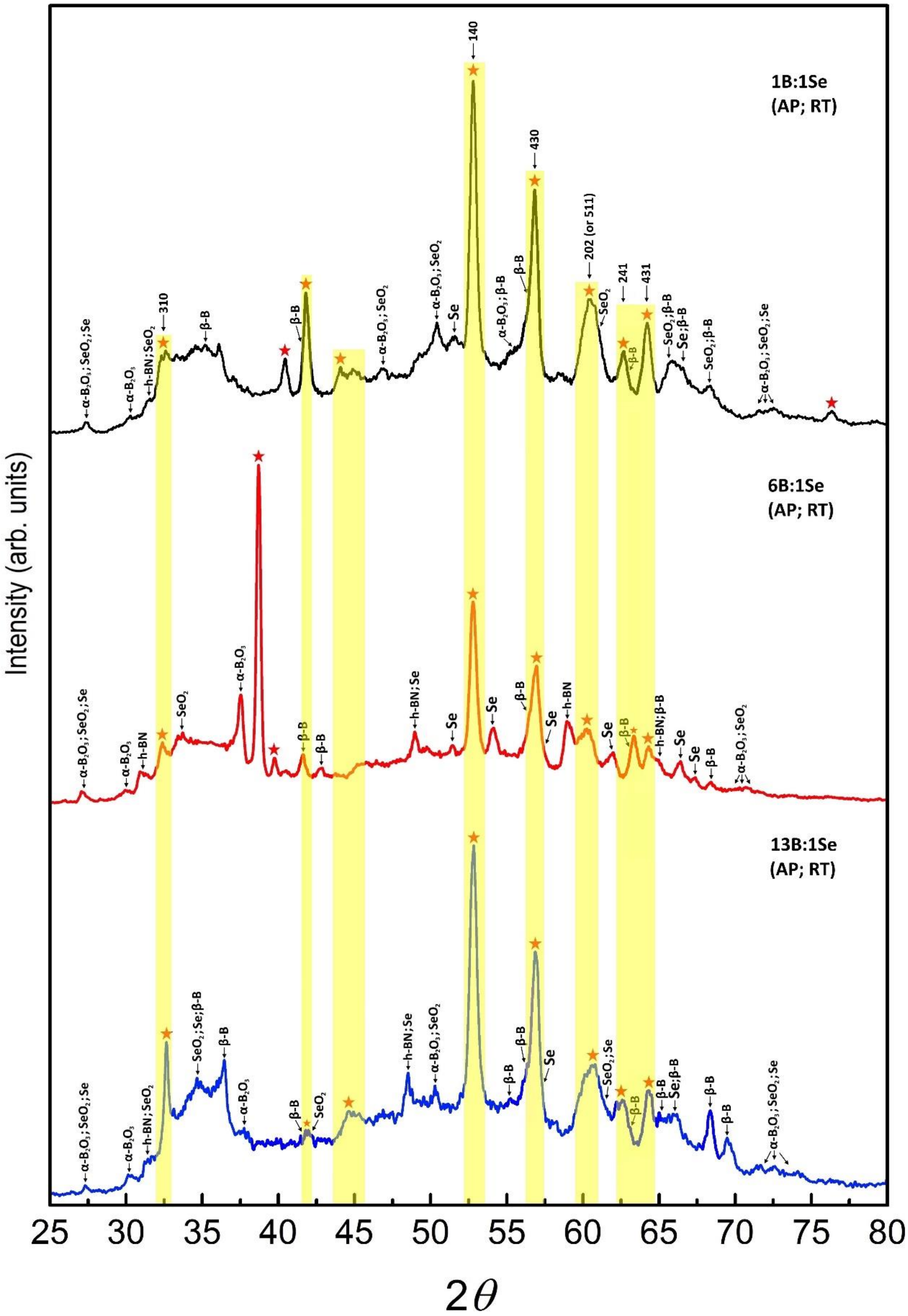

Figure V.7. XRD patterns acquired in Run 01-03 at ambient conditions. The diffraction peaks of Se, β-B, *h*-BN, α-B_2O_3 and γ-SeO_2 are singed. The "new" peaks appeared after Se melting are marked by the red stars. The common peaks of XRD patterns from different experiments are highlighted by the yellow lines. The *hkl* indexes of common "new" peaks for orthorhombic unit cell have been proposed by primary/rough unit cell refinement/search.

As one can see from Figure V.7, the 2θ values (or positions) of almost all of the "new" peaks, which can be supposedly attributed to the new B-Se or B-Se-O compound, nicely coincide (see Table 2).

Run 01	Run 02	Run 03	Proposed *hkl* indexes
32.66	**32.40**	**32.65**	310
	38.70		
	39.75		
40.44			
41.79		41.72	
44.07		44.63	
52.78	**52.78**	**52.83**	140
56.85	**56.91**	**56.87**	430
60.49	**60.27**	**60.49**	202 (or 511)
62.68	**63.32**	**62.61**	241
64.23	**64.32**	**64.31**	431
76.34			

Table 2. The 2θ values of the "new" peaks in XRD patterns of the recovered samples in Run 01-Run 03. The common "new" peaks for all three runs are marked by bold font. The *hkl* indexes of common "new" peaks for orthorhombic unit cell have been proposed by primary/rough unit cell refinement/search.

The recovered samples have been also studied by Raman spectroscopy in 200-2500 cm^{-1} frequency range at room temperature. For example, the Raman spectra of Run 02 and Run 03 are presented in Figure V.8. It should be noticed that the Raman spectra have been measured two weeks after the synthesis (Figure V.8 *a*) and then after ~11 months (Figure V.8 *b*).

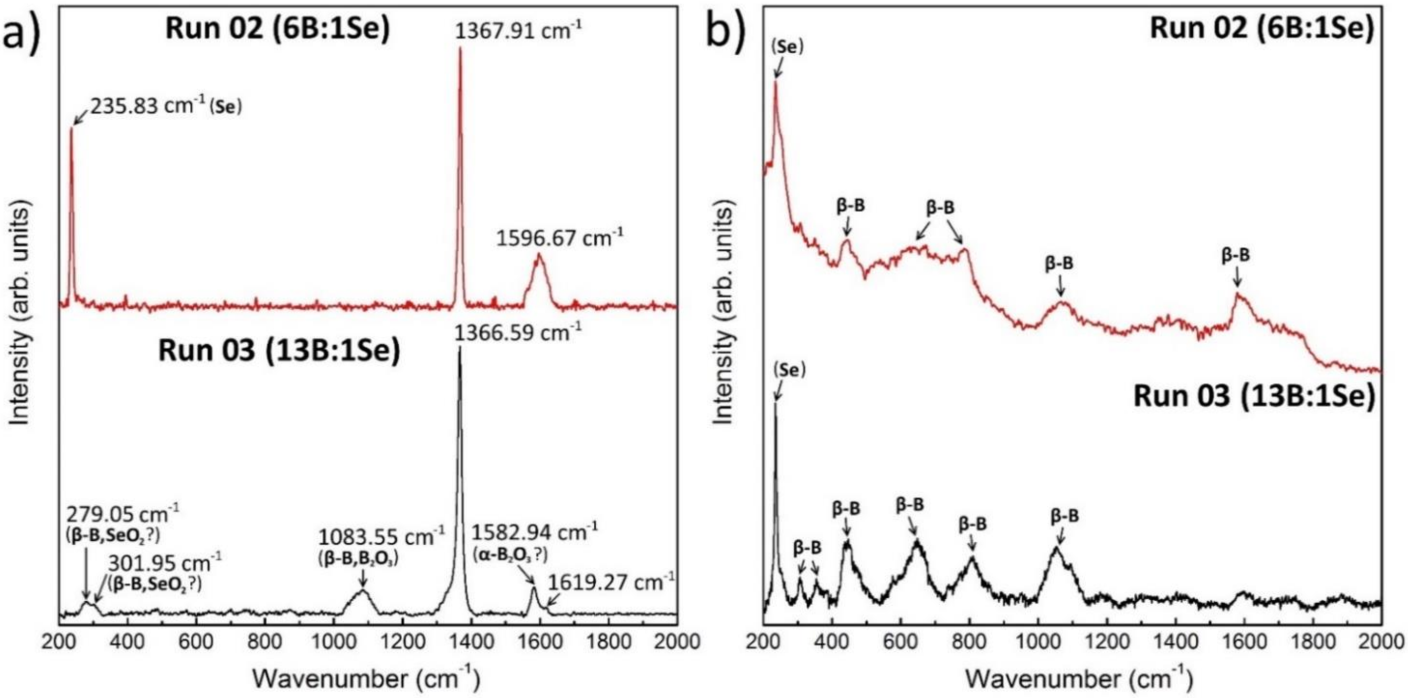

Figure V.8. The Raman spectra of the samples of Run 02 (red) and Run 03 (black) at ambient conditions: a) measured 2 weeks after experiments; b) measured 11 months after experiments. The phonon frequencies of the most intensive bands are signed. The Raman bands of Se, β-B, SeO_2 and β-B_2O_3 are signed.

As one can see in Figure V.8 *a* the Raman spectrum of the sample recovered from Run 02 contains three bands at 235.83, 1367.91 and 1596.67 cm^{-1}. According to Ref. 279 the Raman band at 235.83 cm^{-1} should be referred to α-Se. Thus the presumable B-Se or B-Se-O compound obtained in Run 02 has only two Raman bands. In the Raman spectrum of the sample recovered from Run 03 one can find six bands at 279.05, 301.95, 1083.55, 1366.59, 1582.94 and 1619.27 cm^{-1}. Unlike the Raman spectrum of the sample of Run 02 no bands regarding to α-Se have been found. On other hand, according to the literature review the bands at 279.05, 301.95, 1083.55 and 1582.94 cm^{-1} can be attributed to the Raman bands of β-B [72], SeO_2 [278] and α-B_2O_3 [225]. Thus, as well as in Run 02 only two bands at 1366.59 and 1619.27 cm^{-1} might refer to the possible B-Se or B-Se-O compound. It should be noticed that the comparison of two Raman spectra reveals the common bands at ~1367 and ~1600 cm^{-1}. Also it should be marked that in both spectra the Raman band at ~1367 cm^{-1} is the most intensive. The Raman spectra measured 11 months after the experiments (see Figure V.8 *b*) did not reveal any peaks around 1367 and ~1600 cm^{-1} and on the contrary contain the bands of Se and β-B. This fact indicates that assumed B-Se or B-Se-O compound is probably metastable and decomposes at ambient conditions.

Thus, taking into account all observations described above the following suppositions/conclusions can be made:

1) In spite of the fact that in Figure V.3 some of the common “new” peaks have been observed, it seems very likely that in Run 01-04 (with the different starting B:Se ratios) at

almost the same HP-HT conditions the different products (presumably the new B-Se or B-Se-O compounds) have been synthesized;

2) Based on the similar common "new" peaks which cannot be attributed to the by products (*h*-BN, B_2O_3, SeO_2) or to the starting reagents (B or Se) in the XRD patterns measured at ambient conditions right after temperature and pressure release (in all runs except of Run 04) we can suppose that these "new" peaks might be referred to the presumable new B-Se or B-Se-O compound. This supposition is supported by the similarity of the Raman spectra of the recovered samples. Thus, we can conclude that the different presumable new compounds (or the mixture of them) observed at HP-HT are highly metastable and during decompression and cooling rapidly transformed to the common phase/compound;
3) According to the Raman measurements have been made during the year after the experiments, the obtained presumably new B-Se or B-Se-O compound is metastable at ambient conditions.

The question of the stoichiometry of the presumable B-Se or B-Se-O compound obtained at downstroke and temperature release is still open. In order to investigate its chemical composition all of the recovered samples were analyzed with help of scanning electron microscope (SEM) permitting to provide the energy-dispersive X-ray spectroscopy (EDS). EDS is one of the most powerful techniques of the elemental analysis. In order to obtain the reasonable data the recovered samples have been specially polished. Nonetheless, according to these measurements no B-Se or B-Se-O compounds have not been found (only the separate B and Se have been observed), which nicely matches with the observations made in Raman studies. Hence, it can be rather confidently deduced that the probable new compound registered right after decompression is also metastable and decomposes after into B and Se. Herein it should be noticed that the SEM measurements have been performed four months after the HP-HT experiments.

In spite of the fact that elemental analysis did not give us any information about the chemical composition of the presumable new compound obtained after HP-HT synthesis, some suppositions about its stoichiometry can be done. Herein it should be emphasized that all our suppositions have been done for the presumably new binary B-Se compound. As it has been mentioned above the molar ratios of B and Se in starting mixtures varied from 1:1 to 13:1. Hence, we might assume, that there is no dramatic correlation between boron content in the starting mixture and in the product of HP-HT synthesis, which leads us to the supposition about 1:1 stoichiometry of B and Se in final product. On other hand, the formation of the by-products as, for example α-B_2O_3 and γ-SeO_2, have been observed as well. Moreover almost all of the XRD patterns (see Figure V.3÷7) revealed the presence of unreacted Se and β-B. Taking this into account we can expect the deviation from the 1:1 stoichiometry. Thus, based on all suppositions and observations stated above, we might suppose that the general formula of obtained new B-Se compound can be $B_{1-x}Se_{1-y}$, where $0<x,y<1$.

As far as we supposed that the stable phase of presumably new B-Se or B-Se-O compound forms only at downstroke and slow temperature decrease we provided the primary/rough unit cell refinement/search using the XRD spectra (and only common "new" diffraction peaks) presented in Figure V.7 using DICVOL04 and WinPLOTR packages in FullProf software. The search have been implemented for all crystal symmetries except of triclinic one. According these coarse estimations the observed "new" peaks can be attributed to the hexagonal, tetragonal, orthorhombic and monoclinic crystal symmetries. However in case of orthorhombic crystal symmetry rather close lattice parameters have been obtained for the samples of all runs (see Table 3).

Experiment	a, Å	b, Å	c, Å	V, Å^3
Run 01	8.9(2)	7.1(1)	3.1(2)	200.1
Run 02	8.7(2)	7.1(1)	3.3(1)	202.5
Run 03	8.9(1)	7.1(1)	3.2(1)	203.7

Table 3. The lattice parameters and the unit cell volumes of the samples recovered from Run 01-Run 03 assumed for orthorhombic crystal symmetry.

The unit cell of the presumable orthorhombic B-Se or B-Se-O compound is less than the sum of the unit cell volumes of β-B (~262.2 Å^3) and trigonal Se (~78.3 Å^3).

11.2 Conclusions

As it has been noticed in Chapter I, the B-Se system is rather poorly studied, especially under extreme conditions, first of all due to such difficulties in its study, as: tendency towards vitrification, sensitivity to hydrolysis, high-temperature synthesis conditions, leading to contamination by capsule or crucible material, etc. Thus, the synthesis and characterization of the new binary compounds in B-Se system is rather difficult and time consuming.

In this chapter we described our preliminary studies in B-Se system. The *in situ* HP-HT synthesis have been provided in PEP at synchrotron SOLEIL PSICHE beamline, using the B and Se powders mixed in different ratios (1:1, 6:1 and 13:1). The results of XRD measurements and Raman studies of samples obtained in these synthesis clearly indicate the new binary B-Se or ternary B-Se-O compound formation. However, it should be underlined here, that the obtained results are not enough to firmly state the structure and the composition/stoichiometry of this compound. The elemental analysis provided four months later did not reveal any B-Se or B-Se-O compound. The Raman measurements performed 11 months later also did not reveal the bands which can be attributed to the new compound. Thus, the conclusion about the metastability at ambient conditions of the obtained probable new compound can be done. The similar XRD and Raman data of the samples obtained from the HP-HT synthesis with different B:Se molar ratios indicate the absence of the direct connection between the reagents and the product stoichiometries. Considering only the probable new binary B-Se compound we assumed the possible formula of the new compound: $B_{1-x}Se_{1-y}$, where $0<x,y<1$. According to the coarse structure fitting/search, the structure of the presumably new compound might possibly belong to the orthorhombic syngony.

In order to confidently clarify chemical composition (consequently the stoichiometry), stability, structure and physical properties of the possible new compound obtained in this work the further more deep and detailed investigations are needed.

12 Conclusions and perspectives

As it was mentioned in the introduction of this thesis, the boron compounds synthesized under extreme conditions (HP-HT) have raised the interest of the researches from various scientific fields due to their chemical inertness, extreme mechanical (wear resistance, hardness, etc.) and physical (thermosconductivity/ thermoelectricity, conductivity/semiconductivity, neutron scattering length, etc.) properties and the opportunity for various applications in industry. In spite of the constantly growing interest, there are still many ill-studied groups/systems of boron compounds which seem rather promising and requiring a deeper and detailed investigation, as for example boron chalcogenides. The synthesis and investigation of boron chalcogenides at ambient and extreme conditions is rather challenging due to diverse chemistry of boron and therefore a big number of possible contaminations, low Z number of boron and hence the need of precise and powerful analytical equipment (as for example the high brilliant synchrotron radiation), etc.

Presented in this thesis is a detailed experimental study of the boron chalcogenides properties at ambient and under extreme conditions. Due to the time constraints of the present work we chose one boron chalcogenide from each binary system (B-O and B-S) with the most promising properties: β-B_2O_3 and *r*-BS. These compounds have been studied using different experimental analytical techniques like XRD (including *in situ* synchrotron HP XRD measurements), Raman scattering and IR transmission spectroscopy coupled with *ab initio* LCAO calculations. It should be noted that various high pressure apparatus (PEP, TTP, MAP, MDAC) have been employed for β-B_2O_3 and *r*-BS synthesis and *in situ* properties investigations. In this framework, the preliminary synthesis of a new compound in B-Se system at extreme conditions have been performed at PSICHE beamline of synchrotron SOLEIL.

B-O system

The high-pressure phase of boron (II) oxide (β-B_2O_3) has been obtained from HP-HT synthesis in LVP (TTP). The structure and phase purity of β-B_2O_3 have been confirmed using powder XRD. In spite of the fact that, due to the outstanding hardness (~16 GPa) β-B_2O_3 has been studied before [93,111,113,115-117,121,123-125], the following additional studies on its properties have been performed:

1) The refinement of the EoS of β-B_2O_3, as the previous report [111] presented the EoS data of downstroke in pressure range from 42 to 12 GPa, lacking the low pressure range;
2) The detailed investigation of β-B_2O_3 phonon nature at ambient and under extreme conditions.

Thanks to our studies on equation of state we obtained a new bulk modulus (B_0) and its first pressure derivative (B_0`) values, which slightly differed from ones reported before [111]. The measurements accuracy provided in our research are significantly more accurate than those done *Nieto-Sanz et all*. The *ab initio* LCAO calculations performed for β-$B_2O_3$ at zero temperature gave rather close $B_0$ and $B_0$` values to the experimental ones. The close B_0 and B_0` parameters obtained in us and *Nieto-Sanz et all.* allowed us to assume that two datasets of these studies can be considered as the common/whole one. Thus, we calculated the bulk modulus value of β-B_2O_3 in 0-42 GPa pressure range. The pressure dependencies of the lattice parameters, B-O distances and O-B-O angles in β-B_2O_3 have been also studied and described.

A complete phonon study of β-B_2O_3 by means of Raman and IR spectroscopies at ambient pressure and room temperature has been performed. The implemented *ab initio* calculations of the phonon mode frequencies and modes visualization permitted us to assign the experimentally observed bands to the phonon modes for the first time. Moreover, the effect of ^{10}B isotope substitution in β-B_2O_3 Raman spectrum has been studied and described. *In situ* HP Raman measurements coupled with *ab initio* calculations of the phonon frequencies for the reduced unit cell volumes permitted us to completely describe the phonon properties of β-B_2O_3 up to 46 GPa. Thus, in our work, new data, essential for the further optical and phonon studies information about structure and phonon properties of β-B_2O_3 at ambient and under high pressures have been obtained.

Concerning some future perspectives for β-B_2O_3 investigations, the following experiments/studies shedding more light on the compound properties might be proposed:

1) The hardness measurements in monocrystal β-B_2O_3 along *a*, *b* and *c* directions;
2) The Brillouin spectroscopy measurements, permitting to determine the elastic constants, which are very important characteristics, especially for hard materials;
3) The electronic structure and optical properties studies at ambient and under high pressures should be performed, as so far there is only one theoretical work [120] devoted to this important theme;
4) More generally, an attempt for the synthesis of the hypothetical γ-B_2O_3 [93] at HP-HT conditions should be made.

There is no doubt that the further scientific work according to the directions listed above will be performed.

B-S system

Rhombohedral boron monosulfide (*r*-BS) has been synthesized by us at HP-HT conditions using different LVPs (MAP and TTP). The structure and phase purity of *r*-BS have been confirmed using powder XRD. Rhombohedral BS belongs to the $A^{III}B^{VI}$ layered semiconductors family. The many $A^{III}B^{VI}$ compounds (e.g. InS, InSe, GaSe, etc.) have been already widely studied and some variants of technical application, as materials of solid state batteries, non-linear optics or solar cells have been proposed [238-240]. Unlike these materials, *r*-BS is rather ill studied and there is only one work [154] devoted to the synthesis of *r*-BS and the phase diagram of B-S system. Thus, we have concluded that complete and detailed studies on the following directions were needed:

1) The exploring of the *r*-BS phase stability in a wide pressure range;
2) The study of phonon properties of *r*-BS at ambient and under high pressures.

As a result of our HP XRD studies, the parameters of EoS parameters of *r*-BS have been obtained for the first time. The bulk modulus has been determined to be equal to 48.4 GPa, which is the highest B_0 value among all $A^{III}B^{VI}$ layered semiconductors. The B_0 and B_0` values have been also estimated by the *ab initio* LCAO calculations. However, the provided *ab initio* calculations were not highly precise due to the complicated nature of the interlayer interactions. The anisotropy of the *r*-BS unit cell compression and even of the one layer compression has been observed and described in details. According to our work relatively high bulk modulus of *r*-BS can be explained by the more rigid layers and intralayer space compared to the other $A^{III}B^{VI}$ compounds.

We observed the formation of the HP BS phase around 30 GPa. The new BS phase likely belongs to the cubic syngony with two most probable structure motives: NaCl ($Fm\overline{3}m$) or CsCl ($Pm\overline{3}m$). However, due to the low quality of the XRD data only the lattice parameters of the hypothetical BS cubic phase have been refined. The EoS parameters of the new phase have been estimated in 30-42 GPa pressure range. The B_0 value has been estimated to be 204.4 GPa.

In our work, the phonon study of *r*-BS using Raman and IR spectroscopy techniques at ambient pressure and room temperature have been performed for the first time. Based on the results of *ab initio* calculations of the phonon mode frequencies and modes visualization, the modes assignment has been provided. The isotope substitution effect of ^{10}B in *r*-BS Raman spectrum has been studied and described. The phonon properties of *r*-BS have been also studied at room temperature and under HP up to 34 GPa by means of Raman spectroscopy. Using the *ab initio* calculations of the phonon frequencies for the reduced unit cell volumes, modes assignment and pressure dependencies of the B-S and B-B bonds, an explanation of the phonon modes behavior under compression has been proposed.

The experiments performed in this work might be further continued with the following studies on:

1) Investigation of the phase stability of the new “pseudo-cubic” BS phase in a wide pressure and temperature ranges;
2) *In situ* investigations of the physical properties of the “pseudo-cubic” BS phase combined with the theoretical predictions;

3) The electronic structure studies of *r*-BS at ambient and under high pressures, coupled with theoretical prediction. It would be quite interesting to find out the way of manipulation of the electrical properties (thanks to high structural anisotropy) by applying the pressure and temperature;
4) Investigation of *r*-BS by XRD and Raman techniques at low temperatures in order to completely study the nature of the interlayer interactions and possibly to explore the low-temperature phase transitions.

As well as in case of boron (II) oxide the further more detailed investigations of the *r*-BS and new high-pressure phase properties and structure particularities will be continued.

B-Se system

According to the literature review in the Chapter I devoted to B-Se system there are no binary compounds obtained at high pressures. Thus, in current work we have done the primary attempts of HP-HT synthesis of new compounds in B-Se system. The *in situ* XRD measurements have been provided at PSICHE beamline of synchrotron SOLEIL. The 1:1, 6:1 and 13:1 molar ratios of boron and selenium have been tested. The diffraction patterns measured *in situ* at HP-HT and on the sample recovery revealed common new “unattributed” peaks indicating about the presumably new B-Se or B-Se-O compound formation. The common bands observed in the Raman spectra of the recovered samples are also indicating about one general compound formation. Thus we deduced that there is no distinct correlation between reagent molar ratios and the products of HP-HT reaction. The elemental analysis (using SEM) provided few months after experiments did not reveal any B-Se or B-Se-O compound. The Raman measurements of the recovered samples performed almost one year after experiments also did not reveal any “unattributed” bands, which have been observed before. Based on these facts, we deduced that the obtained presumably new B-Se or B-Se-O compound is metastable at ambient conditions. Considering only the probable binary B-Se compound, in attempts to propose its general formula we assumed the possible formula: $B_{1-x}Se_{1-y}$, where $0<x,y<1$. According to the coarse structure fitting/search, the structure of presumably new compound might possibly belong to the orthorhombic syngony.

There is no doubt that these primary results require further complete and detailed investigations. The next steps in investigation of B-Se should be:

1) Preparation of the PEP assembly in the inert atmosphere (e.g. under Ar or Ne flow using a glove box) in order to eliminate oxygen from the starting reagents (B and Se powders);
2) *In situ* HT-HP studies of the same molar ratios of B and Se in a wider pressure range (possibly using a MAP);
3) Investigation of the P,T conditions of the phase stability of the compound synthesized in our experiments;

4) The full structure refinement (Rietveld refinement) of this compound and the chemical analysis (SEM, STEM) right after recovering;
5) Providing that there are the P,T conditions of stability of the new compound obtained in our preliminary experiments, investigation of its electronic and mechanical properties.

The detailed *in situ* and *ex situ* investigation of the B-Se system under extreme conditions is planned in 2016.

Bibliography

1. H. Davy, Electro-Chemical Researches, on the Decomposition of the Earths; With Observations on the Metals Obtained from the Alkaline Earths, and on the Amalgam Procured from Ammonia. *Phil. Trans. R. Soc. Lond.*, 1808, 98, p. 333-370.
2. L.J. Gay-Lussac, L.J. Thénard, Sur la Décomposition et la Recomposition de l'Acide Boracique. *Ann. Chim. Phys.*, 1808, 68, p. 169-174.
3. E. Weintraub, On the Properties and Preparation of the Element Boron. *J. Ind. Eng. Chem.*, 1911, 3, p. 299-301.
4. H. Moissan, Etude du Bore Amorphe. *Ann. Chim. Phys.*, 1895, 6, p. 296-304.
5. Saint-Claire Deville H., F. Woehler, Ueber das Bor. *Ann. Physik* 1857, 176, p. 635-646.
6. A.W. Laubengayer, D.T. Hurd, A.E. Newkirk, J.L. Hoard**,** Boron. I. Preparation and Properties of Pure Crystalline Boron. *J. Am. Chem. Soc.*, 1943, 65, p. 1924-1931.
7. J.L. Hoard, S. Geller, R.E. Hughes, On the Structure of Elementary Boron. *J. Am. Chem. Soc.*, 1951, 73, p. 1892-1893.
8. J.L. Hoard, R.E. Hughes, D.E. Sands, The Structure of Tetragonal Boron*. J. Am. Chem. Soc.*, 1958, 80, p. 4507-4515.
9. L. Pauling, The Nature of the Chemical Bond. *Ithaca, New York: Cornell University Press*, 1960, p. 644.
10. K. Ploog, E. Amberger, Kohlenstoff-Induzierte Gitter beim Bor: I-Tetragonales $(B_{12})_4B_2C$ und $(B_{12})_4B_2C_2$. *J. Less-Comm. Metals*, 1971, 23, p. 33-42.
11. G. Will, K. Ploog, Crystal Structure of I-Tetragonal Boron. *Nature*, 1974, 251, p. 406-408.
12. D.E. Sands, J.L. Hoard, Rhombohedral Elemental Boron. *J. Am. Chem. Soc.*, 1957, 79, p. 5582-5583.
13. R.E. Hughes, C.H.L. Kennard, D.B. Sullenger, H.A. Weakliem, D.E. Sands, J.L. Hoard, The Structure of β-Rhombohedral Boron. *J. Am. Chem. Soc.*, 1963, 85, p. 361-362.
14. E. Amberger, K. Ploog, Bildung der Gitter des Reinen Bors. *J. Less-Common Metals*, 1971, 23, p. 21-31.
15. J. Donohue, *The Structure of the Elements* (John Wiley & Sons, N.Y., 1974).
16. B.E. Douglas, S.-M. Ho, *Structure and Chemistry of Crystalline Solids* (Springer, N.Y., 2006).
17. P. Runow, Study of Alpha to Beta-Transformation in Boron. *J. Mater. Sci.*, 1972, 7, p. 499-511.
18. J. Wentorf, Boron: Another Form. *Science*, 1965, 147, p. 49-50.
19. Y. Ma, C.T. Prewitt, G. Zou, H.-K. Mao, R.J. Hemley, High-Pressure High-Temperature X-ray Diffraction of beta-Boron to 30 GPa*. Phys. Rev. B*, 2003, 67, p. 174116.
20. B.F. Decker, J.S. Kasper, The Crystal Structure of a Simple Rhombohedral Form Boron. *Acta Crystallogr.*, 1959, 12, p. 503-506.

21. R.E. Hughes, C.H.L. Kennard, D.B. Sullenger, H.A. Weakliem, D.E. Sands, J.L. Hoard, The Structure of β-Rhombohedral Boron. *J. Amer. Chem. Soc.*, 1963, 85, p. 361-362.
22. A.R. Oganov, J. Chen, C. Gatti, Y. Ma, Y. Ma, C.W. Glass, Z. Liu, T. Yu, O.O. Kurakevych, V.L. Solozhenko, Ionic high-pressure form of elemental boron. *Nature*, 2009, 457, p. 863-867.
23. M. Vlasse, R. Naslain, J.S. Kasper, K. Ploog, Crystal Structure of Tetragonal Boron Related to α-AlB_{12}, *J. Solid State Chem.*, 1979, 28, p. 289-301.
24. O.O. Kurakevych, Y. Le Godec, T. Hammouda, C. Goujon, Comparison of Solid-State Crystallization of Boron Polymorphs at Ambient and High Pressures. *High Pressure Res.*, 2012, 32, p. 30-38.
25. E.A. Ekimov, I.P. Zibrov, A.V. Zoteev, High-pressure high-temperature synthesis and structure of α-tetragonal boron. *Inorg. Mater.*, 2011, 47, p. 1194-1198.
26. A.R. Oganov, C.W. Glass, Crystal Structure Prediction Using ab initio Evolutionary Techniques: Principles and Applications. *J. Chem. Phys.*, 2006, 124, p. 244704-1-15.
27. Q. Zhu, A.R. Oganov, C.W. Glass, H.T. Stokes, Constrained evolutionary algorithm for structure prediction of molecular crystals: methodology and applications. *Acta Crystallogr. B*, 2012, 68, p. 215–226.
28. O.O. Kurakevych, V.L. Solozhenko, Crystal Structure of Dense Pseudo-Cubic Boron Allotrope, pc-B_{52}, by Powder X-ray Diffraction. *J. Superhard Mater.*, 2013, 35, p. 60-63.
29. V.L. Solozhenko, O.O. Kurakevych, Equilibrium p-T Phase Diagram of Boron: Experimental Study and Thermodynamic Analysis. *Sci. Rep.*, 2013, 3, p. 2351-1-8.
30. L.V. McCarty, J.S. Kasper, F.H. Horn, B.F. Decker, A.F. Newkirk, A New Crystalline Modification of Boron. *J. Am. Chem. Soc.*, 1958, 80, p. 2592.
31. E. Amberger, W. Dietze, Zur Bildung Von Alpha-Rhomboedrischem, Rotem Bor. *Z. Anorg. Allg. Chem.*, 1964, 332, p. 131-139.
32. F.H. Horn, Boron, Synthesis Structure and Properties, Proceedings of the Conference on Boron. *Gen. Elec. Co.*, 1960, p. 110-115.
33. V.L. Solozhenko, O.O. Kurakevych, A.R. Oganov, On the Hardness of a New Boron Phase, Orthorhombic γ-B_{28}. *J. Superhard Mater.*, 2008, 30, p. 428-429.
34. A. Masago, K. Shirai, H. Katayama-Yoshida, Crystal Stability of α- and β-Boron, *Phys. Rev. B*, 2006, 73, p. 104102-1-10.
35. M.J. van Setten, M.A. Uijttewaal, G.A. de Wijs, R.A. de Groot, Thermodynamic Stability of Boron: The Role of Defects and Zero Point Motion. *J. Am. Chem. Soc.*, 2007, 129, p. 2458-2465.

36. R.J. Nelmes, J.S. Loveday, D.R. Allan, J.M. Besson, G. Hamel, P. Grima, S. Hull, Neutron-and X-Ray Diffraction Measurements of the Bulk Modulus of Boron. *Phys. Rev. B*, 1993, 47, p. 7668-7673.
37. B. Albert, H. Hillebrecht, Boron: Elementary Challenge for Experimenters and Theoreticians. *Angew. Chem. Int. Ed.*, 2009, 48, p. 8640-8668.
38. H. Werheit, U. Kuhlmann, Is the Established Structure of α-rhombohedral Boron Correct? Comparative Study of IR-active Phonons with B_6O, $B_{4.3}C$ and β-Rhombohedral Boron. *J. Phys.: Condens. Matter*, 2012, 24, p. 305401-305409.
39. F.H. Horn, Zone-Refined Boron. *J. Appl. Phys.*, 1959, 30, p. 1612-1613.
40. D. Emin, Icosahedral Boron-Rich Solids. *Phys. Today*, 1987, 40, p. 55-62.
41. O.A. Golikova, Boron and Boron-Based Semiconductors. *Phys. Status Solidi A*, 1979, 51, p. 11-40.
42. K. Soga, A. Oguri, S. Araake, M. Terauchi, A. Fujiwara, K. Kimura, Li- and Mg-doping into Icosahedral Boron Crystals, α- and β-Rhombohedral Boron, Targeting High-Temperature Superconductivity: Structure and Electronic States. *J. Solid State Chem.*, 2004, 177, p. 498-506.
43. B. Callmer, An Accurate Refinement of the β-Rhombohedral Boron Structure. *Acta Crystallogr. Sect. B*, 1977, 33, p. 1951-1954.
44. S. Hoffmann, H. Werheit, Phase Transition in β-Rhombohedral Boron Near 550 K. *Solid State Sci.*, 2012, 14, p. 1572-1577.
45. G.A. Slack, C.I. Hejna, M.F. Garbauskas, J.S. Kasper, X-Ray Study of Transition-Metal Dopants in Beta-Boron. *J. Solid State Chem.*, 1988, 76, p. 52-63.
46. M.A. White, A.B. Cerqueira, C.A. Whitman, M.B. Johnson, T. Ogitsu, Determination of Phase Stability of Elemental Boron. *Angew. Chem.*, 2015, 127, p. 1-5.
47. T. Ogitsu, F. Gygi, J. Reed, Y. Motome, E. Schwegler, G. Galli, Imperfect Crystal and Unusual Semiconductor: Boron, a Frustrated Element. *J. Am. Chem. Soc.*, 2009, 131, p. 1903-1909.
48. D. Prasad, M.M. Balakrishnarajan, E.D. Jemmis, Electronic Structure and Bonding of Beta-Rhombohedral Boron Using Cluster Fragment Approach. *Phys. Rev. B*, 2005, 72, p. 195102-1-6.
49. A.R. Pitochelli, M.F. Hawthorne, The Isolation of the Icosahedral $B_{12}H_{12-2}$ Ion. *J. Am. Chem. Soc.*, 1960, 82, p. 3228-3229.
50. E.D. Jemmis, D.J. Prasad, Icosahedral B-12, Macropolyhedral Boranes, Beta-Rhombohedral Boron and Boron-Rich Solids. *Solid State Chem.*, 2006, 179, p. 2768-2774.
51. M.M. Balakrishnarajan, E.D. Jemmis, Electronic Requirements of Polycondensed Polyhedral Boranes. *J. Am. Chem. Soc.*, 2000, 122, p. 4516-4517.
52. T. Ogitsu, E. Schwegler, G. Galli, β-Rhombohedral Boron: At the Crossroads of the Chemistry of Boron and the Physics of Frustration. *Chem. Rev.*, 2013, 113, p. 3425-3449.

53. M. Widom, M. Mihalkovic, Symmetry-Broken Crystal Structure of Elemental Boron at Low Temperature. *Phys. Rev. B*, 2008, 77, p. 064113-1-8.

54. A. Masago, K. Shirai, H. Katayama-Yoshida, The Pressure Dependence of Solid Boron. *Mol. Simulat.*, 2004, 30, p. 935-939.

55. R. Schmechel, H. Werheit, Correlation Between Structural Defects and Electronic Properties of Icosahedral Boron-Rich Solids. *J. Phys. Condens. Matter*, 1999, 11, p. 6803-6813.

56. H. Werheit, H.G. Leis, On the Conductivity Mechanism of β-Rhombohedral Boron. *Phys. Stat. Sol.*, 1970, 41, p. 247-253.

57. A. Szadkowski, Thermally Activated Hopping in Beta-Rhombohedral Boron. *J. Less-common Met*, 1979, 67, p. 551-556.

58. T. Lundström, B. Lönnberg, J. Bauer, Thermal Expansion of β-Rhombohedral Boron. *J. Alloys Comp.*, 1998, 267, p. 54-58.

59. H. Werheit, M. Laux, U. Kuhlmann, Interband and Gap State Related Transitions in P-Rhombohedral Boron. *Phys. Stat. Sol. B*, 1993, 176, p. 415-432.

60. G. Gewinner, L. Kubler, J. Koulmann, A. Jaeglé, EPR Investigation of Paramagnetic Centers in Beta-Rhombohedral Boron. *Phys. Stat. Sol. B*, 1973, 59, p. 395-402.

61. C.D. Siems, Quantitative-Evaluation of the Electron-Paramagnetic Resonance Anisotropy of Beta-Rhombohedral Boron. *J. Less-common Met.*, 1979, 67, p. 155-160.

62. D.N. Sanz, P. Loubeyre, M. Mezouar, Equation of State and Pressure-Induced Amorphization of Beta-Boron from X-Ray Measurements up to 100 GPa. *Phys. Rev. Lett.*, 2001, 89, p. 245501-1-4.

63. R.F. Kimpel, R.G. Moss, Melting Point of 98.9 to 99.6 (Pure Boron). *J. Chem. Eng. Data*, 1968, 13, p. 231-234.

64. S. Krishnan, P. C. Nordine, J. K. R. Weber, R.A. Schiffman, Optical-Properties and Melting-Point of Pure Boron. *High Temp. Sci.*, 1991, 31, p. 45–57.

65. F.N. Tavadze, I.A. Bairamashvili, G.V. Tsagareishvili, K.P. Tsomaya, N.A. Zoidze, Structure of Boron Crystals Grown from Melt. *Sov. Phys. Crystallogr.*, 1965, 9, p. 768-770.

66. J.L. Hoard, A.E. Newkirk, An Analysis of Polymorphism in Boron Based upon X-Ray Diffraction Results. *J. Am. Chem. Soc.*, 1960, 82, p. 70-76.

67. J.O. Carlsson, Factors Influencing the Morphologies of Boron Deposited by Chemical Vapor-Deposition. *J. Less-Common Met.*, 1980, 70, p. 77-96.

68. T. Ogitsu, E. Schwegler, The α-β Phase Boundary of Elemental Boron, *Solid State Sci.*, 2012, 14, p. 1598-600.

69. H. Werheit, R. Franz, States of Thermal Equilibrium in β-Rhombohedral Boron and Their Alteration by Optical Excitation. *Phys. Status Solidi B*, 1984, 125, p. 779-784.

70. E.Y. Zarechnaya, L. Dubrovinsky, N. Dubrovinskaia, Y. Filinchuk, D. Chernyshov, V. Dimitriev, N. Miyajima, A.El Goresy, H.F. Braun, S. van Smaalen, I. Kantor, A. Kantor, V. Prakapenka, M. Hanfland, A.S. Mikhaylushkin, I.A. Abrikosov, S.I. Simak, Superhard Semiconducting Optically Transparent High Pressure Phase of Boron. *Phys. Rev. Lett.*, 2009, 102, p. 185501-1-4.
71. R.H. Wentorf, Behavior of Some Carbonaceous Materials at Very High Pressures and High Temperatures. *Science*, 1965, 147, p. 49-50.
72. G. Parakhonskiy, N. Dubrovinskaya, E. Bykova, R. Wirth, L. Dubrovinsky, Experimental Pressure-Temperature Phase Diagram of Boron: Resolving the Long-Standing Enigma. *Sci. Rep.*, 2011, 1, p. 1-7.
73. A.R. Oganov, V.L. Solozhenko, Boron: a Hunt for Superhard Polymorphs. *J. Superhard Mater.*, 2009, 31, p. 285-291.
74. A.R. Oganov, J. Chen, C.Gatti, Y. Ma, C.W. Glass, Z. Liu, T. Yu, O.O. Kurakevych, V.L. Solozhenko, Ionic High-Pressure Form of Elemental Boron. *Nature*, 2009, 460, p. 292.
75. Y. Le Godec, O.O Kurakevych, P. Munsh, G. Garbarino, V.L. Solozhenko, Equation of State of Orthorhombic Boron, γ-B_{28}. *Solid State Commun.*, 2009, 149, p. 1356-1358.
76. S. Hayun, A. Weizmann, H. Dilman, M.P. Dariel, N. Frage, Rim Region Growth and Its Composition in Reaction Bonded Boron Carbide Composites with Core-Rim Structure. *J. Phys. Conf. Ser.*, 2009, 176, p. 012009-1-7.
77. M.L. Wilkins in Boron and Refractory Borides, (Ed.: V. I. Matkovich), Springer, Berlin, 1977, p. 633-648.
78. R. Telle, Borides, a New Generation of Hard Substances, *Chem. Unserer Zeit*, 1988, 22, p. 93-99.
79. R. Riedel, Novel Ultrahard Materials. *Adv. Mater.*, 1994, 6, p. 549-560.
80. D. Emin, Unusual Properties of Icosahedral Boron-Rich Solids. *J. Solid State Chem.*, 2006, 179, p. 2791-2798.
81. G.A. Slak, K.E. Morgan, Some Crystallography, Chemistry, Physics, and Thermodynamics of $B_{12}O_2$, $B_{12}P_2$, $B_{12}As_2$, and Related Alpha-Boron Type Crystals. *J. Phys. Chem. Solids*, 2014, 75, p. 1054-1074.
82. G. Will, K.H. Kossobutzki, X-RAY Structure-Analysis of Boron-Carbide, $B_{13}C_2$. *J. Less-Common Met.*, 1976, 44, p. 87-97.
83. V.I. Matkovich, Interstitial Compounds of Boron. *J. Am. Chem. Soc.*, 1961, 83, p. 1804-1806.
84. B. Morosin, G.H. Kwei, A.C. Lawson, T.L. Aselage, D. Emin, Neutron Powder Diffraction Refinement of Boron Carbides – Nature of Intericosahedral Chains. *J. Alloys Compd.*, 1995, 226, p. 121-125.
85. H. Werheit, Are There Bipolarons in Icosahedral Boron-Rich Solids? *J. Phys.: Condens. Matter*, 2007, 19, p. 186207.

86. V.V. Brazhkin, A.G. Lyapin, R.J. Hemley, Harder than Diamond: Dreams and Reality *Philosoph. Mag. A*, 2002, 82, p. 231-253.
87. J.M. Leger, J. Haines, The Search for Superhard Materials. *Endeavour*, 1997, 21, p. 121-124.
88. P.F. McMillan, New Materials from High-Pressure Experiments. *Nature Mater.*, 2002, 1, p. 19-25.
89. H.F. Rizzo, W.C. Simmons, H.O. Bielstein, The Existence and Formation of the Solid B_6O. *J. Electrochem. Soc.*, 1962, 109, p. 1079-1082.
90. D. He, Y. Zhao, L. Daemen, J. Qian, T.D. Shen, T.W. Zerda, Boron Suboxide: As Hard as Cubic Boron Nitride. *Appl. Phys. Lett.,* 2002, 81, p. 643-645.
91. A.R Badzian, Superhard Material Comparable in Hardness to Diamond. *Appl. Phys. Lett.*, 1988, 53, p. 2495-2497.
92. A.R. Badzian, Superhard Material Comparable in Hardness to Diamond. *Appl. Phys. Lett.*, 1988, 53, p. 2495-2497.
93. V.A. Mukhanov, O.O. Kurakevych, V.L. Solozhenko, On the Hardness of Boron (III) Oxide. *J. Superhard Mater.*, 2008, 30, p. 71-72.
94. S. Lee, S. W. Kim, D. M. Bylander, L. Kleinman, Crystal Structure, Formation Enthalpy, and Energy Bands of B_6O. *Phys. Rev. B*, 1991, 44, p. 3550-3554.
95. T. Lundström, H. Bolmgren, On Refractory Boron Compounds Crystallizing in b4c-Type Structures. *Jpn. J. Appl. Phys. Ser.*, 1994, 10, p. 1-4.
96. T. Lundström, Y.G. Andreev, Superhard Boron-Rich Borides and Studies of the B-C-N System. *Mater. Sci. Eng. A*, 1996, 209, p. 16-22.
97. T. Lundström, Structure and Bulk Modulus of High-Strength Boron Compounds. *J. Solid State Chem.*, 1997, 133, p. 88-92.
98. M. Kobayashi, I. Higashi, C. Brodhag, F. Thevenot, Structure of B_6O Boron-Suboxide by Rietveld Refinement. *J. Mater. Sci.*, 1993, 28, p. 2129-2134.
99. H. Hubert, B. Devouard, L.A.J. Garvie, M.O. Keeffe, P.R. Buseck, W.T. Petuskey, P.F. McMillan, Icosahedral Packing of B-12 Icosahedra in Boron Suboxide (B_6O). *Nature*, 1998, 391, p. 376-378.
100. P.F. McMillan, H. Hubert, A. Chizmeshya, W.T. Petuskey, L.A.J. Garvie, B. Devouard, Nucleation and Growth of Icosahedral Boron Suboxide Clusters at High Pressure. *J. Solid State Chem.*, 1999, 147, p. 281-290.
101. M. Olofsson, T. Lundström, Synthesis and Structure of Non-Stoichiometric B_6O. *J. Alloys Compd.*, 1997, 257, p. 91-95.
102. H. Hubert, L.A.J. Garvie, B. Devouard, P.R. Buseck, W.T. Petuskey, P. F. McMillan, High-Pressure, High-Temperature Synthesis and Characterization of Boron Suboxide (B_6O). *Chem. Mater.*, 1998, 10, p. 1530-1537.

103. H.T. Hall, L.A. Compton, Group 4 Analogs and High Pressure High Temperature Synthesis of B_2O. *Inorg. Chem.*, 1965, 4, p. 1213-1216.

104. V. Srikanth, R. Roy, E.K. Graham, D.E. Voigt, B_xO - Phases Present at High-Pressure and Temperature. *J. Amer. Ceram. Soc.*, 1991, 74, p. 3145-3147.

105. X. Liu, X. Zhao, W. Hou, W. Su, A New Route for the Synthesis of Boron Suboxide B_7O. *J. Alloys Compd.*, 1995, 223, p. L7–L9.

106. T. Endo, T. Sato, M. Shimada, High-Pressure Synthesis of B_2O with Diamond-Like Structure. *J. Mater. Sci. Let.*, 1987, 6, p. 683-685.

107. T. Endo, T. Sato, M. Shimada, *Mater. Sci. Monogr.*, 1987, 38C, p. 2623-2628.

108. A.V. Nemukhin, F. Weinhold, Boron Oxides – Ab Initio Studies with Natural Bond Orbital Analysis. *J. Chem. Phys.*, 1993, 98, p. 1329-1335.

109. T. Endo, H. Takizawa, M. Shimada, *New Funct. Mater.*, 1993, C, p. 107-112.

110. M.P. Grumbach, O.F. Sankey, P.F. McMillan, Properties of B_2O: An Unsymmetrical Analog of Carbon. *Phys. Rev. B*, 1995, 52, p. 15807-15811.

111. D. Nieto-Sanz, P. Loubeyre, W. Chrichton, M. Mezouar, X-ray Study of the Synthesis of Boron Oxides at High Pressure: Phase Diagram and Equation of State. *Phys. Rev. B*, 2004, 70, p. 214108-1-6.

112. F.C. Kracek, G.W. Morey, H.E. Merwin, The System, Water-Boron Oxide. *Am. J. Sci.*, 1938, 35A, p. 143-171.

113. F. Dachille, R. Roy, A New High-Pressure Form of B_2O_3 and Inferences on Cation Coordination from Infrared Spectroscopy. *J. Am. Ceram. Soc.*, 1959, 42, p. 78-80.

114. S.V. Berger, The Crystal Structure of Boron Oxide. *Actu Chem. Scad.*, 1953, 7, p. 611-622.

115. J.D. Mackenzie, W.F. Claussen, Crystallization and Phase Relations of Boron Trioxide at High Pressures. *J. Am. Ceram. Soc.*, 1961, 44, p. 79-81.

116. G.E. Gurr, P.W. Montgomery, C.D. Knutson, B.T. Gorres, The Crystal Structure of Trigonal Diboron Trioxide. *Acta Cryst. B*, 1970, 26, p. 906-915.

117. W.F. Claussen, J.D. Mackenzie, Crystallization of B_2O_3 at High Pressures. *J. Am. Chem. Soc.*, 1959, 81, p. 1007.

118. C.S. Yoo, J. Akella, H. Cynn, M. Nicol, Direct Elementary Reactions of Boron and Nitrogen at High Pressures and Temperatures. *Phys. Rev. B*, 1997, 56, p. 140-146.

119. V.L. Solozhenko, O.O. Kurakevych, V.Z. Turkevich, V.D. Turkevich, Phase Diagram of the B-B_2O_3 System at 5 GPa: Experimental and Theoretical Studies. *J. Phys. Chem.*, 2008, B112, p. 6683-6687.

120. D. Li, W.Y. Ching, Electronic Structures and Optical Properties of Low-and High-Pressure Phases of Crystalline B_2O_3. *Phys. Rev. B*, 1996, 54, p. 13616-13622.

121. V.V. Brazhkin, Y. Katayama, Y. Inamura, M.V. Kondrin, A.G. Lyapin, S.V. Popova, R.N. Voloshin, Structural Transformations and Anomalous Viscosity in the B_2O_3 Melt under High Pressure. *JETP Letters*, 2003, 78, p. 393-397.
122. O.O. Kurakevych, Superhard Phases of Simple Substances and Binary Compounds of the B-C-N-O System: from Diamond to the Latest Results. *J. Superhard Mater.*, 2009, 31, p. 139-157.
123. V.L. Solozhenko, O.O. Kurakevych, Y. Le Godec, V.V. Brazhkin, Thermodynamically Consistent p-T Phase Diagram of Boron Oxide B_2O_3 by In Situ Probing and Thermodynamic Analysis. *J. Phys. Chem. C*, 2015, 119, p. 20600-20605.
124. C.T. Prewitt, R.D. Shannon, Crystal Structure of a High-Pressure form of B_2O_3. *Acta Cryst. B*, 1968, 24, p. 869-874.
125. C. Yoo, H. Cynn, M. Nicol, Elementary Reactions of Nitrogen and Oxygen with Boron and Carbon at High Pressures and Temperatures. *Rev. High Pressure Sci. Technol.*, 1998, 7, p. 1054-1060.
126. W.D. Schubert, H. Neumeister, G. Kinger, Hardness to Toughness Relationship of Fine-Grained WC-Co Hardmetals. *Int. J. Refract. Met. Hard Mater.*, 1998, 16, p. 133-142.
127. A.L. Mackay, A Dense Non-Crystallographic Packing of Equal Spheres. *Acta Crystallogr.*, 1962, 15, p. 916-918.
128. E. Weintraub, *Trans. Am. Electrochem. Soc.*, 1909, 16, p. 165-184.
129. R.A. Pasternak, Crystallographic Evidence for The Existence of B_7O. *Acta Cryst.*, 1959, 12, p. 612-613.
130. S. LaPlaca, B. Post, The Boron Carbide structure Type. *Planseeberichtefür Pulvermetallurgie*, 1961, 9, p. 109-112.
131. P.M. Bills, D. Lewis, Nonstoichiometry of Boron Suboxide (B_6O). *J. Less-Common Met.*, 1976, 33, p. 343-345.
132. C. Brodhag, F. Thevenot, Hot-Pressing of Boron Suboxide $B_{12}O_2$. *J. Less-Common Met.*, 1986, 117, p. 1-6.
133. V.L. Solozhenko, O.O. Kurakevych, P. Bouvier, First and Second-Order Raman Scattering of B_6O. *J. Raman Spectrosc.*, 2009, 40, p. 1078-1081.
134. V.L. Solozhenko , O.O. Kurakevych, V.Z. Turkevich and D.V. Turkevich, Synthesis of B_6O Boron Suboxide at Pressures up to 1 GPa. *J. Superhard Mater.*, 2005, 27, p. 12-16.
135. V.L. Solozhenko, C. Lathe, On the Melting Temperature of B_6O. *J. Superhard Mater.*, 2007, 29, p. 259-260.
136. T.L. Aselage, D.R. Tallant, D. Emin, Isotope Dependencies of Raman Spectra of $B_{12}As_2$, $B_{12}P_2$, $B_{12}O_2$, and $B_{12+x}C_{3-x}$: Bonding of Intericosahedral Chains. *Phys. Rev. B*, 1997, 56, p. 3122-3129.

137. X. Jiao, H. Jin, Z. Ding, B. Yang, F. Lu, X. Zhao, X. Liu, L. Peng, Synthesis of Boron Suboxide from Boron and Boric Acid under Mild Pressure and Temperature Conditions. *Mater. Res. Bull.*, 2011, 46, p. 786-789.
138. O.O. Kurakevych, V.L. Solozhenko, Experimental Study and Critical Review of Structural, Thermodynamic and Mechanical Properties of Superhard Refractory Boron Suboxide B_6O. *J. Superhard Mater.*, 2011, 33, p. 421-428.
139. Y. Wang, Y. Wang, T. Yao, H. Li, L. Wub, M. Yang, J. Zhang, H. Gou, Metallization and Softening of B_6O at High Pressure. *J. Alloys Compd.*, 2014, 600, p. 71-77.
140. V.A. Mukhanov, O.O. Kurakevych, V.L. Solozhenko, The Interrelation Between Hardness and Compressibility of Substances and Their Structure and Thermodynamic Properties. *J. Superhard Mater.*, 2008, 30, p. 366-378.
141. A. Sommer, P.N. Walsh, D. White, Mass Spectrometric and Infrared Emission Investigation of the Vapor Species in the B-S System at Elevated Temperatures. *J. Chem. Phys.*, 1960, 33, p. 296-297.
142. P. Hagenmuller, F. Chopin, C.R. Hebd, Chimie Minerale - sur le Systeme Bore-Soufre. *Seances Acad. Sci.*, 1962, 255, p. 2259-2260.
143. F.T. Greene, P.W. Gilles, New Classes of High Molecular Weight Boron Sulfides. *J. Am. Chem. Soc.*, 1962, 84, p. 3598-3599.
144. F.T. Greene, P.W. Gilles, High Molecular Weight Boron Sulfides. II. Identification, Relative Intensities, Appearance Potentials, and Origins of the Ions. *J. Am. Chem. Soc.*, 1964, 86, p. 3964-3969.
145. H.-Y. Chen, P.W. Gilles, High Molecular Weight Boron Sulfides .5. Vaporization Behavior of Boron-Sulfur System. *J. Am. Chem. Soc.*, 1970, 92, p. 2309-2312.
146. H.-Y. Chen, B. Conard, P.W. Gilles, High Molecular Weight Boron Sulfides .6. Unit Cell of Monoclinic Diboron Trisulfide. *Inorg. Chem.*, 1970, 9, p. 1776-1777.
147. H.-Y. Chen, P.W. Gilles, High Molecular Weight Boron Sulfides. VIII. Vapor Pressures of B_2S_3 (g) and B_4S_6 (g) over Stoichiometric B_2S_3. *J. Phys. Chem.*, 1972, 76, p. 2035-2038.
148. H. Diercks, B. Krebs, Crystal Structure of B_2S_3: Four-Membered B_2S_2 Rings and Six-Membered B_3S_3 Rings. *Angew. Chem.*, 1977, 16, p. 313.
149. B. Krebs, Thio-and Seleno-Compounds of Main Group Elements-Novel Inorganic Oligomers and Polymers. *Angew. Chem.*, 1983, 22, p. 113-134.
150. B. Krebs, H.U. Hürter, B_8S_{16}-An “Inorganic Porphine”. *Angew. Chem.*, 1980, 92, p. 481-482.
151. O. Conrad, C. Jansen, B. Krebs, Boron-Sulfur and Boron-Selenium Compounds - From Unique Molecular Structural Principles to Novel Polymeric Materials *Angew. Chem. Int. Ed.*, 1998, 37, p. 3208-3218.

152. H.U. Hürter, B. Krebs, H. Eckert, W. Müllerwarmuth, Solid-State B-11 NMR-Studies on Boron Chalcogenide Systems. *Inorg. Chem.*, 1985**,** 24, p. 1288-1292.
153. D.C. Carlson, *Diss. Abstr.*, 1967, 27, 2664.
154. T. Sasaki, H. Takizawa, K. Uheda, T. Endo, High pressure synthesis of binary B-S Compounds. *Phys. Stat. Sol. B*, 2001, 223, p. 29-33.
155. T. Sasaki, H. Takizawa, K. Uheda, T. Yamashita, T. Endo, High-Pressure Synthesis and Crystal Structure of B_2S_3. *J. Solid State Chem.*, 2002, 166, p. 164-170.
156. V.I. Matkovich, Interstitial Compounds of Boron. *J. Am. Chem. Soc.*, 1961, 83, p. 1804-1806.
157. M.P. Pardo, J. Flahaut, A New Variety of GaS, Rhombohedral 3R Metastable - Formation And Structural Study. *Mater. Res. Bull.*, 1987*,* 22, p. 323-329.
158. R.N. Sinclair, C.E. Stone, A.C. Wright, S.W. Martin, M.L. Royle, A.C. Hannon, The Structure of Vitreous Boron Sulphide. *J. Non-Cryst. Solid.*, 2000, 293, p. 383-388.
159. O. Sologub, Y. Matsushita, T. Mori, An Alpha-Rhombohedral Boron-Related Compound with Sulfur: Synthesis, Structure and Thermoelectric Properties. *Scr. Mater.*, 2013, 68, p. 289-292.
160. L. Pauling, Covalent Chemical Bonding of Transition Metals in Pyrite, Cobaltite, Skutterrudite, Millerite and Related Minerals. *Can. Mineral.*, 1978, 16, p. 447-452.
161. J. Jiang, J. Yuana, A. Bleloch, Cluster Scale Composition Determination in a Boron-Rich Compound. *Appl. Phys. Lett.*, 2007, 91, p. 113107-113109.
162. S. Hosoi, H. Kim, T. Nagata, K. Kirihara, K. Soga, K. Kimura, K. Kato, M. Takata, Electron Density Distributions in Derivative Crystals of Alpha-Rhombohedral Boron. *J. Phys. Soc. Jpn.*, 2007, 76, p. 044602–044608.
163. R.C. Melucci, P.G. Wahlbeck, Mass Spectrometric Observations of Gaseous Boron Selenides. *Inorg. Chem.*, 1970, 9, p. 1065-1068.
164. W.E. Hutchinson, H.A. Eick, Preparation and Properties of Boron Sesquiselenide. *Inorg. Chem.*, 1962, 1, p. 434-436.
165. H. Bolmgren, T. Lundström, The Crystal-Structure of a New Boron Selenide, $B_{12}Se_{2-X}B_X$. *J. Alloys Compd.*, 1993, 202, p. 73-76.
166. H. Liander, Artificial Diamonds. *ASEA Journal*, 1955, 28, p. 97-98.
167. F.P. Bundy, H.T. Hall, H.M. Strong, R.H. Wentorf, Man-Made Diamonds. *Nature*, 1955, 176, p. 51-55.
168. H.R. Wentorf, Cubic Form of Boron Nitride. *Chem. Phys.*, 1957, 26, p. 956-960.
169. Y. Akahama, H. Kawamura, Raman Scattering and X-Ray Diffraction Experiments for Phase III of Solid Hydrogen. *J. Phys.: Conf. Ser.*, 2010, 215, p. 012195-1-5.
170. W.A. Bassett, Diamond Call and the Nature of the Earths Mantle. *Ann. Rev. Earth Planet. Sci.*, 1979, 7, p. 357-384.

171. G.J. Piermarini, S. Block, J.D. Barnett, R.A. Forman, Calibration of Pressure-Dependence of R1 Ruby Fluorescence Line to 195 kbar. *J. Appl. Phys.*, 1975, 46, p. 2774-2780.
172. O. Grasset, Calibration of the R Ruby Fluorescence Lines in the Pressure Range [0-1 GPa] and the Temperature Range [250-300 K]. *High Pressure Res.*, 2001, 21, p. 139-157.
173. S. Rekhi, L.S. Dubrovinsky, S.K. Saxena, Temperature-Induced Ruby Fluorescence Shifts up to a Pressure of 15 GPa in an Externally Heated Diamond Anvil Cell. *High Temp.-High Pressures*, 1999, 31, p. 299-305.
174. D.D. Ragan, R. Gustavsen, D. Schiferl, Calibration of the Ruby R(1) and R(2) Fluorescence Shifts as a Function of Temperature from 0 to 600-K. *J. Appl. Phys*., 1992, 72, p. 5539-5544.
175. H.K. Mao, P.M. Bell, J.W. Shaner, D.J. Steinberg, SPECIFIC VOLUME Measurements of Cu, Mo, Pd, and Ag and Calibration of Ruby R1 Fluorescence Pressure Gauge from 0.06 to 1 Mbar. *J. Appl. Phys.*, 1978, 49, p. 3276-3283.
176. J.D. Barnett, S. Block and G. J. Piermarini, Optical Fluorescence System for Quantative Pressure Measurement in Diamond-Anvil Cell. *Rev. Sci. Instrum.*, 1973, 44, p. 1-9.
177. J.M. Besson, R.J. Nelmes, New Developments in Neutron-Scattering Methods under High-Pressure with the Paris-Edinburgh Cells. *Physica B*, 1995, 213, p. 31-36.
178. M. Mezouar, T. Le Bihan, H. Libotte, Y. Le Godec, D. Hausermann, Paris-Edinburgh Large-Volume Cell Coupled with a Fast Imaging-Plate System for Structural Investigation at High Pressure and High Temperature. *J. Synchrotron Radiat.*, 1999, 6, p. 1115-1119.
179. D.L. Decker, High-Pressure Equation of State for NaCl, KCl, and CsCl. *J. App. Phys.*, 1971, 42, p. 3239-3244.
180. F. Birch, Equation of State and Thermodynamic Parameters of NaCl to 300-kbar in the High-Temperature Domain. *J. Geophys. Res.-Solid Earth and Planets*, 1986, 91, p. 4949-4954.
181. D.L. Heinz, R. Jeanloz, The Equation of State of the Gold Calibration Standard *J. App. Phys.*, 1984, 55, p. 885-893.
182. Y. Le Godec, D. Martinez-Garcia, M. Mezouar, G. Syfosse, J.P. Itie, J.M. Besson, Thermoelastic Behaviour of Hexagonal Graphite-like Boron Nitride. *High Press. Res.*, 2000, 17, p. 35-46.
183. W.A. Crichton, M. Mezouar, Noninvasive Pressure and Temperature Estimation in Large-Volume Apparatus by Equation-of-State Cross-Calibration. *High Temp.-High Press.*, 2002, 34, p. 235-242.
184. L.G. Khvostantsev, V.N. Slesarev, V.V. Brazhkin, Toroid Type High-Pressure Device: History and Prospects. *High Press. Res.*, 2004, 24, p. 371-383.
185. S. Zhai, E. Ito, Recent Advances of High-Pressure Generation in a Multianvil Apparatus Using Sintered Diamond Anvils. *Earth Sci. Front.*, 2011, 2, p. 101-106.
186. E. Ito, D. Yamazaki, T. Yoshino, H. Fukui, S. Zhai, A. Shatzkiy, T. Katsura, Y. Tange, K. Funakoshi, Pressure Generation and Investigation of the Post-Perovskite Transformation in

$MgGeO_3$ by Squeezing the Kawai-Cell Equipped with Sintered Diamond Anvils. *Earth Planet. Sci. Lett.*, 2010, 293, p. 84-89.

187. N. Kawai and S. Endo, The Generation of Ultrahigh Hydrostatic Pressures by a Split Sphere Apparatus. *Rev. Sci. Instrum.*, 1970, 41, p. 1178-1181.
188. N. Kawai, M. Togaya and A. Onodera, New Device for Pressure-Vessels. *P. Jpn. Acad. B-Phys.*, 1973, 49, p. 623-626.
189. D. Walker, M.A. Carpenter and C.M. Hitch, Some Simplifications to Multianvil Devices for High Pressure Experiments. *Am. Mineral.*, 1990, 75, p. 1020-1028.
190. J. Osugi, K. Shimizu, K. Inoue, K. Yasunami, A Compact Cubic Anvil High Pressure Apparatus. *Rev. Phys. Chem. Jpn.*, 1964, 34, p. 1-6.
191. R.C. Liebermann, C. Robert, Multi-Anvil, High Pressure Apparatus: a Half-Century of Development and Progress. *High Pressure Res.*, 2011, 31, p. 493-532.
192. K.D. Leinenweber, J.A. Tyburczy, T.G. Sharp, E. Soignard, T. Diedrich, W.B. Petuskey, Y. Wang and J.L. Mosenfeld, Cell Assemblies for Reproducible Multi-Anvil Experiments (the COMPRES assemblies). *Am. Mineral.*, 2012, 97, p. 353-368.
193. L.D. Son, G.M. Rusakov, N.N. Katkov, The Phase Diagram of Carbon in the Vicinity of Graphite-Diamond Transition. *Doklady Phys.*, 2006, 51, p. 56-59.
194. A.P. Hammersley, S.O. Svensson, M. Hanfland, A.N. Fitch, D. Häusermann, Two-Dimensional Detector Software: From Real Detector to Idealised Image or Two-Theta Scan. *High Pressure Res.*, 1996, 14, p. 235-248.
195. J. Rodriguez-Carvajal, Recent Advances in Magnetic Structure Determination by Neutron Powder Diffraction. *Physica B*, 1993, 192, p. 55-69.
196. T. Roisnel, J. Rodriguez-Carvajal, Proceedings of the 7th European Powder Diffraction Conference (EPDIC 7), 2001, 118-123.
197. A. Boultif, D. Louer, Powder Pattern Indexing with the Dichotomy Method. *J. Appl. Cryst.*, 2004, 37, p. 724-731.
198. E. Laine, I. Lähteenmäki, The Energy Dispersive X-ray Diffraction Method: Annotated Bibliography 1968-78. *J. Material of Science*, 1980, 15, p. 269-278.
199. A. King, N. Guignot, P. Zerbino, J.P. Itié, M. Bord, G. Renaud, M. C. N. Lenoir, M. Bornert, *in preparation*.
200. Y. Wang, T. Uchida, R. Von Dreele, M.L. Rivers, N. Nishiyama, K. Funakoshi, A. Nozawac, H. Kanekod, A New Technique for Angle-Dispersive Powder Diffraction Using an Energy-Dispersive Setup and Synchrotron Radiation. *J. Appl. Cryst.*, 2004, 37, p. 947-956.

201. T.A. Strobel, O.O. Kurakevych, D.Y. Kim, Y. Le Godec, W. Crichton, J. Guignard, N. Guignot, G.D. Cody, A.R. Oganov, Synthesis of β-Mg_2C_3: A Monoclinic High-Pressure Polymorph of Magnesium Sesquicarbide. *J. Inorg. Chem.*, 2014, 53, p. 7020-7027.
202. P. Hohenberg, W. Kohn, Inhomogeneous Electron Gas *Phys. Rev. B*, 1964, 136, p. 864-871.
203. W. Kohn, Nobel Lecture: Electronic Structure of Matter-Wave Functions and Density Functionals. *Rev. Mod. Phys.*, 1999, 71, p. 1253-1266.
204. W. Kohn, L.J. Sham, Self-Consistent Equations Including Exchange and Correlation Effects. *Phys. Rev. A*, 1965, 140, p. 1133-1138.
205. R.A. Evarestov. Quantum Chemistry of Solids, The LCAO First Principles Treatment of Crystals. *Springer*, 2007.
206. http://www.theochem.uni-stuttgart.de/pseudopotentials/index.en.html.
207. R. Dovesi, V.R. Saunders, C. Roetti, R. Orlando, C.M. Zicovich-Wilson, F. Pascale, *CRYSTAL09 User's Manual* (University of Torino, Torino, 2009).
208. F.D. Murnaghan, The Compressibility of Media Under Extreme Pressures. *Proc. Natl. Acad. Sci.*, 1944, 30, p. 244-247.
209. K. Parlinski, Z.Q. Li, Y. Kawazoe, First-Principles Determination of the Soft Mode in Cubic ZrO_2. *Phys. Rev. Lett.*, 1997, 78, p. 4063-4066.
210. H. Kraus, V.B. Mikhailik, L. Vasylechko, D. Day, K.B. Hutton, J. Telfer, Yu. Prots, Effect of Ca Doping on the Structure and Scintillation Properties of $ZnWO_4$. *Phys. Stat. Sol. (a)*, 2007, 204, p. 730-736.
211. J.C. Chervin, B. Canny, J.M. Besson, Ph. Pruzan, A Diamond Anvil Cell for IR Microspectroscopy. *Rev. Sci. Instrum.*, 1995, 66, p. 2595-2598.
212. H.K. Mao, J. Xu, P. M. Bell, Calibration of the Ruby Pressure Gauge to 800 kbar under Quasi-Hydrostatic Conditions. *J. Geophys. Res.*, 1986, 91, p. 4673-4676.
213. A. Dewaele, F. Datchi, P. Loubeyre, M. Mezouar, High Pressure-High Temperature Equations of State of Neon and Diamond. *Phys. Rev. B*, 2008*,* 77*,* p. 094106-1-9.
214. W.B. Holzapfel, Progress in the Realization of a Practical Pressure Scale for the Range 1-300 GPa. *High Pres. Res.*, 2005, 25, p. 87-96.
215. R. Orlando, R. Dovesi, C. Roetti, Ab Initio Hartree-Fock Calculations for Periodic Compounds - Application to Semiconductors. *J Phys.-Cond. Mat.*, 1990, 2, p. 7769-7789.
216. http://www.theochem.unito.it/crystal_tuto/mssc2013_cd/tutorials/index.html; MgO example
217. H.J. Monkhorst, J.D. Pack, Special Points for Brillouin-Zone Integrations. *Phys Rev B*, 1976, 13, p. 5188-5192.
218. Z. Wu, R.E. Cohen, More Accurate Generalized Gradient Approximation for Solids. *Phys Rev B*, 2006, 73, p. 235116-1-6.

219. O.O. Kurakevych, V.L. Solozhenko, 300-K Equation of State of Rhombohedral Boron Subnitride. *Solid State Commun.*, 2009, 149, p. 2169-2171.
220. P. Vinet, J. Smith, J. Ferrante, J. Rose, Temperature Effects on the Universal Equation of State of Solids. *Phys. Rev. B*, 1987, 35, p. 1945-1953.
221. C.J. Sahle, C. Sternemann, C. Schmidt, S. Lehtola, S. Jahn, L. Simonelli, S. Huotari, M. Hakala, T. Pylkkänen, A. Nyrow, K. Mende, M. Tolan, K. Hämäläinen, M. Wilke, Microscopic Structure of Water at Elevated Pressures and Temperatures. *Proc. Nat. Acad. Sc.*, 2013, 110, p. 6301-6306.
222. R. Letoullec, J.P. Pinceaux, P. Loubeyre, The Membrane Diamond Anvil Cell: A New Device for Generating Continuous Pressure and Temperature Variations. *High Pressure Res.*, 1988, 1, p. 77-90.
223. F. Pascale, C.M. Zicovich-Wilson, F. Lopez, B. Civalleri, R. Orlando, R. Dovesi, The Calculation of the Vibrational Frequencies of Crystalline Compounds and Its Implementation in the CRYSTAL Code. *J. Comput. Chem.*, 2004, 25, p. 888-897.
224. A.K. Soper, C.J. Benmore, Quantum Differences between Heavy and Light Water. *Phys. Rev. Lett.*, 2008, 101, p. 065502-1-4.
225. S.K. Sharma, B. Simons, J.F. Mammone, Relationship between Density, Refractive Index and Structure of B203 Glasses at Low and High Pressures. *J. Non-Cryst. Sol.*,1980, 42, p. 607-618.
226. B.N. Meera, J. Ramakrishna, Raman Spectral Studies of Borate Glasses. *J. Non-Cryst. Sol.*,1993, 159, p. 1-21.
227. A.F. Murray, D.J. Lockwood, Raman-Spectrum of $ZN_4O(BO_2)_6$. *J. Phys. C: Solid State Phys.*, 1976, 9, p. 3691-3700.
228. S.C. Neumair, G. Sohr, S. Vanicek, K. Wurst, R. Kaindl, H. Huppertz, The New High-Pressure Sodium Tetraborate HP-$Na_2B_4O_7$. *Z. Anorg. Allg. Chem*. 2012, 638, p. 81-87.
229. Y. Li, G. Lan, Pressure-Induced Amorphization Study of Lithium Diborate. *J. Phys. C: Solid State Phys.*, 1996, 57, p. 1887-1890.
230. G.L. Paul, W. Taylor, Raman Spectrum of $Li_2B_4O_7$. *Phys. C: Solid State Phys.*, 1982, 15, p. 1753-1764.
231. A. Elbelrhiti Elalaoui, A. Maillard, Raman Scattering and Non-Linear Optical Properties in $Li_2B_4O_7$. *J. Phys.: Condens. Matter*, 2005, 17, p. 7441-7454.
232. S.I. Furusawa, S. Tange, Y. Ishibashi, K. Miwa, Dielectric Properties of Lithium Diborate ($Li_2B_4O_7$) Single-Crystal? *J. Phys. Soc. Japan*, 1990, 59, p. 1825-1830.
233. A.V. Vdovin, V.N. Moiseenko, Y.V. Burak, Vibrational Spectrum of $Li_2B_4O_7$ Crystals. *Opt. Spect.*, 2001, 90, p. 555-560.
234. Y. Lin, G. Xiong, G. Lan, H. Wang, L. Xu, High-Pressure Raman Spectra of Lithium Triborate Crystal and Pressure-Induced Phase Transitions. *J. Phys. Chem. Solid.*, 1994, 55, p. 113-117.

235. J. Hanuza, M. Maczka, Polarized Raman and IR Spectra of Non-Centrosymmetric PbB_4O_7 Single Crystal. *J. Raman Spec.*, 2008, 39, p. 409-414.

236. K.A. Cherednichenko, Y. Le Godec, A. Kalinko, M. Mezouar, J.P. Itié, V.L. Solozhenko, *in preparation*.

237. V.L. Solozhenko, O.O. Kurakevych, Y. Le Godec, A.V. Kurnosov, A.R. Oganov, Boron Phosphide Under Pressure: In Situ Study by Raman Scattering and X-ray Diffraction. *J. App. Phys.*, 2014, 116, p. 033501-1-5.

238. A.V. Kosobutsky, S.Yu. Sarkisov, V.N. Brudnyi, Structural, Elastic and Electronic Properties of GaSe under Biaxial and Uniaxial Compressive Stress. *J. Phys. Chem. Solid.*, 2013, 74, p. 1240-1248.

239. L. Ghalouci, B. Benbahi, S. Hiadsi, B. Abidri, G. Vergoten, F. Ghalouci, First Principle Investigation into Hexagonal and Cubic Structures of Gallium Selenide. *Comp. Mat. Sci.*, 2013, 67, p. 73-82.

240. J. Pellicer-Porres, A. Segura, C. Ferrer, V. Munoz, A. San Miguel, A. Polian, J.P. Itié, M. Gauthier, S. Pascarelli, High-Pressure X-Ray-Absorption Study of GaSe. *Phys. Rev. B*, 2002, 65, p. 174103-1-7.

241. V.A. Mukhanov, P.S. Sokolov, V.L. Solozhenko, On Melting of B_4C Boron Carbide under Pressure. *J. Superhard Mater.*, 2012, 34, p. 211-213.

242. R. Letoullec, J.P. Pinceaux, P. Loubeyre, The Membrane Diamond Anvil Cell: A New Device for Generating Continuous Pressure and Temperature Variations. *High Pressure Res.,* 1988, 1, p. 77-90.

243. A. Bergner, M. Dolg, W. Kuechle, H. Stoll, H. Preuss, Ab Initio Energy-Adjusted Pseudopotentials for Elements of Groups 13-17. *Mol. Phys.*, 1993, 80, p. 1431-1441.

244. G.S. Orudzhev, E.K. Kasumova, Ab Initio Investigation of the Pressure Influence on Elastic Properties of the GaS Layered Compound. *Phys. Solid State*, 2014, 56, p. 619-625.

245. M. Gatulle, M. Fischer, A. Chevy, Elastic Constants of the Layered Compounds GaS, GaSe, InSe, and Their Pressure Dependence I. Experimental Part. *Phys. Stat. Sol. (b)*, 1983, 119, p. 327-336.

246. V. Panella, G. Carlotti, G. Socino, L. Giovannini, M. Eddrief, C. Sebenne, Elastic Properties of GaSe Films Epitaxially Grown on the Si (111)1×1-H Surface, Studied by Brillouin Scattering. *J. Phys.: Condens. Matter*, 1999, 11, p. 6661-6668.

247. A. Polian, J.M. Besson, M. Grimsditch, H. Vogt, Elastic Properties of GaS under High Pressure by Brillouin Scattering. *Phys. Rev. B*, 1982, 25, p. 2767-2775.

248. U. Schwarz, D. Olguin, A. Cantarero, M. Hanfland, K.Syassen, Effect of Pressure on the Structural Properties and Electronic Band Structure of GaSe. *Phys. Stat. Sol. B*, 2007, 244, p. 244-255.

249.V.Y. Altshul, V.K. Bashenov, Long-Wavelength Phonons and Elastic Constants in Layer Compounds GaS, GaSe, and InSe. *J. Phys. Stat. Sol. (b)*, 1980, 98, p. K5-K8.

250.V. Panella, G. Carlotti, G. Socino, L. Giovannini, M. Eddrief, K. Amimer, C. Sebenne, Brillouin Scattering Study of Epitaxial InSe Films Grown on the Surface. *J. Phys.: Condens. Matter*, 1997, 9, p. 5575-5580.

251.J. Pellicer-Porres, E. Machado-Charry, A. Segura, S. Gilliland, E. Canadell, P. Ordejon, A. Polian, P. Munch, A. Chevy, N. Guignot., GaS and InSe Equations of State from Single Crystal Diffraction. *Phys. Stat. Sol. B*, 2007, 244, p. 169-173.

252.J. Pellicer-Porres, A. Segura, A. San Miguel, V. Munoz, High-Pressure X-Ray Absorption Study of InSe. *Phys. Rev. B*, 1999, 60, p. 3757-3763.

253.H. d'Amour, W.B. Holzapfel, A. Polian, A. Chevy, Crystal Structure of a New High Pressure Polymorph of GaS. *Solid State Commun.*, 1982, 44, p. 853-855.

254.F. Wilhelm, P. Voisin, J. Jacobs, G. Garbarino, H. Vitoux, R. Steinmann, A. Snigirev, I. Snigireva and A. Rogalev, *ESRF user meeting*, 2014, Grenoble.

255.M. Hanfland, H. Beister, K. Syassen, Graphite under Pressure – Equation of State and 1st-order Raman Modes. *Phys. Rev. B*, 1989, 39, p. 12598-12603.

256.V.L. Solozhenko, G. Will, F. Elf, Isothermal Compression of Hexagonal Graphite-like Boron Nitride up to 12 GPa. *Solid State Comm.*, 1995, 96, p. 1-3.

257.V.L. Solozhenko, E.G. Solozhenko, Equation of State of Turbostratic Boron Nitride. *High Pressure Res.*, 2001, 21, p. 115-120.

258.Z. Dong-Wen, J. Feng-Tao, Y. Jian-Min, First-Principles Calculation of Static Equation of State and Elastic Constants for GaSe. *Chin. Phys. Lett.*, 2006, 23, p. 1876-1879.

259.Zs. Rak, S.D. Mahanti, K.C. Mandal, N.C. Fernelius, Doping Dependence of Electronic and Mechanical Properties of $GaSe_{1-x}Te_x$ and $Ga_{1-x}In_xSe$ from First Principles. *Phys. Rev. B*, 2010, 82, p. 155203-1-10.

260.D.W. Zhang, F.T. Jin, J.-M. Yuan, First-Principles Calculation of Static Equation of State and Elastic Constants for GaSe. *Chin. Phys. Lett.*, 2006, 23, p. 1876-1879.

261.T.C. Chiang, J. Dumas, Y.R. Shen, Brillouin-Scattering in a Layer Compound GaSe. *Solid State Commun.*, 28, 1978, p. 173-176.

262.B. Wen, R. Melnik, S. Yao, T. Li, Pressure Dependent Phase Stability Transformations of GaS: A First Principles Study. *Mater. Sci. Semicond.*, 13, 2010, p. 295-297.

263.M. Takumi, A. Hirata, T. Ueda, Y. Koshio, H. Nishimura, K. Nagata, Structural Phase Transitions of Ga_2Se_3 and GaSe under High Pressure. *Phys. Stat. Sol. (b)*, 2001, 223, p. 423-426.

264. A.M. Kulibekov, H.P. Olijnyk, A.P. Jephcoat, Z.Y. Salaeva, S. Onari, K.R. Allakhverdiev, Raman Scattering under Pressure and the Phase Transition in ε-GaSe. *Phys. Stat. Sol. (b)*, 2003, 235, p. 517-520.

265. J.C. Chervin, B. Canny, J. M. Besson, Ph. Pruzan, A Diamond Anvil Cell for IR Microspectroscopy. *Rev. Sci. Instrum.*, 1995, 66, p. 2595-2598.

266. A. Polian, K. Kunc, A. Kuhn, Low-Frequency Lattice-Vibrations of Delta-GaSe Compared to Epsilon-Polytypes and Gamma-Polytypes. *Solid State Comm.* 1976, 19, p. 1079-1081.

267. A. Kuhn, A. Chevy, R. Chevalier, Crystal Structure and Interatomic Distances in GaSe. *Phys. Status Solidi* A, 1975, 31, p. 469-475.

268. R.M. Hoff, J.C. Irwin, R.M.A. Lieth, Raman Scattering in GaSe. *Can. J. Phys.*, 1975, 53, p. 1606-1614.

269. J.C. Irwin, R.M. Hoff, B.P. Clayman, R.A. Bromley, Long Wavelength Lattice Vibrations in GaS and GaSe. *Solid State Comm.*, 1973, 13, p. 1531-1536.

270. A. Polian, J.M. Besson, J.C. Chervin, Phonon Modes and Stability of GaS up to 200 Kilobars. *Phys. Rev. B*, 1980, 22, p. 3049-3058.

271. M.J. Taylor, Raman and Infrared Spectra and Vibrational Assignments of Gallium (II) Sulphide. *J. Raman Spectrosc.* 1973, 1, p. 355-358.

272. V.L. Solozhenko, O.O. Kurakevych, P. Bouvier, First and Second-Order Raman Scattering of B_6O. *J. Raman Spectrosc.*, 2009, 40, p. 1078-1081.

273. S. Ovsyannikov, A. Polian, P. Munsch, J.-C. Chervin, G. Le Marchand, T.L. Aselage, Raman Spectroscopy of $B_{12}As_2$ and $B_{12}P_2$ up to 120 GPa: Evidence for Structural Distortion. *Phys. Rev. B*, 2010, 81, p. 140103-1-4.

274. J.W. Pomeroy, M. Kuball, H. Hubel. N.W.A. van Uden, D.J. Dunstan, R. Nagarajan, J.H. Edgar, Raman Spectroscopy of $B_{12}As_2$ under High Pressure. *J. Appl. Phys.*, 2004, 96, p. 910-912.

275. M. Gauthier, A. Polian, J.M. Besson, A. Chevy, Optical Properties of Gallium Selenide under High Pressure. *Phys. Rev. B*, 1989, 40, p. 3837-3854.

276. V.V. Brazhkin, S.V. Popova, R.N. Voloshin, Pressure-Temperature Phase Diagram of Molten Elements: Selenium, Sulfur and Iodine. *Physica B*, 1999, 265, p. 64-71.

277. L. Properzi, A. Polian, P. Munsch, A. Di Cicco, Investigation of the Phase Diagram of Selenium by Means of Raman Spectroscopy. *High Pressure Res.*, 2013, 33, p. 35-39.

278. D. Orosel, O. Leynaud, P. Balog, M. Jansen, Pressure-Temperature Phase Diagram of SeO_2. Characterization of New Phases. *J. Solid State Chem.*, 2004, 177, p. 1631-1638.

279. E.C. Oliveira, E. Deflon, K.D. Machado, T.G. Silva, A.S. Mangrich, Structural, Vibrational and Optical Studies on an Amorphous $Se_{90}P_{10}$ Alloy Produced by Mechanical Alloying. *J. Phys. Condens. Matter*, 2012, 24, p. 115802-1-6.

List of illustrations

Chapter I..........5

Chapter II 30

List of tables

Résumé

Cette thèse porte sur l'étude des chalcogénures de bore sous conditions extrêmes. Après un bref examen de la littérature (Chapitre I) sur le bore et ses composés sous haute pression (HP), la partie expérimentale (Chapitre II) donne une description des appareils HP utilisés dans ce travail de thèse. Les techniques d'analyses employées sont décrites ainsi que les grands principes des calculs théoriques ab initio utilisés.

La partie suivante est consacrée à β-B_2O_3 et *r*-BS. Le chapitre III présente les résultats de diffraction X *in situ* à HP et les mesures de phonons (Raman et IR) de β-B_2O_3 à température ambiante. Les données expérimentales ont été examinées et complétées par des calculs ab initio. Avec le jeu de données obtenues, les descriptions complètes des modifications sous pression de la structure de β-B_2O_3 et du comportement des phonons en compression à température ambiante ont été faites.

Le chapitre IV présente les résultats de diffraction X in situ à HP et de spectroscopie vibrationnelle sur *r*-BS à température ambiante. En combinaison avec les calculs théoriques, la structure et la nature des phonons de *r*-BS sur une large plage de pression à température ambiante sont décrites. En outre, la formation d'une nouvelle phase HP métastable de BS est présentée et sa structure probable ainsi que son équation d’état sont discutés.

Le chapitre V concerne la première étude in situ de diffraction X sous HP-HT du système B-Se. Selon les résultats de diffraction X et des mesures Raman effectuées sur les échantillons récupérés, un nouveau composé a été synthétisé. Ce composé est métastable à l’ambiante. Sa composition chimique et sa structure probable sont discutées.

Mots clés: chalcogénures de bore, conditions extrêmes, haute pression, diffraction X.

Abstract

This thesis deals with the study of the boron chalcogenides under extreme conditions. After a short review of boron and boron compounds under extreme conditions (Chapter I), the experimental part (Chapter II) provides a brief description of the high-pressure devices used in this PhD work. The employed analytical techniques are described as well as the main principles of the performed *ab initio* theoretical calculations.

The following part is devoted to our experimental and theoretical studies of β-B_2O_3 and *r*-BS. Chapter III presents the results of *in situ* high pressure XRD and phonon measurements (Raman and IR) of β-B_2O_3 at room temperature. The experimental data were considered and completed with results of *ab initio* calculations. Based on the total obtained dataset the complete description of β-B_2O_3 structure change and phonon behavior under compression at room temperature are done.

Chapter IV contains the results of *in situ* high pressure XRD and vibrational spectroscopy studies on *r*-BS at room temperature. In combination with results of theoretical calculations the structure and phonon nature of *r*-BS in a wide pressure range at ambient temperature are described. Also, the formation of a new metastable high-pressure phase of BS is described and its probable structure and EoS are discussed.

The last part (Chapter V) concerns the primary *in situ* XRD HP-HT studies in B-Se system. Based on the results of XRD and Raman measurements of the recovered samples, a new compound was synthesized. This compound was found to be metastable at ambient conditions. Its probable chemical composition and structure are discussed.

Keywords: boron chalcogenides, extreme conditions, high pressure, X-ray diffraction.